Macroporous Fluorine Doped Tin Oxide Photoelectrodes for Solar Water Splitting

Danielle Victoria Jowett

Doctor of Philosophy

University of York

Chemistry

August 2016

Abstract

Fluorine doped tin oxide (FTO) is widely used as a back contact transparent conducting oxide (TCO) in photoelectrodes for solar energy applications. Using relatively complex methods, a variety of materials can be deposited over FTO to form porous electrodes, which are desired for their higher surface areas. The present work shows how it is conceptually much simpler to template the TCO electrode, producing macroporous electrodes, which allows relatively simple methods to be used to deposit secondary materials for solar water splitting.

Macroporous FTO electrodes (macFTO) were fabricated to give highly conductive and structurally ordered electrodes. The fluorine content was analysed using solid state NMR and was found to be as low as 0.5 atom%, 100 times smaller than the precursor Sn:F ratio. The capacitance of electrodes was used to determine the surface area enhancement of macFTO compared to planar FTO (pFTO), which was found to be 12 times greater.

As macFTO is an ordered porous, or photonic, electrode, there is a possibility that an increase in light absorption efficiency could be observed. An investigation found that the stop band of macFTO was angular dependent, and the electrode could enhance the lifetime of embedded dyes. The emission lifetime of embedded Rudcbpy, a ruthenium based dye, was found to increase by a factor of 1.8, while the lifetime of coumarin 440/460 was increased by a factor of 1.4 when the stop band overlapped the emission profile of the dye, consistent with literature.

Finally, visible light absorbing materials and catalysts for water oxidation were deposited over macFTO, showing that simple techniques could be used to deposit a variety of useful materials. Independently, both $BiVO_4$ and CdS nanoparticles were successfully deposited over macFTO. Only a low CdS nanoparticle loading was required to show that the macFTO electrodes were conductive and capable of supporting photocurrents, with up to a 100 fold increase in the photocurrent density observed compared to equivalent planar electrodes due to the surface area enhancement. The activity of macFTO-$BiVO_4$ electrodes towards water oxidation was then tested with the use of a co-catalyst (CoPi). It was found that the activity of the macroporous electrode was substantially better than equivalent planar electrode, with oxygen evolution rates of 74 µL hr^{-1} produced with a bias of 1.6 V_{RHE}, and faradaic efficiencies for oxygen evolution reaching 100%.

Table of Contents

Table of Figures

Table of Tables

Acknowledgements

Firstly, thanks to my two supervisors, Richard Douthwaite and Martin Cockett, without whom this work wouldn't have been possible. To the members of the RED group, past and present, especially Rob Mitchell and Natalie Pridmore, thanks for the help and advice, its guided me throughout my PhD, even after you moved on to bigger and better things!

For contributions to this work I would like to thank John (who worked very hard to get this project started); Pedro (for the NMR work) and Laurence (for help with the lifetime instrument). A special shout-out to Natalie (again), Sindhu and Alison for all your electrochemistry advice and I promised a special thanks to Philip Seaton for designing a bit of software for me… it made analysis of made data that much easier ☺

A massive *massive* thanks to our glassblower Abby, you made me so much glassware and tinkered with it so many times, I actually have no words to say how helpful you have been. Right at the end you and so many others helped keep me going, and for that I will be forever grateful. I will miss our chats. Also, I wish to thank Chris in the mechanical workshop and Chris and Tim in electronics for helping me with various parts of my project.

To all those in the office, thanks for putting up with me and keeping me sane! In no particular order, a big thanks to Dan, Tom, Ellis, Phil, Andrew, Yury, Chris, Sindhu (again), Natalie (again!), Ben (and all the chocolate in those last few weeks), Luisa (and your coffee), Ester, Lucy, Lewis and Lucia. My thanks also go to the team in teaching labs (David, Phil, Charlotte, Liza and Helen). You provided a welcome break from my research and inspired my new career!

I would like to thank my family for their unending patience and support, you kept me going through the many rough times. Grandad, you deserve a special mention for proof-reading my entire thesis several times! Finally, to my fabulous fiancée Jamie, you have supported me through the good times and the bad, a PhD is an emotional rollercoaster and without you I'm sure I would have fallen off. For all the times I was angry, sad, tired and just plain cranky – thanks for not giving up on me! I promise to be less cranky from now on! ☺

Thanks, everyone, for your support!

Declaration

The research presented in this thesis was carried out at the University of York between October 2012 and December 2015. This work is, to the best of my knowledge, original and my own, except for the following:

Part of this thesis is based on joint work with Mr Menglong Zhang (PhD student). The project was initially started by Menglong Zhang, and thus his contributions are as follows:

- Synthesis of some polystyrene templates, some of which were synthesised and characterised by Dr Robert Mitchell or Manglong Zhang
- Method development, including:
    - Synthesis of all planar electrodes and measurement of their conductivity
    - Optimisation of the synthetic conditions used to make the macFTO electrodes
    - Synthesis of electrodes for the study on changing the calcination temperature and changing the fluorine content
- Some diffuse reflectance spectra, as referenced in text
- Some XRD data, as referenced in text
- Some EDX data, as referenced in text
- Some SEM images, as referenced in text
- All TEM images, some of which were imaged by Dr Robert Mitchell
- Synthesis of CdS nanoparticles
- Development of CdS bath deposition method
- Deposition of CdS nanoparticles as either preformed nanoparticles or via the bath method

The majority of this work is contained within Menglong Zhang's thesis,[1] unpublished as of the date of submission of the present work.

Dr Pedro Aguiar ran and analysed the solid state ^{19}F NMR.

This thesis has not been submitted for any other degree at this or any other university.

Chapter 1
Introduction

Chapter 1. Introduction

1.1. The Energy Crisis

The history of solar energy conversion is longer than one might expect. In 400BC ancient Greeks and Romans were using the suns heat to warm areas of their home. Move forward to the mid 1800's and solar heat was being "harvested by dozens of scientists all over the world".[2] By the early 1900's, dozens of patents for the use of solar heat were being filed in the US patent office,[3] and by the mid-1900's wide spread interest developed in the solar photovoltaic field.[4-6] However, due to the drop in oil prices (1970-80's), funding support for the field dropped, and interest has only relatively recently been regenerated.[7]

One of the earliest pioneers in solar energy was Captain John Ericsson,[8] a naval engineer, who developed a steam engine driven by heat from the sun. In 1868 he published a paper where he said "(In) a couple of thousand years (we) will completely exhaust the coal fields of Europe, unless, in the meantime, the heat of the sun be employed",[8] some remarkable foresight. Today, we can apply the same statement to oil and natural gas reserves: ultimately, unless we can find an alternate energy source, we will exhaust our fuel reserves. But before this, another problem will develop: the burning of fossil fuels (and other carbon rich fuels) produces carbon dioxide, which contributes to global warming.[9] As more and more energy is being used every year, more carbon dioxide is being produced, contributing further to global warming. To reduce this, new and existing technology needs to be developed to harness energy with low/zero carbon content *before* fossil fuels run out. Such sources would include wind, hydro and indeed, solar power.

Global energy consumption is predicted to double from current levels (~13.7 TW) to 27 TW by 2050.[9] While estimated calculations show that the current levels of fossil fuels (including everything from gas and oil to coal, shale and tar) can sustain the world for several centuries (at an energy consumption of 25 – 35 TW),[9] a massive problem will develop in regards to climate change. To combat this, CO_2 emission levels are to be controlled,[10] and to be able to meet this control, carbon-free or neutral energy sources must start becoming prevalent. This could include nuclear fission, carbon capture and storage and/or renewable energy (with the largest supply being the sun).[9] Of these, there are various reasons as to why the sun, as a renewable energy source, is the most practical step forward for most countries.[9]

Solar energy is the most viable source of energy for many reasons, not only is there enough energy given out in 1 hour to power the planet for a year,[9,11-13] the technology is free from chemical and noise pollution,[11] so no harm to the environment or climate will come from its use,[14] and electricity production can be done in-situ.[11] Furthermore, some types of devices can be integrated with, for example, windows, thus providing decorative and even aesthetically pleasing uses.[13]

It is noted however, that the availability of solar energy from solar panels is restricted to daylight hours, meaning that if the energy is not used, it is lost. Consequently, methods of storing solar energy are needed, and this can be achieved in many ways.

1.1.1. Energy Storage

Commercial solar energy use is primarily through the use of silicon solar cells,[15] but dye sensitised solar cells (DSSC) are becoming more widespread.[11,16] Both silicon solar cells and DSSCs produce electricity directly and do not actually store the energy for later use. These types of devices can be coupled with, for example, a battery[9,17] to store the energy but this has its own drawbacks, such as cost and reliability.[18]

An alternative solution is to couple the solar cell to a chemical reaction. The choice of chemical reaction determines the fuel that is produced. For example, water is a cheap and abundant chemical, and can be split to form oxygen (Equation 1-1) and hydrogen (Equation 1-2),[19] of which hydrogen is a high energy density fuel by mass.

$$2H_2O \xrightarrow{h\upsilon} 4H^+ + 4e^- + O_2 \qquad E^\Theta = 1.23\ V_{RHE}$$

Equation 1-1

$$4H^+ + 4e^- \longrightarrow H_2 \qquad E^\Theta = 0.00\ V_{RHE}$$

Equation 1-2

Hydrogen is therefore highly competitive with conventional fuels by weight (120 – 142 MJ kg^{-1} compared to 20 – 60 MJ kg^{-1} for liquid fuels), but less competitive by volume (~8 MJ L^{-1} compared to 20 – 30 MJ L^{-1}) as shown in Figure 1-1[20]

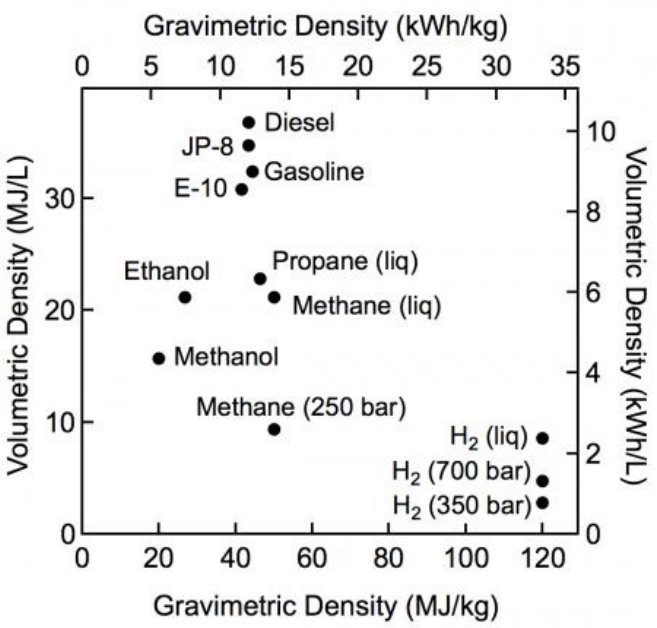

Figure 1-1: Energy density of selected fuels, reproduced from U.S. Department of Energy[20]

This has implications on how the hydrogen should be stored (gas *vs*. liquid), but overall suggests that hydrogen could be very competitive as a fuel. Furthermore, the combustion of hydrogen produces only water as a by-product. This means that not only is hydrogen combustion carbon free, but the product of the reaction can be used to re-form the fuel (by water splitting).

Although hydrogen is the fuel of interest, it is important to develop the oxygen evolution half reaction as well because this is the harder reaction to drive due to the complexity of the half reaction (4 electrons are required). Even if hydrogen evolution is made as efficient as possible, it will still be limited by the efficiency of oxygen evolution, so it is important to develop both half reactions to gain maximum efficiency.

1.2. Solar Water Splitting

Nature splits water every day in photosynthesis, a relatively well understood process. Nature uses abundant metals as catalytic centres, in combination with well-designed and highly specific proteins, to split water. The advantages of this are that photosynthesis is a fast and efficient process. However, the organic scaffolds are susceptible to oxidative damage and other chemical processes, which reduce the lifetime of the active sites. For nature, and thus living systems, this is not a problem because the active sites and proteins can be regenerated. However, in artificial systems it is not possible to have the same continual renewal of the active sites, leading to the need for an alternative approach.[21]

1.2.1. Bio-inspired and Molecular Approaches

Using a bio-inspired approach to device design is one method of fabricating devices that are capable of splitting water. The advantages of using enzymes as catalysts are; very fast turnover rates, commonly on the order of hundreds per second for water oxidation centres;[22,23] high efficiencies, so only a small amount of enzyme is needed; and high substrate specificities. These all contribute to forming a highly effective catalyst.

However, enzymes are not often desired as catalysts because they are very large, and the turnover per unit area is consequently often small. One option for increasing the activity of biologically based solar cells is to remove some of the peripheral scaffolding of the enzyme.[24] This effectively increases the number of active sites per unit area. However, by removing the active site from the enzyme the activity often decreases because the active site is no longer held in the precise orientation allowing for the most efficient activity.

An alternative approach is to try to replicate nature by developing molecular arrays that resemble enzyme actives sites.[25-28] For example, Brimblecombe *et al.*[29] have used a manganese cubane structure (Mn_4O_4), which resembles that of photosystem II (Mn_3CaO_4) to catalyse the oxidation of water. This functional analogue, in combination with a ruthenium dye to absorb light, drives water splitting with no external bias.

Andreiadis *et al.*[27] present in their review a series of artificial molecular assemblies based on natural compounds: they either mimic the structure or function of the target enzyme. Examples include analogues of the [Fe-Fe]-hydrogenase[30] and the [Fe-Ni]-hydrogenase,[31] while other molecular assemblies include catalysts based on earth abundant materials such as iron,[32] cobalt[33,34] and nickel.[35]

The advantage for using artificial molecular assemblies which replicate active sites is that more active sites can be fit on an electrode per unit area compared to an enzyme, which is a key limitation of enzymes. Additionally, materials tend to have a higher stability than molecules because the ligands on molecules can be more easily oxidatively degraded.

1.2.2. Photocatalytic Semiconductors

Another approach to solar water splitting is to use photocatalytic semiconductors. A semiconductor is a solid material that can conduct electricity under some conditions, but not others. Atoms have energy levels which are discrete, but when many atoms bond together in a lattice the energy levels, which are close together in energy, form bands (Figure 1-2). In metals (conductors) the filled energy levels are very close in energy to the empty energy levels, thus it requires little energy to excite an electron from the filled levels to the empty levels. Insulators have a large energy gap (the band gap) between the valence and conduction band. This large energy gap means that electrons cannot be excited between the two bands, and therefore the material cannot conduct electricity. A semiconductor has a band structure between a conductor and an insulator. There is a band gap, but it is small and therefore a small amount of energy, easily gained from heat or light, is enough to excite electrons between bands, allowing or electrical conduction. For photon absorption the energy of the photon must be equal than, or greater to the band gap.

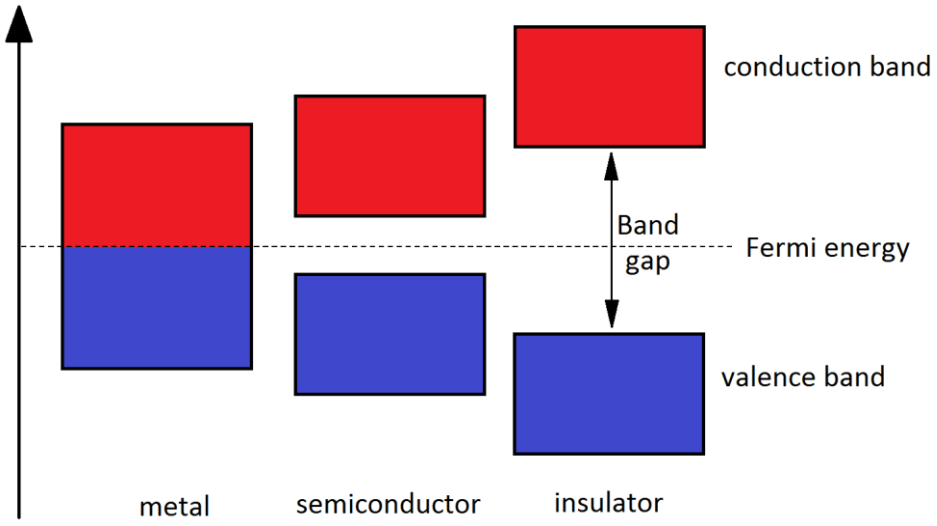

Figure 1-2: Diagram of a semiconductor band structure compared to a metal (conductor) and an insulator

Photocatalytic semiconductors are therefore semiconductors whose electrons can be excited by the application of light. The semiconductor is also capable of catalysing a reaction. Some of the most common semiconductors in current use are silicon and titania, both of which have band gaps larger than 3.0 eV, meaning that they are only active in UV light and access a small percentage of incident light on the Earth's surface. The standard potential for water spitting is 1.23 eV, or < 1000 nm, corresponding to IR and visible light. For reasonable efficiencies the semiconductor of choice should therefore have a band gap of ≤ 2.0 eV,[36] which accounts for the overpotential in a reaction. The overpotential is the deviation between the thermodynamic potential and the experimental potential required for the reaction.

The semiconductor should also have a long excited state lifetime in order to be most efficient. To reduce spontaneous emission and therefore increase the excited state lifetime the excited e^-/h^+ pair can be separated spatially, typically by addition of a secondary material which acts as an electron or hole sink. For this to work the band edges of the semiconductor and secondary material (herein the co-catalyst) must be appropriately aligned. The conduction band must be more negative than the proton reduction potential while the valence band must be more positive than the water oxidation potential (Figure 1-3).

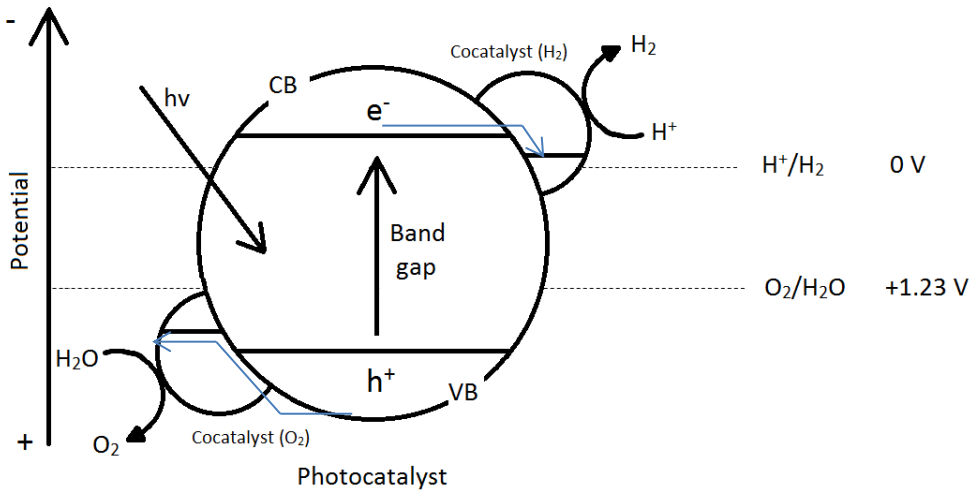

Figure 1-3: Schematic of an idealised water splitting photocatalyst with a co-catalyst for each half reaction.

Figure 1-4 shows the band gap compared to the calculated oxidation and reduction potentials for different known semiconductors. Clearly there are very few semiconductors which can

both absorb visible light and split water alone, which makes it far more likely that two semiconductors will be used in a commercial device, one for each half reaction.

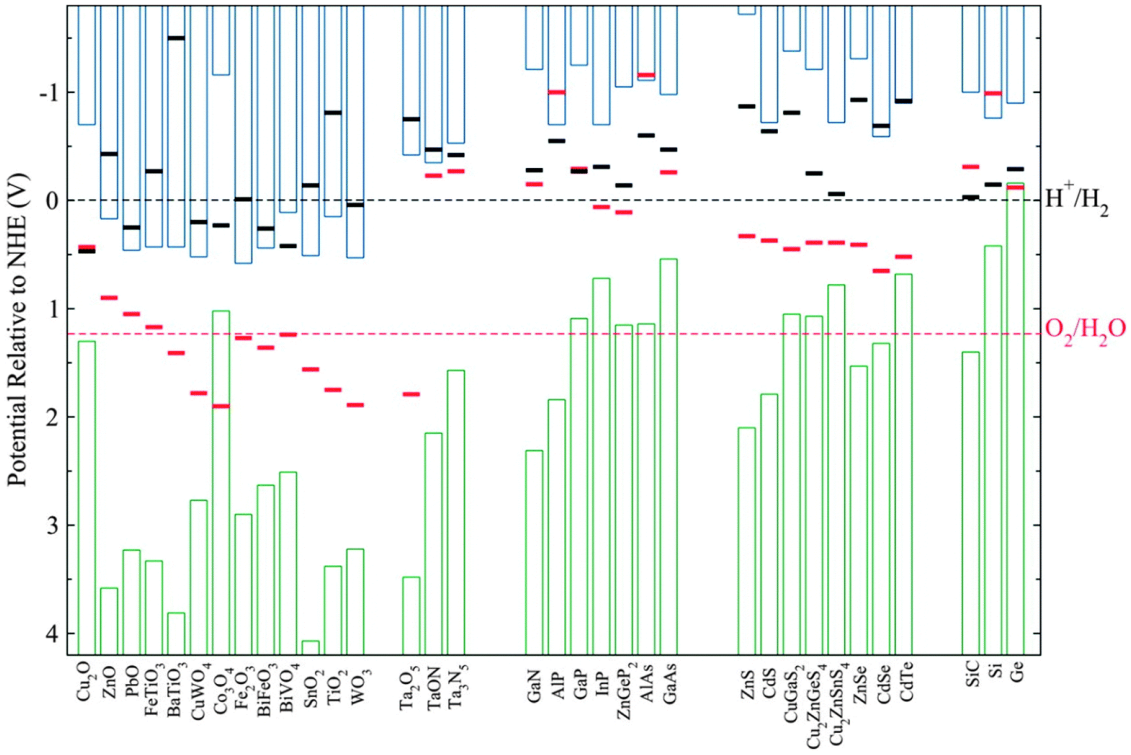

Figure 1-4: Band edge positions for several known semiconductors relative to the normal hydrogen electrode (NHE) at pH 0. The blue bars represent the conduction bands, while the green bars show the valence band. Overlaid are the calculated oxidation potential (red bars) and reduction potential (black bars) and the potentials for hydrogen evolution (black dotted line) and oxygen evolution (red dotted line). Adapted from Berardi et al.[37]

1.3. Solar Fuel Devices

A complete solar water splitting system must have light absorption, charge separation and catalysis. This can be achieved in a single system or by separating light collection and/or charge separation from catalysis, for example using a solar cell coupled with electrocatalysts. Additionally, the device must be made of cheap and abundant materials to ensure that it is a sustainable and affordable process. Completed devices should be scalable for mass production and they also are required to be stable over long periods of time.

1.3.1. Calculation of Device Efficiency

The efficiency of a water splitting device can be expressed in many ways. Typically, the yield of the desired material is related to the number of photons absorbed giving the quantum yield of the device (Equation 1-3):

$$\mathrm{QY}(\%) = \frac{\text{moles of product formed}}{\text{moles of photons absorbed}} \times 100$$

Equation 1-3

The quantum yield is wavelength dependent and therefore is often quoted for a wavelength range. More commonly the IPCE (incident photon to electron conversion efficiency) is quoted, as the devices are measured using electrochemical techniques. This relates the moles of charge carrier to the incident number of moles of photons (Equation 1-4):

$$\mathrm{IPCE}(\%) = \frac{\text{moles of charge collected}}{\text{moles of photons incident}} \times 100$$

Equation 1-4

For devices that have produced fuels, the solar to fuel efficiency (SFE) is quoted, which is based on the IPCE, but takes into account the number of electrons in the chemical reaction.

Alternatively, gas production rates are given as a measure of how efficient the device is. The gas evolution rate that is quoted will depend on which half reaction the device is focussed on (hydrogen or oxygen).

1.3.2. Device Fabrication

Two main device configurations will be discussed in this section, wired and wireless. Both types of device support the photocatalytic materials on a substrate. For a wired configuration, the two half reactions are linked *via* an electrical circuit while for the wireless configuration the two half reactions are linked via an electrical contact separating the two half reactions.

Figure 1-5 gives an example of a wired device. The left hand electrode consists of a hydrogen evolving catalyst (NiMoZn on nickel mesh), while the right hand side has both the photo-absorbing material (a triple junction Si cell) and the oxygen evolving catalyst (cobalt phosphate, CoPi). The CoPi catalyst has a cubane structure, much like the manganese cubane in photosystem II.

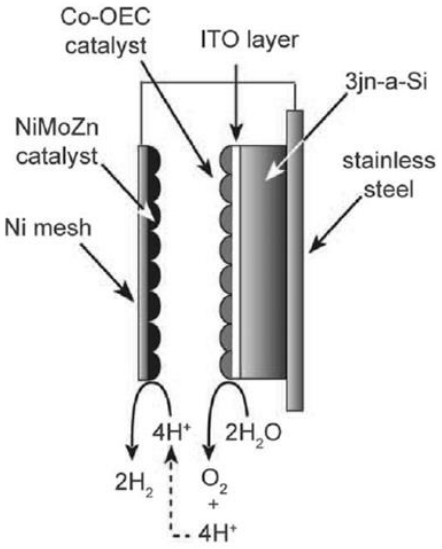

Figure 1-5: Wired device adapted from Nocera et al.[38]

Light is shone through the right hand electrode in the figure where it is absorbed by the Si cell. The excited electrons are then passed through the external wired circuit to the hydrogen evolving electrode, to reduce protons to hydrogen. Meanwhile the positive holes left behind oxidise water to oxygen. This particular device has a solar to fuel conversion efficiency of 4.8 % (the solar cell is 7.7 % efficient, photons to electrons). This device is one of the few that works reasonably well in near neutral conditions. Many of the examples that will be given in this chapter use highly alkaline or acidic conditions and are therefore less desirable. Acidic or alkaline conditions are undesirable because by changing the pH, although one half-reaction may become easier, the other half-reaction becomes harder, so overall there is no benefit. Additionally the materials may be less stable in high or low pH's compared to neutral.

The advantages of the wired set up are that each electrode can be in different conditions, thus optimising each half reaction individually. Additionally, collection of gases is conceptually much simpler as the two electrodes can be easily separated by, for example, a membrane. Furthermore, back reactions can be minimised as the two catalysts are separated.

On the other hand, devices set up like this may suffer large losses due to intrinsic resistances in the external circuit and because there are more redox transfers.[39,40] Furthermore, light must be shone through the over-layer of catalyst, which means that the catalyst layer must be thin and/or optically transparent for the wavelengths which are to be absorbed, otherwise the efficiency will drop because less light is being absorbed. Alternatively, the back contact can be transparent, allowing for back illumination, thus it doesn't matter how opaque the catalyst layer is. For example, a $WO_3/BiVO_4$ nanostructured electrode when illuminated from the back has twice as high a photocurrent (0.8 mA cm^{-2} at 1 V_{RHE} in 0.5 M Na_2SO_4) as when illuminated from the front (0.45 mA cm^{-2}, same conditions).[41]

Nocera *et al.* also report the same device as in Figure 1-5 but in a wireless configuration (Figure 1-6). The hydrogen evolving electrode is now attached to the rear side of the steel back contact. The advantage of a wireless configuration is that designs can move away from planar geometry to, for example, free standing particles in solution, and also realise much more practical cost targets.

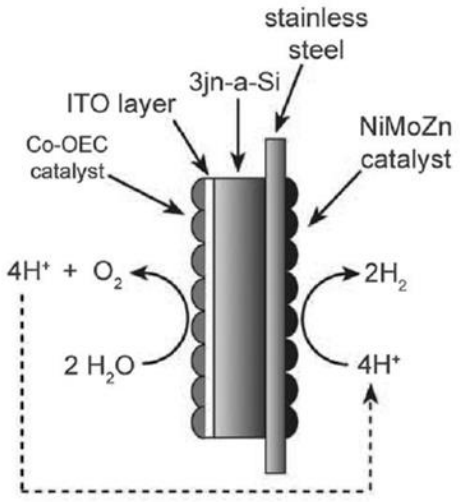

Figure 1-6: Buried junction, or wireless, cell, adapted from Nocera et al.[38]

However, the authors report that the solar to fuel efficiency of this device is only 2.5 % (for the same 7.7 % efficient solar cell). They do state that the wireless cell had not yet been optimised,

suggesting that by decreasing the anode-cathode ion transport distance the efficiency could be brought close to that of the wired configuration, alternatively (or additionally) "future designs (e.g. flow cell or perforated Si cell)" could increase the solar to fuel efficiency.

1.3.3. State of the Art Materials for Solar Water Splitting

The most efficient device to date is a p-$Ga_{0.52}In_{0.48}P$/n-GaAs/p-GaAs electrode[36] (Figure 1-7) which absorbs the entire range of the solar spectrum, giving a solar to hydrogen efficiency of 12.4 % (3 M H_2SO_4, Pt counter electrode). The electrode was reported to be stable, giving a photocurrent of 120 mA cm^{-2} over 20 hours, after which degradation was observed.

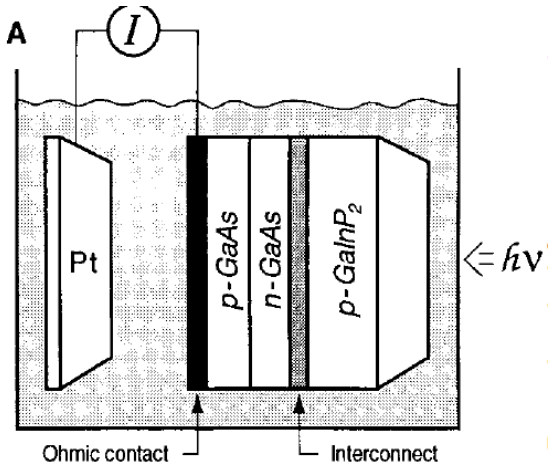

Figure 1-7: Device which uses multiple photo-converters to absorb the full range of the solar spectrum, adapted from Turner et al.[36]

A second cell of note is that of Rocheleau *et al.*[42] who reports a 7.8 % solar to hydrogen efficiency in 1 M KOH for a triple junction Si cell with hydrogen evolution catalyst on one side (CoMo) and oxygen evolution catalyst ($NiFe_xO_y$) on the other, in a wireless configuration. The stability of the electrode was tested over 7200 h and there were no signs of degradation. Additionally, the results were gained with no external bias, which is particularly good because this means the cell will run in just sunlight, no other energy is required. Currently most water splitting devices require an external driving force (the overpotential) and work is focused on developing cells that have no external bias. However, while the reported results are very promising for this water splitting device, take note of the harsh running conditions, which make this device not ideal.

Nocera *et al*.[38] (wired and wireless configurations of this device reported above) built on Rocheleau's work by using a similar set up in near neutral conditions. The authors report that their device will work in regular untreated river water, which is ideal as this will reduce running

costs. Additionally, more neutral pH's can reduce the corrosion rate of some semiconductors. The milder conditions make the device fabrication cheaper (as it can run in just water) but at the expense of the efficiency. The final remarks in the paper discuss how if a more efficient solar cell were used the device efficiency could be improved, opening up options for this particular cell.

One reason that Nocera's cell works so efficiently is that the device is much more stable than other working devices because the oxygen evolution catalyst can self-heal. During oxygen evolution, Co^{2+} dissociates from the electrode and is observed in solution. In the running conditions, Co^{2+} is oxidised to Co^{3+} which is in equilibrium with the Co^{3+} on the electrode (Figure 1-8). This equilibrium drives the reformation of the cobaltate cubane on the electrode surface, thus allowing the cell to maintain stability, which is particularly important. The main instability is from the nickel alloy catalyst for hydrogen evolution, which leaches over time and does not self-heal.

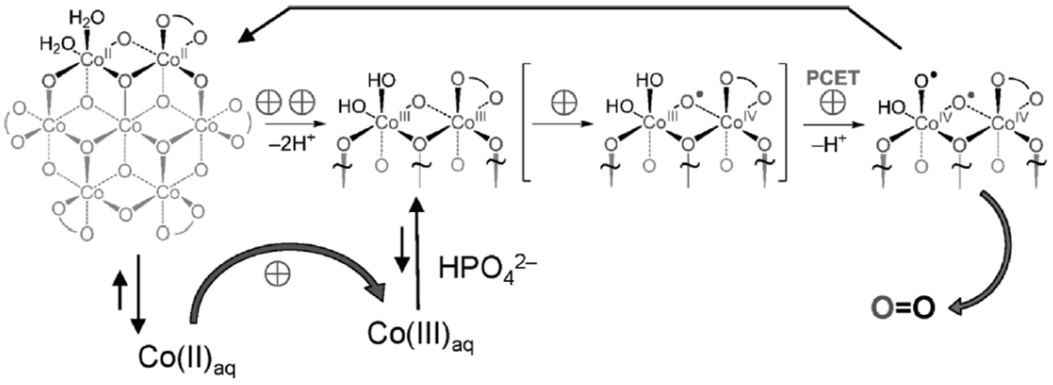

Figure 1-8: Proposed pathway for water splitting by Noceras Co-OEC. Of note is the cycle which allows any dissociated cobalt (II) to reform on the electrode surface from solution. Adapted from Nocera[43]

Materials with UV activity are not as desirable as those with visible light activity, as discussed, however, with correct manipulation reasonable efficiencies can be gained. For example, titania is a very popular semiconductor because of its cost effectiveness, stability and catalytic activity, and is used in a variety of applications from pollutant degradation in waste waters to hydrogen generation.[44-47]

Since the work of Fujishima and Honda in 1972,[48] where they first showed a useful method of splitting water on a titania electrode with a platinum counter electrode with no external bias, there have been many reports which use titania for water splitting. There are many of examples of solar water splitting cells, with various modifications and doping on TiO_2, used in

conjunction with other light absorbers and catalysts to produce efficiencies of ~10%.[45,49-54] Today, because of the wide band gap of titania, work is focused on choosing alternative materials with visible light absorption. It is far easier to choose an alternative visible light absorbing material than modifying and doping titania.

To summarise, although many materials have been studied for solar devices, the need for visible light active materials requires alternatives to silicon and titania to be investigated. Also, to reduce costs all materials should be abundant and readily available, therefore platinum and ruthenium, which are commonly used catalysts for water splitting, would need replacing with more abundant and less costly materials.

1.4. Planar Electrodes for Solar Water Splitting

Other than using multiple photo-absorbers, as described above, many other strategies can be used to increase the efficiency of solar water splitting devices. For example, thicker devices can absorb more light resulting in higher efficiencies.[55-57] The limitation on this is the ability of the semiconductor to separate and transport the charges, so as to avoid recombination. Thin film devices, while absorbing less light, are capable of separating more charges because the charge transport distance is smaller, resulting in a compromise between thickness and maximum light absorption.

Typically, thin films of nanoparticles are used as photo-absorbers, with nanoparticle sizes as small as 10 nm. Materials such as CdS[58-64], CdTe[65] and CdSe[66] have easily tunable nanoparticle sizes, and thus tunable colour and light absorption.[58] Additionally, the use of nanoparticles increases the available surface area which can lead to increased efficiencies.[56] Cadmium based nanoparticles are often used despite their toxicity and instability because of the high light absorption efficiencies. Xie *et al.*[64] improved the photocurrent density of TiO_2 from ~0 mA cm^{-2} under visible light irradiation to 0.25 mA cm^{-2} by incorporating low amounts of CdS nanoparticles. Ogale *et al.*[67] show a 20 times photocurrent improvement with CdS and a 10 fold increase in the IPCE. However, both electrodes were immersed in Na_2SO_4/Na_2S to compensate for the degradation of CdS which is a much easier oxidation reaction. The sulfide source acts both as a hole scavenger, reducing the degradation by oxidation, and as a sulfide source, stabilising the electrode.

Generally oxide semicondutors are more stable than sulfide semiconductors and popular examples include iron based compounds,[68-71] bismuth vanadate[72-79] and bismuth tungstate,[80] copper oxide,[81,82] tungsten trioxide[39,83,84] and perovskites.[85]

Hematite electrodes typically suffer from short electron transport distances (2-4 nm)[86] and slow oxygen evolution kinetics leading to low efficiencies. Despite this, several groups have developed cells with fairly high efficiencies. Mao *et al.*[86] increased the efficiency of a hematite cell from 2.2% to 8.4% with a silver doped core shell assembly. Hung *et al.*[71] increased the photocurrent density by 20 times, again by using a silver co-catalyst, although the cost of silver makes this technique undesirable. By nano-structuring electrodes, improvements in efficiencies have been observed compared to planar electrodes, this has been shown for hematite.[87]

Bismuth vanadate has also been shown to be able to split water with no co-catalyst, but at high overpotentials. It has recently developed much interest because of this and also because of its low toxicity, appropriate band gap and stability.[88] Thin films of bismuth vanadate can produce high IPCE's of up to 80%, but with an external bias of 1.6 V_{RHE}.[89] This bias is quite common for bismuth vanadate based electrodes.

Copper oxides are also a very promising material, but they suffer from stability issues. Wang *et al.*[90] show that introducing a TiO_2 layer between Cu_2O and CuO can increase the photocurrent from 1.3 mA cm^{-2} to 2.4 mA cm^{-2} (-0.36 $V_{Ag/AgCl}$ in 1 M K_2SO_4) while increasing the stability: the unmodified electrode (Cu_2O-CuO) retained only 32% of the initial current over 30 minutes, while the modified electrode (Cu_2O-TiO_2-CuO) retained 75% of the initial current over 30 minutes.

Tungsten trioxide is another semiconductor that is reported to have water oxidation capabilities, but again at high overpotentials[84,91] WO_3 was shown to be stable and efficient, despite the fact that it only absorbs in the blue portion of the solar spectrum. The photocurrents generated were shown to be significant, at 3 mA cm^{-2} at 1 V_{RHE} (1 sun in 1 M $HClO_4$).[92]

Table 1-1 summarises the key advantages and drawback for each material described in this section. Additionally the reader should take note of the relatively complex fabrication methods used to gain higher efficiencies with the materials described.

Table 1-1: Advantages and drawbacks of some semiconductors suitable for use in solar water splitting

Semiconductor	Advantage	Drawback
Cadmium sulfide (CdS)	Suitable band gap High light absorption efficiency	Poor stability Does not actually split water
Hematite (Fe_2O_3)	Suitable band gap	Short electron transport distance Low oxygen evolution kinetics
Bismuth vanadate ($BiVO_4$)	Suitable band gap Good oxygen evolution capabilities Low toxicity High stability	High overpotential
Copper oxides (CuO and Cu_2O)	Suitable band gap	Poor stability
Tungsten trioxide (WO_3)	Suitable band gap Good oxygen evolution capabilities	High overpotential

The use of two of these materials in tandem can further improve cell performance. For example, the combination of cadmium tungstate at tungsten trioxide[93] give a 7 fold increase in the degradation of methylene blue compared to cadmium tungstate alone and 2.3 times greater than tungsten trioxide alone.

While the potential for high photocurrents is promising with some of the above semiconductors, much higher efficiencies are gained when the semiconductors are used in tandem with catalysts because the catalyst can assist with the electron/hole separation (as described in section 1.3.1). Research is focussed on finding an earth abundant catalyst, rather than a precious metal one, because even though the precious metal catalysts have been shown to work very well they are expensive and not sustainable.[94-96] Earth abundant metals include Ni, Fe and Co.[38,81,85,97-100] For oxygen evolution, CoPi is particularly prevalent because of its high stability and ability to self-heal under working conditions (see Nocera cell, Figure 1-5 and Figure 1-6). There are several examples of using CoPi to improve the oxygen evolution capabilities of $BiVO_4$ and Fe_2O_3.[79,101-107] For example, the electrodeposition of a cobalt catalyst layer over α-Fe_2O_3[69] or $BiVO_4$[75] causes a ~350 mV cathodic shift, reducing the onset potential of water oxidation.

1.5. Porous Electrodes for Solar Water Splitting

In the examples seen so far the majority of electrodes have been planar in architecture, but by making the electrodes porous the surface area available for catalysis as well as the electrode-electrolyte interface area can be increased, and thus the efficiency can be increased. Typically this is done by making nanoparticles of the desired material and assembling the electrode in such a way so as to create pores between the individual nanoparticles.[108,109] Other popular methods include growing nano-porous materials, such as nanotubes.[110,111]

One such nanostructured example shows a helical $BiVO_4$-WO_3 array generating a maximum photocurrent density of 5.35 mA cm^{-2} at 1.23 V_{RHE} compared to < 1 mA cm^{-2} for a planar $BiVO_4$-WO_3 electrode and < 1.5 mA cm^{-2} for a planar WO_3 electrode.[112] Alternatively, WO_3-$BiVO_4$ nano-rods were reported to have a photocurrent density of 0.8 mA cm^{-2} (1 V_{RHE} in 0.5 M Na_2SO_4) compared to ~0 mV cm^{-2} for a planar $BiVO_4$ film under the same conditions.[41]

Figure 1-9 gives some of the different morphologies used by Choi *et al.*[76] to increase the photocurrent of $BiVO_4$ electrodes for solar water splitting. In 0.5 M phosphate buffer with 1 M Na_2SO_3 as a hole scavenger the photocurrent density of the electrodes (D, E, F) was found to be 0.5 mA cm^{-2} at 1 V_{RHE}. Addition of catalysts increases the photocurrent to 4 mA cm^{-2}. Planar $BiVO_4$ electrodes typically have low photocurrent densities because of surface recombination (as $BiVO_4$ has a short hole diffusion length of 150 nm[113]), so the photocurrent density reported by Choi *et al.* is on the same order as planar $BiVO_4$ electrodes described in other reports (0.25 mA cm^{-2}).[114] The main advantage presented by Choi comes when the catalyst is added –the surface area of the nanostructured $BiVO_4$ is much higher so there is more area available for catalysis which increases the photocurrent beyond that of the planar electrode.

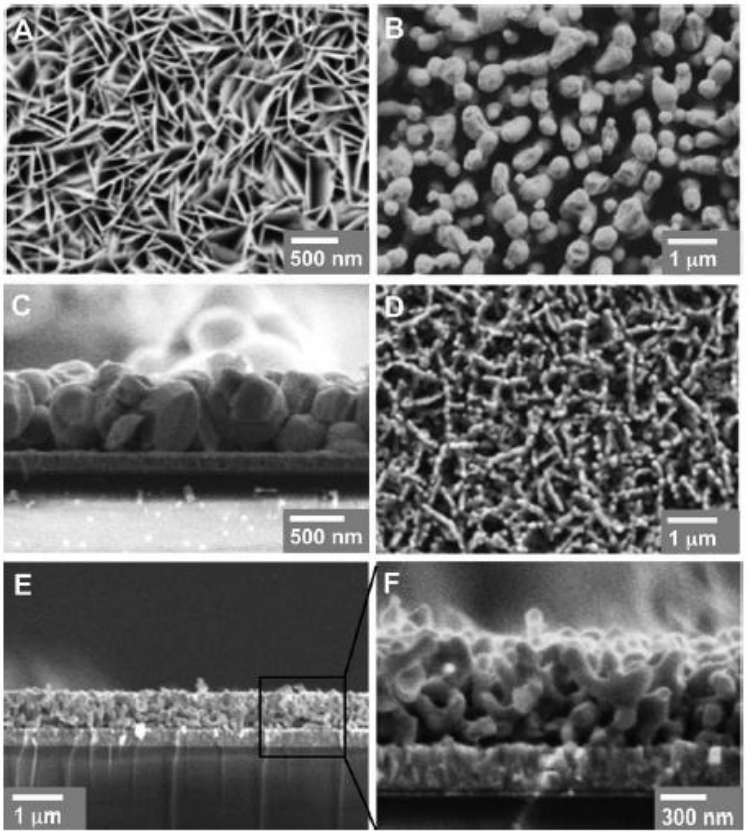

Figure 1-9: Examples of some different nano-morphologies used to increase the photocurrent of $BiVO_4$. Adapted from Choi et al.[76]

Another type of morphology is nano-pillars. If a layer of TiO_2 nano-pillars is used instead of a planar layer of TiO_2 (of the same thickness) the photocurrent density increases from 6 mA cm^{-2} to 11 mA cm^{-2} (note the electrolyte was 0.5 M LiI, 50 mM I_2, 0.5 M 4-tertbutylpyridine in 3-methoxypropionitrile).[57]

The major losses from porous electrodes are through the surface scattering of incident light. It has been shown that the scattering can be reduced by templating the materials into an ordered porous architecture. This is called a photonic material, or in the present work, 'macroporous' is used with the same meaning. There are several types of photonic crystal, classified by the packing. Most commonly opal assemblies (Figure 1-10a)[115] are used because they are easy to assemble from a solution of monodisperse spheres.[116,117] However, it can be difficult to make monodisperse spheres with an appropriate material, thus it is quite often the case that the desired material is templated around the spheres, forming an inverse opal structure (Figure 1-10b)[118]. Other structures mentioned in the literature include the diamond lattice (Figure 1-10c) [119] and the woodpile structure (Figure 1-10d) [120-122] which is useful for layer up assembly.

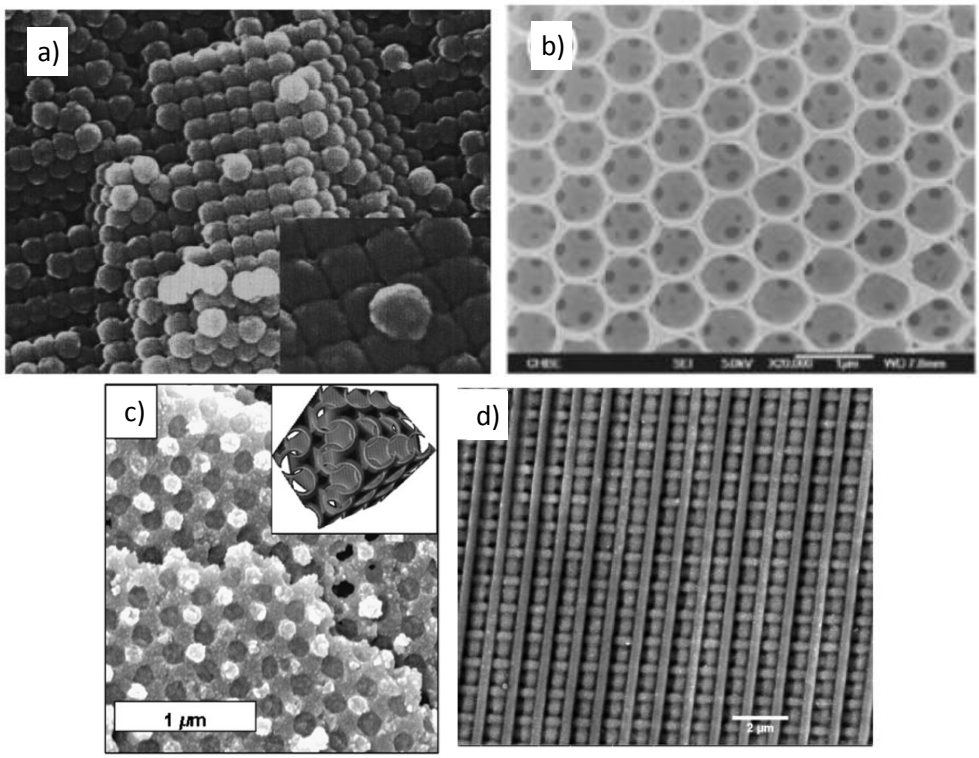

Figure 1-10: Different types of ordered porous networks. Images adapted from the respective references a) opal,[115] b) inverse opal,[118] c) diamond[119] and d) woodpile.[122]

1.5.1. Photonic Materials

Photonic materials are those which have a periodic modulation of the refractive index.[116,123,124] At defined wavelengths (λ) and incident angles (θ) Bragg diffraction will occur in these materials (m is the order of Bragg diffraction, 1): in much the same way as atoms diffract x-rays, photonic crystals will diffract incident light (Figure 1-11). If the incident light is on the order of 400 – 600 nm, and the interplanar spacing ($d_{h,k,l}$) is also between 400 – 600 nm, then the Bragg diffraction will occur in the visible region,[115,116,125] resulting in opalescent materials, such as opal stones, insect shells and butterfly wings.[126]

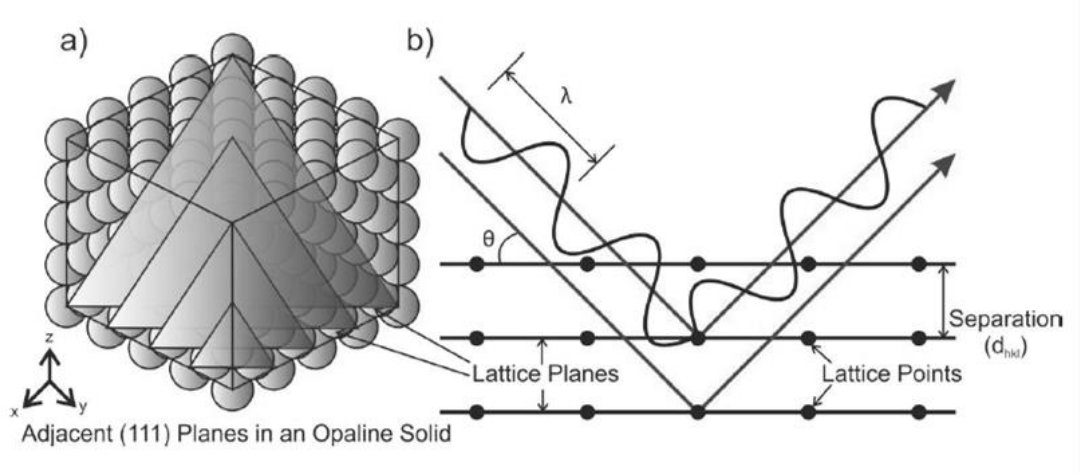

nce b

Figure 1-11: a) Representation of adjacent 111 planes in an opaline structure. b) Bragg diffraction of electromagnetic radiation from lattice planes. In this case the lattice points are colloidal crystal spheres. Adapted from MItchell[127]

Bragg's law (Equation 1-5) gives the conditions for coherent diffraction to be at its strongest. These intense diffractions or reflections give regions called 'stop bands' in photonic crystals – wavelength regions that are completely reflected by the photonic crystal.

$$m\lambda = 2d_{hkl}\sin\theta$$

Equation 1-5

The stop band position (λ) is dependent on the interplanar spacing (d_{hkl}), the average refractive index (n_{av}) and the angle of incidence (θ) according to Equation 1-6:[128]

$$\lambda = \frac{2d_{hkl}}{m}\sqrt{n_{av}^2 - \sin^2\theta}$$

Equation 1-6

The position of the stop band can therefore be shifted by changing any of these parameters. The interplanar spacing is dependent on the periodicity, so by changing the pore size the stop band position can be changed.[115,128-130] A different sized template can be used, or by increasing the thickness of the walls, the pore size can be changed permanently.[115,128,130,131] The pore size can be changed reversibly by applying an external force such as temperature[132,133] or magnetic field.[134,135] Stein *et al.*[136] give an example of an inverse opal ZrO_2 structure which has been templated around different sphere sizes (Figure 1-12, samples A-C). By increasing the template

sphere size the colour of the final material changes from purple through yellow to red and the stop band shifts from ~370 nm to ~570 nm.

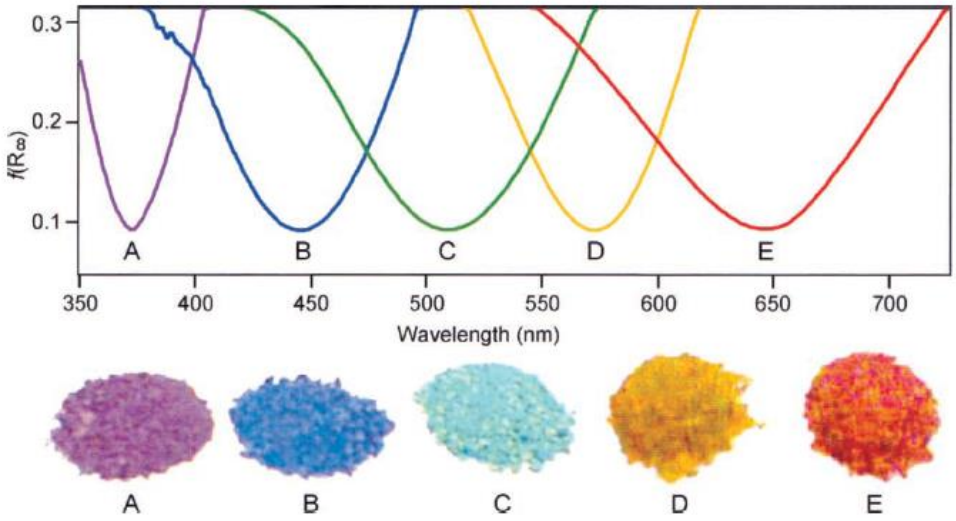

Figure 1-12: Samples of macroporous ZrO_2 with different pore sizes.Samples A-C have diferent pore sizes (200 nm, 250 nm, 285 nm respectively) while the pores in samples D and E have been filled with methanol to change the refractive index contrast (D is sample B filled with methanol and E is sample C filled with methanol). Reproduced from Stein et al.[136]

Changing the refractive index contrast[125,128,131,137] also yields stop bands in different positions. Samples D and E in Figure 1-12 show that by changing the infiltrating material from air (refractive index = 1) to methanol (refractive index = 1.33) the stop band is shifted to longer wavelengths. By increasing the refractive index of the lattice, or changing the wall thickness (filling factor) the stop band is shifted to longer wavelengths[65] and becomes deeper and wider due to the change in lattice parameters.

The stop bands in natural systems such as butterfly wings and beetle shells are three dimensional; the periodic modulation extends in all dimensions and thus the stop band is three dimensional. To create a fully 3D stop band, the structure of the photonic crystal must be of a very high quality,[49,125,129,138,139] for structures that are not as high quality, 2D[128,138,140] or even 1D[123,138] stop bands can form. Clearer, more intense stop bands can be formed in materials that have a high refractive index contrast.[128,141]

At the stop band edges, the group velocity of incident light is slowed by multiple coherent scattering.[124,125,129,138] This 'slow light' can increase the efficiency of a light driven process because the incident light has a higher probability of being absorbed (Figure 1-13). This effect can also contribute to emission rates: if the stop band overlaps the emission profile then the

emitted light is forbidden to propagate through the material and thus must be reabsorbed. The extent of the slow light effect can be measured through the lifetime of fluorescent dyes embedded in photonic materials. This phenomenon is under much debate at the moment, and there are arguments for[142-145] and against[65,117,140,146,147] it. However, few attempts have been made to determine the extent of the photonic effect and apply it to working systems.

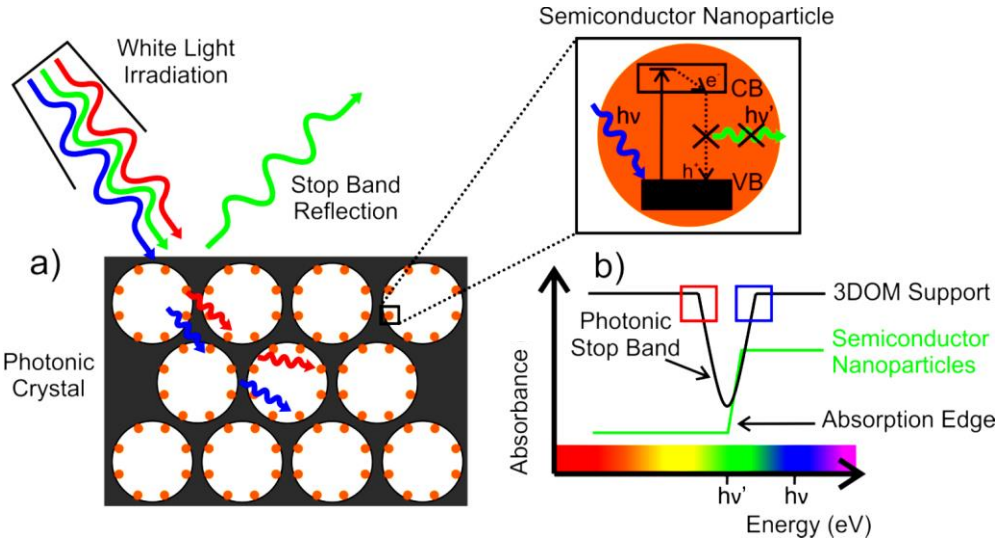

Figure 1-13: a) Schematic showing the photonic stop band effect: incident light is scattered multiple times in the porous structure and the ordered array of pores creates a region (b) where light cannot propagate (shown as the green wavelength), which results in inhibited spontaneous emission. Adapted from R. Mitchell[127]

1.5.2. Making inverse opals

Macroporous electrodes are typically made by using a sacrificial template, though other methods such as microfabrication[128] and gravity sedimentation[148] have previously been employed. The most common template to use is polystyrene spheres,[56,124,128,149,150] though other sacrificial polymers[128] and silica beads[125,151] can also be used. The advantage of organic templates is that they can be burnt away during the calcination step[56,57,124,128,152] (necessary to sinter the semiconductor) whereas silica spheres have to be etched out of the final material with concentrated acid.[125,131] Upon template removal, it is normal to observe a decrease in the pore size, due to contraction from the calcination stage. This is the liquid volume lost from within the precursor,[57] typically on the order of ~33%.[118]

The easiest way to deposit the sacrificial template on a back contact is to use vertical substrate withdrawal, or to slowly evaporate the solvent (Figure 1-14). The sacrificial template deposition can be controlled quite closely by changing the concentration of the deposition solution, as well as controlling other factors like temperature of evaporation or speed of

substrate removal. This is important because it has been found that the number of scattering layers in a photonic crystal can affect the photonic properties: too many layers and light scattering becomes the dominant effect and there is no longer a positive contribution from the stop band. The optimum number of layers was found to be 20-35 lattice planes.[143]

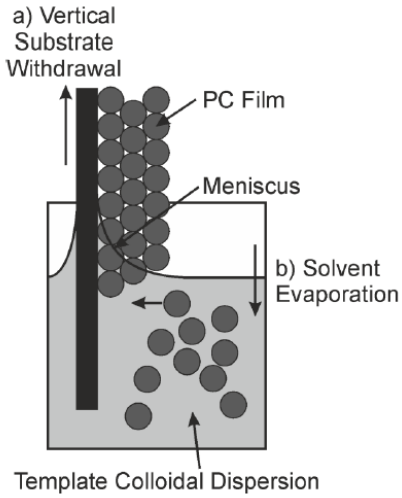

Figure 1-14: Deposition of polystyrene template for macFTO synthesis, adapted from R Mitchell[127]

In most cases the infiltration of the precursor solution is done by first making a sol gel solution with a low boiling point solvent such as ethanol.[57,118] Sol-gels are dependent entirely upon the materials that go into making them, so no two precursors are alike, which makes a general procedure for forming inverse opal macroporous structures of different materials difficult. Additionally, it is important to not overfill the template and form over-layers which will prevent the porous networks from being used effectively.[57]

To simplify the production of macroporous structures of different materials it makes sense to use the sacrificial template to form one macroporous material and then deposit other materials over this using simple techniques, for example drop casting of nanoparticles. This would then be a simple method to produce many different macroporous materials using one method. The macroporous material that will support the photo absorbers and catalysts needs to be carefully chosen because it would need to fulfil several criteria: it should be stable, cheap, earth abundant and conducting (to allow good electron transport in an electrode). It would also be advantageous to be transparent so that light can penetrate all the way through the material. There is a class of materials called transparent conducting oxides that satisfy these conditions. Of these materials, FTO (fluorine doped tin oxide) satisfies all the conditions.

FTO is chemically and temperature stable, with good mechanical toughness, as well as being made of earth abundant materials.

FTO is already widely used as the back contact in solar cells as it is easy to prepare, typically by chemical vapour deposition (CVD).[153] The synthesis of macFTO has been shown before[57] as a relatively simple process. If this is used as the back electrode, and other materials are deposited over the surface, it opens up the possibility for a variety of macroporous electrodes that can be made in a very simple way. This is of interest because currently all macroporous electrodes are made in different ways, that can involve difficult, or costly steps, and finding a simple, cheap and easy way of fabricating macroporous electrodes would provide a variety of macroporous electrodes. Briefly a typical synthesis of a macroporous electrode (Figure 1-15) may include deposition of sacrificial template (mono-disperse polystyrene spheres), infiltration of template with FTO sol-gel, solvent evaporation and electrode calcination to remove template and to sinter the FTO to ensure good electrical connection.

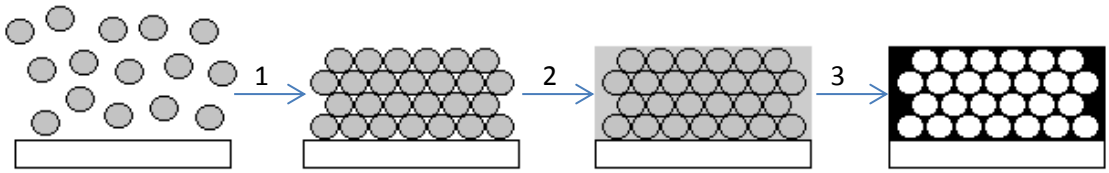

Figure 1-15: Scheme showing the synthesis of macFTO and the deposition of a secondary material. Step 1: deposition of polystyrene spheres, step 2: infiltration of FTO precursor mix, step 3: calcination to remove polystyrene template and sinter the macFTO.

1.5.3. Deposition of Secondary Materials

Secondary materials can be deposited in a variety of ways over macroporous electrodes. Several methods describe how to deposit and make nanoparticles *in-situ*, while others describe the *ex-situ* synthesis and subsequent deposition.

In-situ methods include the chemical bath deposition method (CBD)[115] which was used to deposit CdS nanoparticle layers over mac-SiO_2 and bath methods to deposit CdS nanoparticles whereby the electrode is dipped in a series of solutions to allow adsorption of the relevant species (Cd^{2+} then S^{2-} to form CdS) onto mac-TiO_2.[154] Other methods include hydrothermal deposition, for example Au nanoparticles over mac-TiO_2[152] and some materials can be photo-deposited, such as the Pt nanoparticles deposited on mac-TiO_2 as described by Ozin *et al.* [49]

Ex-situ methods include; deposition of CdTe quantum dots on mac silica via soaking[144], or drop casting of preformed nanoparticles CdSe-ZnS core shell nanoparticles on a macroporous titania structure.[119] In the case where dyes have been used to sensitise opal structures, the dyes are simply deposited using a soaking method: Rhodamine 6G, [117] Rhodamine B base, coumarin and tris(8-hydroxyquinoline)aluminium[155] have all been deposited over organic based opal structures.

Two of the simplest and most universal methods of depositing secondary materials in the macroporous host are drop casting and bath soaking. Figure 1-16 illustrates how either method will result in thin layers of a secondary material over the macroporous host.

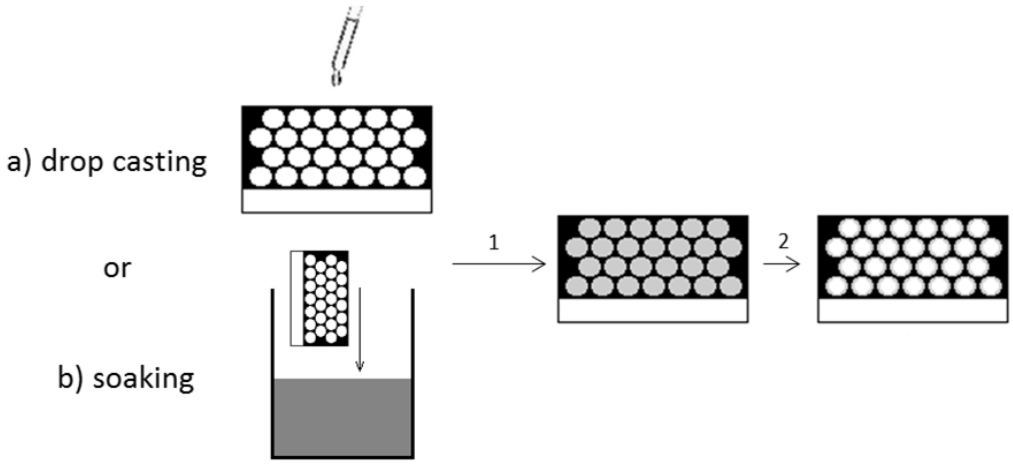

Figure 1-16: Deposition of secondary materials step 1: infiltration of desired secondary material by either a) drop casting or b) soaking followed by step 2: heating to remove excess liquid forming a monolayer of secondary material inside the pores.

1.5.4. Examples of Macroporous Materials Used for Solar Water Splitting

To illustrate the benefits of using macroporous host structures for solar water splitting several examples are given below. It is worth noting that there are not many examples for solar water splitting, there are more examples showing only photocurrent enhancements. Additionally, with the enzyme examples, NADH production fits into the natural water splitting sequence, though it actually produces H_2. It is used here as an example for comparison.

In the first example, two different enzymes NAD^+ (nicotinamide adenine dinucleotide) and GO_x (glucose oxidase) were both immobilised on macroporous gold electrodes (templated over silica spheres which were later etched away before immobilisation of enzymes).[156] Szamocki *et al.* show that by using a pore size of 680 nm and 5 ½ pore layers the activity of the electrode can increase 10 fold over planar electrodes for glucose bio-sensing. The authors also state that

the activity of the electrodes could be increased further by using a thicker electrode (more layers), at which point there may be less control over the number of layers. The number of layers is important because it impacts on the surface area of the electrode. If the number of layers is not controlled, then the surface area is not known and the activity cannot be calculated accurately.

A secondary example uses macroporous TiO_2 loaded with CdS quantum dots. The authors show that by using a smaller pore size (280 nm compared with 900 nm) the loading of the CdS can be increased and therefore higher photocurrents are achieved (4.84 mA cm^{-2} compared to 3.02 mA cm^{-2} at 0 $V_{Ag/AgCl}$). The solar to hydrogen efficiency was calculated to be 2.62 % for the 288 nm diameter pores.[154]

Another example shows that there is a 6.5 times increase in the solar to hydrogen conversion efficiency of a $BiVO_4$ film when moving from a planar film to a macroporous film, the photocurrent density increases from ~0.1 mA cm^{-2} to ~1.5 mA cm^{-2} at 1.23 V_{RHE}.[157]

Chen *et al.*[129] showed that the absorption spectrum of a WO_3 electrode could be enhanced in different regions according to the position of the stop band and the photocurrent showed an enhancement of 3 times at $2V_{SCE}$ (0.1 M Na_2SO_4) when the stop band was overlapped with the absorption profile of WO_3.

In a separate example, Lopez-Lopez *et al.*[158] showed that the photocurrent obtained from a SiO_2 or TiO_2 photoelectrode can be enhanced by a photonic structure, and the enhancement is dependent on the angle of illumination, with the greatest enhancement being 1.2 times at 50° incidence. This is where the stop band edge overlaps the emission profile most strongly.

1.6. Summary and Concluding Remarks

Due to the depletion of fossil fuel resources, alternative energy sources are becoming increasingly necessary. Solar energy is one of the most promising renewable sources, and with the development of storage methods, such as solar fuels, power would be able to be used wherever and whenever it was needed. Hydrogen is an ideal solar fuel because it has a high energy density by mass and is carbon-neutral when burnt.

Solar water splitting has been attempted many times with many different materials. Some devices use a bio-inspired approach with enzymes or active sites catalysing water splitting; others use photocatalytic semiconductors. While enzymes are highly specific and efficient, they take up large amounts of space due to the size of the peripheral protein. In order to increase the number of active sites per unit area photocatalytic semiconductors can often be favoured. There are many different known semiconductors, most of which are unsuitable due to their band gaps: the band gap should be < 1.23 eV to take advantage of visible light. Additionally, the photocatalytic semiconductor must be abundant and cheap so as to be scalable and affordable. A final challenge is charge separation: to ensure efficient devices the semiconductor must be able to separate the photogenerated electrons and holes, avoiding spontaneous recombination.

Semiconductors can be used in tandem with other semiconductors/metal catalysts to broaden the absorbing range and/or increase catalytic activity towards water splitting. There are two key device designs considered in the present work: 1) wired devices (where each half reaction of water splitting occurs on different electrodes) and 2) wireless devices (where the two half reactions occur on opposite sides of the same electrode). Wired devices are typically used because it is conceptually easier to make two electrodes, one for each half reaction, as well as being easier to separate the gases for measurement. However, ultimately a wireless device is desired because it would be more portable and involve less charge loss over the whole system.

Several suitable semiconductors have been used commonly in the literature (described in section 1.4, Table 1-1). Of these, both $BiVO_4$ and WO_3 have limitations which can be fairly easily overcome. A high overpotential can be overcome by using a secondary material in tandem to do the catalysis. The fact that the materials have suitable band gaps and good stability (issues that are not as easily overcome) makes them two of the better choices presented. CdS is also of interest because of the high light absorption properties. While it will

never be a practically used material it will be very useful in proving some key concepts in the present work.

Current electrodes for solar water splitting devices are typically made from planar layers of semiconductors. The limitation of this approach is that there is a relatively small surface area available for catalysis, but by making the electrodes porous there is an increase in the surface area available for catalysis. Several examples exist demonstrating the use of porous architectures for solar water splitting, but a major limitation is from surface scattering.

One way to circumnavigate the losses in efficiency through surface scattering is to template the electrode into an ordered porous network. This type of electrode is called photonic, or macroporous, and can gain benefits from increased absorption due to multiple coherent scattering, resulting in increased absorption, and from the stop band, where light is forbidden to propagate through the material. If the emission band is aligned with the stop band then emission can be forbidden, resulting in increased efficiencies.

Unfortunately, making macroporous electrodes of different materials is not trivial: even though a sol gel technique is used to make most macroporous electrodes, the exact conditions vary depending on the material; there is no common method. To make the synthesis of macroporous electrodes easier it would make sense to produce a template macroporous electrode from a conducting substrate, such as fluorine doped tin oxide (FTO). FTO is already known as a back contact in solar cells, and because the synthesis of macroporous FTO (macFTO) is simple it follows that macFTO could be used as a back contact. The use of macFTO would then allow the subsequent deposition of other materials (producing macroporous electrodes of other materials) *via* simple fabrication methods such as drop casting or soaking.

In conclusion, it is clear that a lot of development is still needed to improve the efficiency and stability of solar fuel devices. Materials used need to be abundant and active under visible light irradiation, as well as being stable for long periods of time. Improving the oxygen production half reaction is particularly important as this is generally the limiting side for overall device efficiency because of the complexity of the reaction. Efficiency can also be improved by structuring the material or the support material as this may allow an enhancement in device performance for any given material. Of particular interest is the photonic or macroporous structure which has been shown to increase the efficiency of solar water splitting devices through both a surface area increase and through the photonic effects.

1.7. Aims of the Project

The overall aim of this project is to demonstrate that by templating the back electrode the efficiency can be increased over a planar electrode. Here efficiency is defined as how much light per unit area is absorbed, and increasing the efficiency would mean being able to reduce losses in the system from, for example, spontaneous recombination. Additionally, it will be shown that other materials can be easily deposited over the back electrode to produce complex architectures (macroporous electrodes) using simple and traditional techniques, much simpler than trying to template the material into the complex architecture itself.

To achieve this, macroporous electrodes must first be made to a high quality and the properties such as conductivity determined. Chapter 2 describes the synthesis and characterisation of macFTO electrodes.

Further to this, as macroporous electrodes can produce beneficial effects from the structure, slow light and the stop band, chapter 3 aims to determine the extent of these effects. It will be determined if the photonic lattice can affect the lifetime of embedded fluorophores by extending the lifetime of said fluorophores.

Finally, in chapter 4 the macFTO electrodes will serve as a template (back electrode) for deposition of light absorbing and catalytic materials. This will simultaneously demonstrate that not only can several different materials be easily and simply deposited over macFTO to form macroporous networks of different materials, but also that the efficiency can be increased with the use of the ordered porous network over planar electrodes. This increase in efficiency can come mainly from the increase in surface area when moving from a planar electrode to a porous electrode, and also from the photonic effects, described in chapter 3. If the materials deposited give high photocurrent densities they can also be tested for activity towards water splitting (with the focus being water oxidation) with the ultimate goal of producing a complete working device that needs no bias to split water, just natural sunlight.

Chapter 5 concludes the present work and shows directions the work could take in the future. Chapter 6 describes the experimental techniques, while chapter 7 (the appendix) gives some extra information and figures relating to the work.

Chapter 2

Fabrication and Characterisation of Macroporous FTO Electrodes

Chapter 2. Fabrication and Characterisation of Macroporous FTO Electrodes

2.1. Introduction

It is important, when designing a photo-electrode, to consider the way in which light will interact with the electrode to generate charges, as well as the subsequent charge transport distances and charge mobility. When designing a 3D photo-electrode, it is also important to consider how to utilise the entire structure efficiently for both light absorption and catalysis. When optically opaque materials are illuminated the internal structure will not be illuminated to anything like the same extent as the outer surface, so there will be little benefit from making a large-volume porous material as most of the light will not be used efficiently. To this end, it is essential that an optically transparent material be used. Additionally, the surface area of large-volume porous materials will be substantially increased, thereby increasing the available sites for catalysis. Further to this, to ensure good charge transport and thus efficiency, the material should also have high conductivity. These three properties (optically transparent, large surface area and high conductivity) are very important, and are not always found together, so material choice is the first important decision to make when designing photo-electrodes.

Transparent conductive oxides (TCO's) are a class of material that fulfil these three requirements and are thus ideal for application as porous electrodes in the subsequent work. TCO's have widespread use in optoelectronics,[159] including a variety of solar cells[160,161] and flat panel displays.[162,163] One well-known and currently widely used material is indium doped tin oxide (ITO), which can be considered unsuitable compared to other TCO's due to the rarity of indium, and its consequent expense. Other important TCO's include AZO (aluminium doped zinc oxide) and FTO (fluorine doped tin oxide). TCO's are often doped as this increases the conductivity of the oxide.

FTO is relatively cheap and is easy to deposit on planar substrates. There are many synthetic routes for this deposition, including chemical vapour deposition,[153,164] spray pyrolysis[165] and more facile solution routes.[118,166] In each case, the resulting films are normally crystalline, with

good conductivity and small grain size. These parameters can be controlled by various heat treatments,[57,167] the concentration of precursors[168] and by changing the fluorine content of the precursor material.[169,170] The doping level or fluorine content of FTO films is often determined using Hall effect measurements[171] which assesses the mobility and carrier concentrations in a film. This type of measurement does not give a direct measurement of the fluorine content, and, in fact, it is not common for the actual fluorine doping level to be quantitatively assessed.

FTO is widely used as a back contact for electrodes used in solar energy applications,[161,165,172] because of its excellent optical and electrical properties.[173] Most of these applications use FTO as a planar electrode on which to deposit other materials, so there are few reports where the FTO electrode is structured. One example is the development of the macroporous fluorine doped tin oxide (macFTO) structure by Yang *et al*,[57] upon which the work in this thesis is based. By structuring the back contact FTO electrode, a more convenient method of enhancing the surface area is uncovered because many visible light absorbing materials suffer from short charge transport distances (on the order of 5-100 nm).[72,174,175] As FTO is a conductive material the charge transport distance is typically longer than in other semiconductors.[176] This increased charge transport distance would effectively reduce recombination by separating electrons from holes and increase the efficiency of solar fuel devices.

Although macroporous face centred cubic (fcc) structured FTO has been used to enhance the light collection efficiency,[57,177,178] there are not any examples of using these structured porous materials for photoelectrocatalysis. The combination of good conductivity and transparency should make FTO an ideal material. Further to these properties, ordered macroporous materials have been shown to display several beneficial phenomena, including the 'slow light effect' and the photonic band gap.[57,119,125,129,152,179-181] The slow light effect is actually an increased optical path length deriving from multiple coherent scattering, which allows any photons that are not initially absorbed by the material to have a greater chance of being absorbed. Ultimately this increases the efficiency of ordered porous materials. The photonic band gap is a wavelength region that is completely reflected by the host material, arising from Bragg reflections. If the stop band region is aligned with the optical profile of a light absorber then the overall device efficiency can be increased. This increase comes from the fact that light with the wavelengths of the stop band cannot propagate through the material thus emission cannot occur, which can be observed experimentally by an increase in the fluorescence lifetime of the light absorber[115,119] or by studying the absorption profile.[129,155]

Ordered macFTO electrodes are made based on the work of Yang *et. al.*[57] and this chapter briefly describes the fabrication of such electrodes and goes on to characterise the conductivity and the fluorine content of macFTO electrodes. Finally, the photoelectrocatalytic properties are probed using electrochemistry to determine the activity of macFTO electrodes to the water splitting reaction, with the main focus being the oxygen evolution reaction. Throughout, the macFTO electrodes will be compared to planar FTO electrodes (pFTO) to ensure that structuring the electrodes does not significantly change the electrode properties compared to the well-known thin films of FTO. There were two different pFTO reference electrodes: a commercial electrode obtained from Sigma Aldrich, and pFTO made in house using a spray coating method. The first FTO reference allows for comparison to current commercial FTO while the latter planar FTO reference allows for direct comparison between the precursor FTO solution used in this work and commercial FTO. If the two planar references are similar then it can follow that the macFTO made using the FTO precursor solution in this work should also be similar, which is useful when direct comparison between commercial pFTO and macFTO is not possible. The comprehensive development and optimisation of macFTO electrode synthesis was performed in the group by M. Zhang.[1]

2.1.1. Aims

The synthesis and characterisation of macFTO electrodes is presented in the following chapter. Initially the conductivity of the electrodes is presented, followed by how changing the fluorine content and changing the calcination temperature affects both the structure and properties of macFTO electrodes. Finally the photoactivity of the FTO electrodes is presented alongside a study for photocatalytic activity towards water splitting. Ultimately this chapter aims to show if macFTO is conductive and can therefore support photocurrents, and how high a photocurrent can be supported.

2.1.2. Electrode Notation

Herein all experiments use supported materials (electrodes) unless otherwise stated. The electrode notation is as follows: where ‘FTO’ is prefixed by ‘mac’ the FTO electrode is macroporous, and where the prefix is ‘p’ the electrode is planar. For electrodes calcined at different temperatures, ‘FTO’ is followed by a sequence of three numbers denoting the calcination temperature in degrees centigrade, for example macFTO-450 describes a macroporous electrode of FTO calcined at 450 °C.

2.2. Conductivity of planar FTO Electrodes

It is important for the macFTO electrodes to be highly conductive so as to allow good electron transport and thus minimise efficiency losses through recombination. For planar electrodes the sheet resistance was measured using a 4-point probe technique, which yields the resistance in Ω m^2/m (ohms area/length). When this value is then divided by the sheet thickness, the units simplify to Ω. For sheet resistance this is commonly referred to as Ω square (to signify that this is a sheet resistance value). The 4-point probe technique requires a good electrical contact with the electrode, which is obtained using pressure. For the planar samples this is not an issue because the samples are planar and compact. For the macroporous samples this is not ideal as the macroporous structure is delicate and cannot be placed under too much pressure as the structure may crumble.

As an alternative, planar FTO electrodes synthesised under the same conditions as the macFTO electrodes, were studied. Theoretically the sheet resistance should be similar as the samples are identically made, except for the template. Sheet resistance measurements were all conducted at room temperature by M. Zhang in the group and are presented briefly here.[1]

The reference commercial pFTO had a sheet resistance of 8 Ω square (determined using a 4-point probe method), which correlated well with the published value of 7 Ω square.[182] The best spray coated pFTO had a sheet resistance of < 10 Ω square, which is comparable to the reference pFTO. As the precursor solution used to make the pFTO and macFTO is the same, it can be assumed that the composition of the final material in both cases will be very similar, and thus the sheet resistance should be similar. However the grain boundary resistances have to be taken into account, as this is the major resistive component in conductive polycrystalline films. In pFTO and macFTO samples the grains were found to be of a similar size by SEM. For pFTO there are many grains interconnected, so if one boundary was particularly resistive there would be an alternative conductive route. Although the total thickness of the macFTO electrodes is greater than that of the pFTO, the FTO layer (the wall) is thinner. Therefore if some of the grain boundaries are particularly resistive the whole sample could be more resistive than expected. This will impact on any catalysis that the electrodes will later support because it will not be as easy to transport the electrons/holes through the electrode. However the sheet resistance results are positive and the electrodes were taken for further study.

It was thought that changing the fluorine content may affect the sheet resistance, so to investigate this, pFTO electrodes were prepared from precursors with different Sn:F ratios. It

should be noted that the final calcination step results in liberation of HF or C_xF_y products meaning the final F-content is often unknown. M. Zhang found that electrodes with high precursor Sn:F ratios (≥ 1) gave large sheet resistances, with values > 20 Ω square, while electrodes made with low precursor Sn:F ratios (< 1) had sheet resistances ≤ 10 Ω square. These sheet resistance values suggest that electrodes made using lower precursor Sn:F ratios are slightly more conductive than those made with higher Sn:F ratios, but overall the sheet resistances are broadly similar suggesting that there is little difference in the conductivity when changing the fluorine content.

The sheet resistance may also change as a function of calcination temperature. Several electrodes calcined at temperatures of 350, 400, 450, 500, 550 and 600 °C were studied. It was found that electrodes calcined at 550 and 600 °C gave sheet resistance values of > 20 Ω square, while at lower calcination temperatures the sheet resistance is lower, at ~10 Ω square. It appears that the calcination temperature also does not have a significant effect on the sheet resistance of the pFTO electrodes, with the electrodes with the highest conductivity (lowest sheet resistance) formed at temperatures of *ca*. 500 °C.

These sheet resistance values can be supported using an electrochemical technique, cyclic voltammetry (CV). A CV indicates how easily the electrodes can support the ferrocene redox couple using peak position and height. Ferrocene is a widely used internal standard[183] because it is a stable, inert and electrochemically reversible species; it is also used to probe electrode surfaces electrochemically.[57,73] The redox peak height of ferrocene gives an indication of the number of electrons transferred in the reaction, while the peak shape gives an indication of how reversible the reaction is on the electrode surface. The final information that can be extracted from the cyclic voltammogram is the peak position. If the redox peaks are close together then the sample is more conductive than if the peak were further apart.

For example, redox peaks which are symmetrical about the redox potential indicate that the redox reaction is electrochemically reversible, as seen in the current work. The shape of the CV depends on the rate of electron transfer compared to the rate of mass transfer. When the rate of electron transfer is fast, the redox peaks are close together (Figure 2-1a). As the rate of electron transfer becomes relatively slow (Figure 2-1d) the redox peaks become more separated.[184]

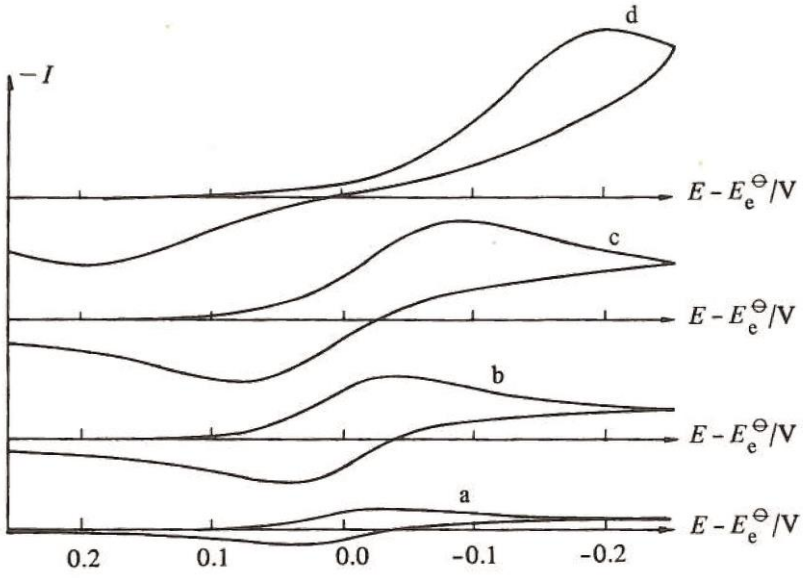

Figure 2-1: The dependence of the shape of the CV on the rate of mass transfer compared to electron transfer; a) relatively fast electron transfer to d) relatively slow electron transfer. Reproduced from[184]

Ideally, the oxidation wave maximum (E_a) is separated from the reduction wave minimum (E_c) by 59 mV (for a one electron process). This is derived from the Butler-Volmer and Cottrell equations,[184] which reduce to Equation 2-1.

$$E_a - E_c = \frac{0.059}{n}$$

Equation 2-1

where n is the number of electrons in the redox process. It should be noted that systems often deviate from the ideal value of 59 mV because of inherent resistances in the system, i.e. solution resistance: typical peak to peak separations are of the order of 100 mV. A smaller peak to peak separation indicates that the studied process has fast kinetics and reaches equilibrium quickly, i.e. electrons are transferred quickly. This therefore infers that the electrode surface is more conductive. Redox peaks which are well separated (much greater than 100 mV) indicate poorly conductive electrodes.[184] Additionally, the peak height or current can give a rough indication of the surface area; take for example two samples, A and B, where sample A has a greater surface area than sample B but is otherwise the same. If the peak current for sample A is greater than that of sample B then sample A is undergoing more redox reactions and this is correlated to the larger surface area.

Figure 2-2 and Table 2-1 show the peak data for pFTO electrodes calcined at different temperatures (prepared by M. Zhang) compared to a commercial planar FTO electrode. The

pFTO electrodes show increasing peak separation from 160 mV to 650 mV (see ΔE_p in Table 2-1) with increasing calcination temperature, indicating decreasing conductivity, which is consistent with the conductivity results. If the pFTO electrodes of different calcination temperatures are compared to the commercial pFTO, it can be seen that the pFTO electrodes made with lower calcination temperatures have better conductivity (closer redox peaks) than the commercial pFTO. At 800 °C calcination temperature the conductivity is worse than the commercial pFTO.

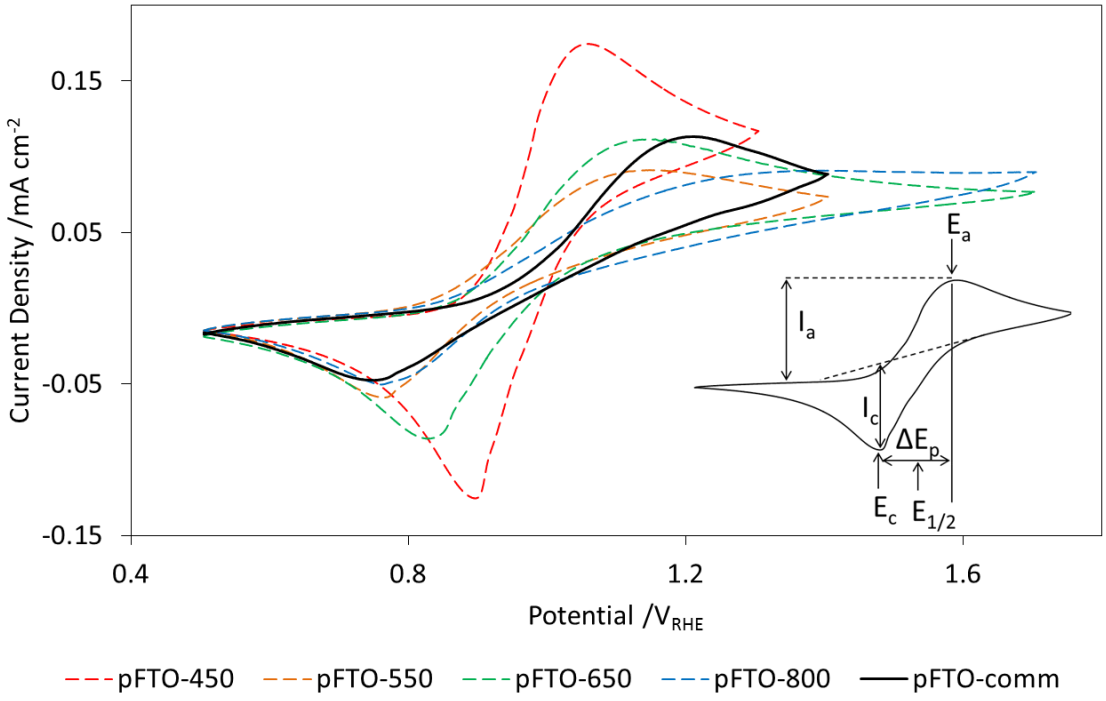

Figure 2-2: Cyclic voltammetry scans, using ferrocene in acetonitrile (0.1 mM) as a surface probe, of pFTO electrodes at various calcination temperatures compared to a commercial electrode of pFTO (pFTO-comm). The scan rate was 20 mV s^{-1} and electrodes were measured at room temperature.

Table 2-1: Peak data for pFTO electrodes with a ferrocene probe (0.1 mM, 25°C, acetonitrile, 20 mV s^{-1}). E_A is the anodic peak potential, E_C is the cathodic peak potential, E_p is the peak separation, $E_{1/2}$ is the redox wave centre, I_A is the anodic peak current and I_C is the cathodic peak current. The peak currents for the platinum electrode references are not given as this is dependent on the surface area of the electrode, which was not comparable.

Electrode		E_a /V_{RHE}	E_c /V_{RHE}	ΔE_p /V	$E_{1/2}$ /V	I_a /mA	I_c /mA
Literature	(Pt electrode)	1.039	0.952	0.087	0.995	-	-
Solution		0.957	0.883	0.074	0.920	-	-
Commercial pFTO		1.300	0.873	0.427	1.087	0.113	-0.047
pFTO-450		1.060	0.896	0.164	0.978	0.175	-0.125
pFTO-550		1.148	0.764	0.384	0.956	0.091	-0.059
pFTO-650		1.156	0.827	0.329	0.992	0.112	-0.086
pFTO-800		1.411	0.762	0.649	1.087	0.091	-0.050
Average pFTO		1.215	0.824	0.391	1.020	0.116	-0.074

Importantly, the redox wave centre ($E_{1/2}$, Table 2-1) is within experimental error for every electrode, and its position (1.020 V_{RHE}) is consistent with experimental and literature data for a platinum electrode in ferrocene (0.995 V_{RHE}). Comparisons are often drawn with platinum electrodes because they are highly conductive and have low overpotentials for most electrochemical reactions.[185] The peak current (averaged to 0.12 mA for the oxidation wave, I_A, and -0.07 mA for the reduction wave, I_C, in Table 2-1) is also within experimental error for all pFTO electrodes, indicating that the surface area is roughly the same for all pFTO electrodes. This shows that changing the calcination temperature does not have a significant effect on the surface area of pFTO electrodes.

In a subsequent study, pFTO electrodes were made using the same calcination temperature (450 °C) but with different precursor fluorine content, to establish the effect of the fluorine content on the conductivity. pFTO electrodes made with different fluorine contents show that changing the fluorine content does not substantially affect the electrode, which is consistent with the conductivity studies. The ferrocene redox wave is centred at the same position as for the pFTO electrodes calcined at different temperatures (0.93 V_{RHE}), and the peak positions are similar for all electrodes, indicating that the electrodes have similar conductivity, which again agrees well with the conductivity measurements. The peak currents are also similar for all

samples (I_a = 0.087 mA, I_c = -0.046 mA) and this is similar to the values gained for the pFTO as a function of calcination temperature, suggesting that all the planar FTO electrodes, regardless of calcination temperature or fluorine content, have similar surface areas.

In summary, it has been shown that neither the calcination temperature nor the precursor Sn:F ratio has a large effect on the sheet resistance of pFTO electrodes. This was initially measured using a 4-point probe, and confirmed with electrochemical analysis in a solution of ferrocene. The electrochemical analysis also showed that in all cases the peak current of the films was similar, indicating that all the measured electrodes had similar surface areas, and the surface area was not substantially affected by changing the fluorine content or the calcination temperature. It can be concluded that the FTO precursor solution produces electrodes that are conductive and similar to a commercial reference pFTO electrode. It therefore can follow that macFTO electrodes made using the same precursor solution and processing temperatures will have the same compositions and potentially also be conductive.

To ensure the best quality of macFTO electrodes, and Sn:F ratio of 0.5 and a calcination temperature of 450°C will be used for the fabrication of further macFTO electrodes.

2.3. Synthesis of Macroporous FTO

The macFTO electrodes were made according to a modified procedure based on Yang *et. al.*[57] where, briefly, a monodisperse polystyrene template self assembles into an fcc array on a conductive glass support. The FTO precursor solution is subsequently infiltrated into the voids, and the electrode is then calcined, leaving behind an inverse opal FTO structure. It was found that both the fluorine content in the precursor solution and the temperature at which the electrode was calcined affected the structural quality of the electrode. The procedure is detailed more comprehensively in the work of M. Zhang.[1]

2.3.1. Synthetic Procedure

The quality of the opal and finally inverse opal structure was assessed throughout the synthetic procedure using scanning electron microscopy (SEM). SEM analysis shows both the structural quality of the macropores, as well as the size of the macropores.

The first step of the synthetic procedure is the self-assembly of monodisperse polystyrene spheres on the substrate. Both the deposition time/temperature and the concentration of the polystyrene solution were varied[1] to gain the best quality films. In this thesis only the best quality films are shown, classified as those with clear stop bands and minimal cracking. Figure 2-3 shows a typical SEM from the self-assembled polystyrene spheres from the first optimised synthetic step. Here one can observe the regular array of spheres from the [111] plane of the fcc lattice, which is always the observed face. There are some dislocations in the lattice (highlighted in the red box) and these are one cause of the cracks observed in the final macFTO structure (Figure 2-5).

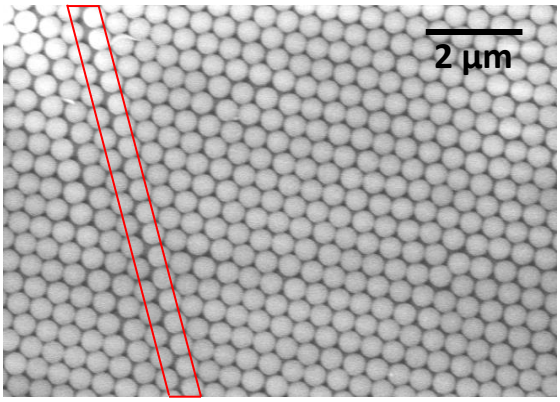

Figure 2-3: SEM of the self-assembled polystyrene template on a piece of FTO glass. The average sphere size of the polystyrene spheres is 420 nm. Highlighted in red is a dislocation in the lattice.

To gain the best macroporous film various parameters were changed, including the volume of precursor solution the electrode was soaked in, the length of soak and the volume of precursor solution added after the soak (to fill in any crack that had formed). This optimisation work was undertaken by M. Zhang in the group.[1] Following infiltration of the FTO precursor and subsequent calcination, the resulting macroporous structure (Figure 2-4) shows the inverse opal ordered array. The pores are typically about 320 nm in diameter while the film is around 30 layers (~10 µm) thick.

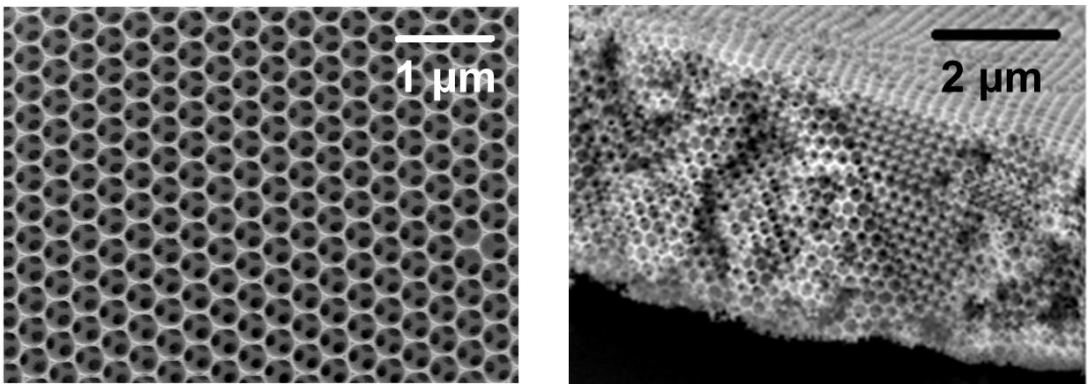

Figure 2-4: SEM images showing the macFTO structural quality. The left hand image shows the top view of an electrode, while the right hand side image shows the side view, displaying the thickness of the electrode (measured in number of pores).

The macFTO typically shows large 'islands' of macroporous material, separated by cracks (Figure 2-5). While some cracks are due to the dislocations carried forwards from the polystyrene template, the primary cause of cracks and voids is film shrinkage. The polystyrene template sphere diameter is around 420 nm, while the pore size is only 320 nm, giving a shrinkage factor of ~20% during the calcination step, consistent with results in the literature.[129,148,168] Initially the precursor solution fills the entirety of voids around the polystyrene spheres, but because the precursor solution is dilute, there is not enough FTO to completely fill the voids after calcination, which causes the entire structure to shrink, leaving behind some voids. Loss of other volatile materials may also contribute to film shrinkage.

It was found that the macroporous structure of macFTO was sensitive to the Sn:F ratio and that the optimum ratio was 1:2. Other ratios gave poor quality macropores showing deformed or fragmented walls by SEM. Subsequent work was conducted using an Sn:F ratio of 1:2.

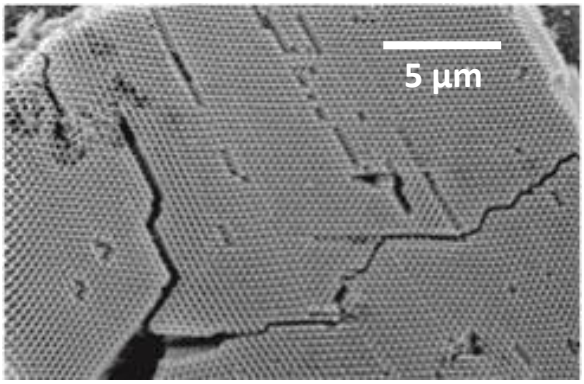

Figure 2-5: Low magnification image of a macFTO electrode showing the formation of cracks, and thus islands, in the macFTO structure.

Figure 2-6 shows the XRD spectrum of an electrode of FTO, the FTO peaks are highlighted with * and all other peaks are from the background (aluminium holder (Al and Al_2O_3) and backing glass (SiO_2)). The FTO structure was found to be essentially SnO_2 rather than $SnO_{1-x}F_x$ (FTO) because the fluorine content is very low. Reference patterns of SnO_2 that contain fluorine show that SnO_2 peaks shift to smaller 2θ with increasing fluorine content, which was not observed in the electrodes studied in the present work. The XRD trace is identical for pFTO and macFTO, indicating they have the same bulk crystalline structure.

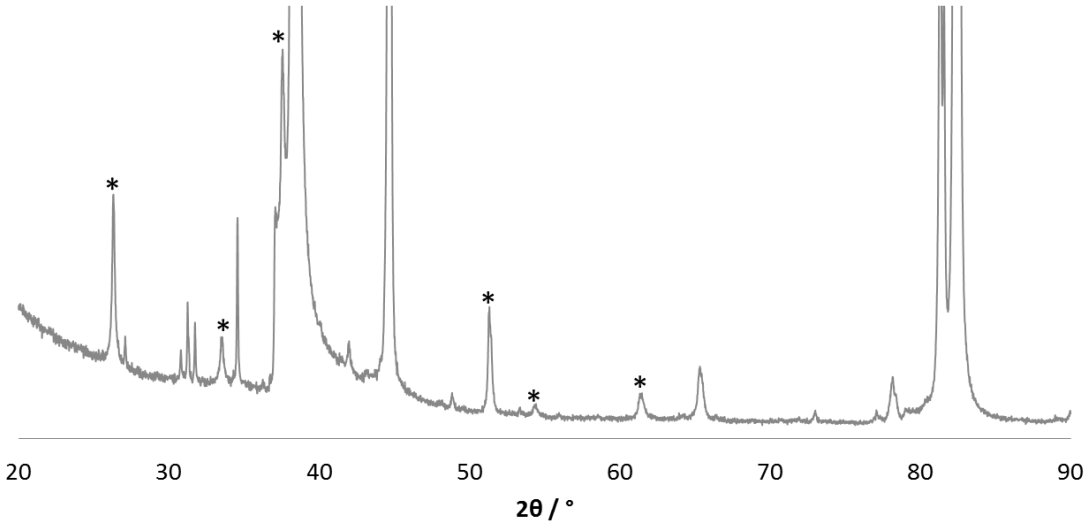

*Figure 2-6: XRD of FTO. The peaks due to FTO are labelled *, while the other peaks are from sources such as the aluminium holder and the underlying glass. SnO_2 pattern number: 91517 (Fiz Karlsruhe ICSD)*

Diffuse reflectance spectroscopy can indicate the position of the band gap, as well as the position of the stop band. The band gap is calculated from the onset of the absorption of the FTO, while the stop band is shown with a peak in the reflectance spectrum. The position of the peak is determined by the interplanar spacing, d_{hkl}, which is related to the pore size, D; the

average refractive index, n_{av}, which is related to the filling factor, ff; and the angle of incidence, θ, according to Equation 2-2, Equation 2-3 and Equation 2-4.[128]

$$\lambda = \frac{2d_{hkl}}{m}\sqrt{n_{av}^2 - \sin^2\theta}$$

Equation 2-2

$$d_{hkl} = \frac{D\sqrt{2}}{\sqrt{h^2+k^2+l^2}}$$

Equation 2-3

$$n_{av} = (n_{wall} \times ff) + (n_{void} \times ff)$$

Equation 2-4

Figure 2-7 shows a typical DRUVS spectrum of a macFTO electrode, measured at 45° incidence. The band gap is calculated to be 3.5 eV from an extrapolation of the band edge, which is close to literature values of 3.8 eV,[186] and the stop band is centred at 567 nm.

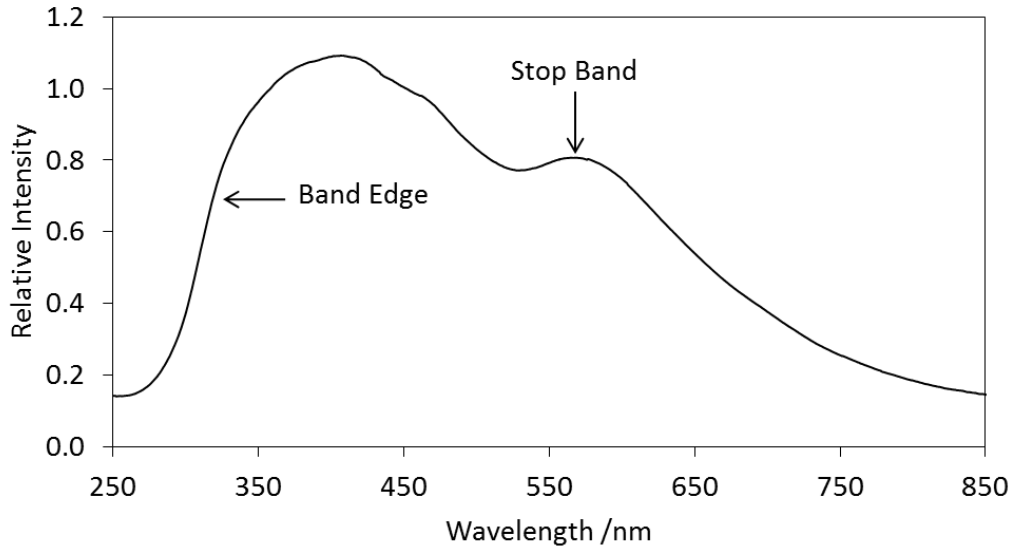

Figure 2-7: A typical diffuse reflectance spectrum of an electrode of macFTO, measured at 45° incidence. The stop band is centred at 567 nm, and this corresponds to the [111] plane.

The filling factor is the only unknown parameter, but it can be determined using Equation 2-2. Given that the stop band position at 45° illumination is 567 nm, and n_{av} is calculated to be 1.32 assuming that n_{wall} is 2.6[186] and n_{void} is 1 (air), then the fill factor is 0.20. An exact replica of an opal structure would be predicted to have a fill factor of 0.26, but the actual filling factor is often much lower than this due to dilution of precursors.[128]

2.3.2. The Effect of Calcination Temperature on the Structure and Conductivity of macFTO and pFTO

As a function of calcination temperature, both the structural quality and the conductivity of the macFTO electrodes can change, as seen with the pFTO electrodes. In order to probe this, the fluorine content was fixed at precursor Sn: F ratio of 1:2, while the calcination temperature was varied. At low calcination temperatures, the macFTO structure quality does not change substantially, but at very high temperatures (800 °C) the FTO begins to melt and the pores start to warp.

Initially, macFTO electrodes were analysed electrochemically by studying the redox chemistry of ferrocene (Figure 2-8) as with the pFTO electrodes. The ferrocene peak position and current, when compared to the pFTO, can give an indication of any change in surface properties when the calcination temperature is varied.

With the planar FTO, the conductivity was found to be similar for all electrodes, so it was assumed that this pattern would follow for identically made macFTO electrodes. M. Zhang[1] found that the best macFTO structure was gained when a calcination temperature of 450 °C was used with a Sn:F ratio of 1:2. This macFTO electrode was probed initially and it was found that the redox peak shape determined by CV was the same as pFTO, as expected (Figure 2-8). The surface area enhancement of macFTO compared to pFTO was found to be three times greater. While this is a positive result, a larger surface area enhancement was expected. A rough calculation of the surface area of a macFTO electrode, based on the electrode dimensions (0.01 x 0.01 x 1 x 10^{-5} m) and the pore diameter (450 nm) gives a surface area enhancement of 70 times (see appendix for details of the calculation), which is substantially larger than the results seen here. This calculation does not take into account the necking between pores (the holes that link the pores together), so it is likely that the surface area enhancement will be smaller than 70 times. Additionally, there may be significant areas of the macFTO electrode that are electro-inactive due to cracking. For a surface area enhancement of only 3 times, most of the electrode would have to be inactive, which is unlikely and therefore it was concluded that the ferrocene probe is not a sensitive enough technique.

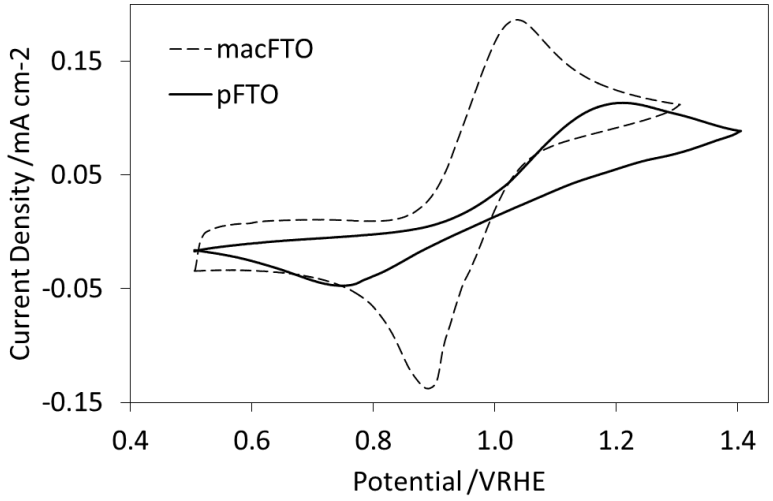

Figure 2-8: Cyclic voltammogram of the ferrocene (0.1mM, acetonitrile, 20 mV s^{-1}, 25°C) redox wave to probe the surface properties of macFTO compared to pFTO.

The surface area enhancement (or surface roughness) of an electrode can also be determined using capacitance measurements. The capacitance is determined by submerging a geometric surface area of 1 cm^2 of the electrode in an aqueous solution of KCl (0.1 M).

The capacitance (C) is defined as the amount of charge stored, q, per volt, E (Equation 2-5):

$$C = \frac{q}{E}$$

Equation 2-5

A plot of the current (in amps) *vs.* the scan rate (in volts per second) should therefore have a linear relationship. This linear relationship would indicate that the electron transport within the material is fast at all scan speeds, which in turn indicates that the electrode is conductive. Deviations from a linear relationship show that mass transfer processes, such as diffusion through solution, become the more dominant processes.

The capacitance is normally measured over a region where the electrode does not undergo any faradaic processes (i.e. does not pass charge to the electrolyte), which means that the cyclic voltammogram (CV) should display a box-like waveform (pFTO, Figure 2-9a). However, because FTO is a semiconductor, the capacitance is dependent on the applied potential, meaning that the CV does not always display the ideal box-like waveform (macFTO, Figure 2-9d). To compensate for the changing capacitance with applied potential, the anodic wave

and the cathodic wave are averaged and subtracted from the original waves (Figure 2-9b and e). This results in a more box-like shape, from which the capacitance can be extracted by plotting the current *vs.* the scan rate (Figure 2-9c and f).

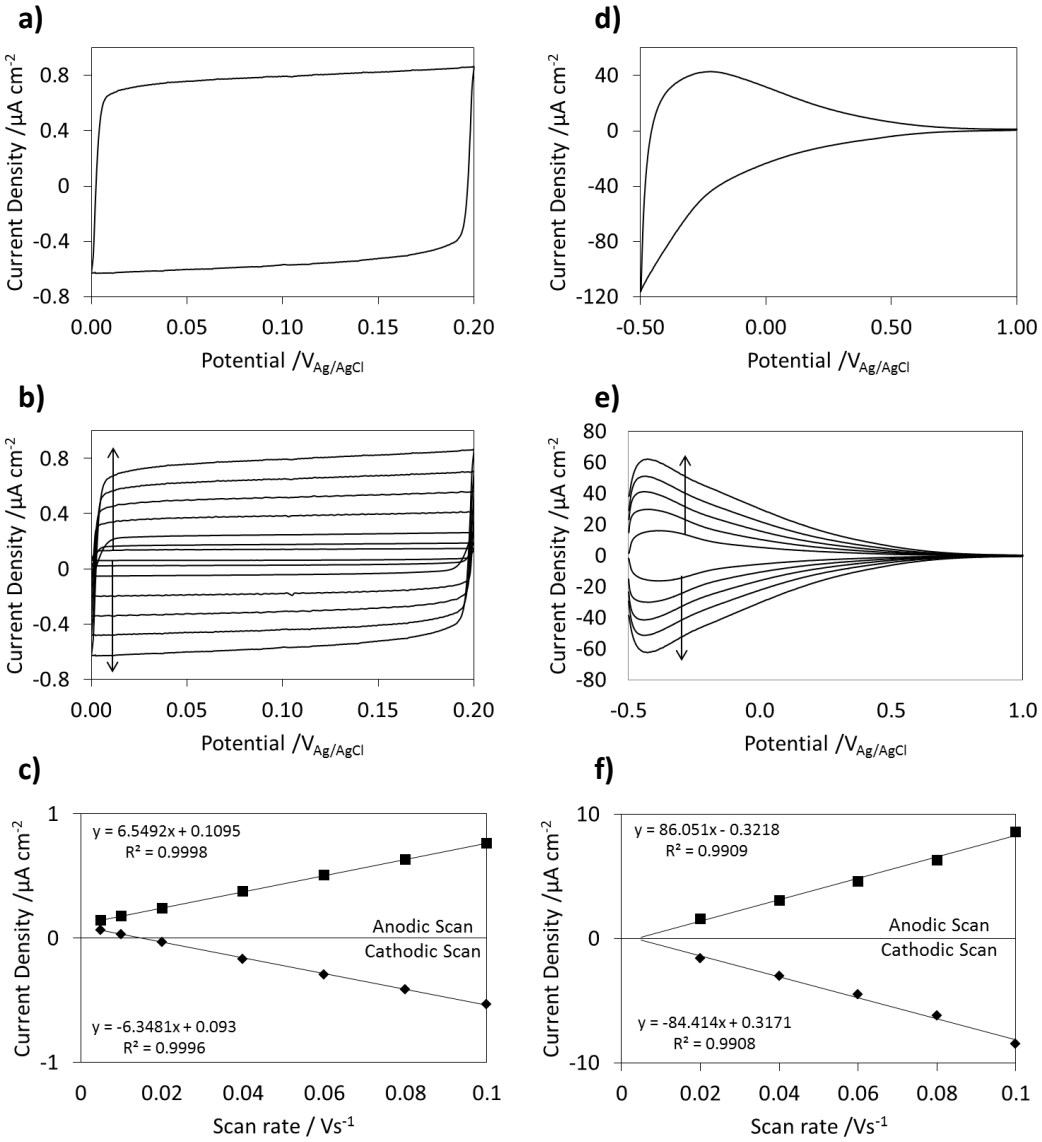

Figure 2-9: Capacitance of pFTO (a – c) and macFTO (d – f). An example of the raw data is given (a, d) followed by the averaged data for each scan rate used (b, e) and finally the current vs scan rate to calculate the capacitance (c, f). The electrodes were measured in 0.1 M KCl (aq) solution at 25°C. Across the potential window of macFTO, the waveform of pFTO was similar. A small window was chosen for convenience. The macFTO electrode, because of the larger quantity of FTO on the electrode, showed different capacitance at different potentials. The larger potential window was used to gain a better average, and thus be more comparable.

Previously it was seen that all the pFTO electrodes, regardless of the conditions used to make them, had similar peak currents when probed with ferrocene, which shows that the surface area is broadly similar. If the capacitance of these electrodes is determined, then it can be

used as a reference for the macroporous electrodes giving a roughness factor. The capacitance of pFTO was found to be ~7 µF in all cases and this is now defined as a roughness factor of 1.

Figure 2-10 clearly shows that the capacitance of the macFTO electrode is much higher than that of the pFTO electrode from the CV. The values for macFTO calcined at different temperatures are shown in the inset of Figure 2-10: the maximum roughness factor is observed for an electrode calcined at 450 °C, with a roughness factor of 12. This value is much more comparable with the calculated 70 times enhancement, though still quite small.

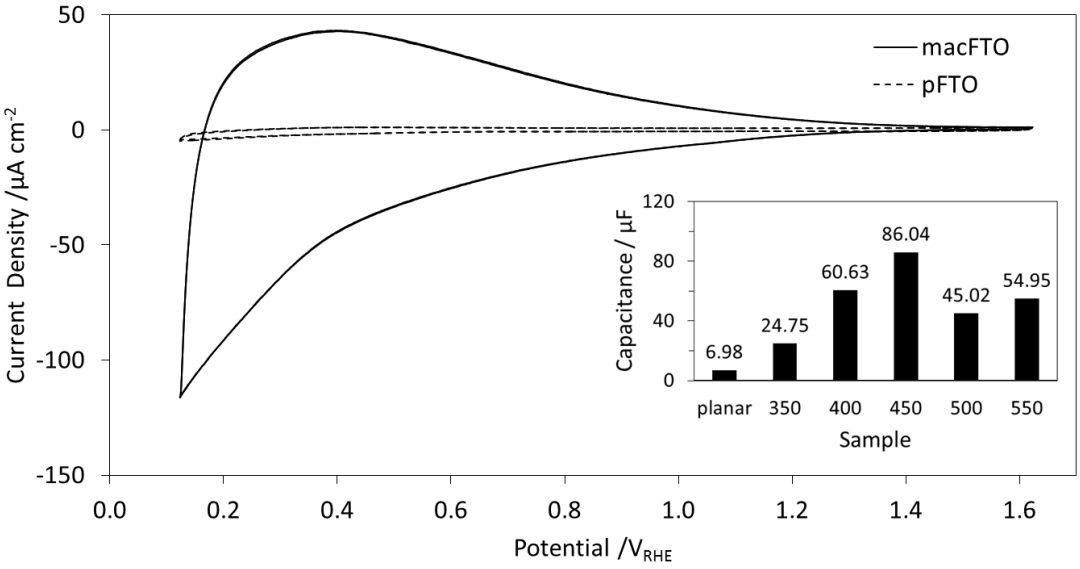

Figure 2-10: Capacitance of a macFTO electrode (Sn:F 0.5, calcined at 450 °C), compared to the commercial pFTO electrode and (inset) the capacitance of macFTO electrodes calcined at different temperatures (°C) compared to the planar FTO electrode.

Initially the electrode calcined at 350 °C showed a large capacitance (52 µF) which quickly deteriorated to a stable value of 25 µF. This behaviour is consistent with the residual carbon (from the incomplete combustion of the polystyrene template) on the electrode surface artificially enhancing the conductivity of the electrode. The increased conductivity yields a larger capacitance and thus suggests falsely a larger surface area.

Between 350 and 450 °C the capacitance increases to a maximum value of 86 µF at 450 °C, after which the capacitance decreases. This is consistent with conductivity measurements on the pFTO electrodes, where the conductivity is highest for electrodes with calcination temperatures ~450 °C. It is apparent that the most conductive electrodes, and those with the largest surface area are those calcined at 450 °C; this is hot enough to fully combust the template, while not too hot as to damage the structure by melting or warping. Additionally,

the doping level is controlled somewhat by the calcination temperature. By changing the calcination temperature the amount of fluorine in the electrode can theoretically be altered which in turn can affect the conductivity. A higher calcination temperature can drive off more fluorine than a lower calcination temperature creating more defect sites and a more conductive electrode. A small number of defect sites are desirable as this has been shown to increase the conductivity of electrodes.[187] Too many defect sites decreases the conductivity, showing there is an optimal number of defect sites and therefore calcination temperature. This is potentially demonstrated in the present results. Furthermore at 450°C the temperature is hot enough to reduce grain boundary resistances by sintering the grains together, but not too hot so as damage the macroporous structure. The apparent surface area from capacitance measurements is greatest at 450 °C, with a 12 times enhancement over the planar electrodes.

2.3.3. Quantification of the Fluorine Content in FTO Powders

For a photonic TCO it is important to optimise the macroporous structure, doping and microstructure in order to optimise the optical and electronic properties respectively. For pFTO it was found the precursor Sn:F ratio had a small effect on conductivity as did the calcination temperature. For mac-FTO four-point probe conductivity was not possible due to the fragility of the films. For macFTO an Sn:F ratio of 1:2 was determined to give the best optical properties, and 450 ^{o}C the greatest roughness factor. The best optical properties are defined as a stop band peak on the DRUVS spectrum that is clear of the baseline by at least a relative intensity of 0.1. Knowledge of the fluorine content in pFTO and mac-FTO films as a function of Sn:F ratio would provide insight into the comparability between pFTO and macFTO films. For example it was unknown if calcination in the presence of the polystyrene template for mac-FTO altered the final F-content and if this is dependent on the initial Sn:F concentration.

For the pFTO electrodes in this study, the calcination temperature was fixed at 450 °C, while the Sn:F ratio was varied between 0 and 1.5. The fluorine content is actually a difficult parameter to measure as the amount of fluorine is so low as to be below the threshold of detection for many techniques, including XPS and EDX. Consequently, many researchers use Hall Effect measurements to estimate the fluorine content from the carrier concentration that is obtained,[153,170,188,189] or infer the fluorine content from conductivity measurements, which for macFTO could not be obtained in the present work.[190]

In this work the fluorine content was quantified with ^{19}F solid state NMR, following the approach taken by Günne *et al*.[187] As there is very little material on a film, a series of powdered FTO samples were made using the same conditions to the macFTO electrodes, and the fluorine content of the powder was assessed. It was found that the fluorine content of the powders quickly saturated, at precursor Sn:F < 0.25 (Table 2-2). At precursor values greater than this, no extra fluorine is incorporated. This compares well with the conductivity studies on the planar electrodes, where the conductivity is similar at 10 Ω square for all precursor Sn:F ratios.

Table 2-2: Summary of the Sn:F ratio determined by ^{19}F NMR for pFTO and macFTO powdered samples

Precursor Sn: Ratio	Sample Sn: F ratio, pFTO	Sample Sn:F ratio, macFTO
0.00	0.0000	-
0.25	0.0088	0.0032
0.50	0.0062	0.0026
0.75	0.0075	0.0020
1.00	0.0045	0.0085
1.50	0.0062	0.0263

Additionally, the fluorine content of the FTO powders was lower than that of the precursor solution by about a factor of 100 (Figure 2-11), yielding a fluorine content of around 0.005 (Sn:F) or 0.5 atom%. Typical values for Hall effect measurements in the literature give the number of F atoms on the order of 5 x10^{20} cm^{-3} which is equivalent to ~3 atom%.[169,187] It is not uncommon for numbers as low as 0.7 atom% to be reported, which is similar to the fluorine content found in this work.

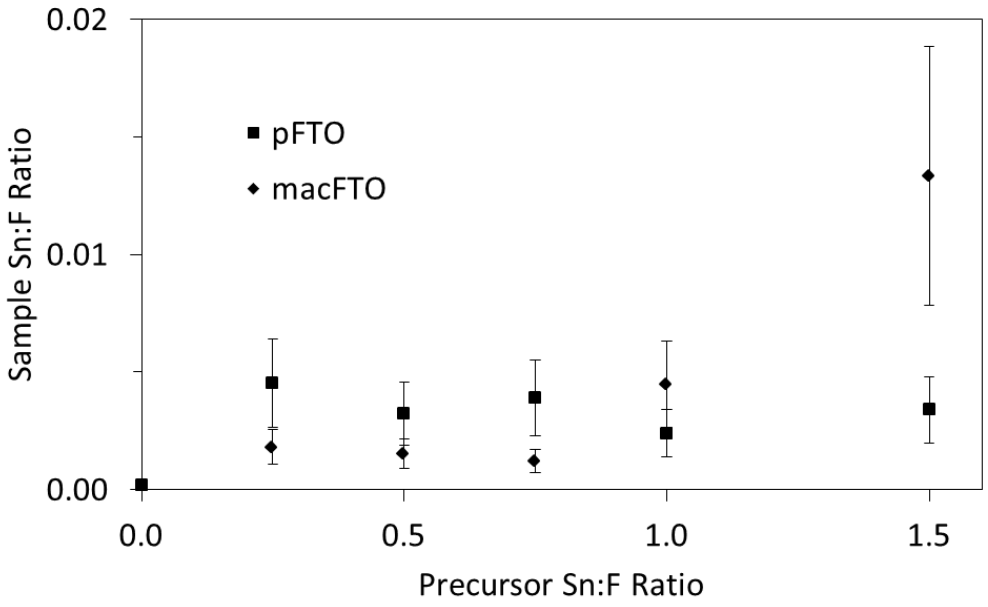

Figure 2-11: Solid state ^{19}F NMR results for the templated (diamonds) and non-templated (squares) FTO powdered samples

Two potential causes of fluorine loss are 1) due to the increase in surface area (i.e. surface fluorine loss as opposed to bulk fluorine loss) and 2) losses of fluorine through C_xF_y products. C_xF_y products form from the reaction of fluorine with the polystyrene template, and, at the calcination temperature used, would be volatile.

To establish if the fluorine loss is due to either of these causes, the powders were compared to a series of non-templated FTO powders (no polystyrene was used in the synthetic process). The amount of fluorine in these powders was also found to be about a factor of 100 lower than the amount of fluorine used in the precursor solution, and there was little difference between the macFTO powders and the non-templated powders. Thus it could be concluded that the fluorine loss was not due to increasing the surface area. The fluorine loss must therefore be primarily due to processes occurring earlier in the calcination process, such as the initial ramp rate, where it is likely that a lot of fluorine precursor (NH_4F) is lost.

It is worth noting that Günne *et al*.[187] also found that after heating, the fluorine content of FTO was much lower than before any heating process: the sample made with 10 mol% fluorine only retained 1.2 mol% fluorine after heating, while the 1 mol% sample only retained 0.4 mol%. Günne *et al*. also found that doping tin dioxide with fluorine significantly reduces the resistivity of the FTO and a high fluorine content was found using NMR. Samples made with 10 mol% fluorine to start with were less resistive (13 Ω square) than those with a 1 mol% (60 Ω square).

Upon heating, however, most of the incorporated fluorine is lost, and so the authors suggest that fluorine itself is not necessary for good conductivity, but instead helps to reduce the grain boundaries upon crystallite formation, which increases the conductivity. This reasoning would also explain why, in the present work, changing the precursor fluorine content has little effect on the conductivity.

As both the conductivity and the fluorine content stay within error when the precursor ratio is beyond 0.25 further electrodes were made using a ratio of 0.5. This ensures that the fluorine content will not fall below 0.5 atom% and also ensures that the conductivity stays within the measured range of < 10 Ω square.

2.4. Photoactivity of FTO Electrodes

The photoelectrochemical activity of pFTO and macFTO electrodes towards the oxygen evolution reaction (Equation 2-6) is important to determine, because these electrodes will be used to deposit visible light absorbing materials and catalysts for the oxygen evolution reaction (Chapter 4).

$$2H_2O \xrightarrow{h\upsilon} 4H^+ + 4e^- + O_2 \qquad E^{\Theta} = 1.23\ V_{RHE}$$

Equation 2-6

Photoactivity was measured by illumination with a xenon arc lamp, with a cut on filter at 420 nm, ensuring only visible light is used. The photocurrent density is given by the difference between the dark current density and the current density under illumination. The onset potential is the potential at which the reaction of interest (water oxidation) begins, measured by extrapolating down to zero current from the gradient of the catalytic wave.

In the dark, the current densities for pFTO and macFTO are negligible, of 0.09 μA cm^{-2} and 2.3 μA cm^{-2} respectively (Figure 2-12). The dark current density for macFTO is not 0 μA cm^{-2} due to charging that occurs in the FTO, which is the capacitance (see section 2.3.2.). The current density for pFTO is also non-zero, but is much smaller than macFTO due to the significantly smaller surface area. The current is normalised to the geometric surface area (1 cm^2) not the 'real' surface area, as this was a difficult parameter to determine. Thus a difference in the current densities will be seen because there is far more material on the macFTO electrode than on the pFTO electrode. A rough calculation to show the difference in surface area is to compare the dark current densities of the two electrodes: macFTO has a dark current density that is ~25 times larger than that of pFTO, which can only be attributed to the increased amount of FTO on the macFTO electrode compared to the pFTO electrode.

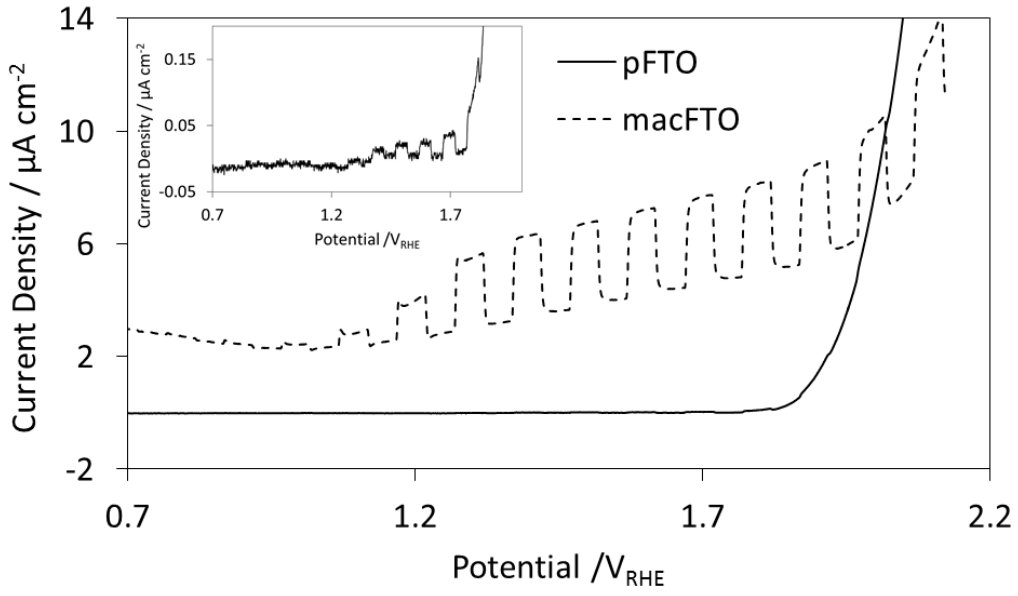

Figure 2-12: Photoactivity of FTO electrodes in phosphate buffer, pH7, with a scan rate of 10 mV s^{-1}.The solid line represents the pFTO electrode measured with a chopped light source (time interval = 20 s) and the dashed line represents the macFTO electrode. The inset shows a magnified section of the pFTO electrode trace, showing the very small current response.

Under illumination, both pFTO and macFTO are shown to absorb negligible visible light with photocurrent densities in the µA regime. The observed photocurrent increases for both electrodes with increasing potential. At 1.23 V_{RHE} pFTO has no measureable photocurrent, while macFTO has a photocurrent (the difference between the dark current and the light current densities) of ~1.2 µA cm^{-2}, at a higher potential of 1.5 V_{RHE} the photocurrent increases to ~0.03 µA cm^{-2} for pFTO and ~3.0 µA cm^{-2} for macFTO. In either case this is still a negligible photocurrent density, which should mean that any photoactive material deposited on FTO is responsible for any photocurrent observed.

Neither pFTO nor macFTO show significant activity towards water oxidation (Figure 2-12). In the dark, the onset potential (the potential at which a reductive or oxidative process begins to occur) for water oxidation for pFTO is 1.95 V_{RHE}, giving an overpotential of 720 mV. For macFTO in the dark the onset potential is 1.90 V_{RHE}, giving an overpotential of 670 mV. Both electrodes have high overpotentials showing that they are inefficient water oxidation catalysts in the dark.

When illuminated, the onset potential for pFTO did not change, which is in line with the very small photocurrent. This means that the overpotential is still high, at 720 mV. The onset potential for macFTO under illumination was reduced to 1.8 V_{RHE} because the photocurrent

density was higher for macFTO. This means the overpotential was reduced, to 570 mV, however this is still a large overpotential, showing that both pFTO and macFTO are poor water oxidation catalysts under illumination.

In summary, the photocurrent for pFTO and macFTO is very small, in the μA regime. macFTO shows a slightly higher photocurrent density than pFTO, which reduces the onset potential for the water oxidation reaction. Despite this, it can be concluded that pFTO and macFTO, in either the dark or when illuminated, have high onset potentials for water oxidation, making these electrodes alone unsuitable for the water oxidation reaction.

2.5. Summary and Conclusions

Planar FTO electrodes were used as an analogue for macFTO electrodes due to the lack of a good electrical contact to perform conductivity measurements. It was found that pFTO prepared using aerosol assisted vapour deposition from a range of Sn:F concentrations gave conductive films comparable with the literature, with sheet resistance values of < 10 Ω square for Sn:F ratios of 0.25 – 1. The sheet resistance was found to change with calcination temperature, with the lowest sheet resistance found for electrodes calcined at 450 °C (8 Ω square). With an Sn:F precursor ratio of 0.25 – 1 the sheet resistance varied slightly (from 8 – 20 Ω square), but at precursor Sn:F ratios > 1 the sheet resistance increased to 60 Ω square. Using ferrocene as a surface area probe, electrochemical analysis was used to support the conductivity study. By studying the redox peak heights, positions and shapes information could be gained on the reaction reversibility and therefore conductivity of the electrodes. The study showed that the most conductive electrodes were formed when the calcination temperature was set at 450 °C, and the fluorine content was set to a precursor Sn:F ratio of 0.5.

macFTO electrodes were made using a templating technique, where the monodisperse polystyrene spheres self-assemble on the electrode surface. There are some defects formed in this process which are transferred into the final structure. These defects likely arise from the imperfect stacking of the polystyrene spheres. Other defects are introduced from shrinkage during the calcination step due to loss of volatile materials. The best structural quality was gained using a precursor Sn:F ratio of 0.5 and a calcination temperature of 450 °C, as shown by SEM.[1] These structural defects do not overall inhibit the quality of the macFTO as a clear stop band can be seen on the DRUVS spectrum, which indicates good ordering. Electrochemical determination of the capacitance can give an indication of the increase in surface area when moving from planar to macroporous electrodes, which is important for catalysis. The surface roughness factor was greatest for electrodes calcined at 450 °C, being 12 times greater for macroporous electrodes than for planar electrodes.

The fluorine content of macFTO was quantified using solid state ^{19}F NMR, which showed that the fluorine content was ~100 times lower in the FTO powders than in the precursor solution as is commonly observed in the literature. The loss of fluorine is primarily due to surface loss of fluorine and loss of fluorine through formation of C_xF_y compounds during the calcination step (where the polystyrene template is being removed). The NMR also showed that the fluorine content was approximately the same for electrodes with precursor Sn:F ratios of ≥

0.25, at around 0.5 atom%. Though the final fluorine content is low compared to the precursor ratio, the pFTO electrodes are still conductive with sheet resistances of < 10 Ω square (recall macFTO electrode conductivity could not be measured). Subsequently, all further FTO electrodes were made with a precursor Sn:F ratio of 0.5, to ensure that the fluorine content would be the same in all the electrodes (at 0.5 atom%).

Finally, electrochemical analysis showed that the photocurrent density of pFTO and macFTO electrodes was very small (< 3 μA cm^{-2} at 1.23 V_{RHE} for all electrodes). The onset potential for the water oxidation reaction on bare FTO electrodes was also very high (> 1.9 V_{RHE}), suggesting that these electrodes will not effectively catalyse the water oxidation reaction alone. This is useful to understand as Chapter 4 details the addition of light absorbing materials and catalysts for the water splitting reaction. Knowing that the activity is very small for pFTO and macFTO electrodes, any activity can be ascribed to the other materials deposited over the FTO electrodes.

The questions that remain open from the work presented in the present chapter are primarily concerned with the conductivity of macFTO. Is macFTO conductive? If so is this due to the fluorine content, or is it due to defects that have arisen from the loss of fluorine, as suggested by Günne *et al*?[187] Some of these questions may be answered in the following chapters, where secondary materials will be deposited over macFTO.

Chapter 3

A Study on the Photonic Effects of macFTO Electrodes

Chapter 3. A Study on the Photonic Effects of macFTO Electrodes

3.1. Introduction

When light interacts with a solid object it can be absorbed, reflected, scattered or dispersed. Porous materials are likely to scatter more light than planar materials leading to losses in the potential light harvesting efficiency. However, porous materials are desired over equivalent non-porous (planar) materials because of the increased surface area available for catalysis and the increased electrode-electrolyte interface area.

A periodic modulation of the refractive index derived from highly ordered porous, or photonic, materials can give electrodes certain beneficial properties. 3D photonic materials are commonly completely reflective to a particular wavelength region: this region is called the stop band. At the edges of the stop band, incident light undergoes multiple coherent scattering which can lead to increased probability of light absorption and/or increased probability of reabsorption of emitted light either by the photonic material itself (if it absorbs light) or from a secondary material deposited in the pores of the photonic material.[191] In both cases this leads to an increase in the overall light harvesting efficiency, simply from an increase in the optical path length and an inability for the light to propagate through the material respectively.

Figure 3-1 gives an example of a macFTO structure where the stop band is at ~500 nm (green light). Wavelengths outside the stop band region (red and blue in the figure) can propagate through macFTO, while the green light is forbidden to travel through the material (incident light of this wavelength is reflected). If a secondary material deposited inside the macFTO material, for example a semiconductor nanoparticle, has an emission wavelength which is inside the stopband, this light is forbidden to propagate through the material, leading to increased light harvesting efficiencies from reduced spontaneous emission.

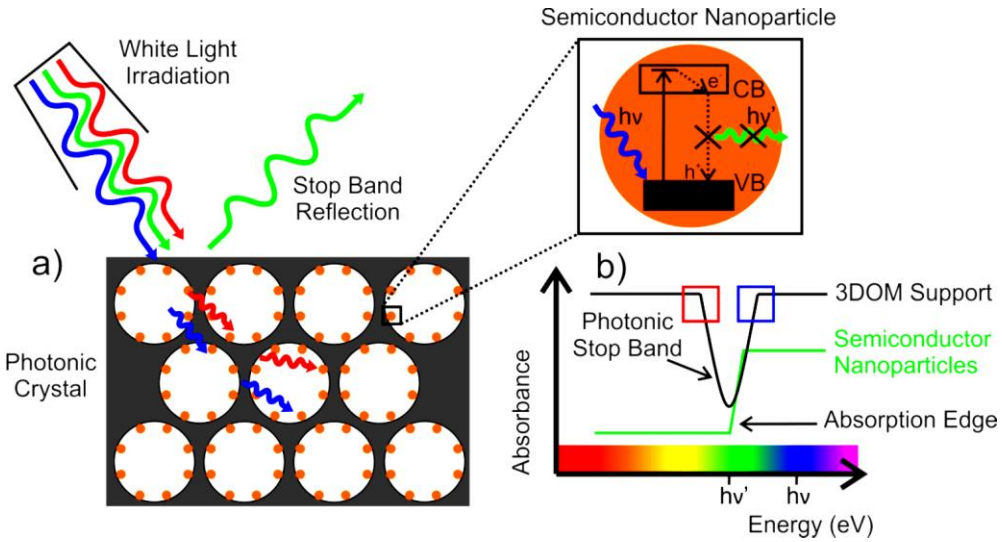

Figure 3-1: a) Schematic showing the photonic stop band effect: the ordered array of pores creates a region (b) where light cannot propagate (shown as the green wavelength), which results in inhibited spontaneous emission. Adapted from R. Mitchell[127]

Photonic materials show an angular dependence as the stop band changes position (λ) with angle of incidence (θ) according to Equation 3-1 (where m is the order of Bragg diffraction, 1, n_{av} is the average refractive index and d_{hkl} is the interplanar spacing):

$$\lambda = \frac{2d_{hkl}}{m}\sqrt{n_{av}^2 - \sin^2\theta}$$

Equation 3-1

This angular dependence is important because not all incident light may hit a solar device with the same incident angle and being able to understand and predict the interactions of the photonic material with the light allows a more efficient device to be fabricated.

3.1.1. The Effect of a Photonic Host Structure

One limiting factor for the efficiency of solar cells is spontaneous emission, arising from the unwanted recombination of an excited electron/hole pair. An additional benefit of ordered porous materials is that if a stop band can be formed that overlaps the absorption band edge, electron/hole recombination can be drastically inhibited meaning the efficiency of the device can be increased.[179] To form a stop band the dielectric contrast between the walls and voids of the pores must be high,[192,193] though some inhibition of spontaneous emission can be achieved with a partially formed stop band.[119] The stop band will only inhibit spontaneous emission if that emission is propagating in the same direction as the refractive index modulation, which opens the possibility for 1D,[194,195] 2D[180,196] and 3D[125,177,197,198] photonic structures. For the work

in this thesis, 3D photonic structures are the most ideal as they will inhibit light propagating in all directions.

There are several examples in the literature of the stop band contributing towards an increase in the efficiency of a solar device. For example, Chen *et al.*[129] showed that the absorption spectrum of macWO_3 could be enhanced in different regions according to the position of the stop band and the photocurrent showed an enhancement of 3 times at 2.3 V_{RHE} when the stop band was overlapped with the absorption profile of WO_3. In a separate paper the same authors showed that slow light at the stop band edge can increase the efficiency of the photoisomerization of azobenzene by a factor of 1.8.[191] They also showed that there is a trade-off between the positive effect of slow photons and the degree of scattering from the porous nature of the photonic crystal, meaning there is a limit of the number of layers there can be in a photonic crystal for maximum effect. The ideal thickness is 27-30 layers of photonic crystal: below this the photonic effect is increasingly weak; above this the scattering effect starts to dominate, which is not beneficial for efficiency enhancement.[125,143,199]

In a separate example, Lopez-Lopez *et al.*[158] showed that the photocurrent obtained from a photoelectrode can be enhanced by a photonic structure, and the enhancement is dependent on the angle of illumination, with the greatest enhancement, a factor of 1.2, achieved at 50° incidence, this is where the stop band edge overlaps the emission profile most strongly. The angular dependence demonstrated by Lopez-Lopez *et al.* is important because it shows that the overlap between the stop band and the emission peak varies with angle of incidence, which is important in a real device because the incidence angle will vary and not all light will be affected to the same extent.

Xiao *et al.*[144] also present work where the fluorescence lifetime of an embedded dye is shown to be modified by the photonic band gap. At particular angles, where the overlap of the band gap and the emission profile is strong, the fluorescence lifetime was observed to be longer than that of the dye not in a photonic host.

In other works, the magnitude[155] and decay rate of emission,[119,142,143] the rate of catalysis,[49] and the fluorescence lifetime of dyes[65,125,145,180,200] have all been shown to be enhanced by the presence of a photonic host structure, which results in an increase in the overall device efficiency. Maximum effect from the stop band is observed when either the stop band overlaps the absorption profile or the emission profile at the stop band edge. In the former

case, the result is increased absorbance through the slow light effect, and in the latter case the light cannot propagate through the electrode material and therefore must be reabsorbed (see Figure 3-1 above).[143]

However, throughout the literature, there are some contrasting reports which show little to no effect of the stop band: Chen *et al.*[148] studied the rate of degradation of organic compounds by photonic TiO_2 (inverse opal structure) and conclude that the observed enhancement is from scattering effects, not the stop band. Megens *et al.*[147] showed no effect of the stop band produced by a colloidal suspension of silica spheres on the emission properties of several dyes, with the fluorescence lifetime remaining 3.5 ns, but a larger effect on the absorption spectrum where the stop band overlaps the profile, shown by a dip in the fluorescence intensity from 1 to 0.2 where the stop band lies (580 nm). A small positive enhancement is seen in the work of Ozin *et al.*[141] on the degradation of methylene blue with photonic TiO_2, at only 1.9 times enhancement over a planar region of the same electrode. Li and Zhang[146] calculate that the photonic band gap effect is weak, with only a 5% change in calculated values, and attribute most of the changes to photoluminescence spectra and lifetimes to chemical and electronic effects, rather than the photonic band gap, meaning that the local environment and, for example, electrostatic interactions, affect the results to a greater extent than any photonic structure.

In summary, the literature shows evidence for a stop band effect but to varying degrees. In some cases the effect can be attributed to scattering effects from porous materials, as opposed to the stop band. It is therefore one aim of the present work to explore the stop band and the extent to which it varies with the incident light angle (Figure 3-2) and to study the extent of any positive effects the stop band may have on the systems of interest. To do this it is first important to find a good model to predict the wavelength position of the stop band as a function of parameters such as angle of incidence (θ), refractive index (*n*) and filling factor (*ff*). A perfect inverse opal structure has a fill factor of 0.26, which means that 26% of the structure is wall material (74% is void/air). If the position of the stop band can be accurately predicted then it becomes much easier to estimate the overlap between emitters and the stop band. Additionally, the correlation between the prediction and experiment can give an indication of the quality of the whole photonic structure and indeed the quality of the prediction: if at some angles the stop band is particularly weak, or deviates from the prediction, then the structure may be of a lower quality (i.e. containing dislocations) in these directions.

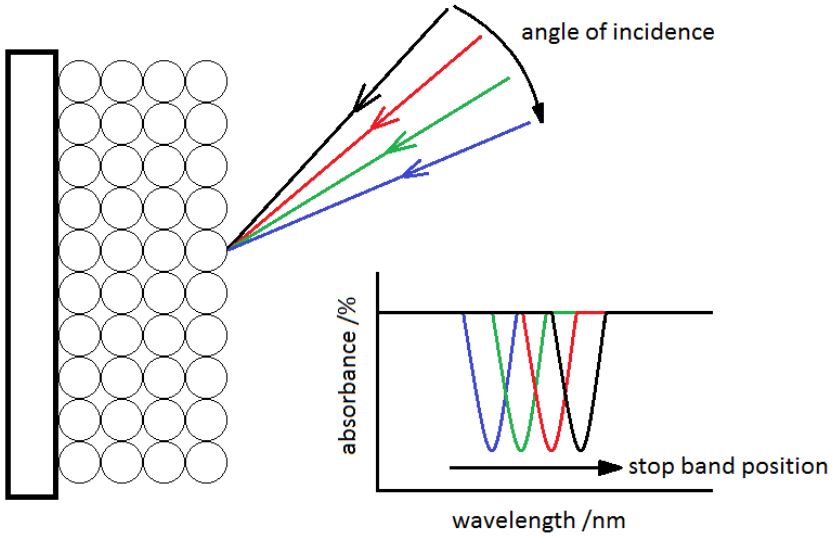

Figure 3-2: Schematic of the experiments in this chapter. As the angle of incidence changes from a large angle (black line) to a small angle (blue line) the stop band position is expected to move from a longer wavelength to a shorter wavelength.

3.1.2. Predicting the Position of the Stop Band

Schroden *et al.*[128] have published a method to predict the position of the stop band. In their work, five vividly coloured powdered macroporous materials were made, with the colour of the powders being dependent on the stop band positon, and thus the reflected colour.

For a randomly orientated powdered macroporous material many different planes are simultaneously exposed to incident light, in contrast to a planar electrode where the photonic film is orientated. It was subsequently shown by Schroden *et al.* that the photonic stop band can only arise from specific planes: the [111], [200], [220] and [311] planes, which were all observed in their fcc inverse opal lattice type samples. The [111] plane is the most intense reflection, with the [200], [220] and [311] reflections having relative intensities of 0.866, 0.612 and 0.522 respectively; reflections with larger *hkl* occur at shorter wavelengths than the [111], which has the longest peak wavelength. The position of the stop band was calculated according to equation (1) in their work (reproduced here, Equation 3-1) and it was found that calculations agreed very well with the experimental results, showing that the calculations were accurate for each plane over several different samples. The stop band position (λ) was found to be dependent on the interplanar spacing (d_{hkl}), the average refractive index (n_{av}) and the angle of incidence (θ) according to Equation 3-1 (where m is the order of Bragg diffraction, 1):

The interplanar spacing can be calculated if the miller indices of the plane of interest and the pore to pore distance (D) are known (Equation 3-2):

$$d_{hkl} = \frac{D\sqrt{2}}{\sqrt{h^2+k^2+l^2}}$$

Equation 3-2

The average refractive index (n_{av}) is given by the refractive index of the wall material (n_{wall}), the refractive index of the pore materials (n_{void} = air = 1) and the filling factor (*ff*) which is the relative volume ratio of 'wall':'void' as in Equation 3-3.

$$n_{av} = (n_{wall} \times ff) + (n_{void} \times ff)$$

Equation 3-3

For FTO in the present work both the refractive index and the filling factor of the photonic structure were initially unknown and were experimentally determined. The refractive index was found to vary from 1.8 to 2.8 and is wavelength dependent.[173,186] In the literature the filling factor is sometimes assumed to be maximal (0.26)[201] and is sometimes calculated to be lower than this.[202] In the present work the filling factor was found to be 0.2 calculated from a single reflectance measurement and a known pore to pore distance, according to the equations given above. The refractive index (*n*) can be calculated from the reflectance (*R*) according to Equation 3-4:[173]

$$n = n_s \sqrt{\frac{\left(1+\sqrt{R}\right)}{\left(1-\sqrt{R}\right)}}$$

Equation 3-4

where n_s is the substrate refractive index. For the electrodes studied in the present work, the substrate is a borosilicate glass, which has a refractive index of 1.52.[203]

3.1.3. Sources of Error on Lifetime Measurements and Angular Dependence

If a dye is embedded in a photonic host, and the stop band is overlapped with the emission profile of the dye, then the emission should be inhibited because that wavelength range of emission is not allowed to propagate through the material. This means that any emitted light has a higher probability of being reabsorbed by the material as it cannot propagate through the structure, which should increase the light harvesting efficiency. There will be two main

effects determining the performance in photonic materials: 1) scattering and 2) slow photon effects. In the case of the fluorescence lifetime of a dye, an increase may be observed for all light incidence angles because increased scattering will increase the optical path length and thus the time it takes the emitted light to exit the material, giving the light a higher probability of being selectively absorbed. For the slow photon effect, the lifetime enhancement should be angle dependent because the stop band will not overlap the emission profile at all angles and thus the lifetime will be affected to different extents at different angles. This angular dependence was shown in the work of Lopez-Lopez *et al.*[158] and Xiao *et al.*[144]

The effect of the stop band is commonly probed with embedded dyes,[65,117,120,155,200] but this method has some drawbacks; the emission profile of a dye is often broad; dyes often suffer from photo-oxidation or bleaching and dyes are generally introduced to a structure through infiltration for which control over the deposition site is difficult.[125] For example the fluorescence lifetime of a dye bound at the surface of a macroporous electrode will not be affected to anything like the same extent as a dye bound in the middle or at the edge base of the electrode. Additionally, by binding a dye to a surface, macroporous or otherwise, the lifetime of the dye may change when compared to the solution behaviour because of a difference in the local environment,[117] which makes it important to use an appropriate sample as a reference.

Further to this, lifetime measurements are inherently complicated because the interpretation of the results depends on the chosen analysis method.[204] A degree of knowledge about the system is important to ensure the results are not over analysed (fitted to too many exponentials) or under analysed (fitted to too few exponentials). It is likely that the data extracted from the macFTO electrodes will fit to a multi exponential decay (Equation 3-5), meaning that there are multiple processes contributing to the overall lifetime.

$$R(t) = B_1 e^{\left(\frac{-t}{\tau_1}\right)} + B_2 e^{\left(\frac{-t}{\tau_2}\right)} + B_3 e^{\left(\frac{-t}{\tau_3}\right)}$$

Equation 3-5

Equation 3-5 was ised to fit all the data presented in this chapter, using a least squares algorithm, where $B_{1/2/3}$ are the pre-exponential factors, t is the time and $\tau_{1/2/3}$ are the fitted lifetimes.

To further complicate the analysis, solid state samples are likely to increase the amount of scattered light received at the detector. Add to this that the electrode is also porous and the amount of scattering increases further. To minimise the effect of scattering the electrodes are normally mounted at 45° to the normal, and tilted at 45° from vertical. As the measurements in the present work involve changing the angle of incidence, there will inevitably be more scattering at particular angles, which may affect some results more than others, increasing the error associated with individual measurements.

Another potential difficulty arises when the different positions within the photonic structure are considered. Due to the macroporous nature of the sample, incident light may be shone upon wall sections or void sections of the electrode, and this positioning cannot be user controlled. This may cause deviations in the data due to the differences in, for example, the extent of the photonic effect: a larger lifetime enhancement may be seen if the light is incident upon a void (as it penetrates further into the electrode) than if it is incident upon a wall.

A further complication to the lifetime measurements is that the dye will be in a fixed orientation on the electrode surface. This binding means that, unlike in solution, the dye profile will not be averaged over a constantly moving molecule, which can take many orientations. It is not guaranteed that the dye will orientate on the electrode surface in the same way for each molecule, meaning that there will be a random orientation of molecules on the electrode surface and a full 3D photonic band gap may be needed to supress emission in all directions to show a clear enhancement. In chapter 2 the structure of macFTO was discussed and it was found that the structure is generally homogenous in three dimensions so this may not be an issue in the present work. However the cracks induced from shrinkage may have an effect at particular angles.

Finally, other effects that may contribute to a lifetime change, that are not related to the stop band or scattering are electronic and chemical effects.[143] For example, if the dye is quite concentrated then reabsorption processes might influence the lifetime considerably, so the dye concentration should always be low. Chemical effects are important if many different samples are being studied: the chemical environment (local structure and electrostatic interactions etc.) should be comparable for both the reference sample and the sample of interest.

3.1.4. Aims

The aims of this chapter are to compare the measured position of the stop band for macFTO with calculated positions as a function of angle of incidence. The information gained from these experiments will then be used to predict at which angles the emission profile of two dyes, bis(2,2'-bipyridine)-4,4'-dicarboxy-2,2'-bipyridine ruthenium(II) dichloride and coumarin 440/460, overlap the stop band of macFTO. This should therefore predict the angles at which any enhancement might be observed. There are many things that may affect either the quality of the data, or the magnitude of enhancement from the macFTO stop band, but as the majority of papers in the literature report that some enhancement is observed, it is expected that the present experiments will give an insight into the quality of the optical effects of the macFTO electrodes.

3.2. A Comparison of the Experimental and Predicted Positions of the Stop Band of macFTO

In chapter 2 the diffuse reflectance spectrum of macFTO showed that the stop band, at 45° light incidence angle, occurred at 567 nm (for clarity this spectrum is given again in Figure 3-3).

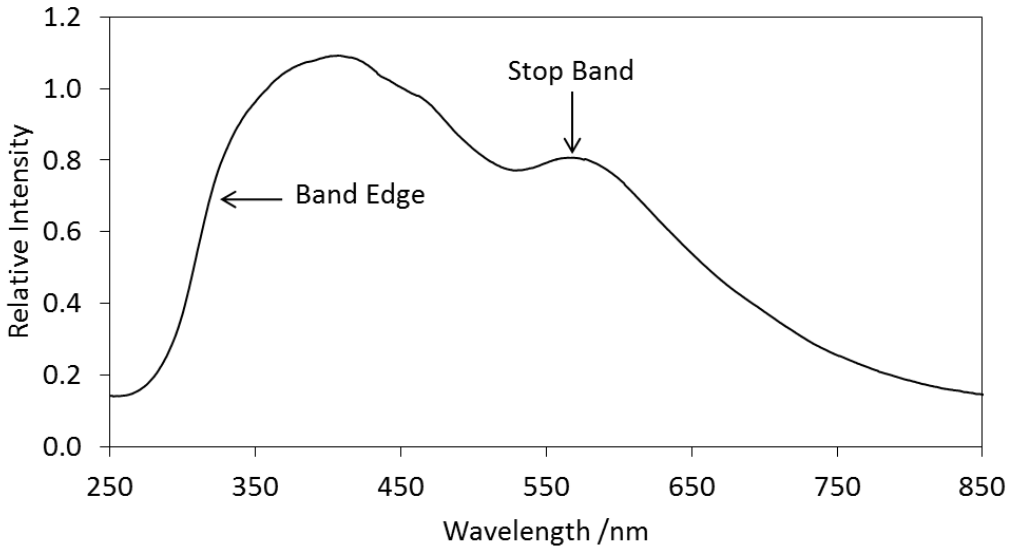

Figure 3-3: Diffuse reflectance spectrum of macFTO at 45°

The filling factor was found to be 0.20 using the information in Figure 3-3 and Equation 1-1. The refractive index of the FTO made in the present work was determined to be 2.6 using the reflectance at various wavelengths and Equation 3-4.

Calculations for the reflection of different planes are presented as a function of incidence angle in Figure 3-4.

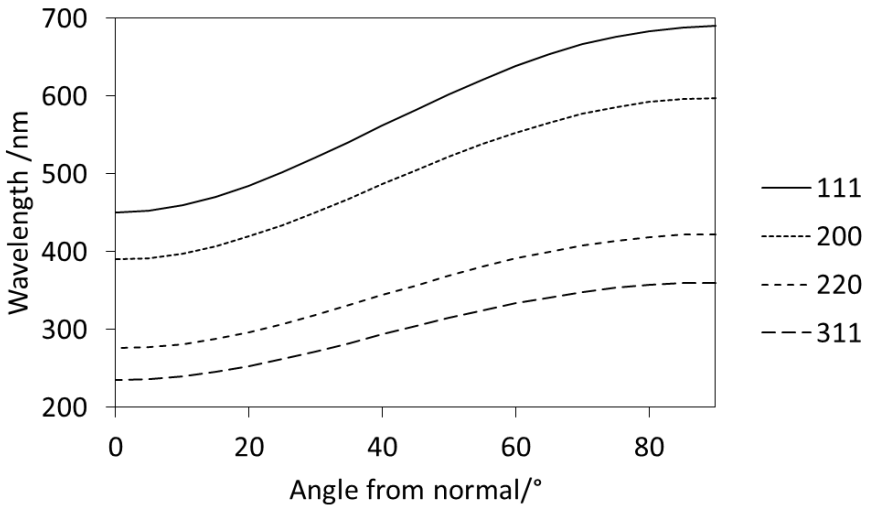

Figure 3-4: Calculation of the stop band shift for the [111], [200], [220] and [311] planes

For all planes, as the angle of incidence moves from the normal (0°) to perpendicular (90°) the stop band position shifts to longer wavelengths. The [111] plane shows the largest wavelength shift of 246 nm with the [200], [220] and [311] planes showing shifts of 213 nm, 150 nm, and 128 nm respectively.

Diffuse reflectance spectra were then taken from 0 to 75°. A full range of results from 0 to 90° could not be obtained due to constraints in the apparatus. In Figure 3-5 there are 2 peaks that are able to immediately be identified: the band edge of FTO (labelled ‘a’, Figure 3-5) and the stop band (labelled ‘c’, Figure 3-5). Peaks were identified using a local maxima algorithm in Origin v9.1 with a 20% difference in peak height as the defining limit for a new peak. All peaks found are reported in Figure 3-5. For most angles studied there are 3 discrete peaks observed.

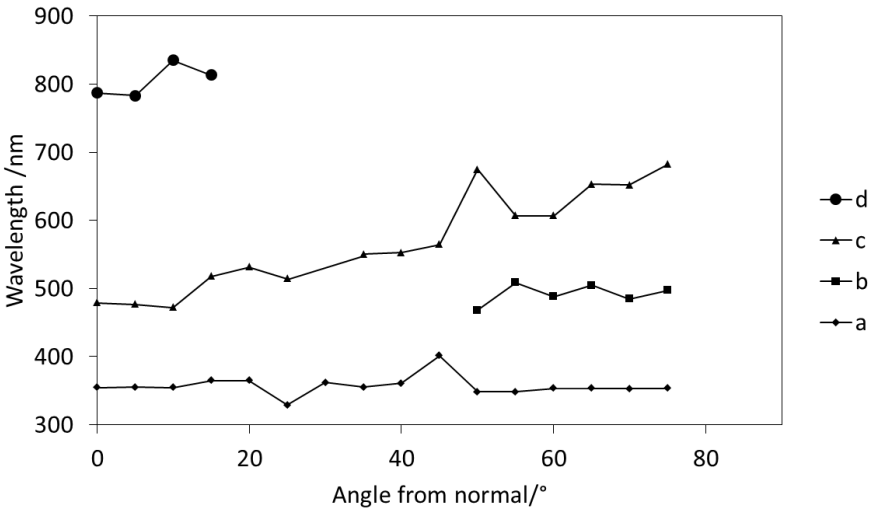

Figure 3-5: Measured peak reflections for a macFTO electrode as a function of incidence angle. Peaks were identified using a local maximum algorithm and all peaks are presented. The DR spectra can be found in the appendix.

The band edge is easily identified because it is present at all angles at the same wavelength (~350 nm). The stop band is also relatively easily identified as the largest peak in each diffuse reflectance spectrum. There is a clear angular dependence of this peak, moving to longer wavelengths with higher angles of incidence, as predicted using Equation 3-1. The remaining two peak sets (b and d) are not complete data sets i.e. the peaks on the diffuse reflectance spectra are not clearly present at all angles. Data set b is only present at higher angles and has a short peak wavelength, moving to slightly longer wavelengths with increasing angle of incidence. Data set d is only present at low angles of incidence, and has a much longer peak wavelength than data set b.

A comparison of the measured peak positions of the stop band for the [111] plane of macFTO as a function of incidence angle with the calculated value in (Figure 3-6) shows excellent agreement.

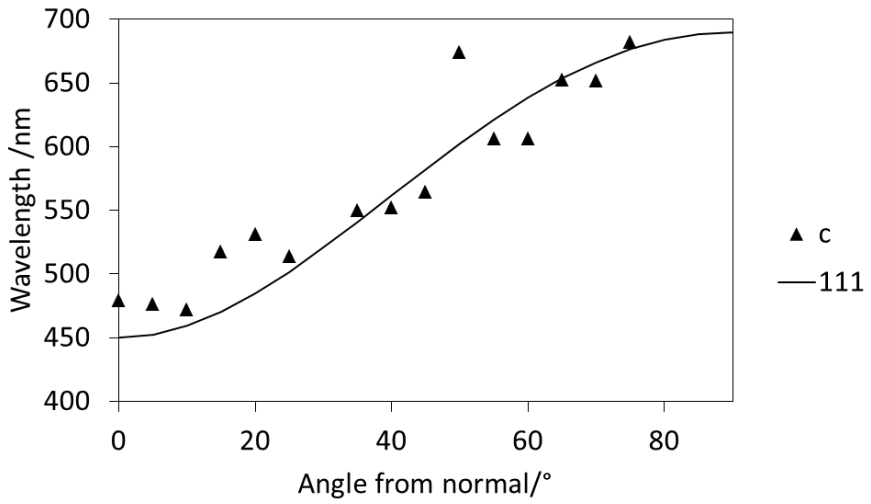

Figure 3-6: Peak position of the stop band with changing angle (open diamonds), compared to the calculation (solid diamonds). The result at 50° showed a consistent error which could not be corrected for, thus it is assumed that there was an error in the measurements. It has been included for completion.

It was not expected that any other angular dependent peaks would be observed, and the remaining data sets (b and d) do not match any of the other 3 allowed reflections for macroporous materials. Figure 3-7 presents the data from Figure 3-5, this time with calculated peak positions for comparison. Data sets b and d compare well with the disallowed planes [100] and [210].

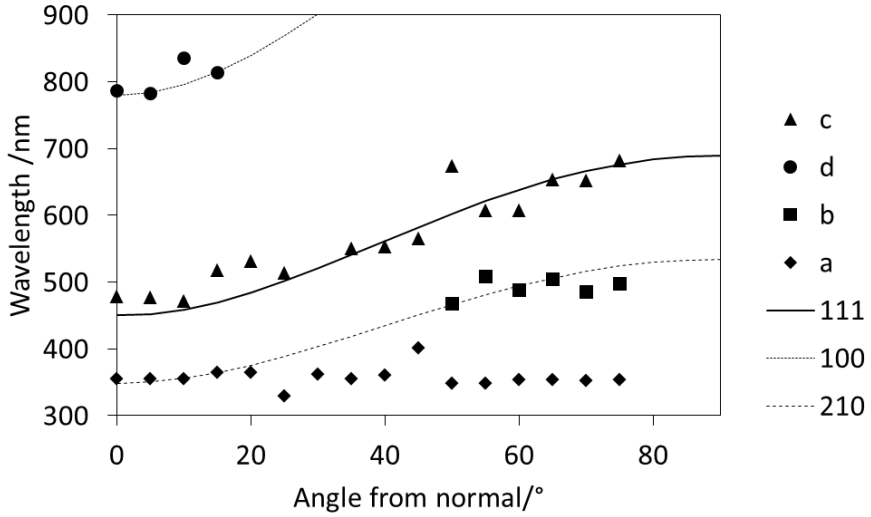

Figure 3-7: Predictions for some disallowed reflections (solid lines) and a comparison with the peak sets b and d. For references, the band edge is shown (a)

As the [100], and [210] planes are disallowed in fcc structures, the peaks cannot solely be due to reflections from these planes. However, the Renninger effect describes how an incident beam can be reflected several times before exiting a material at an angle which is different to

the incident angle. In the present work this may result in the appearance of a disallowed reflection. For example the [210] reflection may appear as a summation of reflections from two or more different planes that are allowed to reflect in the fcc structure. Calculations to determine the exact origin of the disallowed reflections are complex and as such are beyond the scope of this chapter.

In summary, the calculated and experimental stop band position correlate across all angles measured, which provides a clear and predictable shift of the stop band with angle of incidence which will be integral for the lifetime studies, presented in the rest of this chapter. Additionally, the stop band for the [111] plane is present in all calculations showing, in addition to the SEM analysis, that the structure is well-ordered and the photonic band gap is or is approaching three dimensional.

3.3. Emission Lifetime Measurements of Dyes Embedded in FTO

As the lifetime of embedded light absorbers is expected to change when the emission band overlaps the stop band, two dyes (Figure 3-8) with different emission wavelengths were used to probe the stop band and its effect on the lifetime of embedded emissive materials. The first dye, bis(2,2'-bipyridine)-4,4'-dicarboxy-2,2'-bipyridineruthenium(II) dichloride (Rudcbpy) can anchor to the surface of the FTO through the carboxyl groups on the bipyridine moieties. This binding can change the lifetime of the dye when compared to the dye in free solution.[117] The second dye was a mix of coumarin based dyes, chosen because it was thought that the absorption maxima would overlap the stop band at 45° incidence, which was experimentally easier to measure. The coumarin dye mix cannot be bound directly to the FTO as there are no suitable binding groups, but was instead coated onto the FTO by wetting the surface of the FTO with the dye then allowing the solvent to evaporate. The lifetime of the coumarin dye may have a small change because the local environment has changed: the coumarin has moved from solution to solid state.

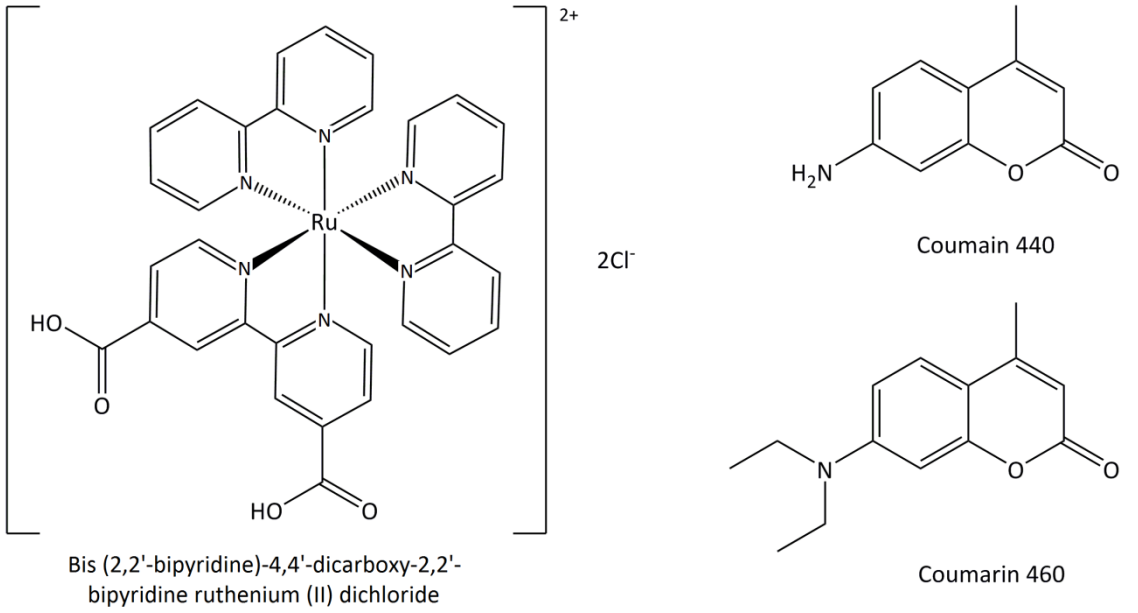

Figure 3-8: The structure of the two dyes used to probe the photonic properties of macFTO

The luminescence decay of the excited state was fitted to the exponential in Equation 3-5. Blank electrodes of pFTO and macFTO were used to determine the instrument response of the system and each dye was measured on equivalent planar electrodes as a reference electrode.

3.3.1. Immobilisation of Bis(2,2'-bipyridine)-4,4'-dicarboxy-2,2'-bipyridine ruthenium (II) dichloride (Rudcbpy) on FTO Electrodes and the Effect of the Photonic Host

Rudcbpy was immobilised on the surface of pFTO (pFTO-Rudcbpy) and macFTO (macFTO-Rudcbpy) films using a soaking technique, where the electrodes were immersed in an ethanolic solution of the Rudcbpy dye, before being removed and rinsed. This cycle was repeated several times to maximise loading. It has been shown that carboxyl groups can bind to surface hydroxyl groups irreversibly,[205,206] which is why repeat soaks were able to increase the loading of the dye on the electrode surface.

To monitor the change in luminescence lifetime with light incidence angle, it is first important to characterise the solution behaviour, which has been documented in the literature and as such makes Rudcbpy an excellent dye to use in this study. Figure 3-9 shows the absorption and emission profile of Rudcbpy, which matches well with literature.[207,208] The absorption peak at 450 nm is typical of Rudcbpy, and is due to a metal to ligand charge transfer (MLCT) transition,[209,210] the emission peak at 620 nm is also agrees well with literature values.[211]

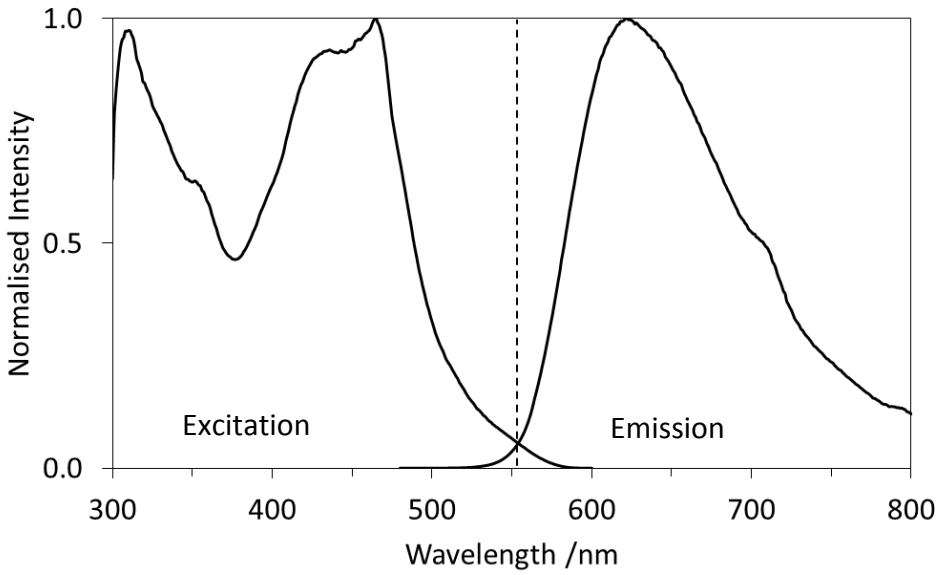

Figure 3-9: The photoluminescence profile of Rudcbpy in ethanol; the absorption maximum is at 450 nm and the emission maximum is 620 nm. Experimental details can be found in the experimental section.

The emission lifetime of the free dye (in solution) was measured from the fit of the decay curve to a single exponential as 367 ns $\pm$ 0.3 ns (Figure 3-10) with a χ^2 of 1.124. This value is in very good agreement with the literature value of 375 ns in phosphate buffer,[212] which is in very good agreement with the experimental value determined here.

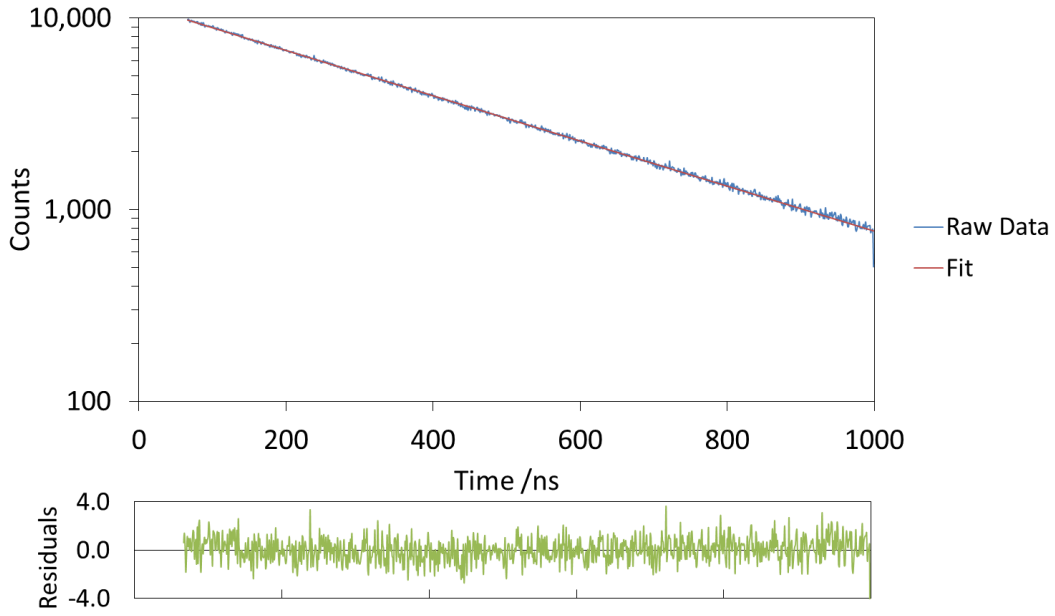

Figure 3-10: The emission lifetime decay curve of Rudcbpy in ethanol, with the raw data in blue, the fit in red and the residual signal in green.

Photoluminescence measurements are performed at 45° incidence in the present work, so it is important to determine if there is any overlap with the stop band of either the absorption or emission profile of Rudcbpy at this angle. The absorption and emission profiles of pFTO-Rudcbpy and macFTO-Rudcbpy are shown in Figure 3-11. pFTO-Rudcbpy has a photoluminescence spectrum that is not substantially different to that of Rudcbpy in solution; the emission profile is the same, and the absorption profile is very similar, with a broad peak centred at 450 nm. For macFTO-Rudcbpy, while the emission profile is very similar to that in solution the absorption profile shows an extended edge, between 500 and 550 nm. This difference in the absorption spectra is consistent with the effect from the stop band, where light absorption increases when the stop band is overlapped with the absorption peak.

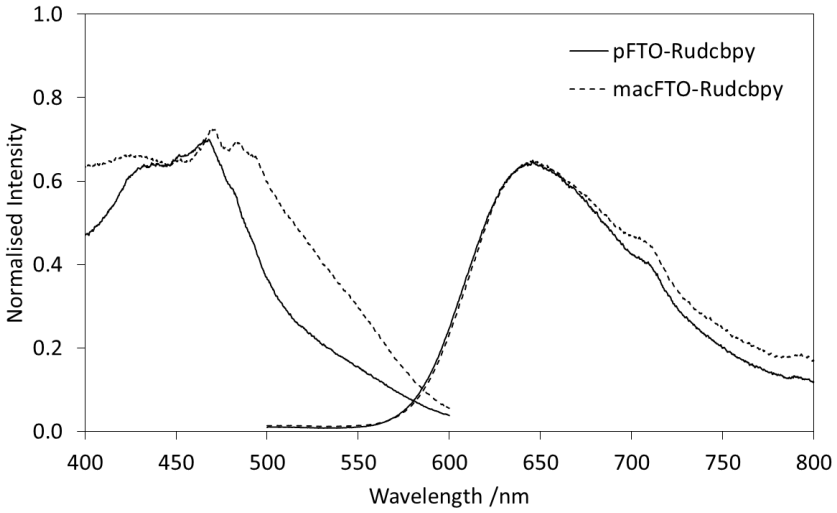

Figure 3-11: Photoluminescence spectra of pFTO-Rudcbpy and macFTO-Rudcbpy. The excitation and emission spectra are shown, with the parameters described in the experimental section.

The predicted change in stop band position with angle of incidence for the [111] plane of macFTO suggests that the maximum overlap is ~25° for the absorption and ~65° for the emission (Figure 3-12). As the enhancement should be seen at the stop band edges, the best enhancement should be seen at angles corresponding to lower (blue edge) or higher (red edge) angles than 25° and 65°.

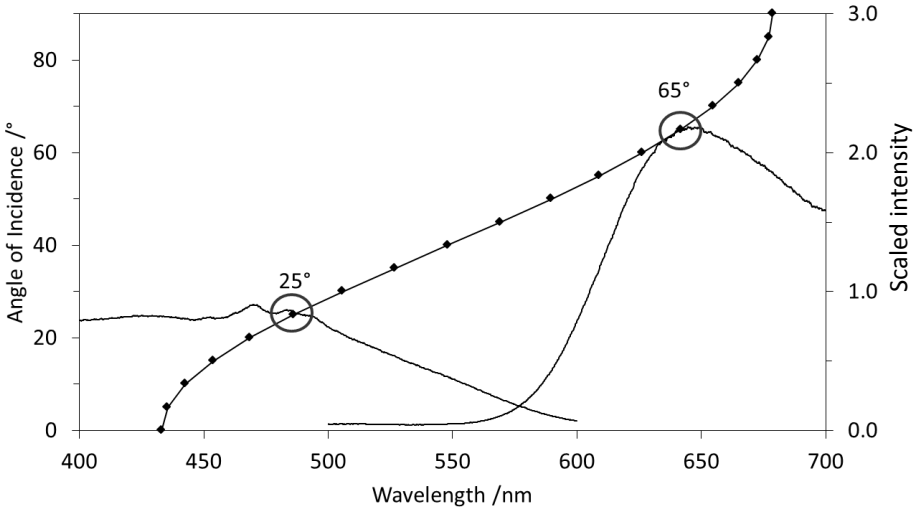

Figure 3-12: The photoluminescence profile of macFTO-Rudcbpy and the prediction of the [111] stop band. The maximum overlap is circled in red for the absorption and emission overlap.

The emission lifetimes of both pFTO-Rudcbpy and macFTO-Rudcbpy were then measured as a function of angle of incidence over 0 to 90°. Two components for pFTO-Rudcbpy, as determined from a bi-exponential fit to the decay curve, were found to be essentially invariant

with angle of incidence (Figure 3-13). The average χ^2 is 1.06, with no χ^2 for any fit being outside 1.00 ± 0.20.

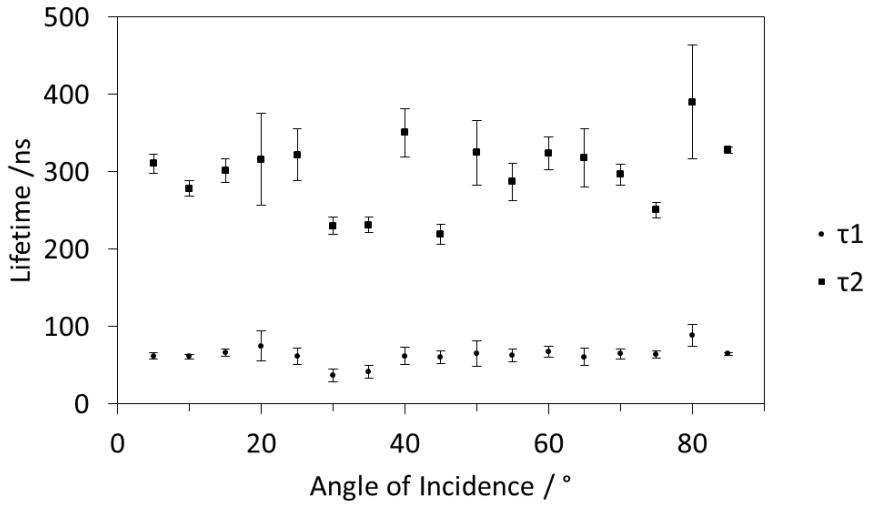

Figure 3-13: Lifetime components of pFTO-Rudcbpy as a function of angle of incidence, with the calculated standard deviation

The shorter lifetime component (τ_1) was not seen in solution, and so could possibly be due to scattering. The longer dominant component (τ_2), contributing 85% of the signal, was measured to be ~75 ns shorter than the solution value. This reduction in lifetime could be attributed to the dye being anchored to the FTO and being quenched non-radiatively. Lifetimes of dyes are known to change depending on the environment that they are in, thus it is not unreasonable to observe a change in the lifetime upon binding Rudcbpy to FTO. For example, Magde *et al.*[213] found that the lifetime of xanthene dyes increased markedly when the solvent was changed from methanol to octanol, and it would be not surprising to see a similar effect here.

The electron transfer between Rudcbpy and FTO should be relatively fast because there is a direct link between the Rudcbpy and the macFTO through the carboxyl group of the Rudcbpy. This can mean that the electron/hole pair can be separated quickly, and the lifetime is increased on average. The result of this in terms of luminescence measurements can be one of two things: 1) the electron and hole eventually recombine and emit, with a much longer lifetime, resulting in a measured lifetime that is significantly longer than that in solution or 2) the electron and hole do not radiatively recombine, instead decaying non-radiatively. This second process will result in an observed lifetime that is shorter than in solution, because it will only be the longer lived components that can be separated from each other, meaning only the short lived components emit and are detected. As the observed lifetime of pFTO-Rudcbpy

is shorter than that of Rudcbpy in solution, it is likely that the excited electron/hole pair loses the excess energy non-radiatively, and therefore the shorter lifetime is observed.

The luminescence decay of macFTO-Rudcbpy electrodes was fitted to a single exponential decay (Figure 3-14). In this case, the lifetime is longer than found for both pFTO-Rudcbpy and Rudcbpy in solution. The average lifetime across all angles is now 424 ns and the average χ^2 is 1.15, with no χ^2 being outside 1.00 ± 0.25. There is no obvious angular dependence, which was expected at ~65°, though the data point at 65° is above the average, and has the longest calculated lifetime of 503 ns $\pm$ 9.72 ns.

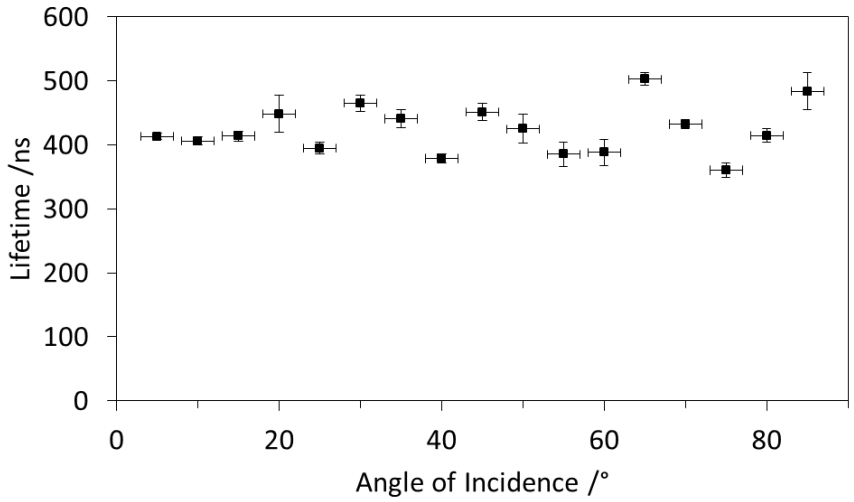

Figure 3-14: Angular dependence of macFTO-Rudcbpy lifetimes

The increase in luminescence lifetime from ~300 ns in pFTO-Rudcbpy to ~425 ns in macFTO-Rudcbpy is probably due to a combination of a reduction in the charge recombination in the macroporous electrodes and scattering from the porous structure. If scattering were the sole reason for the lifetime enhancement, this would correspond to increasing the optical path length by around 40 m (about 1% of the pores in the sample make up this distance), which is very reasonable.

The 70% increase in the lifetime is similar to the increase in lifetime observed by Veerappan *et al*.[214] who observed a 61% increase in the lifetime of TiO_2 electrodes when moving from planar TiO_2 electrodes to macTiO_2 electrodes. They ascribed this change to a decrease in the charge recombination. Additionally, at any angle of incidence the emitted light will still have to travel through the macroporous material, which means that the light has a high chance of interacting with multiple surfaces and being scattered multiple times, which in turn means that the optical

path length is increased, and the light will take a longer period of time to exit the material to be detected, resulting in a longer observed lifetime (the photonic effect).

To confirm whether there was any angular enhancement, macFTO-Rudcbpy was studied further between 60 and 70°, where the best of overlap was expected between the stop band and emission band. Figure 3-15 shows that there may in fact be some enhancement at 62°, which corresponds to the blue edge of the stop band. The measured lifetime is considerably larger than the baseline lifetime of ~400 ns being 557.7 ns ± 45.77 ns, and a factor of 1.8 higher than pFTO-Rudcbpy (~300 ns).

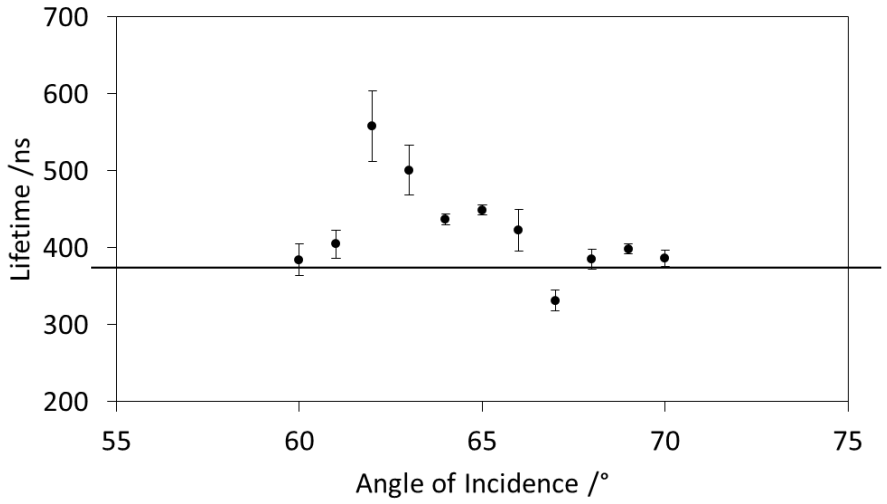

Figure 3-15: High resolution data for macFTO-Ru between 60 and 70°. The error on the angle measurement (±2°) has been left off for clarity. The horizontal line represents the baseline lifetime of macFTO-Rudcbpy

Table 3-1 summaries the results from the Rudcbpy electrodes: the lifetime of pFTO-Rudcbpy was found to be ~300 ns across all angles, which is slightly shorter than in solution (366 ns). The lifetime of macFTO-Rudcbpy was found to be longer than both pFTO-Rudcbpy and Rudcbpy in solution, at ~424 ns across all angles. No angular dependence was immediately obvious for macFTO-Rudcbpy, but a higher resolution study between 60 and 70° (where overlap with the stop band was expected) showed that there may be enhancement of the lifetime at the blue edge of the stop band, at 62°, which is consistent with the calculations. The enhancement is 1.8 times that of pFTO-Rudcbpy, which supports the conclusion that the photonic effect and contribute to extending the fluorescence lifetime of embedded dyes in macroporous structures.

*Table 3-1: Summary table of Rudcbpy electrodes. * these results are directly calculated by the instrument and fitting software. All other results are averages calculated across the entire angle range measured.*

Electrode	Lifetime /ns	Error /ns	χ^2
Rudcbpy (solution)	366.54 *	$\pm$ 0.316 *	1.124*
pFTO-Rudcbpy	63 300	$\pm$ 9 $\pm$ 25	1.06
macFTO-Rudcbpy	425	$\pm$ 14	1.15

3.3.2. Immobilisation of Coumarin 440/460 on FTO Electrodes and the Effect of the Photonic Host

The relatively long fluorescence lifetime of Rudcbpy makes it an inherent challenge to detect longer lifetime components deriving from lifetime enhancement due to the photonic effect. As a result coumarin was chosen as a second suitable dye with a shorter fluorescence lifetime[215] with the hope that the lifetime enhancement would be easier to resolve in the experiments. A solution of coumarin 440/460 was used as this is a well characterised laser dye and as such there was lots of literature available about the dye's behaviour for comparison.

Coumarin 440 and 460 do not have any anchoring groups to bind to the surface of FTO, unlike Rudcbpy. Consequently a different approach was taken to deposit the dye on the surface of the FTO electrodes. A mixture of 20 mL of coumarin 440/460 (herein called coumarin) was deposited by pipetting a known volume of ~0.1 mM dye solution onto the electrode surface before evaporation of the solvent. The deposition was then repeated 3 times to ensure a homogeneous layer and sufficient depth to yield a decent level of fluorescence.

Coumarin 440 has a literature emission maximum at 440 nm, while coumarin 460 has a literature emission maximum at 460 nm.[216] A mixture of coumarin 440 and coumarin 460, should have an emission maximum at the mean of the two components (~450 nm). Similarly the absorption maximum should be the mean of the two components (~360 nm) shown in Figure 3-16.

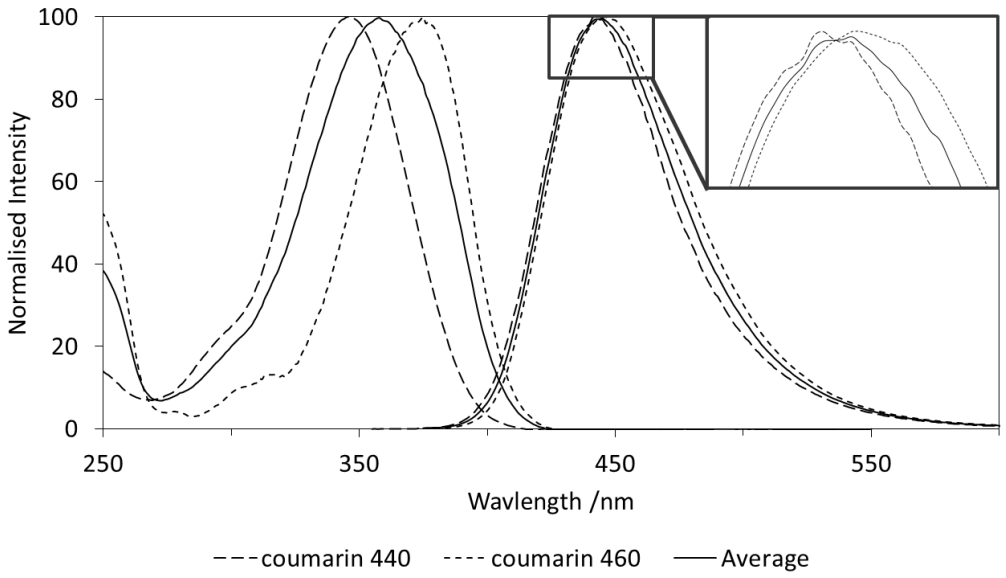

Figure 3-16: Calculated absorption and emission profile with literature data for coumarin 440, coumarin 460 and their average profile. Inset: higher magnification view of the peak apex.

Experimental measurements confirmed this, with an average emission maximum at 452 nm and an average absorption maximum at 393 nm (Figure 3-17). The experimental absorption and emission maxima are at longer wavelengths than predicted; this is likely due instrument errors as the predictions were based on literature data and not experimental data for the two separate dyes.

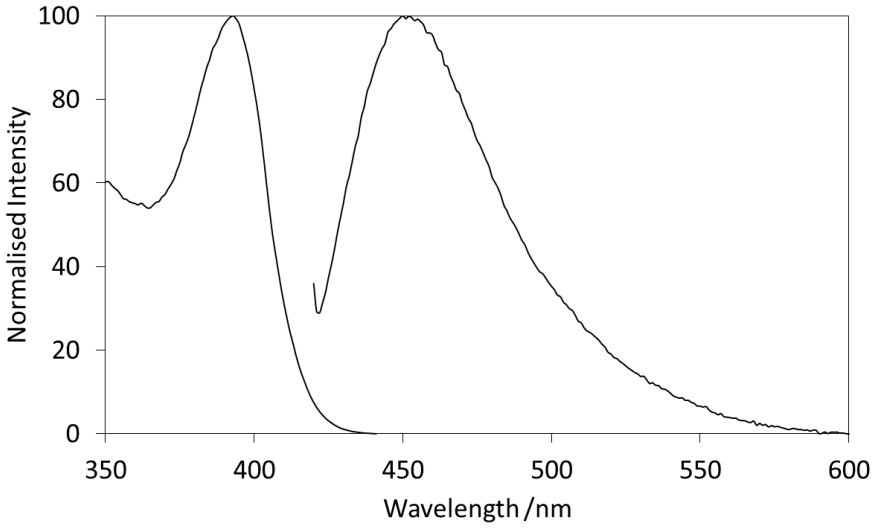

Figure 3-17: Experimentally determined excitation and emission profile of coumarin 440/460 in phosphate buffer (0.1 M). Experimental parameters are given in the experimental section.

The lifetimes of the coumarin 440 and coumarin 460 are two orders of magnitude shorter than Rudcbpy, at 3.64 ns and 3.10 ns respectively.[217] Because the lifetime values are very similar for

each coumarin dye, it may not be possible to distinguish between the two lifetimes, so an average value was assumed for the dye mix, of 3.37 ns, which can be used for data fitting.

Interestingly, the solution data can be fit to both one (the average lifetime) and two (the individual lifetimes for each dye) exponential terms. A single term fit (Figure 3-18) gives a lifetime of 3.5 ± 0.002 ns with an excellent χ^2 of 1.186. This value is consistent with the average lifetime of 3.37 ns. With a second term added, the lifetimes become 3.18 ns and 3.74 ns, with a χ^2 of 1.105, both of which are consistent with the literature lifetime of the two dyes.

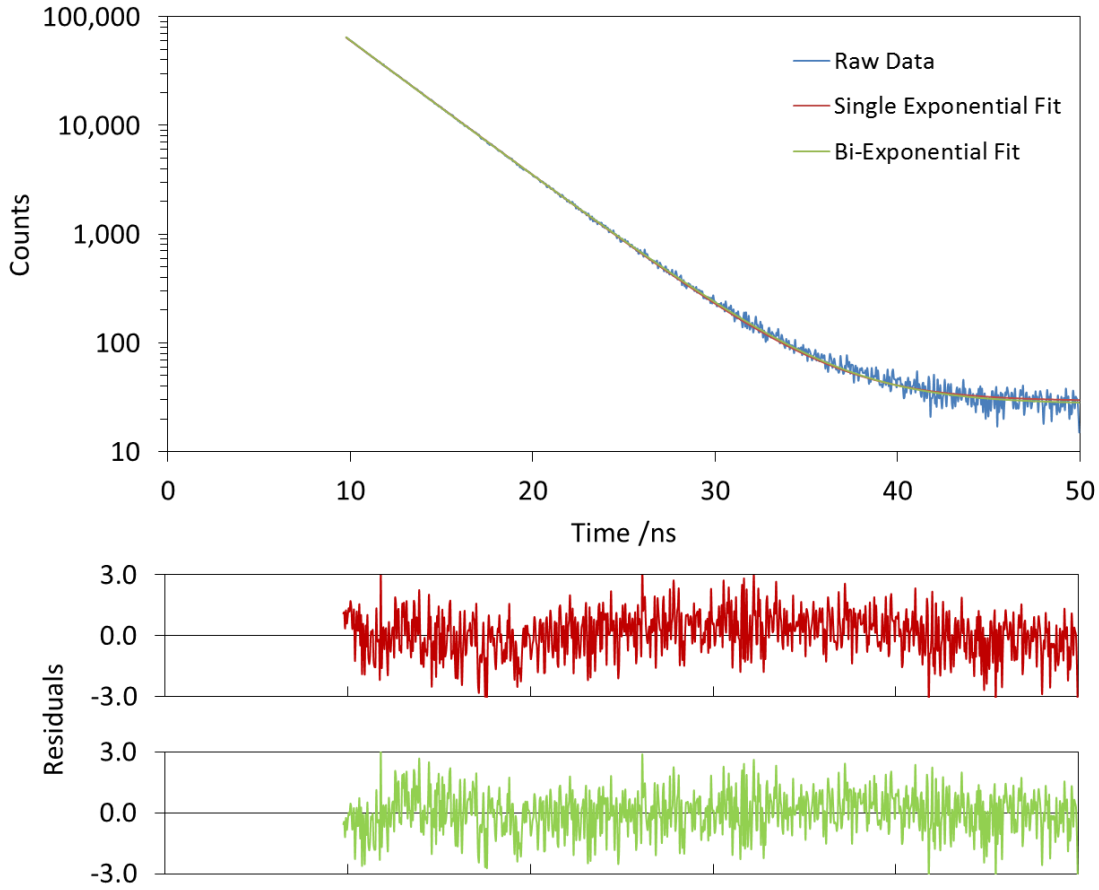

Figure 3-18: Single (red) and bi-exponential (green) lifetime fits of coumarin in ethanol. Although data was taken for the initial 10 ns, it has been excluded in this figure due to overlap with the IRF.

When coumarin was immobilised on pFTO, the absorption and emission profile did not change substantially, as expected, with the maxima lying at 370 nm and 453 nm for the absorption and emission respectively (Figure 3-19). However for macFTO-coumarin, two distinct bands appear in the absorption profile, one at 360nm and one at ~400 nm, which is consistent with the literature data for the two separate dyes. The emission profile however yields a single band consistent with the fact that both dyes emit at a similar wavelength.

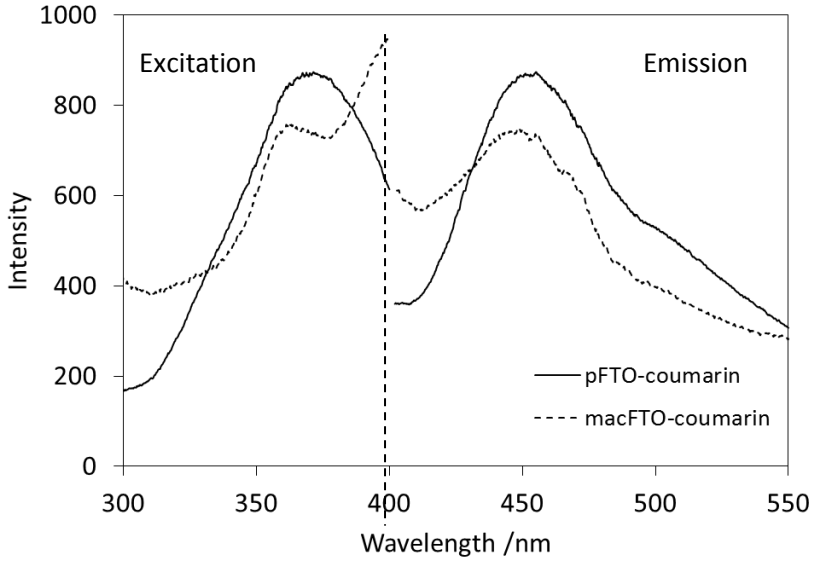

Figure 3-19: pFTO-Coumarin and macFTO-coumarin photoluminescence profile. The second peak in the excitation profile of macFTO-coumarin is the onset of the incident beam. The FWHM is wider than for the planar sample due to scattering effects, thus it can be seen on the macFTO-coumarin sample, and not on the pFTO-coumarin sample.

For coumarin, the absorption profile is not in the same wavelength region as the macFTO stop band, and thus there is negligible overlap. However, the emission does overlap the macFTO stop band at low angles of incidence, with maximum overlap at 13° and some overlap at 0 to 20° due to the broad profile of the emission (Figure 3-20). There should be greatest enhancement at the red edge of the stop band for macFTO-coumarin as this is where the overlap with the stop band edge is greatest.

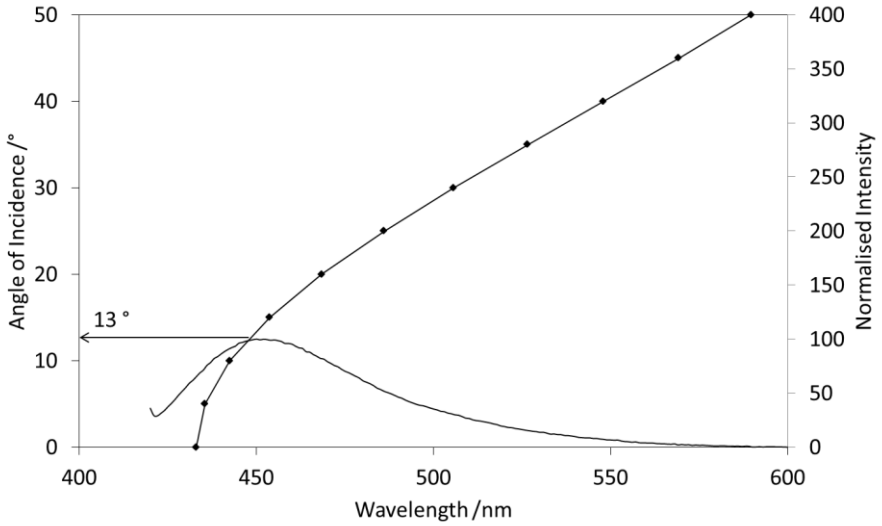

Figure 3-20: Photoluminescence spectra with the predicted positon of the stop band of macFTO

The fluorescence lifetime measurements for pFTO-coumarin showed two lifetime components, one as 3.00 ns and a second at 8.9 ns, both of which were invariant with angle of incidence (Figure 3-21). The shorter lifetime is consistent with the average value for the two coumarin dyes in solution, with the second longer lifetime component attributed to the different chemical environment. The appearance of the longer lifetime component was due to the fact that the electron is not as effectively transferred to the FTO in coumarin due to the lack of a direct bond and so electron transfer takes longer with subsequent radiative decay occurring later than in solution.

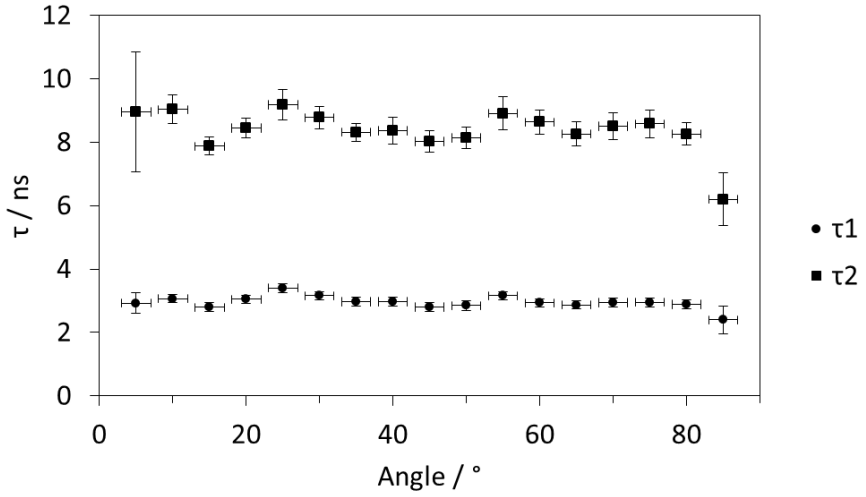

Figure 3-21: The two components of the lifetime of pFTO coumarin with changing incidence angle

The first shorter term contributes 33% of the total signal, meaning the second, longer, term has the largest contribution of 66%.

When macFTO-Coumarin was studied as a function of the angle of incidence, there were again two components to the lifetime (Figure 3-22). Similarly to pFTO-coumarin, there is a short component at ~3 ns, corresponding to unmodified dye. Again, this short lifetime component does not change with angle of incidence, but this time the contribution to the total signal is higher, at 52%. Across all angles there is still a longer component, but now the signal is clearly angle dependent. At high angles the lifetime is similar to the long component seen in pFTO-Coumarin (at 8.37 ns). However at small angles of incidence where the stop band overlaps the emission profile, the lifetime increases to a maximum value at 15° of 11.20 $\pm$ 0.33 ns.

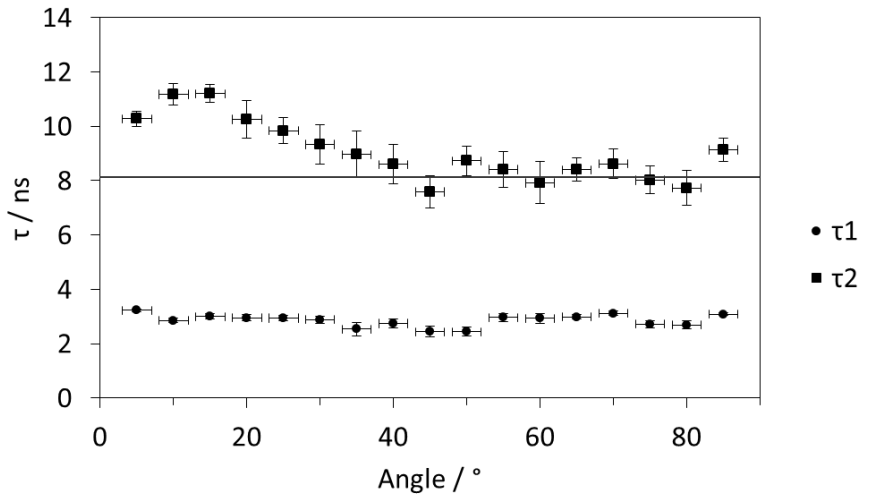

Figure 3-22: The two components of the lifetime of macFTO coumarin with changing incidence angle

To gain further insight into the enhancement of the lifetime at low angles, macFTO-coumarin was studied with higher resolution between 5° and 20° incidence (Figure 3-23). Again, the data was fitted to a two exponential curve, with each signal calculated to contribute 50% of the total signal, as with the lower resolution data. The short component was found to be 2.51 ± 0.17 ns at all angles studied, which is similar to the lower resolution data, as expected. The angular enhancement is also clear to see, at 11-17° incidence, and is clearly above the average unmodified lifetime calculated from the higher angle data. The enhancement in lifetime is seen at angles slightly higher than the stop band maximum, (red edge of the stop band) which is consistent with the literature. The χ^2 for measurements at all angles was within 1.00 ± 0.2, showing a very good degree of correlation between the raw data and the fitted data.

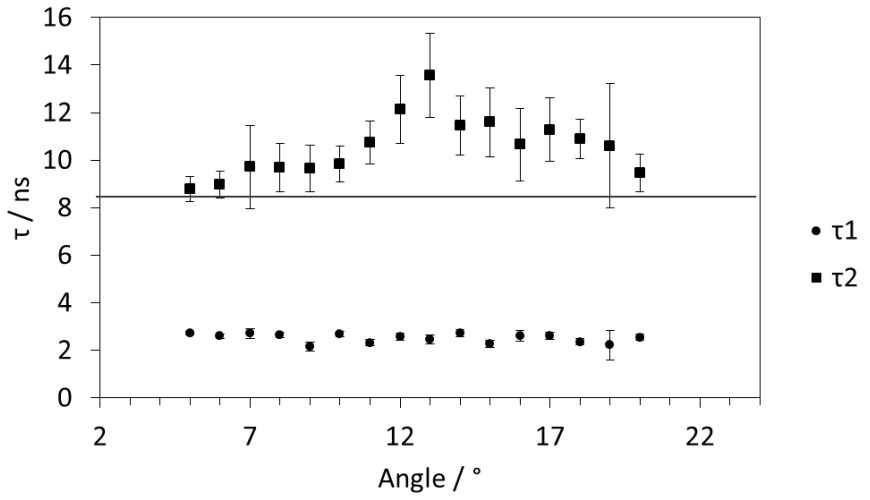

Figure 3-23: The two components of the lifetime of macFTO coumarin with changing incidence angle at low angles only.

The maximum observed enhancement was 11.59 ± 1.44 ns (13°) but the enhancement is not symmetrical about this maximum. The enhancement extends out to higher angles (red edge of the stop band) farther than it does for lower angles (blue edge), which is consistent with the prediction of the overlap where the red edge has better overlap than the blue edge.

In summary, neither the absorption profile nor the emission profile of macFTO-coumarin overlap the stop band at 45° incidence, so no enhancement was expected, and no enhancement was observed for either the absorption and emission profile. Table 3-2 summaries the lifetime data for the coumarin electrodes, which shows that for the lifetime studies there were two exponentials fitted for both the pFTO-coumarin and macFTO-coumarin electrodes. The shorter component was ~3 ns, which is consistent with unbound dye (little to no interaction with the electrode surface). The second longer lifetime was ~8 ns for the planar sample. For macFTO-coumarin the overlap with the stop band was expected at low angles and there was a clear deviation from the baseline lifetime of ~8 ns at these low angles of incidence, showing that there was some angle dependence. The maximum enhancement was ~11 ns, which is a factor of 1.4 larger than the planar sample at these angles.

*Table 3-2: Summary table for coumarin electrodes * these results are directly calculated by the instrument and fitting software. All other results are averages calculated across the entire angle range measured.*

Electrode	Lifetime /ns	Error /ns	χ^2	Relative %
Coumarin (solution)	3.5*	± 0.002*	1.186*	-
pFTO-Coumarin	2.95 8.38	± 0.16 ± 0.50	1.06	33 66
macFTO-Coumarin	2.85 8.37	± 0.13 ± 0.61	1.07	52 48

3.4. Critical Evaluation of Results

The stop band in macFTO was shown to be angular dependent and the peak maximum was tracked using diffuse reflectance over a range of angles (from 85° to 0° incidence). This is concordant with the results of Lopez-Lopez *et al.*[158] who also found that the stop band of macTiO$_2$ and macSiO$_2$ were angular dependent.

Little effect was seen for the absorption or emission profiles of the dyes embedded in macFTO. The edge of the absorption profile of Rudcbpy on macFTO was extended slightly, but not to the extent reported in the literature for other macroporous materials: several reports in the literature show an enhancement in the absorption spectra where the stop band overlaps the spectrum (Figure 3-24 a)),[129] or a dip in the photoluminescence spectra, again where the stop band overlaps most strongly (Figure 3-24, b)).[65]

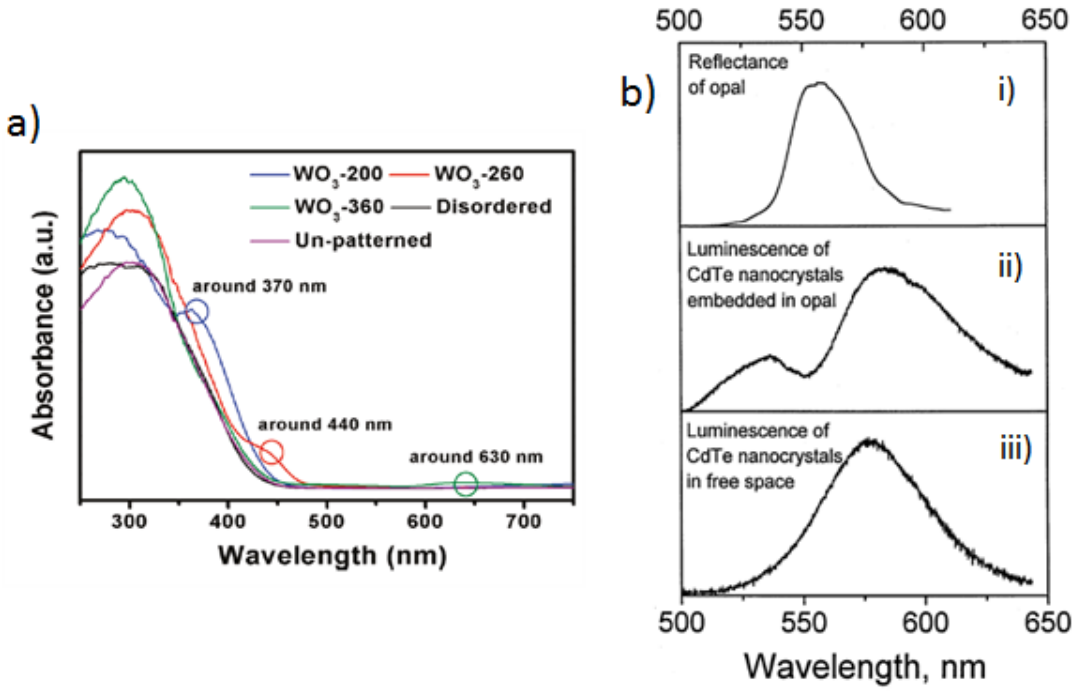

Figure 3-24: a) absorption spectrum of WO$_3$ electrodes, adapted from [129] and b) photoluminescence spectra of CdTe nanocrystals changes when the nanocrystals are embedded in macSiO$_2$ (i) reflection of macSiO$_2$, (ii) modified luminescence of CdTe nanocrystals in macSiO$_2$ and (iii) emission spectrum of CdTe nanocrystals for reference. Adapted from Gaponenko et al.[65]

Additionally, macFTO has been shown to elongate the lifetime of both Rudcbpy and coumarin (440/460) dyes when the stop band overlaps the emission profile strongly. For macFTO-Rudcbpy the lifetime enhancement was 1.8 times greater than pFTO-Rudcbpy at 62° incidence (maximum overlap). For macFTO-coumarin the maximum enhancement was 1.4 times greater than pFTO-coumarin at 15° (maximum overlap).

These results are consistent with several reports in the literature: Xiao *et al.*[144] present an enhanced lifetime for CdTe embedded in mac-SiO_2 of ~1.7 times at the angles where the stop band overlaps the emission profile most strongly. Two different studies on Kiton Red show that the lifetime can be enhanced by a factor of 1.7 – 2.5 if the emission profile of the dye is overlapped with the stop band of a colloidal suspension of polystyrene spheres.[145,200]

In other examples, macTiO_2 sensitised with a perylenediimide derivative was found to have a 5.5 times increase in the lifetime when the stop band overlapped the emission profile strongly[180] while macSiO_2 sensitised with LaF_3:Nd nanoparticles showed a 2.7 times photoluminescence enhancement when the stop band strongly overlaps emission profile of LaF_3:Nd nanoparticles.[125]

Chen *et al.*[191] showed that slow light at the stop band edge can increase the efficiency of the photoisomerization of azobenzene by 1.8 times in a mac-SiO_2 electrode. While the increase in the photocurrent is not a key part of this chapter, the 1.8 times enhancement is similar to the enhancement in the lifetime seen in the present work. All the enhancements reported in the literature (described above) are on a similar scale to the results presented in the present chapter of this thesis.

3.5. Summary and Conclusions

To summarise, diffuse reflectance is a useful tool to analyse the stop band position. The position of the stop band is dependent on the angle of illumination and will change depending on this angle, according to Equation 3-1. It was shown that the stop band position can be easily predicted using Equation 3-1, and this prediction is accurate in terms of the experimentally determined stop band position. In the diffuse reflectance spectrum there were multiple peaks which were angular dependent and did not correspond to the allowed [111] reflection. These peaks were found to be related to the stop band, and other allowed reflections, through the Renninger effect. It is unknown what effect these Renninger peaks will have on any lifetime measurements, so further study is required into both the origin of the peaks and also the effect that they may have on the fluorescent lifetime of embedded materials.

To determine the extent of the effect of the stop band on the optical properties, the photoluminescence and lifetime of two dyes were studied. At 45° incidence, which is the incidence angle for the photoluminescence spectra, the stop band is at ~570 nm, the only overlap at this angle with either dye is with the absorption profile of Rudcbpy. For macFTO-Rudcbpy, the shape of the absorption peak differs from that of the pFTO-Rudcbpy sample, which would be consistent with an effect from the stop band.

The lifetime enhancement from the stop band was much harder to determine because the lifetime value had to be extracted from a complicated decay curve. However, for both dyes studied some angular dependence was observed. For Rudcbpy, which had a long lifetime of 375 ns, the angular dependence was predicted to be observed at the blue edge of the stop band, as the overlap was greater here than at the red edge. An enhanced lifetime was observed for macFTO-Rudcbpy at 62° incidence which was 1.8 times greater than pFTO-Rudcbpy at this angle.

For coumarin 440/460, which had a shorter lifetime of 3.5 ns, it was thought that the angular enhancement may be easier to extract. The enhancement was predicted to be observed at the red edge of the stop band, as the overlap with the stop band edge is greater on the red edge than the blue edge. For macFTO-coumarin, the angular dependence was much easier to observe; there was a clear deviation from the baseline lifetime of ~8 ns at low angles of incidence. The maximum enhancement was at 15°, red shifted compared to the stop band maximum, and was a factor 1.4 times larger than the reference pFTO-coumarin lifetime.

When the Rudcbpy and coumarin electrode series are compared, it can be seen that the angular enhancement is seen for both electrodes, though it is much clearer for the coumarin electrodes than for the Rudcbpy electrodes. In both cases, the enhancement observed when moving from planar to macroporous electrodes was about 1.4-1.8 times greater. This is consistent with much of the literature, showing that there is a positive effect from the photonic structure, but the photonic effect can be relatively weak.

It could be possible to enhance the photonic effect by improving the quality of the macroporous structure. Chapter 2 showed that, while the structure was overall very good, there were some dislocations in the lattice from the synthetic steps. By further developing the method used to make the electrodes an even better structure can be made, which could see a larger enhancement in the lifetime of radiative dyes embedded in macFTO electrodes.

Chapter 4
Photoelectrodes

Chapter 4. Photoelectrodes

4.1. Introduction

In previous chapters it has been shown that by creating an electrode that is ordered porous (macroporous), or photonic, beneficial effects can be gained from the photonic effect. These effects include not only the increased surface area from being a porous electrode, but also the 'slow light effect' and the stop band effect (please see chapter 1: introduction or chapter 3: photonic effects for more details). Due to the periodic modulation of the refractive index from highly ordered porous (photonic) materials, there exists a wavelength region that is completely reflected: this region is called the stop band. At the edges of the stop band, incident light undergoes multiple coherent scattering which can lead to increased probability of absorption and/or increased probability of reabsorption of emitted light.[191]

Discounting the photonic effect, macroporous electrodes can show increased photocurrent densities and conversion efficiencies[218-221] when compared to planar or indeed disordered porous electrodes. The main reasons for this are an increased surface area available for reactions to occur and scattering effects from the porous nature of the electrodes

By using a templated support electrode (macFTO) a variety of different infiltrating materials can be easily deposited into the host material using simple techniques. If instead the infiltrating material was to be templated, considerable difficulties can arise in the fabrication techniques.

This chapter aims to show that not only can different materials be simply incorporated into the host macroporous material (macFTO), but the current densities and conversion efficiencies are increased over equivalent planar electrodes. macFTO exhibits photonic properties (the stop band, leading to slow light and increased probability of re-absorption of emitted light) and these effects are known to increase both the current density and conversion efficiency.

4.1.1. Planar Electrodes: Thin Film Devices

Thin film devices are prevalent in the literature in terms of solar devices because they are easy to fabricate and are desired over thick films because of the electron transport properties. Thin film devices tend to be planar, and made using a variety of simple fabrication techniques including bath/soak coating,[81,222] spray pyrolysis[223], spin coating,[41,224] and screen printing. The

thickness of such layers can be easily controlled by changing factors such as temperature, spin speed, and concentration among others. Quite often repeating cycles of deposition can be used to increase the loading of a material sequentially.[225]

Thin films are essential in solar devices because of the desirable charge transport properties. The transport distance of a charge is determined by the material it is travelling through, and as the charges can only travel a finite distance before recombination becomes the dominant cause of efficiency loss, thin films are desired. This decreases the transport distance of the charge, and thus should increase the overall efficiency.

This requirement for thin layers is in direct contrast with the fact that increasing the thickness of a layer can increase the amount of light that is absorbed,[226-228] and thus the current density (number of charges) that the electrode can generate per unit area. This means there is always a compromise between the maximum amount of material that can be deposited on an electrode and the thickness of the layer before recombination becomes a major source of efficiency loss.

4.1.2. Porous Electrodes

To ensure that as much light as possible is utilised, electrodes are often made porous. This allows the surface area to be increased, which therefore can allow more photons to be absorbed over the same geometric surface area. This maintains the requirement of thin films, but allows more light to be absorbed than in a compact planar film.

A further benefit to using porous materials is that any guest materials deposited over the porous material are constrained in size by the size of the pores.[229,230] This not only allows the size distribution of the guest material to be smaller and more homogeneous, but there will be a greater contact area between the host porous material and the guest material, as the guest material is smaller (Figure 4-1). Further to this, the guest material can be directly grown on the host surface, which increases the mechanical adhesion and promotes good electrical contact, which can accelerate electron transport and stabilise the material.[99,231] Additionally, there is a greater surface area available for catalysis which can also contribute to an increase in efficiency. Finally, the use of porous electrodes can decrease the size of the gas bubbles that are formed during water splitting, which increases the rate of release from the surface and thus keeps the current density high.[232]

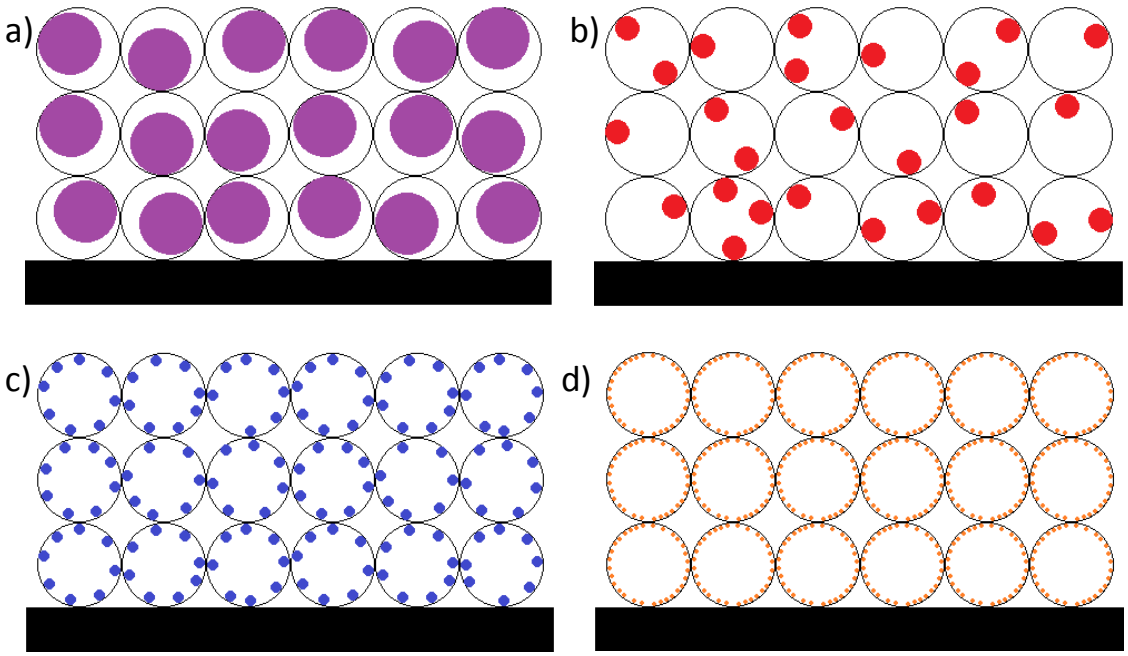

Figure 4-1: Illustration of how the pores can constrain the size of the nanoparticles (a) and how as the guest nanoparticles get increasingly smaller (b,c) the contact area with the host material increases. In situations b,c and d the nanoparticles can form a monolayer, but as the particles are smaller, the space between the deposited nanoparticles is also smaller, and therefore there is a greater contact area.

In any one study, one or more of these factors can contribute to the observed increase in efficiency when moving from planar to porous electrodes. For example, the degradation of rhodamine B over bismuth vanadate was observed to be enhanced when using a porous electrode compared to the planar (compact) version.[230] This is attributed to the increase in surface area. Another example is the use of a porous hierarchical Co_3O_4@$Co_xFe_{3-x}O_4$ film,[99] which was shown to have increased OER performance when compared to a non-porous film. Again this increase was attributed to the surface area increase. There are a variety of other works that credit the increase in activity of a process to an increase in surface area when moving from planar electrodes to porous ones.[231,233-235]

While the increase in activity is very useful, the fact that each of these electrodes was fabricated using a different method which was generally time consuming with many synthetic steps adds complexity to the situation. For example, MOF templating[231,234] or Ni foam templating[99,231] often has many steps. Adding to this, the structures formed are generally uncontrolled,[235] which can be unfavourable for electron transport and/or catalysis, as well as causing diffusion issues through differently sized pores[236] and there may not be particularly good adhesion to the backing substrate, which means there are potential stability issues.[231,237-

[239] Furthermore, the porous nature of the electrode means that there is a lot of surface scattering, and this can lead to losses in efficiency.

4.1.3. Ordered Porous (Macroporous) Electrodes

If an ordered templating system is used such as that in Figure 4-2, many of these undesirable effects can be avoided. For example, all the pores will be the same size and in the same position relative to one another. This both controls the structure and reduces the issues to do with diffusion. If the pores are controlled to be of the same order of magnitude as visible light, then additional beneficial effects can begin to contribute, as described in chapter 3.[115,129,136,143,194,240]

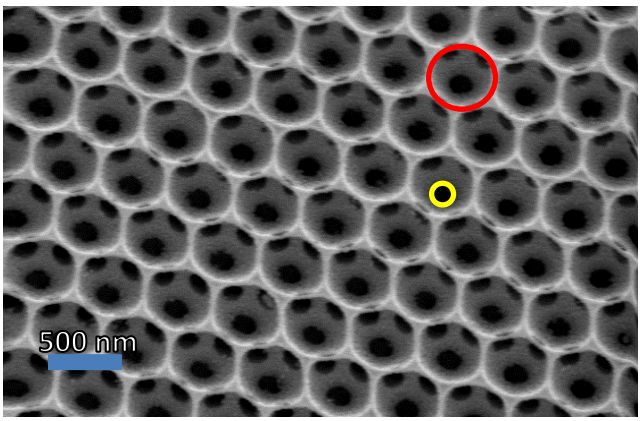

Figure 4-2: Image of an ordered porous electrode (macroporous electrode). The red circle shows the pore size, while the yellow circle shows the window between adjacent pores.

Finally the issue of deposition of secondary materials over the host structure can now be addressed. Previously, to create porous electrodes, many of the materials had to be deposited in different and relatively complex methods, which may not work particularly well. Now, over a templated porous electrode, the deposition step is conceptually much simpler (Figure 4-3). More traditional methods of deposition, such as drop casting, bath or soak methods,[115,144,241] electrodeposition[242] and even spin coating, may be used to deposit materials. There is no need to template the materials in question because they will deposited in a thin film over the already templated backing electrode, thus the construction of macroporous electrodes becomes simpler.

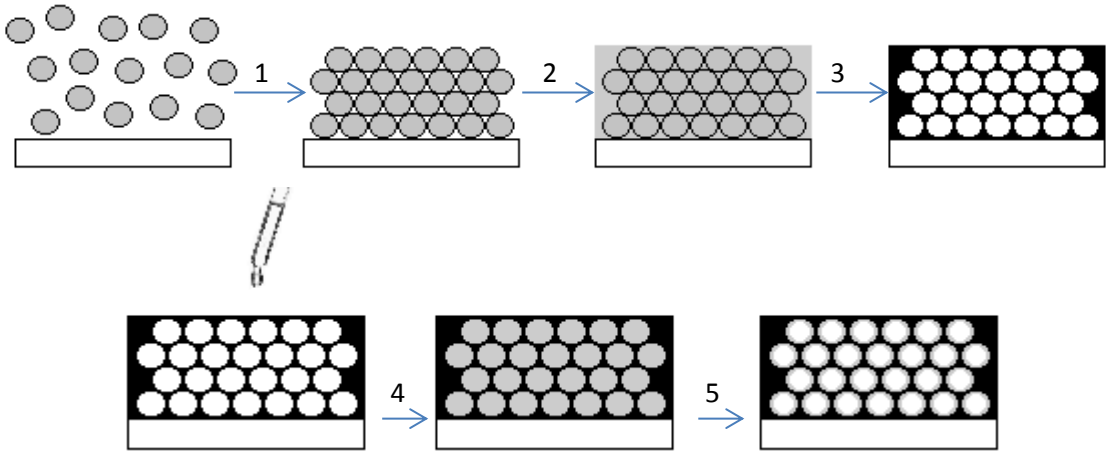

Figure 4-3: Scheme showing the synthesis of macFTO and the deposition of a secondary material. Step 1: deposition of polystyrene spheres, step 2: infiltration of FTO precursor mix, step 3: calcination to remove polystyrene template and sinter the macFTO, step4: infiltration of desired secondary material, step 5: heating to remove excess liquid forming a monolayer of secondary material inside the pores.

There are several examples of templating oxide semiconductors around a colloidal crystal (to make macroporous materials), with varying success. The prevalent technique for forming macroporous electrodes of different materials is a sol-gel technique. Semiconductors such as $BiVO_4$,[243] Fe_2O_3,[242] Fe_3O_4,[135] ZrO_2,[136] SiO_2,[65,244] TiO_2,[49,66,148,166,181,201,245,246] AZO[220] and WO_3[129] have all been templated around spheres to create a macroporous electrode. There are varying degrees of success when doing this, and all the parameters are slightly different, from calcination temperature, to additives to help the gelling process. It is far simpler to use one method to create the macroporous electrode, and then simple well known techniques to deposit secondary materials over the macroporous electrode. On glass supporting electrodes a transparent conducting oxide (TCO) is used so that the electrode can be back illuminated. As discussed in chapter 2, FTO is the preferred TCO material due to cost and abundance of elements. Templating FTO has been done several times: Yang *et al*.[57] use a method similar to the one described in the present work and by the work of M. Zhang (in the group): they template the FTO precursor around a polystyrene template, which they then remove by calcination at a temperature of 400 – 500 °C. Other methods of templating FTO are more complex and involve, for example, long refluxes of the precursors, followed by spray coating a carefully prepared substrate at 400°C.[177] There are no other reports of synthesis of macFTO published from the date of the submission of this work to this author's knowledge. Once this material is made, simple spray coating or bath methods can be used to deposit further materials. Materials that have been simply and easily deposited over macroporous networks are mainly nanoparticles, for example CdTe on macSiO_2[144] and Pt on macTiO_2,[49] which makes deposition of any material over macFTO new.

To demonstrate the application of macFTO, the electrodes described in chapter 2 (macFTO) will be used as a supporting TCO electrode for depositing films of photoactive materials. These materials include CdS and $BiVO_4$. CdS was chosen as it is easy to make small nanoparticles, which will be necessary to fit inside the macFTO pores, and also because CdS has good absorption across the visible light region leading to high photocurrent densities. $BiVO_4$ was chosen because its band gap is also in the visible range, at 2.4 eV and because it is stable under oxidative conditions and has been shown to photo-oxidise water to dioxygen. Both materials can be made as nanoparticles[247,248] which means that there is the opportunity to deposit the materials over macFTO using a simple technique.

After this, the electrodes that show promising activity can be used to actually split water (Figure 4-4).

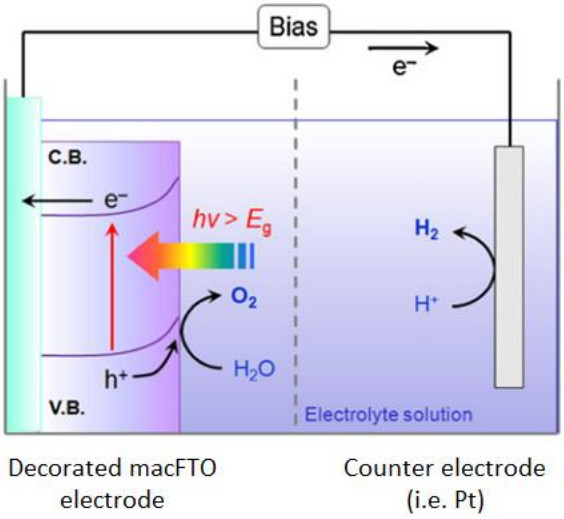

Figure 4-4: Schematic showing how a two electrode system could be used to split water. The macFTO electrode has both light absorbing materials and an oxygen evolution catalyst deposited over it while the counter electrode will be able to evolve hydrogen. Initially the counter electrode will be platinum to avoid limiting the reaction at the cathode. Adapted from Maeda[249]

The focus is on the oxygen evolution reaction, as this is the more difficult of the two half reactions. To effectively drive oxygen evolution a catalyst may be required: a suitable catalyst for water oxidation is CoPi (cobalt phosphate). CoPi works at close to 100% faradaic efficiency and has been shown in many works to be effective.[79,250] Again there are many ways to deposit CoPi over electrodes,[79,101,104] and once again it will be demonstrated that a simple deposition technique can be used to deposit CoPi evenly over the macFTO electrode. Ultimately this will produce a porous electrode that was fabricated using simple techniques, and is versatile, so that many different materials can be deposited.

4.1.4. Calculation of Device Efficiency

For an explanation of the calculation of device efficiency please refer to the introduction.

4.1.5. Aims of the Project

The purpose of this chapter, and the entirety of the present work, is to demonstrate that templating the supporting TCO electrode produces ordered porous electrodes that are versatile, i.e. many different photoactive materials can be deposited using simple traditional techniques. The use of an ordered porous electrode can increase the overall device efficiency because the surface area is much larger than with a planar electrode, and the electron transport properties of a thin film are operative.

To demonstrate this effect, well known materials for light absorption and water oxidation should be deposited over planar and macroporous electrodes. The planar electrode serves as a control, and allows comparison to other works in the literature. The electrodes were initially studied at an angle where minimal photonic effects occur to first determine the activity of the electrodes. Further work on the electrodes presented in this chapter should aim at looking at the electrode activity at angles where the photonic effect is observed, to characterise this effect further.

Additionally, if the electrodes produced were particularly efficient, they were tested for the activity towards either hydrogen evolution or oxygen evolution from water (water splitting), with the ultimate aim of producing an efficient device for water splitting.

The efficiency of a macroporous electrode when compared to a planar electrode will be tested in several ways. Initially the electrodes photocurrent density will be compared when the planar and macroporous electrodes are loaded with the same amount of material. This is expected to give the same current density because there is the same amount of material on each electrode. Then the amount material will be maximised for the macroporous electrode. The same method will be used to deposit material on the planar electrode for comparison. At this point there is expected to be a clear difference in the macroporous electrode when compared to the planar electrode because the surface area is much larger for the macroporous electrode than the planar electrode.

If the electrodes then appear particularly effective, they can be used in the water splitting reaction, where the overpotential for oxygen evolution will be monitored, and the efficiency of

oxygen production can be measured. Ultimately, the aim of the project is to produce 2 working electrodes, one for each half reaction, which will combine to from a working device that requires no external potential to drive the water splitting reaction.

4.1.6. Electrode Notation

In this chapter all FTO electrodes are made using a precursor Sn:F ratio of 0.5 and calcined at a temperature of 450 °C. Further electrode notation is as follows: where 'FTO' is prefixed by 'mac' the FTO electrode is macroporous, and where the prefix is 'p' the electrode is planar. The following notations then refer to the material/s that have been deposited ($CdS/BiVO_4/CoPi$), and the order that they are listed is the order of deposition. For example mac$FTO\text{-}BiVO_4\text{-}CoPi$ describes a macroporous electrode of FTO where first $BiVO_4$ was deposited, then CoPi. For either $BiVO_4$ or CdS there may be further notations in brackets that describe the type of deposition, (np = preformed nanoparticle deposition, bath = bath deposition). For CoPi any notations in brackets describes the deposition conditions (time of deposition, or whether light was used to assist the deposition). The main notations for CoPi are 'edep' signifying that the material was electrodeposited and 'pedep' which signifies that the electrode was deposited using photoelectrodeposition (or light assisted electrodeposition).

It should be noted that all electrochemical experiments in this chapter are illuminated at 90° incidence. At this angle of illumination the stop band position is ~700 nm, which means that for these experiments there should be no photonic effect contributing to the photocurrent density. Any change in photocurrent density can therefore be attributed to the increased surface area and/or increased scattering from the ordered porous material.

4.2. Sensitisation of FTO Electrodes with Cadmium Sulfide (CdS) Nanoparticles

4.2.1. Deposition of the Preformed Nanoparticles on FTO Electrodes and their Photoactivity

In the present work, CdS nanoparticles are used to sensitise FTO and macFTO to visible light. CdS nanoparticles were synthesised according to a modified procedure based on the work of Zhang *et al.*[251] The nanoparticles formed were stabilised with oleic acid ligands to prevent aggregation and maintain solubility in toluene. The characterisation of the macFTO-CdS electrodes presented in the present work was undertaken by M. Zhang[1] and is given briefly here for context. All electrochemical analysis was undertaken by the author of this thesis.

4.2.1.1. Analysis and Deposition of CdS Nanoparticles

The preformed CdS nanoparticles have an absorption profile consistent with literature and clearly absorbed visible light, being bright yellow and having an absorption onset of ~480 nm (2.6 eV) which corresponds well with the literature bulk band gap of CdS (2.4 eV).[252,253]

The preformed CdS nanoparticles (20 μL) were deposited on the surface of FTO electrodes *via* a simple drop casting procedure. It was necessary to calcine the electrodes in air after nanoparticle deposition to remove the stabilising ligands on the CdS nanoparticles. This also served to sinter the nanoparticles to the electrode, to ensure a good electrical connection.

After the deposition of CdS nanoparticles on FTO and subsequent calcination, the colour of the FTO-CdS electrodes did not change (they remained translucent). This observation suggests that very little CdS was deposited as the electrode should be bright yellow in colour if a considerable amount of CdS had been deposited. However, TEM can confirm the presence of CdS nanoparticles (Figure 4-5, darker areas). The nanoparticles appear to be evenly dispersed over the macFTO electrodes and are quite small with an average size of 5-10 nm. The size of the nanoparticles after deposition compares well with the size of the nanoparticles before deposition (~3 nm before deposition)[127] but clearly the nanoparticles have aggregated slightly on the surface of the electrodes compared to in solution.

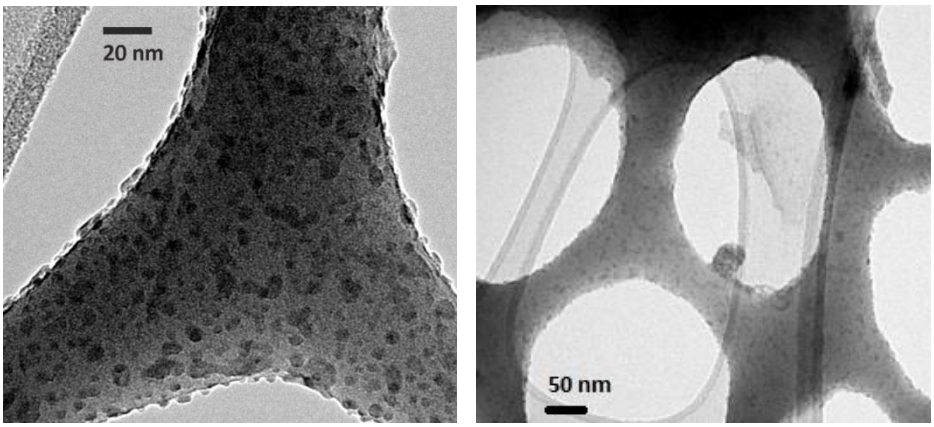

Figure 4-5: TEM images at different magnifications of macFTO-CdS (nanoparticles), best electrode (see Figure 4-7, electrode macFTO-CdS c). The small darker areas are the CdS nanoparticles on the macFTO electrode.

4.2.1.2. Electrochemical Analysis of FTO-CdS Electrodes

In chapter 2 it was shown that pFTO and macFTO electrodes gave very small photocurrent density densities of 0.03 µA cm^{-2} and 3.0 µA cm^{-2} at 1.5 V_{RHE} respectively. To confirm that both the pFTO and macFTO electrodes could be sensitised to the same level, a small amount of CdS nanoparticles was deposited on each pFTO and macFTO electrode. The deposited quantity of CdS was kept the same for each electrode, so if the behaviour of the electrodes is the same the photocurrent density obtained from the CdS sensitised electrodes should be comparable. Controlled potential electrolysis (CPE) shows that at 0$V_{Ag/AgCl}$ the photocurrent density for both macFTO-CdS and pFTO-CdS was ~15 µA cm^{-2} (Figure 4-6), confirming that pFTO and macFTO act in the same way and produce the same amount of photocurrent density when sensitised with the same amount of CdS. This also shows that a simple method can be used to deposit CdS nanoparticles on the surface of macFTO, thus creating a large surface area CdS electrode, with no complicated fabrication techniques.

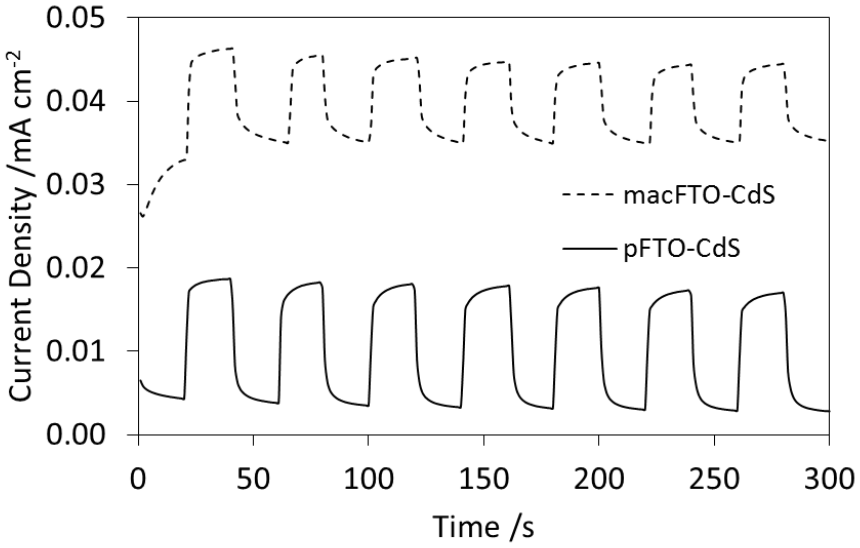

Figure 4-6: The photocurrent density of pFTO-CdS compared to macFTO-CdS when the CdS nanoparticle loading is the same, measured at 0 $mV_{Ag/AgCl}$ (0.86 V_{RHE}) in sulfide/sulfite electrolyte.

To increase the photocurrent density, macFTO electrodes were loaded with increasing amounts of CdS nanoparticles, using the same drop casting method. Figure 4-7 shows the same macFTO-CdS electrode as in Figure 4-6 with increasing amounts of CdS. The current density was increased from only 150 µA cm^{-2} (a, 20 µL of CdS nanoparticle solution) to 0.2 mA cm^{-2} (b, 40 µL of CdS nanoparticle solution) to nearly 1.2 mA cm^{-2} (c, 60 µL of CdS nanoparticle solution).

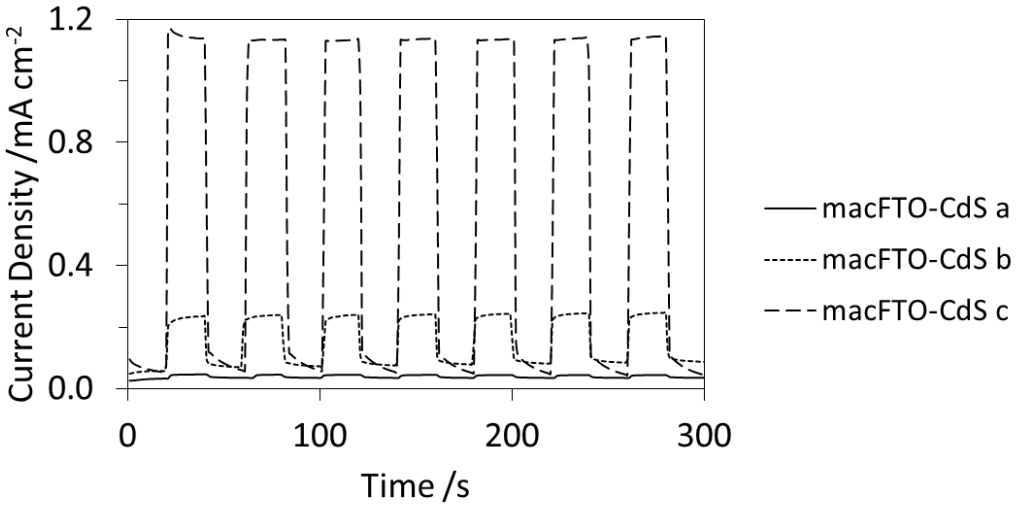

Figure 4-7: The change in the photocurrent density of macFTO-CdS electrodes when the CdS nanoparticle loading is increased from 20 µL of CdS nanoparticle solution to 60 µL of CdS nanoparticle solution, measured at 0 $mV_{Ag/AgCl}$ (0.86 V_{RHE}). If increasing amounts of CdS are deposited on pFTO electrodes the solvent bead on the surface of the electrode, causing agglomeration of the nanoparticles. Thus it was not a fair comparison of the photoactivity.

Interestingly, the low photocurrent density of the macFTO-CdS electrodes was initially increased under the conditions of the experiment: under illumination in a solution of sodium sulfite/sodium sulfide at 0 $V_{Ag/AgCl}$. The most likely explanation for the increase in photocurrent density over time (Figure 4-8) is that the calcination step, necessary to remove the oleic acid ligand, also oxidised some CdS to CdO. Upon irradiation in sulfide/sulfite solution the CdO is converted back to CdS, which can then contribute to the total photocurrent density, resulting in a larger photocurrent density than initially seen.

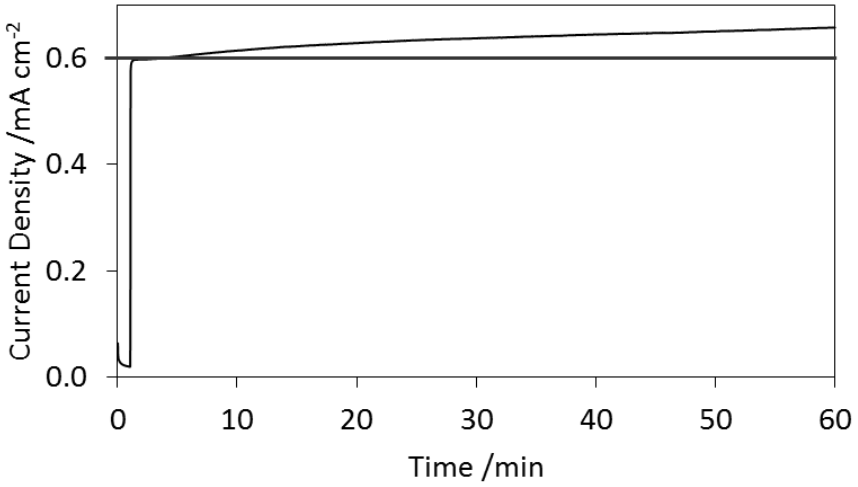

Figure 4-8: The increase in photocurrent density over time of a single macFTO-CdS electrode when irradiated in sodium sulfide/sulfite solution at 0 $mV_{Ag/AgCl}$. The horizontal line gives the initial photocurrent density, to guide the eye.

Following the observation that calcination can degrade the macFTO-CdS electrode and subsequent electrochemical treatment can increase the photocurrent density, the macFTO-CdS electrodes were tested for activity before and after calcination, to probe if the calcination step was necessary or not to gain a large photocurrent density. It was found that when the electrode is not calcined (dashed line) the photocurrent density is much lower at ~0.2 mA cm^{-2} than when the electrode is calcined (solid line) at ~0.8 mA cm^{-2} (Figure 4-9). This demonstrates that the calcination step to remove the stabilising ligands is necessary to ensure a good electrical contact between the macFTO electrode and the CdS nanoparticles. While this means that some CdS may always be converted to CdO (and therefore the photocurrent will decrease) the purpose of these experiments is to examine the current collection of macFTO electrodes compared to pFTO electrodes. As such, the fact that the photocurrent can be measured and increased proves that macFTO electrodes will be suitable as a host electrode for the water splitting reaction.

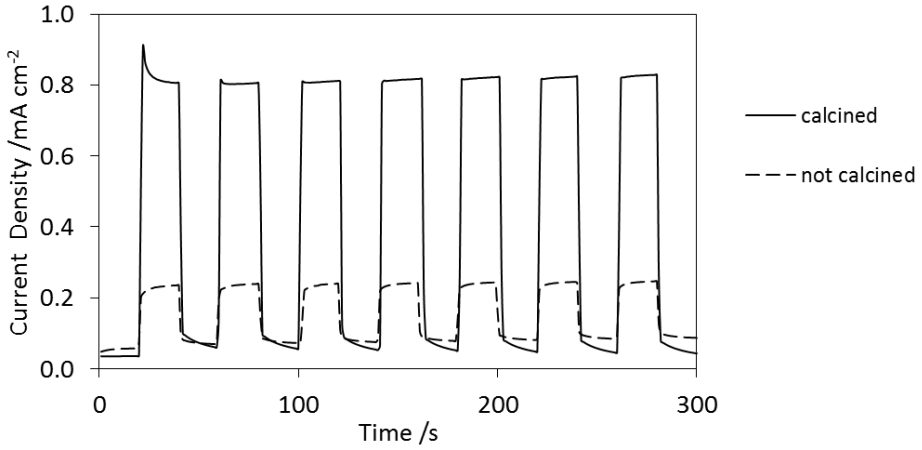

Figure 4-9: Photocurrent density action spectrum showing the difference between using a calcination step after nanoparticle deposition and not calcining the electrodes after nanoparticle deposition

A secondary problem with loading the CdS nanoparticles onto FTO electrodes is the difference in hydrophilicity between the FTO electrode and the CdS nanoparticles in toluene. This hydrophilicity difference causes the nanoparticle solution to bead on the surface of the FTO electrode and not disperse evenly, which in turn means that it is difficult to load large volumes of nanoparticles onto electrodes. Ultimately this problem means that the photocurrent density will not be large. To try to reduce this hydrophilicity problem, and thus increase end photocurrent density, the electrodes were pre-coated in the stabilising ligand (oleic acid). This should promote favourable interactions between the FTO electrode and the CdS nanoparticles allowing better dispersion of CdS nanoparticles over the whole electrode. Figure 4-10 shows the change in photocurrent density when the electrodes are pre-coated in oleic acid before nanoparticle deposition (dashed line) and having no pre-coating before nanoparticle deposition (solid line).

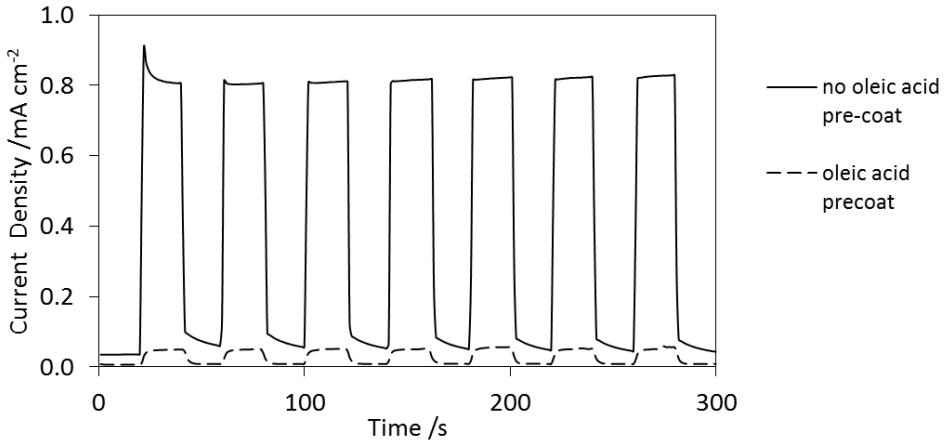

Figure 4-10: Photocurrent density spectrum showing the difference between pre-coating electrodes in oleic acid before nanoparticle deposition and not pre-coating electrodes with oleic acid before nanoparticle deposition. In every case the electrodes were calcined after nanoparticle deposition.

It is immediately apparent that the photocurrent density gained from the electrodes is substantially better when the electrode is not pre-coated with oleic acid with a photocurrent density of ~0.8 mA cm^{-2} compared to ~0.1 mA cm^{-2} when the electrode is pre-coated with oleic acid. This decrease in photocurrent density when oleic acid is used to pre-treat the electrodes can be attributed to the oleic acid interfering with the electrical connection between the CdS nanoparticles and the FTO electrode: oleic acid itself is not conductive and, after calcination, the carbon deposit that may be left behind could be interfering with either the light absorption of CdS or the electrical connection between CdS and FTO. In either circumstance, the photocurrent density is lower than if oleic acid is not used to pre-treat the electrodes. This result is consistent with the calcination test: the presence of oleic acid is detrimental to the observed photocurrent density.

A further difficulty associated with the hydrophilicity difference between FTO and the CdS nanoparticle solution is that achieving a monolayer of CdS is difficult, as the CdS nanoparticle solution does not disperse evenly across the entire macFTO or pFTO electrode surface. Even at the highest loading studied, the CdS coverage on macFTO does not reach that of a monolayer (Figure 4-5, above). The drop casting method does not produce electrodes with sufficiently high photocurrent density for applications in the solar energy field, which means an alternate method of depositing the nanoparticles should be developed.

4.2.2. In-Situ Formation of CdS Nanoparticles on FTO Electrodes and Their Photoactivity

Due to the drawbacks of pre-forming CdS nanoparticles and depositing the CdS nanoparticles using a drop casting method, a method to deposit the CdS *in situ* was developed by M. Zhang in the group. Forming the CdS nanoparticles *in situ* provides several advantages; the precursor solution can be much more concentrated allowing for the faster build-up of CdS layers on FTO electrodes; the nanoparticles do not need to be stabilised with ligands and thus a calcination step in air is not necessary (it is however necessary to sinter the CdS to the FTO, but this can be done under an inert atmosphere); the synthesis and deposition of CdS is much quicker than synthesising CdS nanoparticles separately and depositing them at a later time. There are also no issues with long term stability of the CdS nanoparticles in solution.

Briefly the deposition method involves soaking the electrode in a cadmium bath for 1 minute, drying the electrode under a flow of N_2 then soaking the electrode in a sulfide bath for a further minute before rinsing the electrode under a gentle stream of deionised water and

finally drying the electrode under a flow of N_2. The electrode was then sintered at 500 °C for 2 hours in an argon atmosphere.

It was immediately obvious that more CdS was deposited with a single soak cycle in the CdS bath than with highest loading of CdS preformed nanoparticles: the electrode was a bright yellow-orange colour for both pFTO-CdS (bath) and macFTO-CdS (bath) compared to no colour change with depositing pre-formed nanoparticles. Further evidence for the deposition of CdS nanoparticles is in the DRUVS spectrum (Figure 4-11) as there is a clear dip in the spectrum where CdS absorbs (indicated with an arrow).

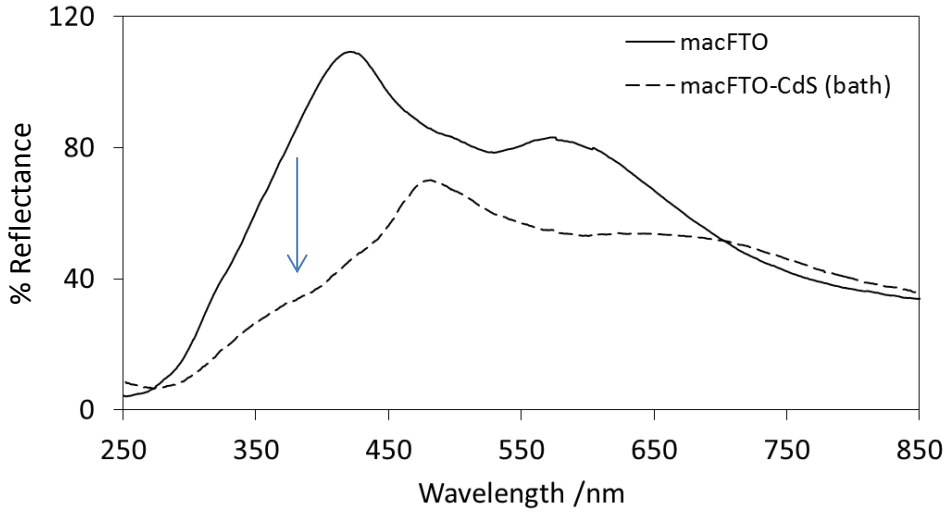

Figure 4-11: A diffuse reflectance spectrum of macFTO-CdS at 45° with one bath cycle. The presence of CdS nanoparticles is clearly shown by the dip in the reflectance profile at 350-450 nm.

Characterisation of the FTO-CdS electrodes was undertaken by M. Zhang in the group, and the work is presented in his thesis.[1] Briefly, the CdS nanoparticles were shown to be dispersed evenly over the macFTO electrode, and the nanoparticle size was found to be 5 – 10 nm by TEM and coated uniformly.

The increase in the amount of CdS is reflected in the larger photocurrent density. After only 1 bath cycle, the photocurrent density was ~0.8 mA cm^{-2}, which is in line with the largest found for the pre-formed nanoparticle electrodes. With additional deposition cycles, the photocurrent density could be increased further (Figure 4-12). The correlation between increasing the number of cycles used to deposit CdS and the photocurrent density obtained was approximately linear and, within the range of electrodes studied, did not reach a maximal

value. This bath method therefore indicates that there is a very simple way of depositing CdS over macFTO, and that the loading can be controlled.

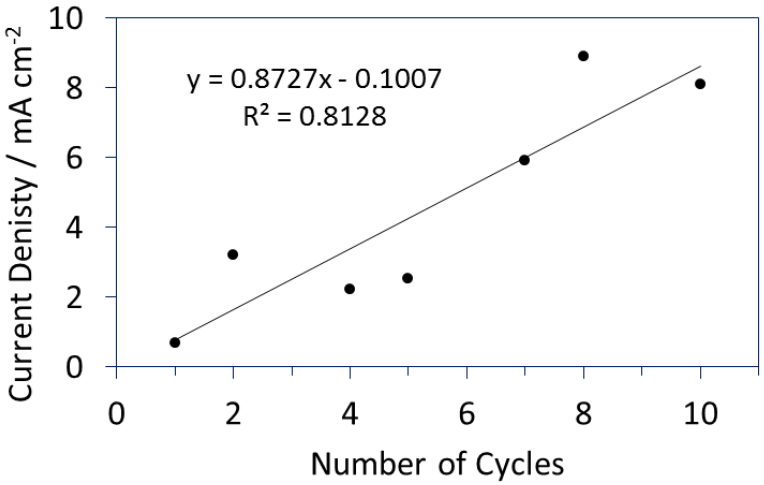

Figure 4-12: Photocurrent density obtained from a macFTO-CdS electrode when the bath cycle number is increased from 1 cycle to 10.

It was found that the optimum CdS loading was at 8 bath cycles. Figure 4-13 shows that the CdS coats the walls of the macFTO at 8 cycles (left), but moving to 10 cycles (right), the quantity of CdS is too high and the pores of the macFTO begin to be filled in with CdS nanoparticles. The filling in of the pores is not desirable as the ordered porous network is necessary to maintain the electrode-electrolyte interface and thus high photocurrent densities. The amount of CdS deposited in 8 cycles was therefore determined to be optimal, and the total mass of CdS deposited was found to be 18.5 $\pm$ 4 mg per electrode (1cm^2 geometric surface area).

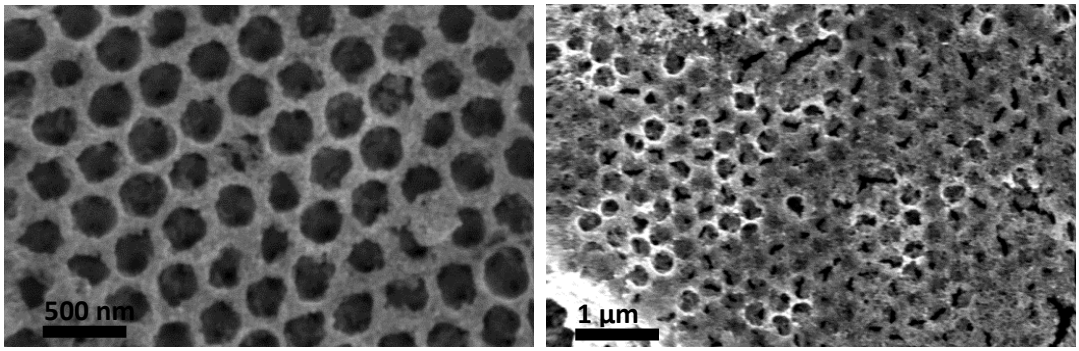

Figure 4-13: SEM images of macFTO-CdS at optimal 8 cycles (left) and at overloaded 10 cycles (right)

For the optimally loaded electrode, at 8 bath cycles, the photocurrent density was found to be ~8 mA cm^{-2} (Figure 4-14). If this is compared to a pFTO-CdS electrode made in the same way, it

can be seen that the photocurrent density is much higher for macFTO-CdS (bath) than pFTO-CdS (bath). The photocurrent density for pFTO-CdS (bath) was found to be ~0.1 mA cm^{-2} which is perhaps much smaller than expected, but this can be rationalised by the fact that the CdS did not disperse well over the pFTO because the solution beads and therefore does not disperse well. Additionally, the surface roughness of the pFTO is found to be very low, which does not provide very many nucleation sites for the CdS nanoparticles to begin growth. On macFTO the surface is much rougher than on pFTO and there is much more surface for nucleation sites, which thus allows more CdS to be deposited resulting in a higher photocurrent density. While the quantity of CdS could not be accurately characterised, it is likely that much of the increase in photocurrent density comes from the fact that there is far more CdS on the macFTO electrode than on the pFTO electrode.

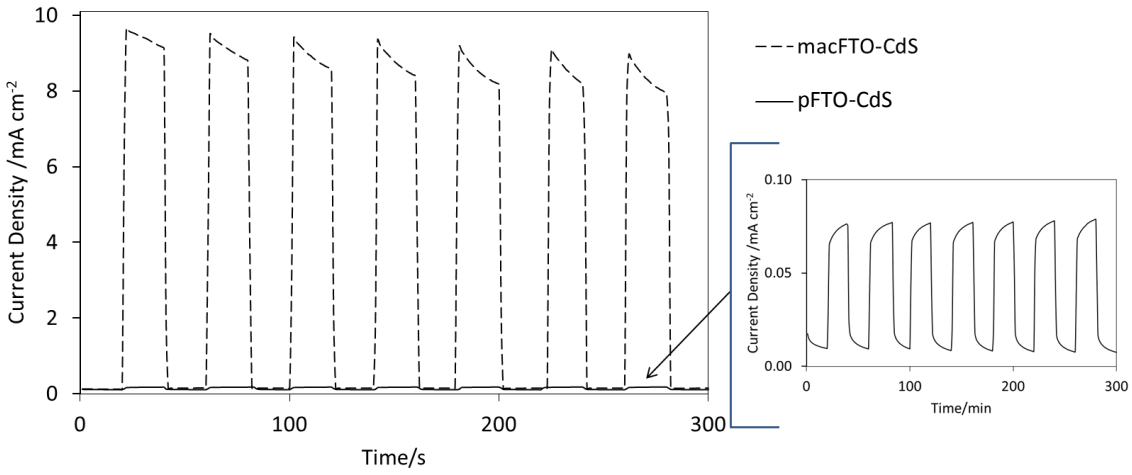

Figure 4-14: Chopped current density of macFTO-CdS compared to pFTO-CdS both electrodes at 8 cycles loading, inset: magnification of the pFTO-CdS trace at 8 cycles. From this type of plot both the photocurrent density and the dark current density can be determined. Conditions: sulfide/sulfite electrolyte, room temperature, light source as in experimental section.

For any bath electrode studied it was apparent that the stability of the electrode would be an issue. In Figure 4-14 the photocurrent density decreases from 9.5 mA cm^{-2} to 8 mA cm^{-2}, which is a 16% decrease, in only 5 minutes. Even over a 2 minute CV experiment (inset, Figure 4-15) the photocurrent density noticeably decreases. Over longer periods of time, the photocurrent density decreases by a total of 57 % over 1 hour (Figure 4-15). The initial decrease in photocurrent density accounts for the majority of the photocurrent density loss: over the first 5 minutes, 32 % of the photocurrent density is lost, whereas over the last 50 minutes of the experiment only 12% of the initial photocurrent density is lost. The initial loss could be due to the dissociation of some excess CdS nanoparticles from the electrode surface, which is supported by evidence gained when handling the electrodes; some CdS is easily wiped off the

electrode surface. Other losses could be due to the oxidation of CdS to species such as CdO as described earlier, during the course of the experiment.

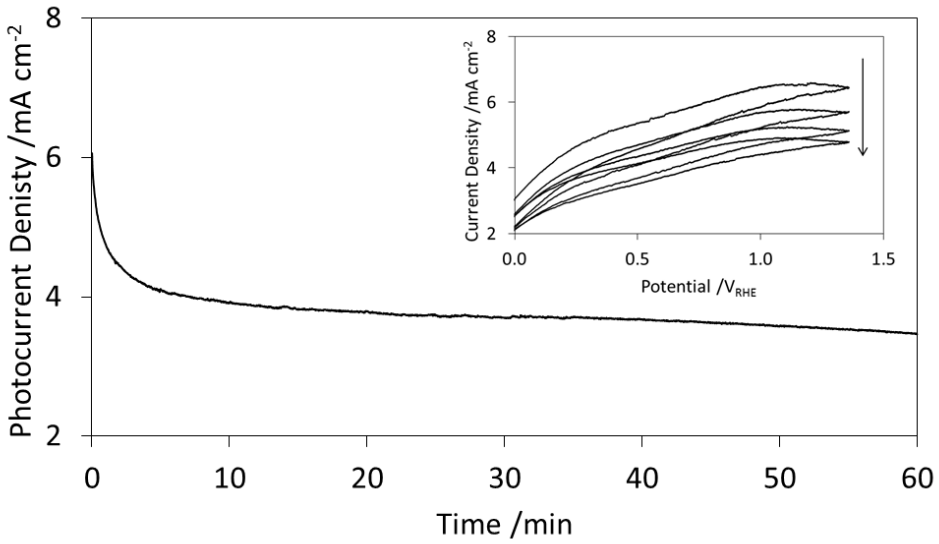

Figure 4-15: Stability test (CPE) of macFTO-CdS at 8 bath cycles loading in the light with the potential held at 0 $mV_{Ag/AgCl}$. Inset: A CV experiment at a scan rate of 100 mV s^{-1} on the same electrode as for the long-time stability test. Note: The CV experiment was run before the CPE.

4.2.2.1. Gas Evolution on macFTO-CdS electrodes

As the photocurrent density from macFTO-CdS (bath, 8 cycles) was quite high at no bias, it was thought that it would be possible to drive the evolution of hydrogen at platinum (the counter electrode). It is unlikely that CdS electrodes would be good candidates of oxygen evolution as they are very unstable at 0 $V_{Ag/AgCl}$, and oxygen evolution requires at least 1.8 $V_{Ag/AgCl}$ (1.23 V_{RHE}) which is very oxidising for CdS electrodes. It is thus expected that they would degrade too quickly to be useful, but could provide sufficient potential to drive the hydrogen evolution reaction at a counter electrode.

The open circuit potential of macFTO-CdS was determined to be +0.22 V in the light and – 0.54 V in the dark (> 420 nm) (Figure 4-16). This corresponds to an open circuit photocurrent density of 0.62 mA cm^{-2} (Figure 4-17). At this point it should be noted that the gas evolution on the electrode was only measured after the first initial photocurrent density decrease (stability tests, Figure 4-15).

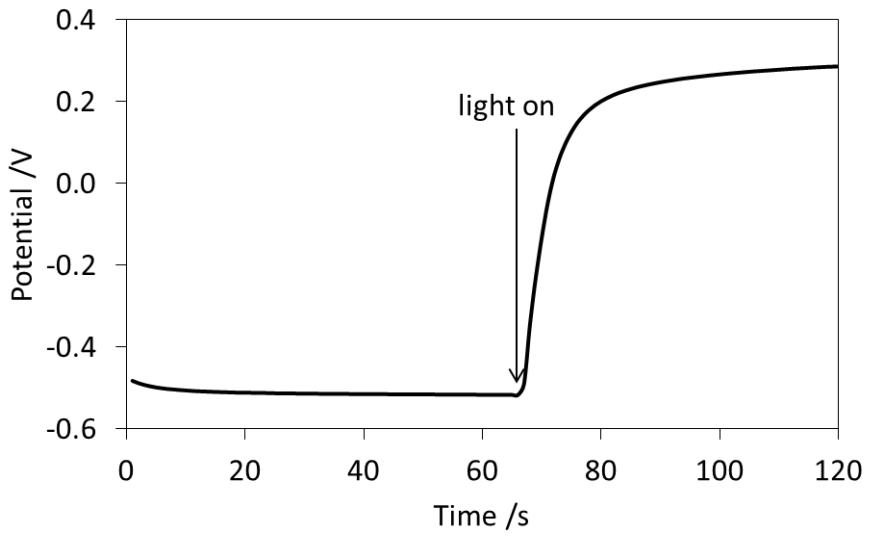

Figure 4-16: Determination of the open circuit potential of macFTO-CdS electrodes in the dark (LHS) and in the light (RHS)

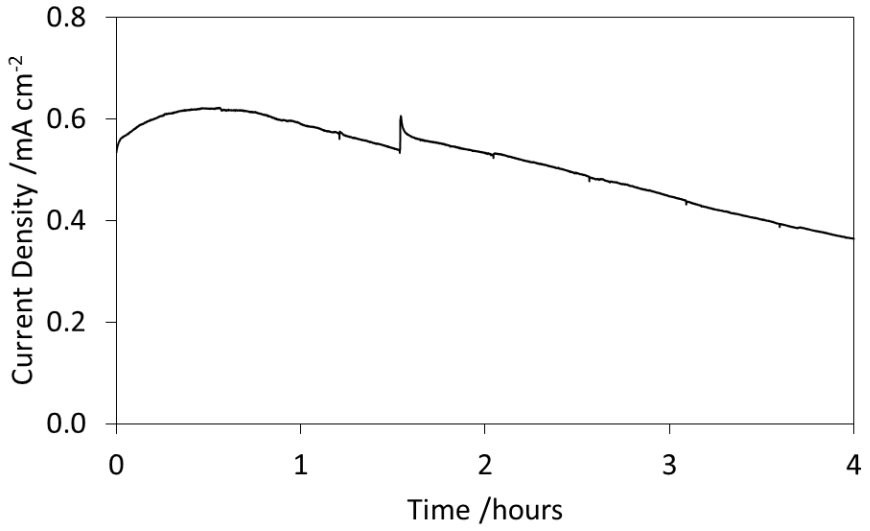

Figure 4-17: Gas evolution on Pt countered by macFTO-CdS at open circuit potential in the light (-0.54 V)

There are a few interesting features in Figure 4-17; over the first 20 minutes the photocurrent density increases, from 0.54 mA cm^{-2} to 0.62 mA cm^{-2}. This photocurrent density increase can be attributed to the fresh sulfide/sulfite solution converting some CdO to CdS. After this initial increase, the photocurrent density gradually decreases over 4 hours from 0.62 mA cm^{-2} to 0.36 mA cm^{-2}. The decrease in photocurrent density is most likely due to the oxidation of CdS to CdO and accounts for a loss of 33% over 4 hours, compared to the initial photocurrent density.

The maximum photocurrent obtained in the present work for macFTO ~4 mA cm^{-2} is comparable to the photocurrents seen in the literature for CdS decorated porous systems.

Karuturi *et al.*[254] find 6.2 mA cm^{-2} for a macTiO_2-ZnO (nanobush)-CdS system, while Zhu *et al.*[60] find a photocurrent of 7.5 mA cm^{-2} for a macTiO_2-ZnO-CdS electrode.

Gas evolution was observed on the counter electrode as a constant, but slow, stream of bubbles. In other experiments when a bias was applied to the system, the stream of bubbles was much greater, reflective of the higher current density obtained at a bias. The gas was confirmed to be hydrogen by gas chromatography (GC) and the total volume of gas measured over 4 hours was 0.73 mL (0.18 mL hr^{-1}, 8.64 µmol hr^{-1}). Other works in the literature produce similar volumes of hydrogen from CdS decorated electrodes, for example Fang *et al.*[252] produce 4 µmol hr^{-1} H_2 on a CdS-Au@TiO_2 electrode, where the TiO_2 is disordered under a 300 W xenon lamp in 0.25:0.35 M Na_2S:Na_2SO_3. Lee *et al.*[255] use a macroporous TiO_2 electrode decorated with CdS and produce 100 µmol hr^{-1} H_2, but this is at an applied voltage of -0.85 $V_{Ag/AgCl}$ (-0.24 V_{RHE}) where the rate of H_2 production would be expected to be higher. The running conditions were 0.35 M Na_2SO_3 and 0.24 M Na_2S and a 300 W xenon lamp.

By integrating the curve of current density *vs* time, the total charge passed during the experiment can be determined, and this can be used to calculate the faradaic efficiency of hydrogen evolution.

The faradaic efficiency can be calculated according to Equation 4-1 and Equation 4-2, where F is the faraday constant (96485 A s mol^{-1}) and e^- is the number of electrons in the process (2 for H_2 evolution):

$$\text{Faradaic Efficiency} = \frac{\text{Volume of gas evolved}}{\text{Total volume expected}} \times 100$$

Equation 4-1

$$\textit{Total volume expected} = \frac{It}{Fe^-} \times 24.4$$

Equation 4-2

The amount of charge passed during the 4 hours of experiment was 7.42 C which corresponds to 0.94 mL (45 µmol (11.28 µmol hr^{-1})). This is the maximum volume of H_2 expected if there are no losses in the system. Using this data, the faradaic efficiency was calculated to be 78%. As

platinum was used to evolve hydrogen it was expected that the faradaic efficiency would be over 90%, the fact that it is not suggests that some of the H_2 gas has escaped.

4.2.2.2. Incident Photon-to-Electron Conversion Efficiency Measurements

Finally, the IPCE (incident photon-to-electron conversion efficiency) could also be determined for macFTO-CdS electrodes compared to pFTO-CdS electrode with 8 cycles of CdS deposition (Figure 4-18).

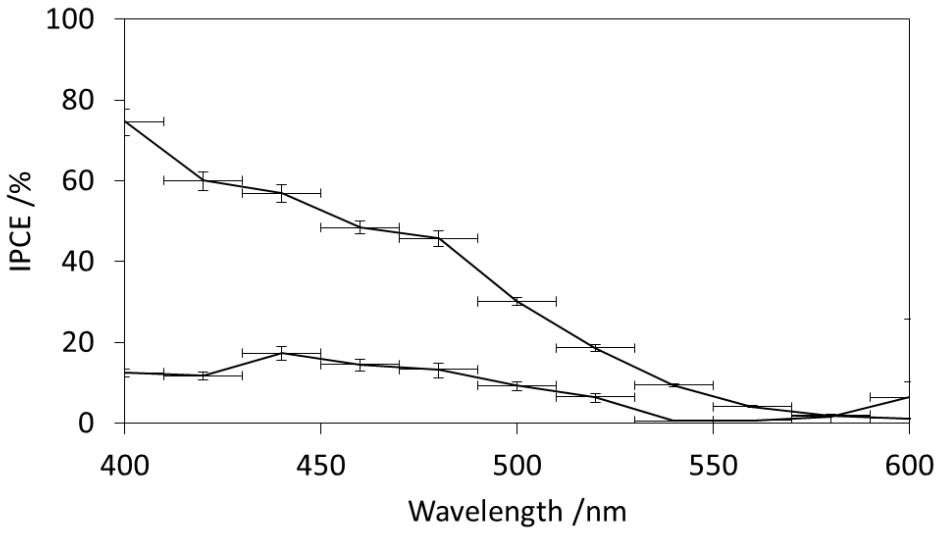

Figure 4-18: IPCE of macFTO-CdS compared to pFTO-CdS

pFTO-CdS has a IPCE of ~15% at 400 - 500 nm, which then drops off to <1% at higher wavelengths of > 500 nm, consistent with the absorption profile of CdS. macFTO has a much higher IPCE, of ~50% (45 to 60%) from 400 to 500 m. Again this drops off to <2% at longer wavelengths of > 500 nm. This is consistent with reports of the IPCE for CdS electrodes in the literature where the IPCE is ~60% or less at 450 nm.[60,256,257]

To calculate a maximum current density if the electrode were to be illuminated under 1 sun, the IPCE should be integrated over all wavelengths. Using software provided by OPVAP[258] and the raw data the maximum current output from the macFTO-CdS electrode was calculated to be 6.13 mA cm^{-2}. This value is in good agreement with other author's calculations of maximum current density (~6 mA cm^{-2}),[259] but in their electrode the CdS has been deposited with a PbS layer over nanoparticulate TiO_2, in order to enhance photocurrent density. In this thesis a similar photocurrent (6 – 8 $mAcm^{-2}$) has been generated using only CdS nanoparticles, showing

that the macFTO structure may be enhancing the amount of photocurrent density achieved from a single electrode.

4.2.3. Conclusions: Sensitisation of FTO Electrodes with CdS Nanoparticles

Though CdS will never be a useful material in solar water splitting applications due to its instability and toxicity, it has served in the present work as a means to show that macFTO is conductive and can support useful photocurrents. Conductivity of macFTO was shown by using low loadings of CdS nanoparticles: the fact that a current was generated from individual nanoparticles (rather than a continuous film) shows that the macFTO conducts photogenerated electrons. Additionally the macFTO-CdS electrodes could support photocurrents of up to 8 mA cm^{-2}. To achieve the highest photocurrent density a bath method was used, where an electrode was soaked in the precursors. This produced a much thicker layer of CdS nanoparticles than depositing preformed nanoparticles from solution.

Furthermore, macFTO-CdS was used to drive hydrogen evolution at a Pt electrode with efficiencies of up to 78%, which could be increased by ensuring all the H_2 was collected.

Finally the IPCE was found to be substantially higher for macFTO-CdS than pFTO-CdS, at 50% compared to 15% at 400 - 500 nm. This compares favourably with the literature and is attributed to greater light absorption due to greater CdS loading for the macFTO-CdS.

4.3. Sensitisation of FTO Electrodes with Bismuth Vanadate ($BiVO_4$) Nanoparticles

Having established that; 1. macFTO can support photocurrents using CdS and that 2. gas evolution is possible using the system described in this work, the next step was to examine a photoactive material that will produce oxygen. $BiVO_4$ meets these requirements and is suitable to use as a photoelectrode material.

4.3.1. Preformed Nanoparticles of $BiVO_4$: Deposition and Electrochemical Analysis

The $BiVO_4$ nanoparticles formed in the present work are synthesised according to the method of Sun *et al.*[248] and have an average diameter of ~20 nm, determined by SEM (Figure 4-19), which compares well with the average reported size of 20 nm. The nanoparticles are slightly irregular in shape, but resemble spheres. The nanoparticles are initially formed using EDTA as a stabilising agent, but this is removed during the calcination step of the macFTO synthesis. The nanoparticles are not soluble in water, but disperse evenly and can be used from a suspension.

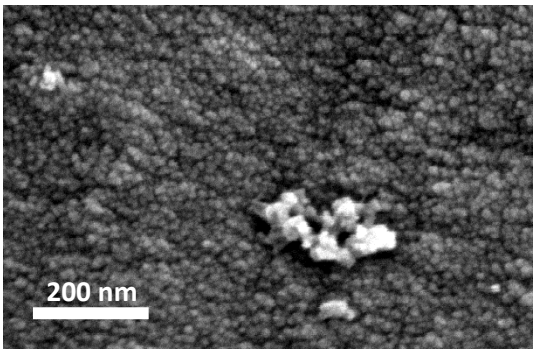

Figure 4-19: SEM image of $BiVO_4$ nanoparticles synthesised using the EDTA templating method as described by Sun et al. The nanoparticles cover the entire electrode (grey areas). The brighter objects are surface agglomerates of $BiVO_4$ nanoparticles.

$BiVO_4$ has a reported band gap of around 2.4 eV,[74,260,261] which gives $BiVO_4$ a bright yellow colour. The $BiVO_4$ made in the present work is also bright yellow in colour and thus is expected to show visible light activity, with a band gap of similar magnitude. The band gap was determined using a tauc plot (Figure 4-20) to be 490 nm (2.55 eV), which is consistent with the band gap of monoclinic $BiVO_4$ in the literature.

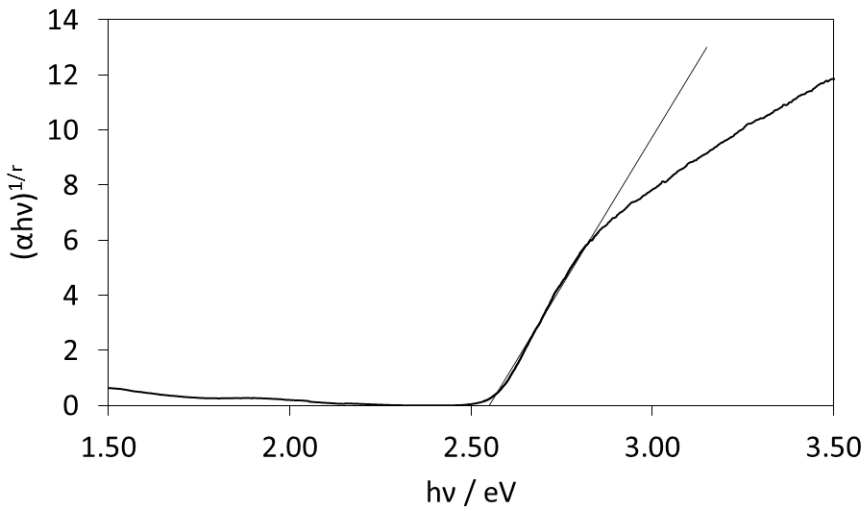

Figure 4-20: Tauc plot for macFTO-$BiVO_4$, r was set to a direct allowed transition (r = ½). The band edge was calculated to be 2.55 eV (486 nm).

Additionally, the XRD (Figure 4-21) of $BiVO_4$ nanoparticles confirms the presence and structure of monoclinic $BiVO_4$.[262] When the nanoparticles are discrete, the Scherrer equation can be used to estimate the size. However, the nanoparticles described in the present work are closer to a film of nanoparticles rather than discrete nanoparticles and therefore the Scherrer equation is invalid.

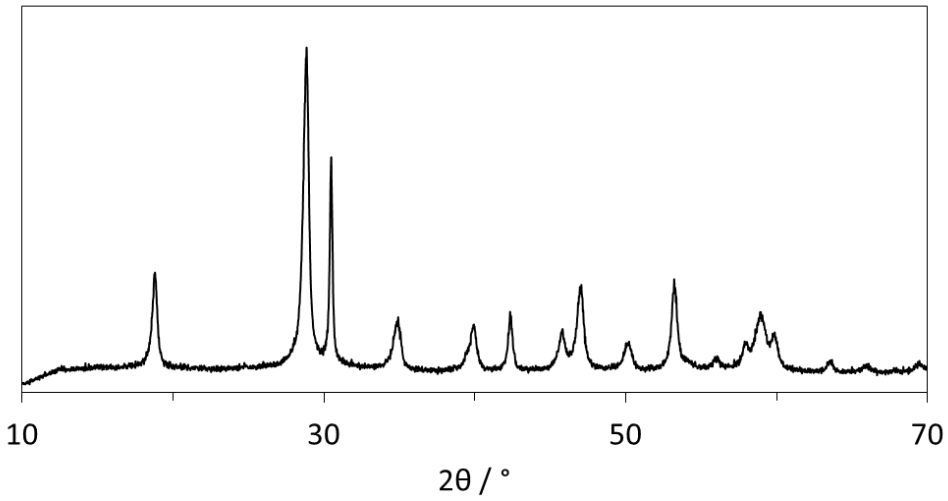

Figure 4-21: XRD of $BiVO_4$ nanoparticles

4.3.2. Deposition of Preformed $BiVO_4$ Nanoparticles

Similarly to the CdS preformed nanoparticles, the preformed $BiVO_4$ nanoparticles did not disperse well over either the pFTO or macFTO electrodes. By both drop coating with a pipette and evaporation techniques, it was clear by eye that the electrodes were only coated over the surface of macFTO, and that the coating was too thick as the $BiVO_4$ easily flaked off.

Consequently, no experimental data could be collected for FTO-$BiVO_4$ electrodes deposited via either of these methods, and a bath method was developed for deposition of $BiVO_4$ nanoparticles *in situ*, in an attempt to produce thinner, conformal $BiVO_4$ layers.

4.3.3. Deposition of $BiVO_4$ Nanoparticles Using a Bath Method

Briefly, the bath method involves soaking the substrate in a solution of Bi^{3+}, V^{5+} and EDTA (a chelating agent), before being dried on a hotplate at 100 °C. The electrodes were then rinsed with deionised water and dried at 100 °C on a hotplate before calcination at 450 °C.

The pFTO-$BiVO_4$(bath) and macFTO-$BiVO_4$(bath) electrodes are bright yellow in colour, indicating successful deposition of $BiVO_4$ on FTO. Additionally, the XRD analysis shows that the $BiVO_4$ is monoclinic (Figure 4-22). The XRD spectrum is more complex than that of $BiVO_4$ nanoparticles, as the FTO gives large peaks which overlap the weaker $BiVO_4$ peaks in many instances. However, there are clear peaks which can be attributed to $BiVO_4$ (*). The XRD spectrum of macFTO-$BiVO_4$ is identical to that of pFTO-$BiVO_4$.

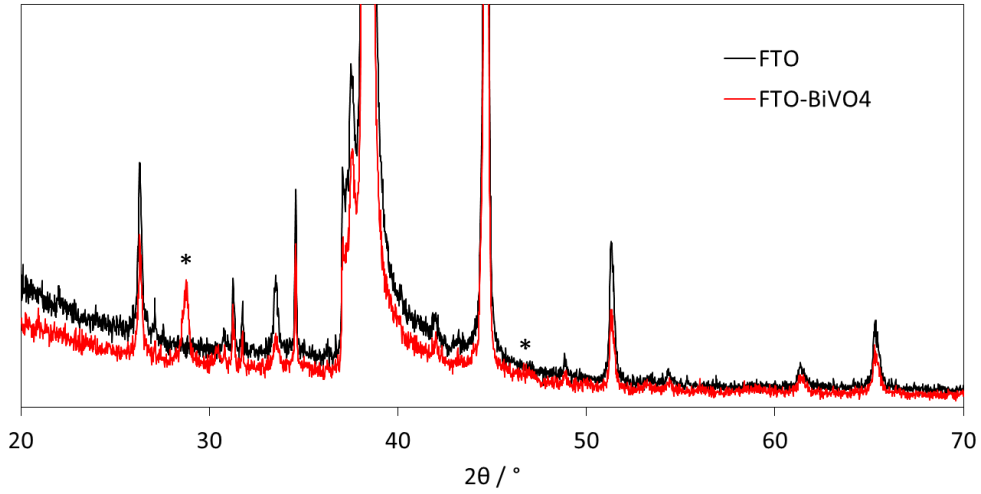

Figure 4-22: XRD of FTO-$BiVO_4$ (red) compared to FTO (black). Both macFTO-$BiVO_4$ and pFTO-$BiVO_4$ show exactly the same peaks (see appendix), showing that the $BiVO_4$ formed is monoclinic in both cases.

Further evidence for the presence of $BiVO_4$ on macFTO is the dip in the DRUVS spectrum when compared to a bare electrode, which is consistent with the absorption profile of $BiVO_4$ (Figure 4-23). Following the addition of $BiVO_4$ to pFTO electrodes (Figure 4-23, left) it appears as if the band edge of pFTO shifts to longer wavelengths, from 350 nm (FTO) to 450 nm. This apparent shift is the result of the overlay of the absorption profile of $BiVO_4$ with the band edge of FTO.

macFTO-$BiVO_4$ shows the same trend (Figure 4-23, right), with the band gap in the same positions.

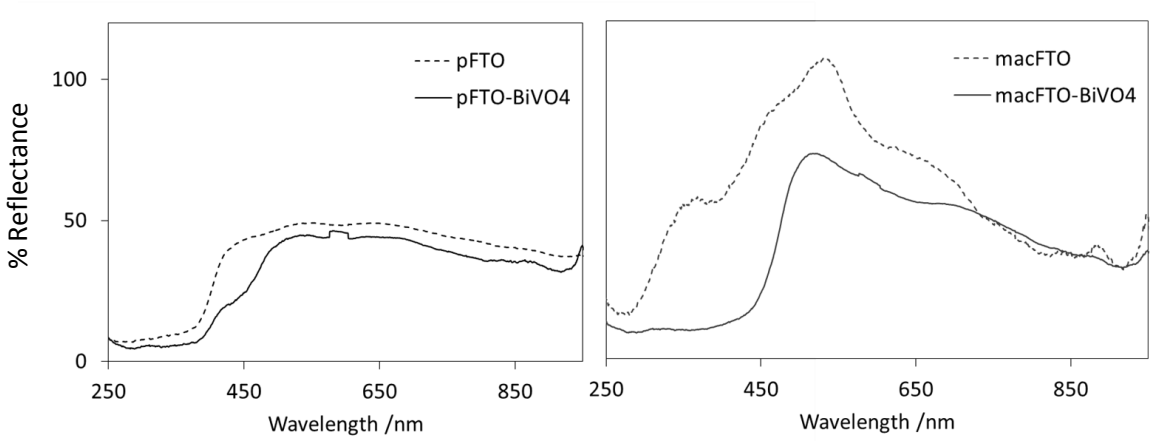

Figure 4-23: left: DRUVS spectrum of pFTO compared to pFTO-$BiVO_4$ and right: DRUVS spectrum of macFTO compared to macFTO-$BiVO_4$.

At 45° incidence (the standard angle of incidence for DRUVS measurements) the stop band is positioned at ~550 nm. As the absorption profile of $BiVO_4$ extends to 500 nm, the blue edge of the stop band overlaps with the $BiVO_4$ absorption profile. This causes the stop band to appear cut off at the blue edge. There are no other significant changes to the DRUVS spectrum upon addition of $BiVO_4$.

SEM analysis shows the size and dispersion of the $BiVO_4$ nanoparticles. Figure 4-24, left, shows that when the nanoparticles are dispersed over pFTO electrodes using the bath method the dispersion is uneven. This results in large aggregates of nanoparticles. The individual nanoparticles are still quite small (at ~20 nm) but aggregate together in large clusters of 1-2 µm in diameter.

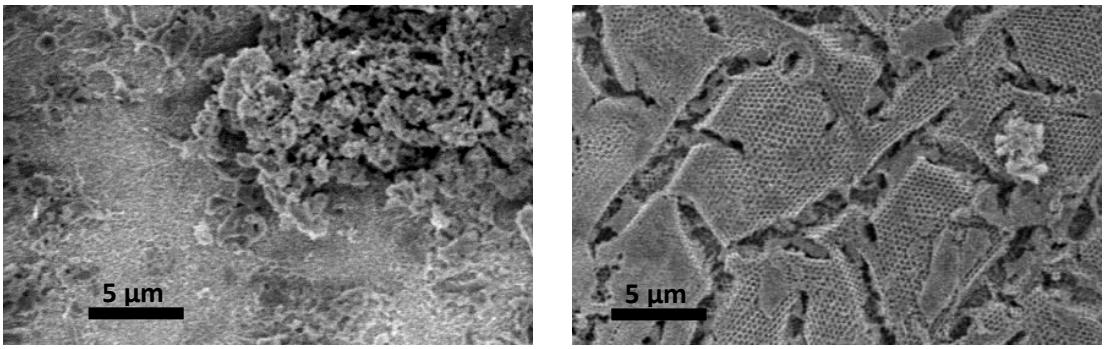

Figure 4-24: SEM images of pFTO-BiO_4 (left) and macFTO-$BiVO_4$ (right) both made with only 1 bath soak.

On the macFTO (Figure 4-24, right), the dispersion of $BiVO_4$ nanoparticles appears to be more homogeneous. There are a few regions on the macFTO where the nanoparticles have agglomerated, so that there is an over-layer of $BiVO_4$ on the macFTO, and some of the pores have been partially filled in, but on the whole the macFTO remains porous with a thin layer of $BiVO_4$. EDX mapping gives the distribution of the elements, which for all electrodes showed an equal distribution of Bi and V over the pFTO and macFTO, with a Bi:V ratio of 1.06.

4.3.3.1. Photocurrent Density Measurements of FTO-$BiVO_4$ electrodes

$BiVO_4$ is known to be much more stable to oxidative corrosion than CdS, so the electrode photocurrent density could be measured in an aqueous solution of phosphate buffer at pH7, which are more realistic running conditions for a water splitting device. The photocurrent density of FTO-$BiVO_4$ (1 bath cycle) was found to be 0.35 µA cm^{-2} for pFTO-$BiVO_4$ and 30 µA cm^{-2} for macFTO-$BiVO_4$ at 1.2V_{RHE} (Figure 4-25).

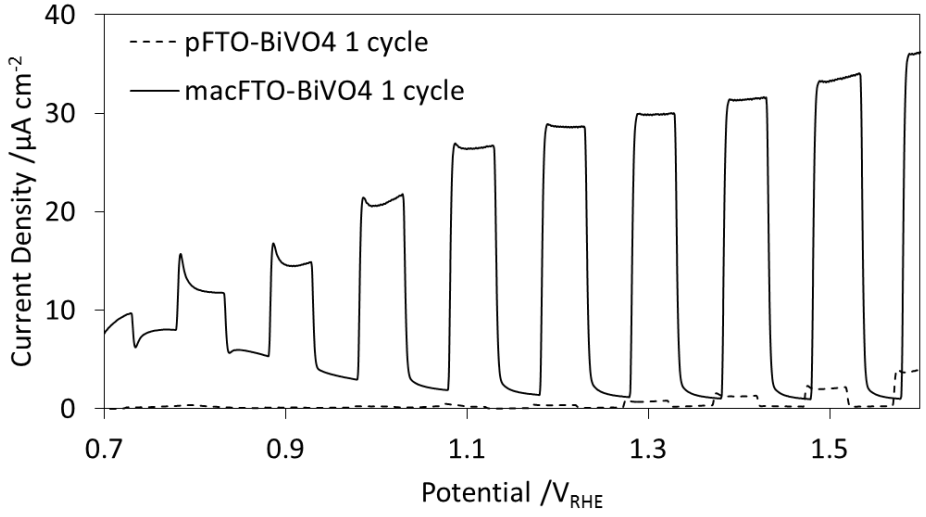

Figure 4-25: LSV of pFTO-$BiVO_4$ and macFTO-$BiVO_4$ measured in phosphate buffer, pH7, with 1 deposition cycle, bath.

The fact that the macFTO electrode shows a much higher photocurrent density than the pFTO electrode (~30 µA cm^{-2} compared to < 1 µA cm^{-2} respectively) is related to the increase in surface area. As both electrodes have been treated in the same manner, the 100 fold increase in the photocurrent shows that for the same geometric area of FTO electrode, the macFTO is superior to the pFTO.

In order to increase the photocurrent density of the $BiVO_4$ electrodes, multiple bath deposition cycles were attempted (Figure 4-26). Unlike the CdS electrodes, further deposition cycles of $BiVO_4$ did not increase the photocurrent density linearly.

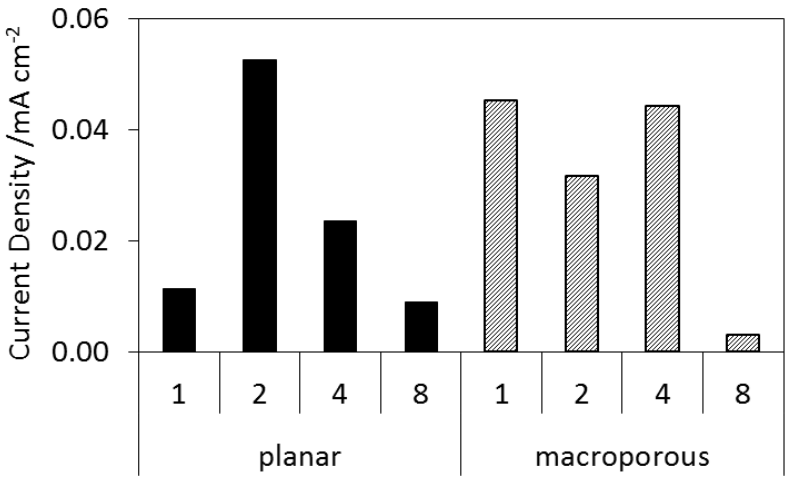

Figure 4-26: Photocurrent density of the planar and macroporous FTO-$BiVO_4$ electrodes as a function of number of deposition cycles at 1.623V_{RHE} (1$V_{Ag/AgCl}$).

For pFTO-$BiVO_4$ the number of cycles used to gain the highest photocurrent density was 2, after 2 cycles the photocurrent density decreases. It would be expected that as the $BiVO_4$ layer thickness increased (with increasing number of deposition cycles) the photocurrent density would increase until the layer thickness increased beyond the hole diffusion distance in $BiVO_4$ (hole diffusion length is 150 nm).[113] When the layer thickness exceeds the hole diffusion length the probability of recombination increases, and thus the current density decreases. Additionally, as the layer thickness increased the $BiVO_4$ started flaking of the FTO electrode. This physical degradation added to the current density loss.

For macFTO-$BiVO_4$ the highest photocurrent density was approximately the same for up to 4 cycles, suggesting that the $BiVO_4$ layer was forming slowly inside the macropores. At 8 cycles, the photocurrent density decreased by over 15 times, suggesting that the pores had filled with $BiVO_4$, and the electrode-electrolyte contact area had reduced (because the pores were filled in; Figure 4-27). Additionally, an over layer of $BiVO_4$ began to form over the macFTO electrode, which wouldn't allow light to penetrate all the way through the electrode, thus all the available $BiVO_4$ cannot absorb light to produce current density.

In line with these observations, and in order to gain the best photocurrent density from both planar and macroporous electrodes, $BiVO_4$ was deposited using the bath method with only 1 cycle.

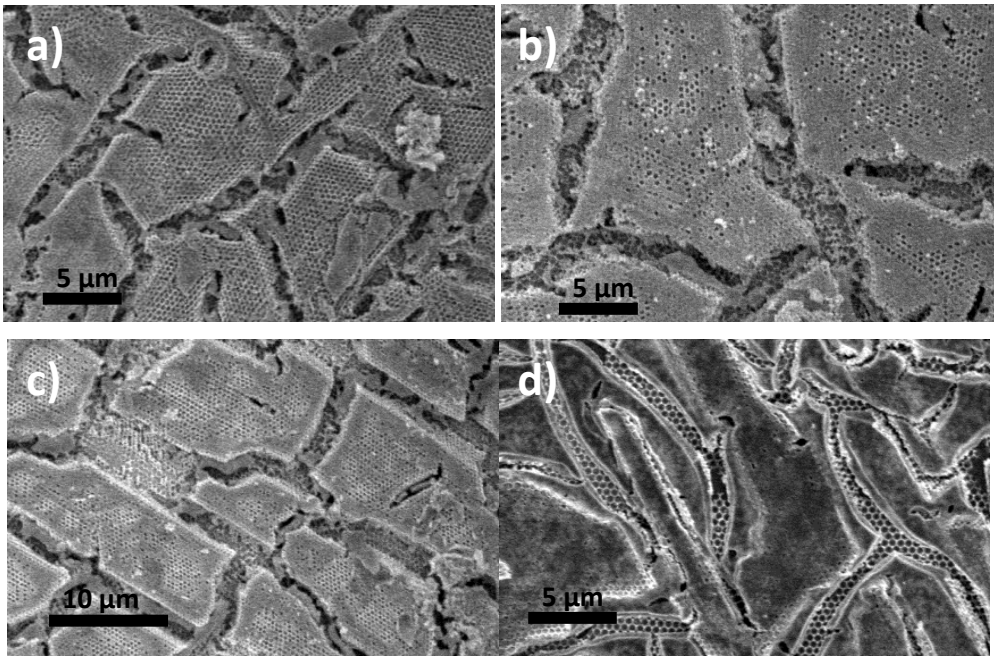

Figure 4-27: SEM images of macFTO-$BiVO_4$ electrodes at a = 1 soak, b = 2 soaks, c = 4 soaks and d = 8 soaks. Only the soak 1 electrode has a clear macFTO structure. For electrodes b and c the pores are partially filled in and for electrode d the pores are completely covered with an over-layer of $BiVO_4$. For reference the SEM images of the pFTO-$BiVO_4$ cycle deposition study are given in the appendix.

As the current density could not be increased by increasing the number of deposition cycles, other parameters, such as the temperature used to deposit $BiVO_4$, were varied. It was found that by lowering the drying temperature from 100 °C to 60 °C the photocurrent density could be increased from only 0.03 mA cm^{-2} at 1.5 V_{RHE} to 0.3 mA cm^{-2} (Figure 4-28). There is no apparent change in the colour, band gap, polymorph or structure of the $BiVO_4$ so the origin of the increase in photocurrent density is unknown. It may be that the nanoparticles formed were slightly smaller, or dispersed more evenly over the electrode during drying (as there was more time as the solution evaporated).

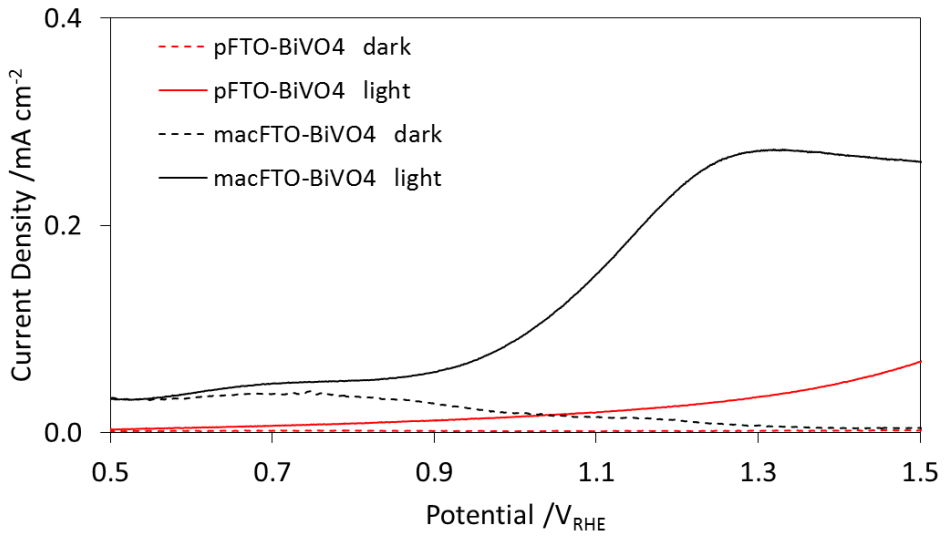

Figure 4-28: Current density LSV of pFTO-$BiVO_4$ and macFTO-$BiVO_4$ in both the dark and the light. The photocurrent density of both electrodes is now substantially higher than the initial electrodes. The LSV was measured in phosphate buffer, pH7, at room temperature.

The band edge of $BiVO_4$ is reported to be close the water splitting potential for oxygen evolution,[100,263,264] which makes $BiVO_4$ a suitable photoanode (for water oxidation) and as such $BiVO_4$ should be able to split water without a co-catalyst. Figure 4-28 shows how the onset potential for water oxidation changes with the addition of light to the system for both pFTO-$BiVO_4$ and macFTO-$BIVO_4$. In the dark the onset potential for water oxidation was found to be > 1.6 V_{RHE} for both pFTO-$BiVO_4$ and macFTO-$BiVO_4$ electrodes. The presence of light should drop the onset potential, as some of the potential necessary to drive water splitting is being gained from the light. This was indeed found to be the case for macFTO-$BiVO_4$, with the onset potential dropping to 0.95 V_{RHE} for macFTO-$BiVO_4$. The onset potential for pFTO-$BiVO_4$ was much higher than for macFTO-$BiVO_{4+}$ in the light, possibly due to the thickness of $BiVO_4$ which will be greater in pFTO-$BiVO_4$ than for macFTO-$BiVO_4$. This will lead to more recombination and therefore lower photocurrents in pFTO-$BiVO_4$ as well as a higher onset potential.

If the electrodes are viewed while the electrochemical experiments are taking place, a constant stream of bubbles can be seen at potentials higher than +2 V_{RHE}. At more realistic running potentials (+1 V_{RHE}) there is very little gas produced in the light for either electrode. This means that the volume of gas produced from either electrode was not sufficient to quantify on the timescale used for these experiments (3-4 hours), but it has been shown that the electrodes do in fact work to support photocurrents and photocatalysis. The onset potentials for $BiVO_4$ based electrodes is reported to be >0.8 V_{RHE}.[265,266]

If the photocurrent density of these macFTO-$BIVO_4$ electrodes is compared to what is currently being achieved in the literature it is found that the results presented in this thesis for macFTO-$BiVO_4$ electrodes are very similar. Lichterman *et al.*[114] reports photocurrent densities of ~0.25 mA cm^{-2} for a planar $BiVO_4$ electrode at +1 V_{RHE}, while Abdi *et al.*[72] reports photocurrent densities of ~1 mA cm^{-2} for tungsten doped $BiVO_4$ electrodes (both for AM1.5 simulated light).

Nanorod arrays of WO_3-$BiVO_4$ produce current densities as high as 0.8 mA cm^{-2} (1 V_{RHE} in 0.5 M Na_2SO_3 as a hole scavenger)[41] and some planar $BiVO_4$ electrodes have current densities on the order of 0.25 mA cm^{-2} at AM1.5 (this is one of the higher values reported).[114] Another synthesis of $BiVO_4$ porous electrodes produces current densities as high as 1.67 mA cm^{-2} at 1.83 V_{RHE} (0.5 M Na_2SO_4) but this is *via* a series of steps involving both ion exchange and hydrothermal-annealing processes, much more complex than the method reported is the present work.[267]

$BiVO_4$ photoanodes prepared *via* the electrochemical reaction of a Bi metal electrode and vanadium precursor can produce photocurrent densities of > 5 mA cm^{-2} at 1.25 V_{RHE} for sulfite oxidation (1 M Na_2SO_3), which often produces higher current densities as the reaction is less complex (requires less electrons) than for water oxidation.[268]

Because the water oxidation kinetics are slow on $BiVO_4$, it is not uncommon to see doping with tungsten, in which case the photocurrent densities are higher: A helical $BiVO_4$-WO_3 array generates current densities of 5.35 mA cm^{-2}, over five times larger than the current density from an equivalent planar $BiVO_4$-WO_3 electrode. [112]

However, the fabrication of most of these electrodes is more complex than with the macFTO-$BiVO_4$ electrodes given in the present work. Additionally, it is likely that the electrodes presented in the current work are made with thinner layers of $BiVO_4$, this is constrained using the pores of the macFTO.

4.3.3.2. Stability of FTO-$BiVO_4$ Electrodes

$BiVO_4$ is known to be stable under oxidative conditions[72,103] and a stability test to show how stable the electrodes are under working conditions proves this to be true (Figure 4-29). Except for the initial decrease, which is partially due to the settling period in an electrochemical experiment, the photocurrent density is stable at ~57 µA cm^{-2} for macFTO-$BiVO_4$ and ~30 µA cm^{-2} for pFTO-$BiVO_4$ at +1 $V_{Ag/AgCl}$. The photocurrent density loss is only 2.5% for macFTO-$BiVO_4$ over the course of the experiment, whereas for pFTO-$BiVO_4$ it is 25%. In the last 30 minutes of

the experiment both electrodes are stable; macFTO-$BiVO_4$ is the most stable, in fact the current density increases slightly (+4%) while for pFTO-$BiVO_4$ the photocurrent density loss is ~4%. This analysis is supported by the CV scans; for macFTO-CdS the CV showed a clear decrease in current density, but both pFTO-$BIVO_4$ and macFTO-$BiVO_4$ are far more stable, after the first scan, which is often discarded to allow the electrode to stabilise, the photocurrent density barely decreases at all (Figure 4-29, right).

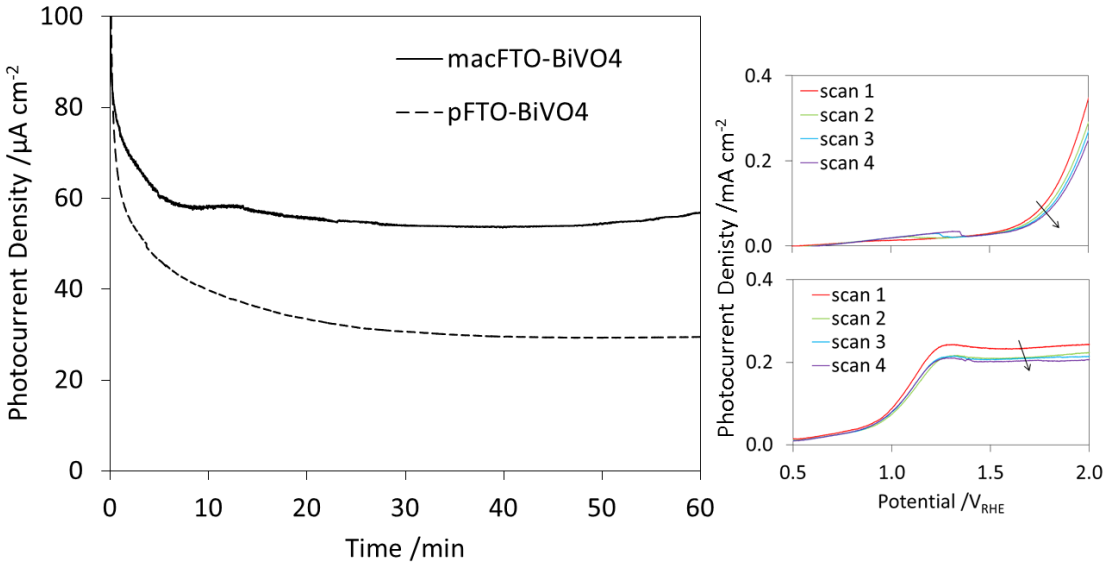

Figure 4-29: Stability test for $BiVO_4$ electrodes. Left: 1 hour CPE at +1$V_{Ag/AgCl}$ in the light, right top: first 4 scans of a CV in the light of pFTO-$BiVO_4$ and right bottom: fist 4 scans of a CV in the light of macFTO-$BiVO_4$

Several examples of using $BiVO_4$ to split water exist, but many of them use other materials in tandem to improve the oxygen evolving efficiencies, which involve relatively complex fabrication methods. For example, by doping $BiVO_4$ with tungsten as well as using a surface passivating TiO_2 layer the onset potential for water oxidation can be shifted to lower potentials by 500 mV (to -0.1 V_{RHE}) while the current density increases by 5.5 times.[73] This clearly demonstrates a gap in the literature for simple fabrication of electrodes for solar water oxidation.

Initially pFTO-$BiVO_4$ electrodes were studied, to show how macFTO can improve the activity of $BiVO_4$ towards water splitting. Figure 4-30 shows the SEM images for a pFTO-$BiVO_4$ electrode before and after electrochemical analysis with gas evolution. It is apparent that there is no significant change during the electrochemical analysis and gas evolution. Before electrochemical analysis (Figure 4-30 left), and after electrochemical analysis (Figure 4-30

right) the $BiVO_4$ nanoparticles are whole nanoparticles ~ 16.5 nm in diameter, agglomerated together to form larger 'islands' of material on the pFTO.

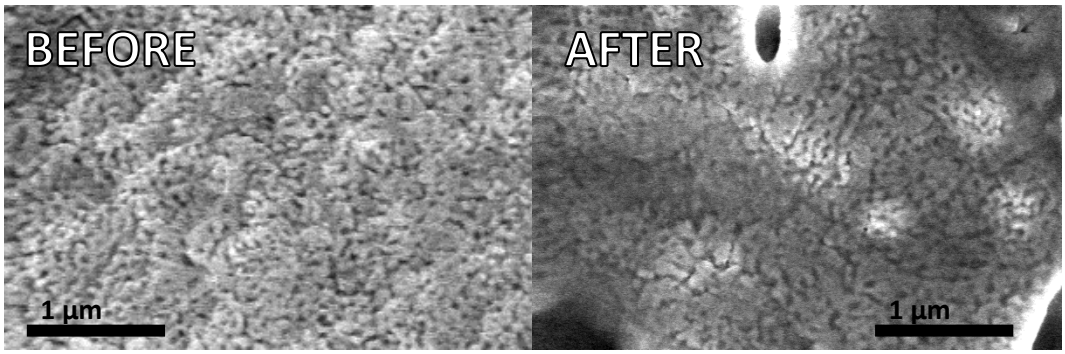

Figure 4-30: SEM images of pFTO-$BiVO_4$ before and after electrochemical analysis.

For macFTO-$BiVO_4$ (Figure 4-31) there also appears to be no significant structural change of the electrode during electrochemical analysis with gas evolution. In either the before or after images, the $BiVO_4$ nanoparticles are very small and cannot be visualised using SEM. The macropores are clear of obstruction in both cases and the nanoparticles appear to be an even coat over the entire electrode.

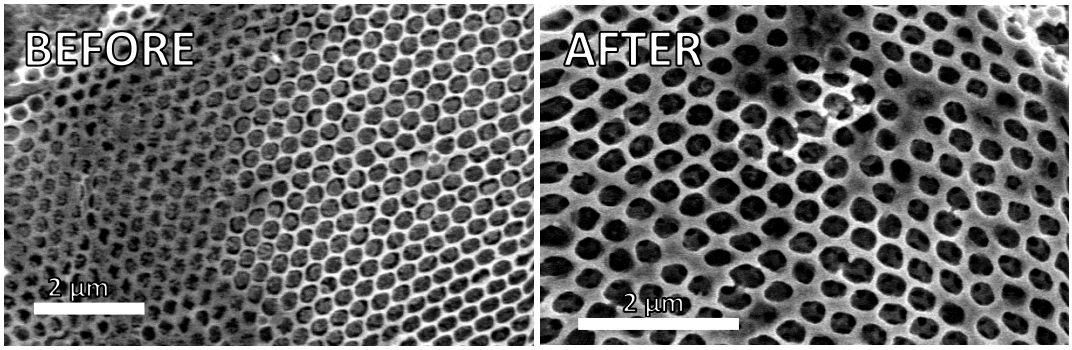

Figure 4-31: SEM images of macFTO-$BiVO_4$ before and after electrochemical analysis.

4.3.3.3. IPCE Measurements for $BiVO_4$ Electrodes

Finally, the IPCE of the FTO-$BiVO_4$ electrodes was determined. It was found that the IPCE of pFTO-$BiVO_4$ was very low, at only ~1% in the absorbing region (< 480 nm). These values are lower than reported in the literature (~30% at < 480 nm),[79] likely because there is a very thin layer of $BiVO_4$ in the samples presented in this work. This was to ensure that the pFTO-$BiVO_4$ samples were comparable to the macFTO-$BiVO_4$.

For macFTO the IPCE gradually increased from ~3% at 500 nm to ~10% at 380 nm. This shape is consistent with the absorption profile of $BiVO_4$. Porous electrodes of $BiVO_4$ have achieved

similar IPCE's to macFTO-$BiVO_4$,[79,262] while the addition of hole scavenging agents such as methanol can increase the IPCE by a factor of 2, showing there is room for improvement for these electrodes.[92,262] Additionally the use of surface passivating agents, such as $AgNO_3$ can increase the IPCE and the long term photocurrent stability of $BiVO_4$.[262]

An integration of the spectrum allows the theoretical maximum current density under solar light to be calculated. For the macFTO-$BiVO_4$, the predicted maximum theoretical current density is 0.52 mA cm^{-2} calculated using the raw data and OPVAP software.[258]

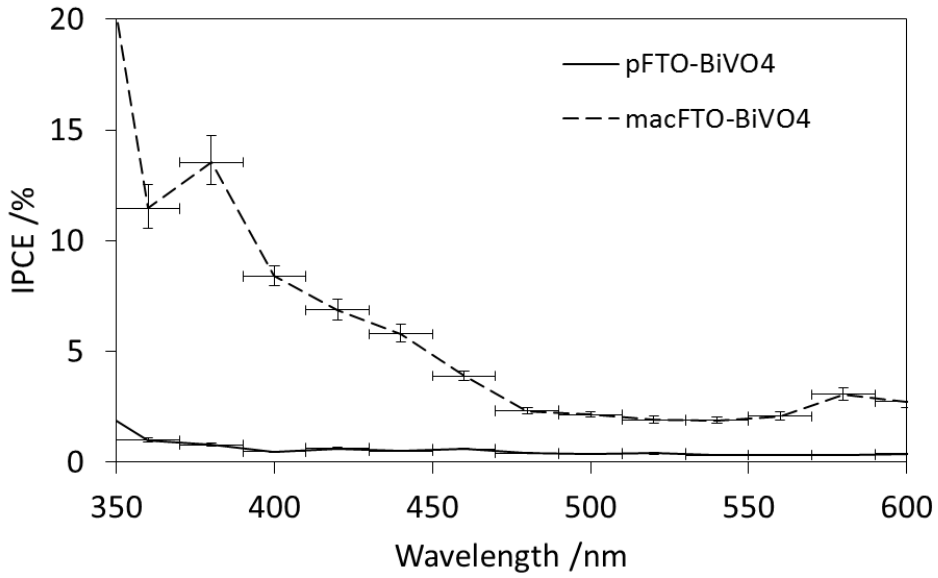

Figure 4-32: IPCE of FTO-$BiVO_4$ electrodes

4.3.4. Summary of Findings

The use of macFTO to template $BiVO_4$ has been demonstrated. Photocurrent densities of macFTO-$BiVO_4$ were found to be greater than equivalent pFTO-$BiVO_4$ electrodes, showing the templating method was successful at increasing the photocurrent density.

The preformed nanoparticles did not disperse well on either pFTO or macFTO electrodes, so an in situ deposition method was used to coat the electrodes. Unlike the CdS electrodes, only 1 bath cycle was necessary to deposit a suitable amount of $BiVO_4$, enough to have the largest photocurrent density possible without filling in the macropores of FTO.

$BiVO_4$ is also capable of splitting water if a high enough overpotential is applied. At +2 V_{RHE} bubbles of O_2 are visible on the $BiVO_4$ electrodes. At lower running potentials (+1 V_{RHE}) there is

not enough O_2 produced to give accurate measurements of efficiency, due to the low current density.

Compared to CdS, $BiVO_4$ is much more stable, where macFTO-CdS electrodes lost up to 60% of the photocurrent density, macFTO-$BiVO_4$ lost <5% of the initial photocurrent density. For pFTO-$BiVO_4$ the total loss is much higher at 33%, likely due to some of the $BiVO_4$ flaking off the electrode surface during measurements.

Finally, the IPCE of $BiVO_4$ electrodes was determined to be ~1% for pFTO-$BiVO_4$ at 380 nm, and ~10% for macFTO-$BiVO_4$ at 380 nm this is a factor increase of 10, which is consistent with the increase in surface area of the electrode which leads to an increase in absorbance because more of the electrode surface is exposed to light (macroporous). These results show that macFTO-$BIVO_4$ is more efficient at converting light in to useful electrons than pFTO-$BiVO_4$.

4.4. Deposition of Cobalt Phosphate Electrocatalyst on macFTO Electrodes Sensitised with $BiVO_4$ and CdS

Cobalt phosphate is a widely used electrocatalyst for water oxidation because it operates in mild conditions, such as pH7 at room temperature, and it will work in just water (no need for a buffer solution). Additionally, Nocera *et al*.[38,43,105] have shown that the cobalt phosphate (CoPi) catalyst can self-assemble from a solution of Co^{2+} upon oxidation and that it can self-heal during operation, making it an ideal catalyst to work with for water oxidation.

4.4.1. Choosing a CoPi Deposition Method

There are several different methods to deposit CoPi on an electrode. Initially CoPi was drop cast onto electrodes form a solution of Co^{2+} in phosphate buffer, pH7, however this deposited far too much CoPi on the electrode surface, even at very low concentrations. Furthermore the deposition was not homogeneous, so some areas of the electrode had thick CoPi layers, while other areas had no CoPi.

A secondary method uses bath deposition to coat the electrode in CoPi, either by soaking and then removal to dry, or by letting the residual solution evaporate before removing the electrode. This allowed a more suitable amount of CoPi to be deposited, but the amount of CoPi could not be monitored or controlled, making this method unsuitable for use.

Electrodeposition is a simple method used to deposit CoPi catalysts. By applying +1 $V_{Ag/AgCl}$ CoPi is deposited over the entire electrode surface in a controlled manner. Unfortunately, oxygen is evolved at the same time that CoPi is deposited, and it is therefore not trivial to extract the amount of CoPi deposited from the electrochemical data. With careful measurements of the amount of O_2 produced, the amount of CoPi can be extracted from the results. Alternatively the upper limit of CoPi deposited can be determined as demonstrated by Suendranath *et al*.[269]

+1 $V_{Ag/AgCl}$ was used to deposit CoPi from a solution of Co^{2+} in phosphate buffer. It was possible to deposit even layers of CoPi over both pFTO, macFTO, pFTO-$BiVO_4$ and macFTO-$BiVO_4$ electrodes to drive oxygen evolution using the electrodeposition technique. The amount of CoPi deposited could be increased by increasing the time used to deposit CoPi.

Another method used to deposit CoPi on FTO electrodes was light assisted electrodeposition (or photoelectrodeposition). This method is the same as for electrodeposition except for the

potential applied. Because light is used, part of the potential needed to deposit CoPi can be gained from the light and thus the running potential can be lowered. For this deposition method, a potential of +0.3$V_{Ag/AgCl}$ was used in tandem with a light source (>420 nm only) to deposit CoPi from a solution of Co^{2+} in phosphate buffer.

4.4.2. Deposition of CoPi and Gas Evolution Measurements

4.4.2.1. Electrodeposition of CoPi

Electrodeposition of CoPi has been reported many times[79,102,105,106] and therefore this method was initially tested. By holding the potential at +1$V_{Ag/AgCl}$ CoPi was deposited over the electrodes evenly as a dark brown/black layer. The colour progressively darkened with time, and at the same time oxygen evolution started and became faster (i.e. more bubbles were observed forming on the electrodes with increasing time of deposition).

Because of the simultaneous oxygen evolution it was difficult to assess exactly how much CoPi had been deposited during the time of the experiment. As previously described, it would be possible to extract the amount of CoPi deposited if the amount of gas produced was known accurately, but the amount of oxygen produced was often so low as to be below the detection limit of both the burette system and the GC. This means that the amount of CoPi must be estimated using a different method.

It is known that the amount of charge passed during CoPi deposition is the sum of both the deposition of CoPi and the production of oxygen. It can be assumed that for every unit of CoPi deposited a certain proportion of the charge passed is due to the CoPi deposition and the rest is due to oxygen evolution. From this it is assumed that there is a constant ratio between the amount of CoPi deposited and the total charge passed. This simplifies matters because the total charge passed can be used as a proxy for the amount of CoPi deposited. While this means the exact amount of CoPi deposited is not known, it does allow the same amount of CoPi to be deposited on different electrodes.

Initially, planar electrodes had 568 mC of charge passed to deposit CoPi. This resulted in a dark brown/black layer being deposited over the electrode, and relatively fast oxygen evolution-bubbles were seen streaming from the surface. To deposit the same amount of CoPi per surface area on a macFTO electrode, 6816 mC of charge was passed (a 12 fold increase, calculated from the surface area increase seen with capacitance measurements in chapter 2). Again the electrodes produced were a dark brown/black colour, and oxygen evolution was

relatively fast. Unfortunately, this amount of CoPi takes a long time to deposit, and is not actually stable under measurement conditions (+1.5 V_{RHE} and in phosphate buffer only). Over 24 hours in the dark (Figure 4-33) the CoPi layer on pFTO-CoPi degraded so that no deposit was visible to the eye, initially suggesting that all the CoPi had been removed. As there was substantial degradation on the pFTO electrode, the macFTO electrode was not tested. Nocera[43] reports that the CoPi catalyst maintains water splitting activity in 'mild conditions' and that the catalyst does not need to be immersed in a Co^{2+} solution to maintain activity. Under harsher conditions (i.e. alkaline) CoPi has been shown to degrade by up to 28%,[270] therefore it can be concluded that the conditions that the present experiments were conducted in must have been too harsh for the CoPi catalyst to be stable (i.e. the running potential was too high). This is also consistent with the observations of Kanan *et al.*[105] who show that the CoPi on the electrode surface must reach equilibrium with the CoPi in solution in order for the electrode to be stable. If the electrode presented in this thesis is degrading until equilibrium is established, then most of the CoPi on the electrode may dissociate into solution as there is a relatively large volume of solution compared to the electrode surface area.

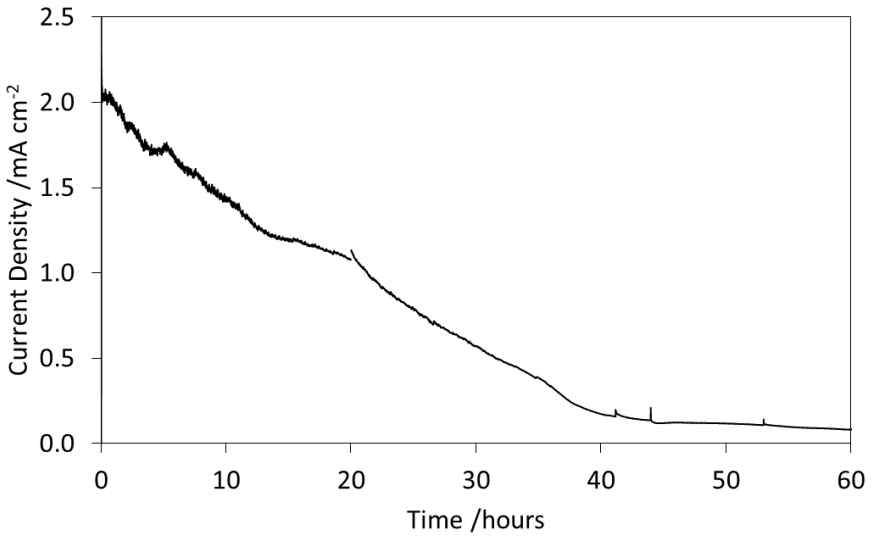

Figure 4-33: Stability test of pFTO-CoPi (thick layer, 6816 mC) at 1.5$V_{Ag/AgCl}$ (1.93 V_{RHE}) in phosphate buffer, pH 7.

With closer analysis, it was seen that the FTO electrodes still produced a small volume of gas bubbles after the stability test, which they would not do if there were no CoPi present. Furthermore, the electrochemical data showed reduced onset potentials and increased current densities when compared to an electrode that had not had any CoPi present. Unfortunately, the photocurrent density obtained from photosensitised electrodes (FTO-$BiVO_4$-CoPi) dropped substantially when illuminated either from the front or the back of the

electrode. This could have been because the CoPi layer was too thick for the light to penetrate efficiently or because too much CoPi was added, resulting in more recombination. This is not ideal because if the photocurrent density is small that means that the light is not helping to drive the water splitting reaction, which means that a higher potential will be needed to gain the same current density.

As the CoPi catalyst is reported to be stable,[38,105,106,269] it was assumed that the CoPi layer that was deposited on the electrodes was too thick for purpose, especially as the photoactivity was lost. In order to produce more stable electrodes less CoPi was deposited, and the potential used for gas evolution measurement was dropped to +1 $V_{Ag/AgCl}$ (1.62 V_{RHE}) because this is a more realistic running potential for this kind of experiment (as ideally water splitting should be run with a total bias of +1.2 V_{RHE}). The summation of this means that far less gas will be produced than seen with the previous CoPi electrodes, which means that it will be more difficult to measure the amount of gas produced.

To determine the optimal loading of CoPi, and to ensure that the photocurrent density remained high, the photocurrent density of both pFTO-$BiVO_4$-CoPi and macFTO-$BiVO_4$-CoPi electrodes was monitored throughout the electrodeposition of CoPi. This was done by submerging the electrode in the CoPi deposition solution and applying +1 V_{RHE} for a known period of time. After this the electrode was rinsed with deionised water and dried under a flow of N_2 before electrochemical measurements were performed in phosphate buffer. To deposit more CoPi the electrode was rinsed with deionised water and dried under a flow of N_2 before being re-submerged in the deposition solution and +1 V_{RHE} was applied for further time.

Figure 4-34 shows the change in current density (left) and photocurrent density (right) for pFTO-$BiVO_4$-CoPi with different CoPi deposition times (in seconds) ranging from 0 seconds (dark red) to 3600 seconds (black). In the dark (Figure 4-34 left) it is not clear if the onset potential or the photocurrent changes with increasing amounts of CoPi, but in the light (Figure 4-34 right), the photocurrent increases after just a 100 s deposition time from 0 mA cm^{-2} to 0.2 mA cm^{-2} at +1 V_{RHE}. After 100 s deposition time, the photocurrent seems to decrease until at 3600 s it once again approaches 0 mA cm^{-2}.

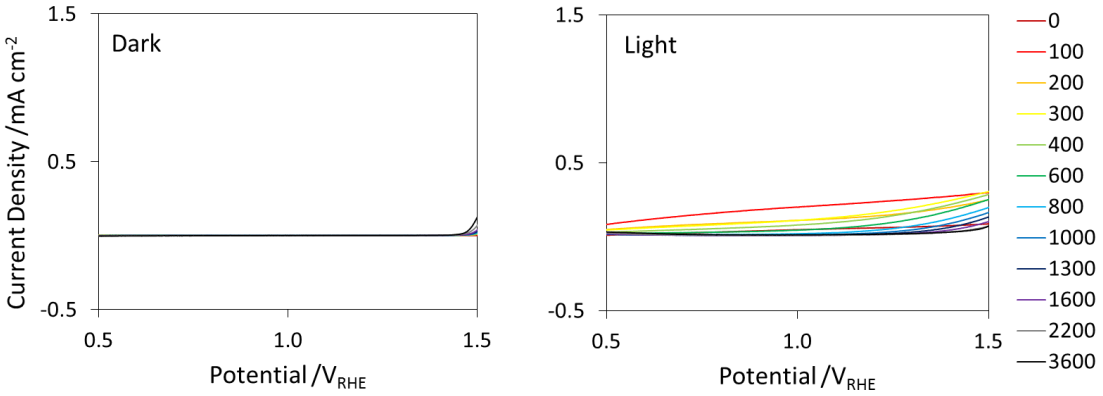

Figure 4-34: photoactivity change with changing CoPi quantity for pFTO-$BiVO_4$ electrodeposition. The legend describes the total time of deposition in seconds. The small peak at 1.5 V_{RHE} is due to a small volume of NaCl leaking out of the reference electrode (onset seen in LHS image).

If macFTO-$BiVO_4$-CoPi is now considered it can be observed that, in the dark, there again doesn't appear to be any change in the current density with increasing amounts of CoPi, even though there were some bubbles appearing on the surface of the electrode during the course of the experiment. When light is shone on the electrode, the results are very different. Now, a clear decrease in the onset potential is measured, from 0.6 V_{RHE} to ~0.35 V_{RHE}, as well as the increase in the photocurrent density, from 0.29 to 0.55 mA cm^{-2} at +1 V_{RHE}. This is consistent with what has been observed in the literature: with the addition of CoPi to a $BiVO_4$ electrode the onset potential has been observed to drop by up to 350 mV[43] when CoPi is added to an electrode surface, with more specific examples giving onset potentials of CoPi-$BiVO_4$ systems to be 0.3 V_{RHE}.[79,250]

Interestingly the pattern in the data shows that the first 100 s increases the photocurrent density by the most, and after 100 s the photocurrent density decreases slightly at potentials lower than +1 V_{RHE} (at higher potentials the photocurrent density stays roughly the same, at 0.85 mA cm^{-2}). This behaviour can be explained in terms of light absorption. The most light will be absorbed by the electrode with no catalyst, but the charges are not used effectively due to recombination on the electrode surface, due to the short transport distance in $BiVO_4$. With the deposition of a small amount of catalyst, the charges are able to be separated far more efficiently, thus increasing the photocurrent density obtained. However, with further deposition of catalyst, the catalyst layer that is formed may interfere with light absorption, meaning that less photons are absorbed, decreasing the photocurrent density.

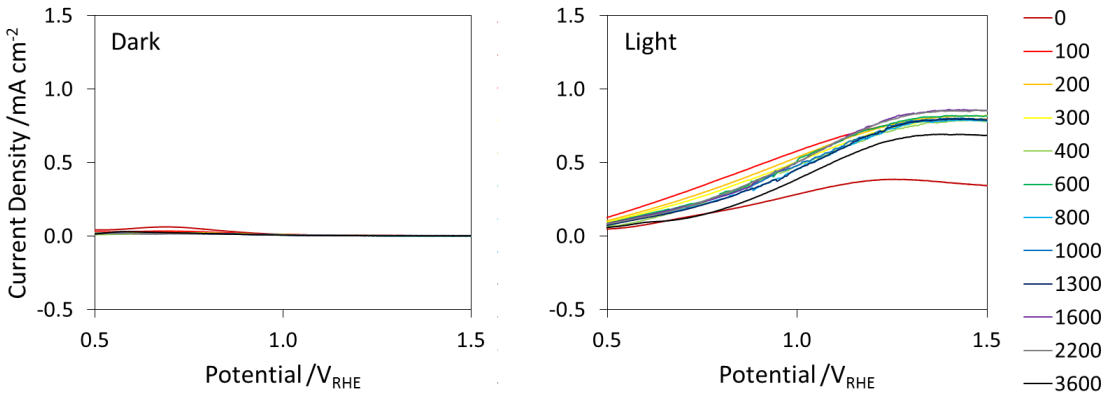

Figure 4-35: Photoactivity change with changing CoPi quantity for macFTO-$BiVO_4$ electrodeposition, phosphate buffer, pH7, room temperature

To summarise, for the planar electrode increasing the amount of CoPi deposited increases the photocurrent density, while the current density (in the dark) remains unchanged. The largest change is seen with a deposition time of 100 seconds, and after this the change is very slight. For the macFTO electrodes, the current density changes very little in the dark with increasing amounts of CoPi, but in the light both a decrease in the onset potential and an increase in the photocurrent density is seen.

4.4.2.2. Photoelectrodeposition of CoPi

There are some reports in the literature that suggest photoelectrochemically depositing CoPi will produce higher photocurrent density in the final electrode than electrochemically depositing CoPi.[101,104,250] The rationale for this is that by applying light to the electrode during CoPi deposition the point defects in the photoactive species (in this case $BiVO_4$) are identified.[75] The CoPi, instead of being deposited evenly over the electrode surface, is now concentrated in the defect regions, which allows any holes for oxidation produced during the course of the experiment to be used more efficiently (*i.e.* for gas evolution) and not lost due to recombination. In this case, the CoPi may not act as a co-catalyst, but more like a surface passivation agent (by reducing the surface trap states). In either case the electrodeposition of CoPi is beneficial to both the onset potential and the current density. The elucidation of the role of CoPi is not the focus of this work, and therefore will not be further commented on.

Photoelectrodeposition (pedep) of CoPi uses the same solution as with electrodeposition: 0.5 mM $Co(NO_3)_2$ solution in 0.1 M phosphate buffer pH 7. The difference between photoelectrodeposition and electrodeposition is in the application of light which means that the applied potential used to deposit CoPi can be lowered from +1 $V_{Ag/AgCl}$ to +0.3 $V_{Ag/AgCl}$. As with the electrodeposition technique, to ensure that minimal photocurrent density is lost with

the deposition of CoPi, both the current density and the photocurrent density were monitored with CoPi deposition time for both a planar and macroporous electrode pre-coated with $BiVO_4$.

Figure 4-36 shows the current density (left) and photocurrent density (right) for pFTO-$BiVO_4$-CoPi (pedep). Once again the current density in the dark is largely unchanged with the addition of increasing amounts of CoPi. When the photocurrent density was measured it was found that the photocurrent density was very similar to the electrodeposition method: the first 100s of deposition gave the largest increase in the photocurrent density, and thereafter the photocurrent density dropped (due to the layer of CoPi over the $BiVO_4$ which prevents light absorption).

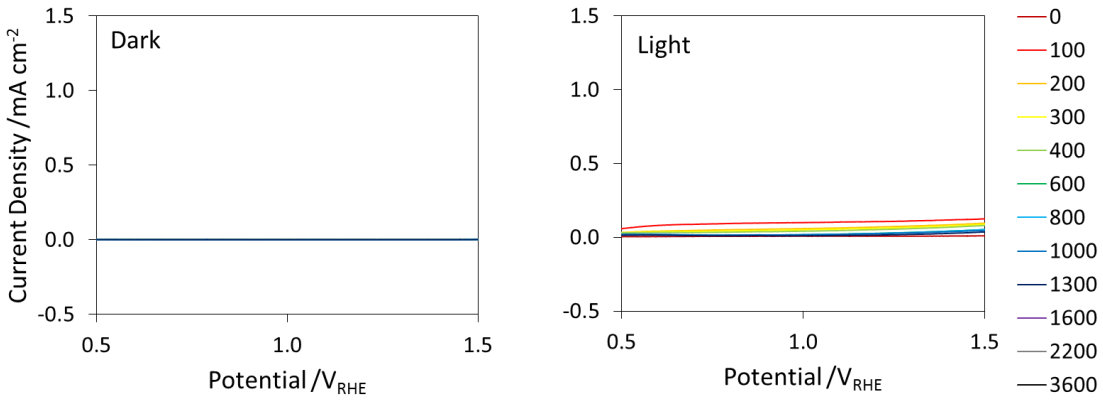

Figure 4-36: Photoactivity change with changing CoPi quantity for pFTO-$BiVO_4$ photoelectrodeposition

The current density and photocurrent density for macFTO-$BiVO_4$-CoPi are shown in Figure 4-37. In the dark (left) there is again little change in the current density, but in the light, the onset potential decreases from 0.6 V_{RHE} (measured) to 0.35 V_{RHE} (extrapolated). The photocurrent density increases after the first 100 s of deposition, and decreases thereafter, which is consistent with the CoPi blocking light absorption by the $BiVO_4$.

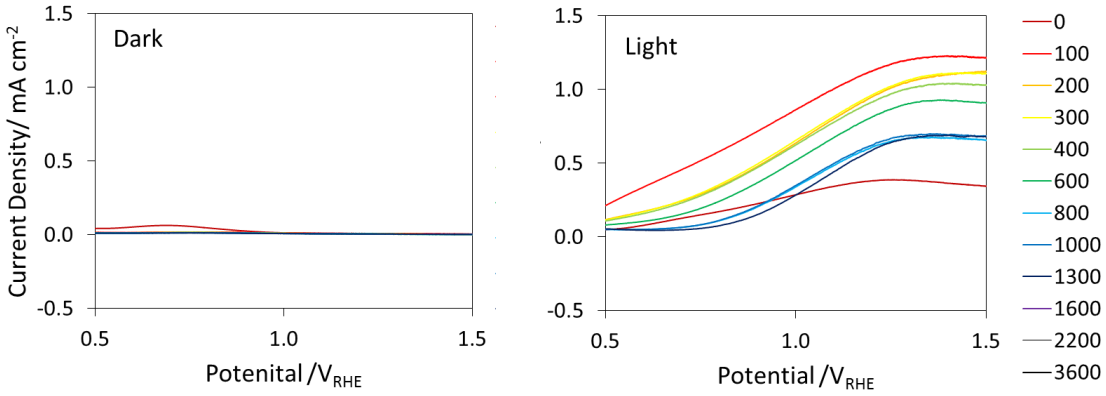

Figure 4-37: Photoactivity change with changing CoPi quantity for macFTO-$BiVO_4$ photoelectrodeposition

4.4.2.3. A Comparison of the Electrodeposition and Photoelectrodeposition Techniques

To summarise the previous findings, a deposition time of 100 seconds provided the largest decrease in onset potential for all electrodes studied. In most cases the onset potential could be lowered by up to 70 mV. When this is considered with the fact that for some electrodes studied the current density and/or photocurrent density densities actually decreases with further application of CoPi, it was deemed that 100 seconds was the optimal time to deposit CoPi on FTO electrodes. All further electrodes that consist of CoPi will have only deposited CoPi for 100 seconds.

In order to establish if electrodeposition or photoelectrodeposition of CoPi is the better technique, both techniques were used to deposit CoPi on pFTO-$BiVO_4$ and macFTO-$BiVO_4$ for 100 seconds (Figure 4-38). If the macroporous electrodes are first considered (solid lines), the onset potential is lower for the photoelectrodeposition technique (red lines) than for the electrodeposition technique (black lines) by 22 mV (onset potentials are extrapolated where the data is not available, Table 4-1) by fitting a straight line to the region between 0.5 and 1 V_{RHE} and reading off the onset potential where the current density is 0 A cm^{-2}. Additionally, the photocurrent density is higher for the photoelectrodeposition technique when compared to the electrodeposition technique across the entire range of potentials studied. This suggests that the photoelectrodeposition is providing some additional benefits over the electrodeposition technique, which is probably related to the deposition of catalyst over the defect sites in the $BiVO_4$, as discussed.

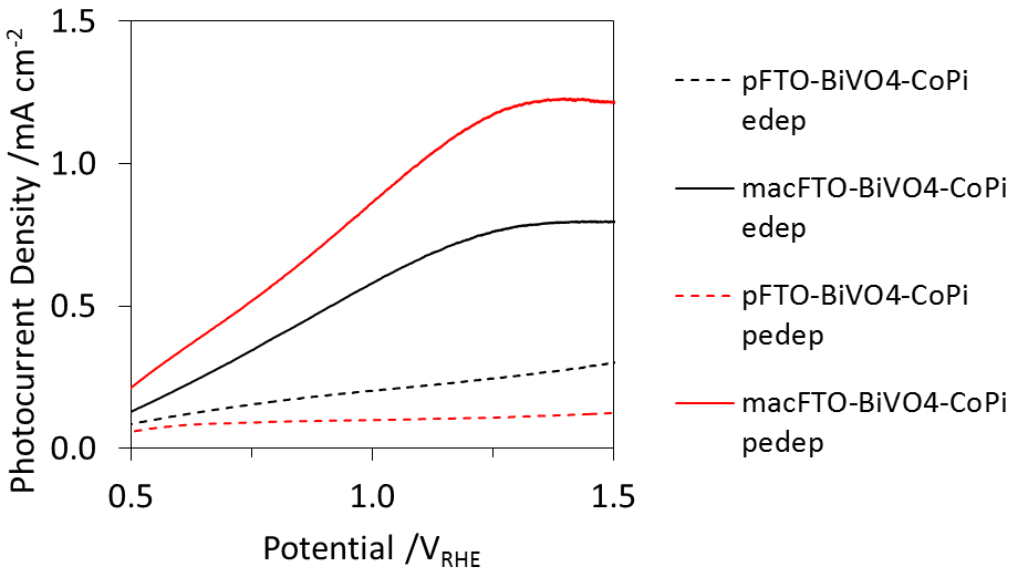

Figure 4-38: Comparison of the electrodeposition (edep, black) and photoelectrodeposition (pedep, red) techniques for planar electrodes (dashed lines) and macroporous electrodes (solid lines). The potential range measured was limited to no less than 0.5 V_{RHE} to ensure that the electrode did not degrade during the course of measurements. Onset potentials are extrapolated where the data is not available due to stability constraints.

Table 4-1: Table of photocurrent densities for macFTO-$BIVO_4$-CoPi and pFTO-$BiVO_4$-CoPi electrodes where the CoPi has been deposited either by an electrodeposition or photoelectrodeposition technique. No values are reported for planar electrodes, as these electrodes show no significant visible light activity.

Electrode	Photocurrent density at +1 V_{RHE} /mA cm^{-2}	Onset Potential in the light /V_{RHE}
pFTO-$BiVO_4$-CoPi (edep)	0.20	-
pFTO-$BiVO_4$-CoPi (pedep)	0.10	-
macFTO-$BiVO_4$-CoPi (edep)	0.58	0.372
macFTO-$BiVO_4$-CoPi (pedep)	0.86	0.350

For the planar electrode the case is a bit different: as there is no significant photoactivity, a comparison cannot be drawn with macFTO-$BiVO_4$; however the photocurrent density can be compared. The photocurrent density is lower for the photoelectrodeposition technique than the electrodeposition technique. This can be explained in terms of the amount of $BiVO_4$ present. Unlike macFTO-$BiVO_4$ where the amount of deposited $BiVO_4$ appears to be fairly constant, pFTO-$BiVO_4$ has very varied amounts of $BiVO_4$ deposited because of the tendency of the deposition solution to bead on the electrodes surface, which causes the $BiVO_4$ to form in thicker layers than if it was well dispersed. This in turn means that the $BiVO_4$ is more likely to

flake off the electrode surface at any point, causing fairly large discrepancies in the photocurrent densities obtained for pFTO-$BiVO_4$ electrodes.

In summary, as it is the macroporous electrodes that are of more importance to the present study, it was found that the photoelectrodeposition of CoPi produces the better electrodes, both in terms of a lower onset potential and higher photocurrent density when compared to the electrodeposition of CoPi. In all cases, the current densities achieved with the macFTO electrodes were higher than the pFTO electrodes, which shows that templating the backing electrode has a beneficial effect. Additionally, simple methods have been used to deposit the CoPi over macFTO electrodes.

The current densities reported for macFTO-$BiVO_4$-CoPi electrodes are comparable to those found in the literature. Typically, $BiVO_4$ electrodes are modified in another way, additional to the CoPi catalyst. This increases the photocurrent densities obtained, but at the expense of further, potentially complex synthetic steps.

One example gives similar photocurrent densities to those presented in the present work: photocurrent densities of 0.7 mA cm^{-2} at 1 V_{RHE} in 0.1 M potassium phosphate buffer (pH 6.7) were obtained for nanoparticulate electrodes of $BiVO_4$-CoPi formed by spin coating an acidic mixture of bismuth nitrate and vanadyl acetylacetone, with subsequent photoelectrodeposition of CoPi. [75]

Pilli *et al.* present two papers where the $BiVO_4$-CoPi electrodes are prepared in different ways. In the first, porous SiO_2-$BiVO_4$ electrodes are made using a surfactant assisted, metal organic decomposition technique. CoPi was photoelectrodeposited and the photocurrent densities obtained were 1.6 mA cm^{-2} at 1.1 $V_{Ag/AgCl}$. For comparison, the SiO_2-$BiVO_4$ electrode produced a photocurrent density of 0.3 mA cm^{-2} at 1 $V_{Ag/AgCl}$.[271]

A similar electrode consists of 1D WO_3 rods coated in highly porous $BiVO_4$, which was then coated in CoPi (WO_3-$BiVO_4$-CoPi) using a photoelectrochemical technique. These electrodes had photocurrent densities of 2.8 mA cm^{-2} at 1$V_{Ag/AgCl}$ compared to 2.4 mA cm^{-2} for a WO_3-$BiVO_4$ electrode and 1.5 mA cm^{-2} for a porous $BiVO_4$ electrode.[272]

One of the best examples include the work of Zhang *et al.* who show that the addition of CoPi to a hydrogenated $BiVO_4$ electrode increases the photocurrent density from ~1.5 mA cm^{-2} to ~4

mA cm^{-2} at 1 V_{RHE}, while the onset potential shifts from 0.53 to 0.23 V_{RHE}. This specific electrode was made using a complex method consisting of several steps including electrodeposition of bismuth, treatment with vanadate solution, heat treatment, etching in NaOH and hydrogenation before electrodeposition of CoPi.[273]

To summarise the literature results, $BiVO_4$ electrodes coated with CoPi typically produce photocurrent densities on the order of 0.7 – 2.5 mA cm^{-2}, results which are consistent with those presented in the present thesis. The best photocurrent density was 4 mA cm^{-2}, but this electrode was made with a complex synthetic route, unlike the work presented in the present thesis.

4.5. Gas Evolution Measurements

Gas evolution from FTO electrodes was measured in two ways: 1) to use a system of 2 inverted burettes in which the fluid level indicated the volume of gas produced; 2) to inject 150 µL of the headspace of the electrochemical cell into a GC, calibrated for both hydrogen and oxygen. In both cases the electrodes evolving hydrogen and oxygen were kept in separate compartments because platinum, which is used to drive the hydrogen evolution reaction, is also capable of driving the oxygen reduction reaction. Additionally, if large amounts of gases are produced, the mixing of hydrogen and oxygen can become a safety issue.

In all cases, the potential used for CoPi deposition was either +1 $V_{Ag/AgCl}$ (Kanan *et al.*[105]) or +0.3 $V_{Ag/AgCl}$ with the simultaneous application of light (Zhong *et al.*[104]). The solution used to deposit CoPi was a 0.5 mM $Co(NO_3)_2$ in phosphate buffer (0.1 M), pH 7, in both cases. In all cases the electrodes were measured for activity in phosphate buffer, pH 7, and the potential used to study oxygen evolution was +1 V_{RHE}. The time scale for each reaction was typically 3 hours.

4.5.1. The Activity of FTO Electrodes towards Oxygen Evolution

4.5.1.1. Planar Electrodes

pFTO was shown in chapter 2 to have no significant current density in the dark or in the light. Over the course of a 3 hour experiment, held at +1 $V_{Ag/AgCl}$, only 2 mC of charge was passed in the dark, and, consistent with the lack of photoactivity, only 2 mC of charge was passed in the light (Table 4-2). 2 mC of charge produces only 0.004 µmol of O_2 (100% efficiency) and this is not enough gas to be measured accurately, so the efficiency of the reaction could not be determined.

With the addition of $BiVO_4$ to pFTO the current density remains low, but the photocurrent density increases substantially to 0.033 mA cm^{-2}. This value is lower than previously reported in the present work due to the lower working potential used. The charge passed was 0.5 mC (0.001 µmol O_2) in the dark, which equates to too little gas to be measured, and 356 mC (0.99 µmol O_2) in the light. Unfortunately, not enough gas was produced to be measured accurately.

The activity of the catalyst, CoPi, alone on the pFTO electrode also produces too little gas to measure, with 0.09 µL (0.004 µmol O_2) of gas produced, either in the dark or the light (as CoPi is not photoactive).

With a combination of $BiVO_4$ and CoPi on pFTO the photocurrent density is increased over bare pFTO (values). The charge passed for pFTO-$BiVO_4$-CoPi (edep) was 2 mC (0.004 µmol) in the dark and 312 mC (0.87 µmol) in the light. For pFTO-$BiVO_4$-CoPi (pedep) the charge passed was 2 mC (0.004 µmol) in the dark, which is the same as for the electrodeposited electrode, but is three times higher than the edep electrode in the light, at 968 mC (3.57 µmol) which suggests that there is a secondary effect increasing the amount of charge passed (surface passivation, as previously discussed).

*Table 4-2: pFTO electrode data for O_2 production. *as the pFTO-CoPi electrode has already been shown to not have any photoactivity it was not tested in the light. Data shown is from in the dark.*

	Current density /µA cm^{-2}	Charge /mC	Predicted no. of moles /µmol	Actual no. of moles /µmol	FE /%
Electrode, DARK					
pFTO	0.14	2	0.004	0	0
pFTO-$BiVO_4$	0.04	0.5	0.001	0	0
pFTO-CoPi	0.13	1	0.004	0	0
pFTO-$BiVO_4$-CoPi (edep)	0.17	2	0.005	0	0
pFTO-$BiVO_4$-CoPi (pedep)	0.17	2	0.005	0	0
Electrode, LIGHT					
pFTO	0.23	2	0.007	0	0
pFTO-$BiVO_4$	33.00	356	0.994	0	0
pFTO-CoPi*	0.13	1	0.004	0	0
pFTO-$BiVO_4$-CoPi (edep)	28.86	312	0.87	0.90	103
pFTO-$BiVO_4$-CoPi (pedep)	89.64	968	2.70	3.57	133

The faradaic efficiency is a measure of how well the generated charges are converted into useful product. For all electrodes in the dark, too little gas was evolved, so no accurate measurements could be taken, and thus the faradaic efficiency could not be determined. However, in the light the electrodes that contained both $BiVO_4$ and CoPi produced the most O_2 gas and this was enough to be measured. For pFTO-$BiVO_4$-CoPi (edep) the faradic efficiency was calculated to be 103% while for pFTO-$BiVO_4$-CoPi (pedep) the faradaic efficiency was found to be 132%.

The faradaic efficiency is essentially 100% for the pFTO-$BIVO_4$-CoPi samples as expected for systems using the CoPi catalyst. The error on the values is likely from a small air leak, which will let oxygen into the system. Air leaks were monitored by using N_2 as an internal standard. If the N_2 peak area increased over time, it was deduced that there was an air leak in the system.

The relative ratio between the H_2 and O_2 values can be used to compare electrodes. Here the faradaic efficiency of the photoelectrodeposited CoPi electrode is higher than that of the electrodeposited CoPi, showing once again that photoelectrodeposition is a superior method of depositing the CoPi catalyst, as more gas is evolved than under the same conditions with an electrodeposited CoPi electrode. This can again be attributed to the secondary effect of the CoPi which is to act as a surface passivating agent.

Other sources of error which may contribute to the overestimate of the faradaic efficiency are the fact that most of the gas measurements are at the detection limit of the burette system ($\pm$ 0.02 mL), which would make some measurements unreliable. Additionally, some gas (oxygen or hydrogen) may absorb into the electrolyte solution, though at room temperature the amount of oxygen that dissolves in water is very low. To help compensate for this the solution was not purged of air, so as little gas would be lost as possible. Further factors include heat from the lamp (which would only affect experiments run in the light) as this was observed to warm the water slightly, as for the longer experiments some condensation was observed on the walls of the electrochemical cell.

4.5.1.2. Macroporous Electrodes

As with pFTO, macFTO was shown in chapter 2 to have no significant current density in either the dark or the light. Over the course of a 3 hour experiment, held at +1 $V_{Ag/AgCl}$, only 9 mC of charge was passed, corresponding to 0.026 µmol O_2, and this increased to only 25 mC (0.070 µmol O_2) in the light Table 4-3). These values produce too low a gas volume to be measured accurately.

With the addition of $BiVO_4$ to macFTO, the current density remains low, but the photocurrent density increases substantially to 0.058 mA cm^{-2}. Again too little gas was produced to be measured accurately, with only 1 mC of charge passed in the dark (0.0018 µmol O_2) and 631 mC in the light (1.76 µmol O_2).

For comparison, when only CoPi is deposited on macFTO electrodes only 14 mC of charge is passed in the dark (0.039 µmol O_2) and 42 mC in the light (0.12 µmol O_2). There is a slight increase in the charge passed in the light because macFTO does have a small photo-response.

macFTO-$BiVO_4$-CoPi has a larger photocurrent density when compared to macFTO, macFTO-$BiVO_4$ or macFTO-CoPi. For the electrodeposited electrode the charge passed was 11 mC in the dark (0.031 µmol O_2) and 1835 mC in the light (5.12 µmol O_2). For the photoelectrodeposited electrode the charge passed was higher, with 12 mC in the dark (0.034 µmol O_2) and 3150 mC in the light (8.78 µmol O_2). This is a factor increase of 1.7 times better for the photoelectrodeposited electrode than for the electrodeposited electrode.

Table 4-3: macFTO electrode data for O_2 evolution

	Current density /μA cm^{-2}	Charge /mC	Predicted number of moles /μmol	Actual number of moles /μmol	FE /%
Electrode, DARK					
macFTO	0.87	9	0.026	0	0
macFTO-BiVO4	0.06	1	0.0018	0	0
macFTO-CoPi	1.28	14	0.039	0	0
macFTO-BiVO4-CoPi edep	1.04	11	0.031	0	0
macFTO-BiVO4-CoPi pedep	1.13	12	0.034	0	0
Electrode, LIGHT					
macFTO	2.32	25	0.070	0	0
macFTO-BiVO4	58.44	631	1.76	0	0
macFTO-CoPi	3.84	42	0.12	0	0
macFTO-BiVO4-CoPi edep	169.91	1835	5.12	4.46	87.3
macFTO-BiVO4-CoPi pedep	291.63	3150	8.78	9.82	111.9

As seen with the planar electrodes, for all macroporous electrodes in the dark no gas could be detected, thus the faradaic efficiency cannot be calculated. In the light the two electrodes which produced measurable volumes of gas were the two electrodes with both $BiVO_4$ and CoPi. The faradic efficiency was calculated to be 87% for the electrodeposited CoPi and 112% for the photoelectrodeposited CoPi, which again are close to 100% efficient, as expected for this catalyst. The major source of error is due to small leaks in the system which increase the volume of oxygen detected.

There are few reports of $BiVO_4$ electrodes tested for oxygen evolution, demonstrating a clear gap in the literature. Most literature reports on current densities and onset potentials (as

described above) rather than for oxygen evolution rates. Described below are a few examples for context of the present results.

Nakamura *et al*. report an oxygen evolution rate of ~2.5 µmol hr^{-1} for a powdered $BiVO_4$ sample in 0.01 M $AgNO_3$ (as a sacrificial electron acceptor) illuminated with > 420 nm.[274] The sacrificial electron acceptor will increase the rate of oxygen evolution over tests in, for example, buffer solution. Much higher oxygen evolution rates, of up to 8.88 µmol hr^{-1} O_2 (AM1.5G), were obtained for $BiVO_4$ systems modified with cobalt oxide catalyst in KOH (pH 13) electrolyte, which is used for stability.[114] This system is supported on an FTO electrode, and gives comparable results to the ones presented in this thesis.

A similar electrode, with a FeOOH catalyst instead of a cobalt based one, has an oxygen evolution rate of ~1 µmol hr^{-1} in 0.1 M KH_2PO_4 (pH 7) AM1.5G, assuming 100% faradaic efficiency.[100] This is significantly lower than the results of macFTO-$BiVO_4$-CoPi, but this may be due to the different catalyst and the fact that the $BiVO_4$ is not a porous layer.

To summarise, all electrodes in the dark produced too little gas to be measured, but the electrodes in the light performed substantially better. Electrodes that had both $BiVO_4$ and CoPi produced measurable volumes of gas, and the faradaic efficiencies were calculated to be 100%. In most cases the faradaic efficiency was overestimated and this was due to intrinsic errors in the burette system and leaks which let air in (artificially enhancing the amount of gas produced). To correct for these errors, a new electrochemical cell was designed to link directly with the GC to do *in-situ* measurements. This test was only performed on the best electrode to date (macFTO-$BiVO_4$-CoPi pedep). It was found that using the direct GC setup air leaks were avoided and the faradaic efficiency dropped from 112% to 96.4 %. Initially this appears much lower than with the burette system, but the error on GC measurements gives a 5% error on the faradaic efficiency, which puts both results at ~100% efficient.

IPCE Measurements

The IPCE measurements for the $BiVO_4$ electrode series are presented in Figure 4-39. It was found that the IPCE for the macroporous electrode is substantially higher than for planar electrodes: pFTO-$BiVO_4$ had an IPCE of < 1% at 380 nm, while macFTO-$BiVO_4$ had an IPCE of ~15% at 380 nm. With the addition of CoPi by photoelectrodeposition, the IPCE increases for both pFTO-$BiVO_4$ and macFTO-$BiVO_4$. This is expected because the catalyst acts to improve the electron transport, which means that the incident photons which are converted into electrons can be more effectively used (higher photocurrent). The IPCE of pFTO-$BiVO_4$-CoPi (pedep) was found to be ~5% at 380 nm, while the IPCE of macFTO-$BiVO_4$-CoPi was found to be ~60% at 380 nm. For both electrodes the IPCE increased upon the addition of CoPi, and the most efficient electrode was found to be macFTO-$BiVO_4$-CoPi (pedep).

Interestingly, the IPCE for the non-absorbing region (> 500 nm) is higher for the macFTO electrodes than for the planar electrodes. This could be due to the scattering effects of macFTO, which as a highly porous material is very likely to scatter some incident light.

As $BiVO_4$ is widely used in the literature as a light absorbing material in solar devices, there are some pieces of literature with which the IPCE can be compared. Pilli *et al*.[79] found the IPCE of $BiVO_4$ electrodes to be about 35% which was increased to ~60% 400-450 nm when CoPi was added to the electrode, while Seabold *et al.*[100] found that the IPCE of a planar $BiVO_4$ electrode modified with FeOOH catalyst for oxygen evolution was ~60% between 400-450 nm, both results are similar to the present work.

The IPCE spectrum also matches very well with the absorption spectrum of macFTO-$BiVO_4$.

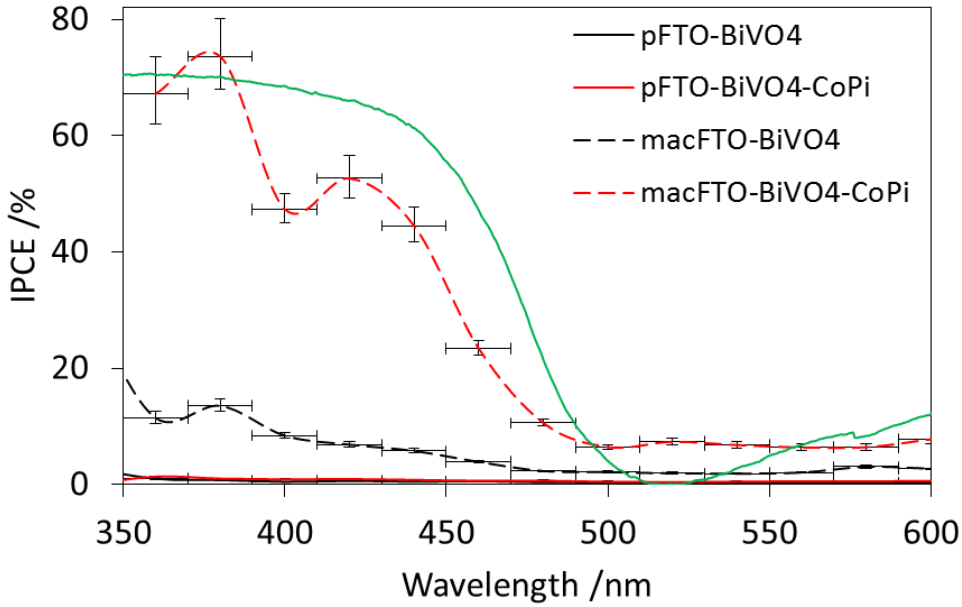

Figure 4-39: IPCE for $BiVO_4$ electrodes with and without CoPi at +1 $V_{Ag/AgCl}$. The green line represents the absorption spectrum of macFTO-$BiVO_4$ for reference.

The predicted theoretical maximum current for macFTO-$BiVO_4$-CoPi edep is 0.9 mA cm^{-2} and for macFTO-$BiVO_4$-CoPi pedep it is 2.8 mA cm^{-2} (values calculated using raw data and OPVAP software).[258]

4.6. Summary and Conclusions

The aim of the present work was to demonstrate that templating the supporting TCO electrodes could improve the activity of electrodes for water splitting. By using well known materials on the electrodes a comparison can be drawn with other works in the literature to demonstrate the efficiency of the electrodes in the present work.

Initially, CdS was used as a proof of principle and it was found that the same amount of CdS nanoparticles deposited over planar and macroporous electrodes show that macroporous electrode act in the same way as planar electrodes, and give the same current densities. This proves that macFTO is conductive for photoelectrons and can support photocurrents. After this study, the loading of CdS nanoparticles was increased as much as possible to demonstrate that the macroporous electrode could produce superior current densities compared to planar electrodes. A maximum photocurrent density of ~8 mA cm^{-2} was achieved for macFTO-CdS, whereas pFTO-CdS gave only 0.1 mA cm^{-2} under the same conditions. Additionally, CdS could be deposited *via* a simple technique, which means that templating the TCO electrode allows for simple electrode fabrication.

Furthermore, the photocurrent density of macFTO-CdS was sufficiently high that it could drive the HER with no applied bias. An IPCE of ~60% was achieved for macFTO-CdS, compared to only 20% for pFTO-CdS. CdS is known to be unstable and indeed macFTO-CdS was shown to be very unstable. Up to 60% of the initial activity of the macFTO-CdS electrode was lost in 1 hour of measurement at 0 $V_{Ag/AgCl}$.

A more stable material that is well known in the literature for water splitting reactions is $BiVO_4$. $BiVO_4$ is also known to split water by itself, with fairly high overpotentials. The current densities achieved with $BiVO_4$ instead of CdS were much smaller (about 1 mA cm^{-2} at +1 V_{RHE}) but far more stable: less than 5% of the initial activity was lost over 1 hour at +1 $V_{Ag/AgCl}$.

To lower the potential required to drive water splitting, a co-catalyst was used. Cobalt phosphate (CoPi) is a highly efficient co-catalyst that may also work as a surface passivating agent if deposited under photoassisted conditions. CoPi can be deposited in a variety of methods, and the two most successful methods studied in the present work were electrodeposition and photoelectrodeposition. Both methods were trialled for the lowest overpotential and the higher photocurrent density densities. It was found that for both

techniques a deposition time of 100 seconds was optimal to lower the over potential and to increase the photocurrent density.

The gas evolution on the $BiVO_4$ series of electrodes in 0.1 mol dm^{-3} phosphate buffer, pH 7, (with and without CoPi) show that both planar and macroporous electrodes are not active in the dark, as not enough current density is generated to produce measureable amounts of gas. However for the macroporous electrodes that have both $BiVO_4$ and CoPi enough gas is produced in the light that the efficiency of the electrodes can be measured. The faradaic efficiency was found to be ~100% for all electrodes studies, which is consistent with the literature on CoPi. The electrodes where CoPi had been deposited using photoelectrodeposition appears to have a slightly higher faradaic efficiency for both planar and macroporous electrodes.

Finally the IPCE of the $BiVO_4$ electrodes was found to be ~60% for macFTO-$BiVO_4$-CoPi (pedep) and ~15% for macFTO-$BiVO_4$. The equivalent planar electrodes had very low efficiencies (<5%).

Overall the present work has shown that templating the back electrode (FTO) can produce electrodes capable of sustaining high photocurrent densities. Several different photoactive materials and catalysts can be easily deposited over the templated back electrode using simple techniques. These electrodes have then been used to show that gas evolution (water splitting) can be driven efficiently with these electrodes.

Chapter 5

Conclusions and Future Work

Chapter 5. Conclusions and Future Work

5.1. Summary of Project Aims and Conclusions

The main aim of this project was to develop ordered porous (macroporous) electrodes made from transparent conducting materials that were capable of supporting a variety of photoactive materials and catalysts deposited in a simple way. The use of macroporous electrodes makes the nano-structuring of photoactive materials simple, because a layer of nanoparticles may be used. Additionally, macroporous materials may also display the photonic effect, which has been shown to increase the light harvesting efficiency of many different electrodes.

Further aims of the project were to show that the macroporous electrodes could be used for the photocatalytic splitting of water, focussing on the oxygen evolution half reaction as this is conceptually more difficult, due to the 4 electron transfer.

Macroporous electrodes should be able to absorb more light per unit area, thus increasing the light absorption efficiency, compared to planar electrodes. This is because by structuring the back electrode a thin film of photoactive material can be deposited over the surface, compared to a thick film which, although it absorbs more light can have higher recombination rates. Finally, if both the OER and the HER electrodes can be developed, then a complete working device could be made that would perform water splitting efficiently.

5.1.1. Chapter 2: Fabrication and Characterisation of macFTO

It was shown in chapter 2 that FTO was a suitable transparent conducting oxide to template into a macroporous electrode. It was found that this could be done using a relatively simple technique, and the parameters to make the electrode were optimised to produce the most conductive and structurally perfect electrode possible.

The conductivity of the macFTO electrodes could not be determined, due to the delicate structure, so planar analogues were used as a guide. The conductivity of the pFTO electrodes was found to be < 10 Ω square for Sn:F rations < 1, showing that the planar electrodes are conductive and the conductivity was comparable to the commercial pFTO electrode (7 Ω square). Electrochemistry was used to further compare the conductivities of pFTO and macFTO electrodes. It was found that the redox wave of the ferrocene probe has a similar peak shape

and position for both electrodes, indicating that they had similar conductivities. The peak shape indicates the reversibility of the reaction, while the peak position indicates the ease of electron transfer (the conductivity).

The capacitance of the electrodes was used to compare the relative surface area of the electrodes. It was found that macFTO had a capacitance 12 times larger than that of pFTO, suggesting a surface area at least 12 times larger.

Comparison of the properties of electrodes with different precursor fluorine contents and different calcination temperatures allowed optimal parameters for the fabrication of macFTO electrodes to be determined. It was found that the capacitance was greatest at 450 °C, suggesting that the surface area was larger when calcined at this temperature. Additionally SEM analysis showed fewer defects with this calcination temperature suggesting that it is optimal.

Changing the precursor Sn:F ratio was found to not have an effect on the final amount of fluorine in the electrodes. At precursor ratios of < 1.0 the final Sn:F ratio was found to be ~0.005 (0.5 atom%). this is significantly lower than the precursor ratio and it was concluded that the major sources of fluorine loss were due to the increase in surface area (surface loss compared to bulk loss) and losses through C_xF_y volatile products during calcination.

Using a calcination temperature of 450 °C and a Sn:F precursor ratio of 0.5 (to ensure 0.5 atom% fluorine) macFTO electrodes were produced with excellent structure (SEM analysis) and optimal properties (such as surface area and conductivity). With these parameters, and a pore diameter of 450 nm, the stop band has a wavelength of ~550 nm at 45° incidence.

The photoactivity of pFTO and macFTO was then assessed. It was found that neither electrode was photoactive (< 15 μA cm^{-2}) under the conditions used throughout this thesis, and the onset potential for water oxidation was very high (> 2 V_{RHE}), suggesting that the electrode would have little effect on any deposited materials.

5.1.2. Chapter 3: Angular Dependence of macFTO Electrodes

Chapter 3 went on to demonstrate that, due to the ordered nature of the electrode, some phenomena, such as the slow light effect and the stop band, may contribute to increasing the overall efficiency of a working device. Because of the porous nature of the electrode, incident

light will undergo multiple coherent scattering (slow light) and therefore have a higher chance of being absorbed, increasing the light absorption efficiency. The stop band forbids light of a certain wavelength (dependent on the position of the stop band) to propagate through material, thus if this overlays with the emission band of an embedded photoactive material an emission can be forbidden, thus increasing the solar to fuel conversion efficiency.

Initially the angular dependence of the stop band was tracked across a range of different angles. The stop band was found to change according to the equation:

$$\lambda = \frac{2d_{hkl}}{m}\sqrt{n_{av}^2 \sin^2\theta}$$

Equation 5-1

Shifting from low angles of incidence (5°) to high angles of incidence (85°) the stop band shifted from short wavelengths (450 nm) to long wavelengths (700 nm). These results were then used to compare the stop band position with the emission profiles of two different dyes (bis(2,2'-bipyridine)-4,4'-dicarboxy-2,2'-bipyridineruthenium(II) dichloride (Rudcbpy) and coumarin 440/460). It was found that the most enhancement in the lifetime of the embedded dye was at the angle where there was most overlap with the stop band. For Rudcbpy this was at 65°, and the lifetime enhancement was 1.8 times and for coumarin this was at 15° with a lifetime enhancement of 1.4 times. These results are consistent with several reports in the literature and show a positive effect of the stop band of the lifetime of embedded dyes.

5.1.3. Chapter 4: Photoelectrodes

The main aim of chapter 4 was to show that macFTO electrodes could produce superior photocurrent densities and water oxidation capabilities compared to pFTO electrodes fabricated in the same way.

Initially CdS nanoparticles were deposited in macFTO using a low concentration. This meant that individual nanoparticles were isolated on the macFTO. Conductivity of macFTO was proved because the electrodes generated a current. The current density could be increased by using more CdS, increasing the amount of light that could be absorbed. Furthermore, the macFTO architecture was shown to be suitable to evolve gases on by using CdS to evolve hydrogen from water.

$BiVO_4$ is known in the literature as a suitable material for solar water splitting, but it requires a high potential (~2 V_{RHE}). Commonly, other materials are used to passivate the $BiVO_4$ or to catalyse the reaction. In the present work it was shown that by using thin layers of $BiVO_4$ over the macFTO structure the amount of light absorbed per unit area could be increased and therefore the photocurrent density could be increased (from < 1 µA cm^{-2} to ~30 µA cm^{-2}).

With the addition of the common catalyst cobalt phosphate (CoPi) the onset potential for water oxidation can be reduced, and simultaneously the photocurrent density increases. Two different methods were used to electrodeposit CoPi over $BiVO_4$: electrodeposition at +1 V_{AgAgCl} and photoelectrodeposition with light at + 0.3 V_{AgAgCl}. It was found that photoelectrodeposition produced electrodes which were capable of generating higher photocurrent densities of up to 0.86 mA cm^{-2} at +1 V_{RHE}, which is an 8.6 fold increase over the pFTO-$BiVO_4$.

The IPCE of $BiVO_4$ based electrodes was determined to be low for planar electrodes (< 1% at 400 nm) and much higher for macFTO-$BiVO_4$ (~10% at 400 nm). With the addition of CoPi the IPCE increased to over 60% for macFTO-$BiVO_4$-CoPi, which gives an integrated photocurrent density of 6 mA cm^{-2} under white light.

Finally, faradaic efficiencies of up to 100% were obtained for macFTO-$BiVO_4$-CoPi when evolving oxygen from water. The gas evolution rate from macFTO electrodes was higher than that of pFTO electrodes by up to 3 times (3.57 µmol from pFTO-$BiVO_4$-CoPi compared to 9.82 µmol from macFTO-$BiVO_4$-CoPi). This clearly demonstrates that macFTO electrode can be used in water splitting applications, and the fact that both $BiVO_4$ and CoPi was deposited using very simple techniques demonstrates the versatility of macFTO.

5.2. Future work

5.2.1. Chapter 2: Synthesis and Characterisation of macFTO Electrodes

In chapter 2, macFTO was synthesised and fully characterised. This work could be supported with further evidence from, for example, XPS or EDX. It would be interesting to see the effect of changing the pore size on the quality of the structure of the macFTO as only one pore size was examined. Furthermore, the electrochemical analysis could be expanded into looking at the activity of pFTO and macFTO electrodes for hydrogen evolution, in order to complete a full solar water splitting device.

The remaining questions about macFTO were primarily to do with quantification of the amount of fluorine in macFTO and how conductive the samples were. A detailed study of the exact position on amount of fluorine could be undertaken, for example by NMR. This could then lead to further understanding of how conductive the macFTO electrodes are, and if this arises from defect sites arising from the loss of fluorine, as Günne et al suggest.[187] Additionally, impedance spectroscopy is a more sensitive electrochemical technique than the standard electrochemistry used in this thesis and could be used to give more information on the conductivity of the electrodes as well as the surface area enhancement. Impedance analysis also allows a study into the different resistances in the system, so it would be possible to identify grain boundary resistances compared to solution resistances, for example.

5.2.2. Chapter 3: Angular Dependence of macFTO Electrodes

There are many possible developments available to gain more information on the study of the angular dependence of macFTO electrodes. The preliminary results shown here were very promising, with a clear indication that the stop band may have an effect on the fluorescence lifetime of embedded materials.

To further the present study, the photoluminescence spectra of the embedded emitters should be studied, not just the lifetime. Several researchers have demonstrated clear effects on the absorption and emission profiles, which was not explicitly observed in the present work. A detailed study could show these effects in the electrodes presented in this thesis. This should be undertaken with a careful consideration of how much dye is to be used, and possibly with different amounts of dye.

Finally, other systems should be used to study macFTO, not just coumarin and Rudcbpy. This should include other well-known dyes, and expand into nanoparticles. For example, much of the work presented in the present thesis used CdS, an efficient light absorber, and $BiVO_4$, a practical material to use for solar water splitting. It would be interesting to see the effect of the photonic structure on these materials as they have been used extensively in the present thesis. Furthermore, the use of different pore sizes in macFTO open up the possibility of using many more luminescent materials to study the photonic effect.

5.2.3. Chapter 4: Photoelectrodes

While this chapter demonstrated the main aim of the project very well, there are many improvements to the techniques used that could be made. For example, the gas evolution studies were difficult and time consuming, and a better cell needs designing that is capable of directly injecting into the GC to get accurate measurements.

Additionally, the work could be expanded on by using a variety of different light absorbers. For example, though hematite is less stable, it may be possible to increase the stability and light harvesting capabilities of hematite by depositing it over macFTO. This would further demonstrate that macFTO is a suitable architecture for easy and simple deposition of a variety of materials.

Linking the work in chapter 4: photoelectrodes with that in chapter 3: angular dependence of macFTO electrodes, the photonic effect could be studied with respect to different photo-absorbers. The photonic effect may increase the photocurrent density gained at particular angles, which would be another way of increasing the photocurrent output of solar water splitting devices.

Finally, if the half reaction for hydrogen evolution could be developed (with suitable light absorbers and catalysts) then a complete working cell can be designed, which will hopefully be able to work with no external bias, as two light absorbing electrodes should provide enough potential between them to drive the water splitting reaction, reaching the ultimate goal of a non-biased water splitting system.

Chapter 6
Experimental

Chapter 6. Experimental

6.1. Synthetic Work

All solvents and materials were purchased from Sigma Aldrich and Fischer Scientific and used as received without further purification, with the exception of bis(2,2'-bipyridine)-4,4'-dicarboxybipyridine ruthenium(II) dichloride, which was made according to a literature procedure.[275]

6.1.1. Polystyrene Synthesis and Deposition

Polystyrene sphere template (typically 450 nm diameter) was prepared using a literature method:[168] Styrene (150 mL) was washed with sodium hydroxide (0.1 mol dm^{-3}, 140 mL) 4 times (to remove inhibitor) and deionised water (140 mL) 4 times to remove excess sodium hydroxide. In a 2 L round bottomed flask fitted with condenser and N_2 inlet, water (1133 mL) and washed styrene (133 mL) were heated to 70˚C under a flow of N_2. After 30 minutes, $K_2S_2O_8$ (0.4422 g in 66 mL water) was added. The resulting solution was stirred at 245 – 360 rpm for 24-28 hours to change the size of the polystyrene spheres formed. To form spheres of 450 nm diameter used predominantly in the present work the solution was stirred at 300 rpm for 26 hours. During this time a white precipitate formed, causing the solution to turn translucent. When complete, the polystyrene solution was allowed to cool, and then filtered through glass wool to remove large agglomerates. This white polystyrene solution (1.3 mL) was diluted in ethanol (82 mL) and water (8 mL) ready for use (polystyrene suspension). This suspension was sonicated for 30 mins to ensure the polystyrene was dispersed well and was then used immediately. The polystyrene spheres were sized using SEM: a drop of solution was dried (room temperature) on a carbon sticky tab attached to an aluminium stub. A 5 keV beam was used to image the sample and the size of the spheres was determined from an average of 30 spheres or greater.

6.1.2. Synthesis of Macroporous FTO Films[57]

Prior to use, the commercial FTO glass was cut to size (2 x 10 x 15 mm) and cleaned in piranha solution (3:1 H_2SO_4:H_2O_2) overnight before being rinsed with deionised water until neutral. Typically, 1 cleaned slide was stood vertically against the wall of a 7 mL glass vial and the polystyrene suspension from section 6.1.1. (3 mL) was added. The solution was evaporated overnight at 50 ˚C, resulting in a continuous opalescent polystyrene film over the FTO-glass.

FTO Precursor Solution was prepared by dissolving $SnCl_4.5H_2O$ (2.4 g) in ethanol (20 mL). A solution of NH_4F (aqueous, saturated, Table 6-1) was added to the $SnCl_4$ solution and sonicated until clear.

Table 6-1: Volume of NH_4F for different Sn:F ratios

Sn:F precursor Ratio	Volume of NH_4F added to 20 mL $SnCl_4.5H_2O$ in ethanol /g
0.00	0.00
0.25	0.12
0.50	0.24
0.75	0.36
1.00	0.48
1.50	0.72

The polystyrene film was soaked in ethanol for 1 hour before being immediately placed into the FTO precursor solution (3.5 mL) for 1 minute. A partial vacuum was then applied to the sample for 1 hour using a desiccator with the house vacuum applied for 1 minute before being sealed before being air dried until damp (approx. 1 min). 20 µL of fresh FTO solution was dropped onto the surface of the film and the sample was then immediately calcined; typical parameters were 450 ˚C for 2 hours, with a ramp rate of 1 ˚C min^{-1}. This method was developed by M Zhang.

6.1.3. Synthesis of Macroporous FTO Powders

Polystyrene solution from section 6.1.1. was centrifuged and the remaining pellet was dried at 50 ˚C overnight. This dry pellet was then gently crushed, using a mortar and pestle, into a coarse powder, ready for use.

Polystyrene powder (0.3 g) was soaked in FTO precursor solution (5 mL, Table 6-1) and air dried in a crucible overnight, before calcination. For non-templated powders, FTO precursor solution (5 mL, Table 6-1) was air dried overnight in a crucible before calcination. Both samples were then calcined at, typically, 450 ˚C for 2 hours, with a ramp rate of 1 ˚C min^{-1}.

6.1.4. Synthesis of Cadmium Sulphide Nanoparticles (CdS)[251]

CdO (12.80 mg) and oleic acid (0.847 g) were added to octadecene (3.1398 g) and heated to 300 ˚C. Sulfur (1.69 mg) suspended in octadecene (2.0 g) was then added to the hot mixture and held for 5 mins. To quench the reaction, the solution was cooled in an ice bath to r.t. When cool, the solution was split in half to aid the cleaning process, toluene (2 mL) was added to each, and the solution made up to 50 mL with ethanol. This suspension was centrifuged at 4400 rpm for 30 mins before being decanted and the washing repeated twice more. When clean the nanoparticles were suspended in toluene (~2 mL), ready for use. The resulting nanoparticles were < 10 nm in diameter, as determined by TEM, and the absorption onset of the nanoparticles was ~480 nm, determined by UV-vis spectroscopy.

6.1.4.1. Coating of FTO with CdS

Nanoparticle deposition: An FTO slide was soaked vertically in the CdS nanoparticle solution at 70 °C for 8 h resulting in a bright yellow-orange deposit on the film. The samples were then calcined in air at 400 °C for 2 h, with a ramp rate of 2 °C min^{-1}, to remove the surface ligands.

In situ deposition: An FTO film was first soaked vertically in a solution of $Cd(Ac)_2$ in ethanol (50 mM) for 1 min and dried under a stream of N_2. The film was then soaked in Na_2S for another 1 min, rinsed with distilled water and dried under N_2. This cycle was repeated from 1 to 10 times. The film was finally heated under argon at 400 °C for 30 min, with a ramp rate of 1 °C min^{-1}, producing bright yellow-orange samples.

6.1.5. Synthesis of $BiVO_4$

6.1.5.1. Nanoparticle Synthesis and Deposition

$Bi(NO_3)_3$ (2.425 g) and EDTA (1.465 g) was added to HNO_3 (40 mL, 2 mol dm^{-3}). The solution was sonicated until dissolved. In a separate flask, NH_4VO_3 (0.585 g) was added to HNO_3 (10 mL, 2 mol dm^{-3}). The two solutions were combined and decanted into hydrothermal bombs, which were then heated to 90°C for 6 hours at 1 °C min^{-1} before being cooled to room temperature. The nanoparticles were yellow in colour with a vivid blue supernatant. The supernatant was carefully drained off and the nanoparticles were cleaned by suspending them in ethanol (30 mL) and centrifuging for 30 minutes at 4000 rpm. This wash was repeated twice more with water and then the nanoparticles could either be dried, ready for use, or re-suspended in water (30 mL) ready for deposition onto FTO slides.

20 µL of the nanoparticle solution just described was deposited onto a slide (either macFTO or pFTO) and the liquid dried by evaporation. At this point the nanoparticle loading can be increased by deposition of further 20 µL aliquots. The samples were then calcined for 2 hours at 450 °C with a ramp rate of 1 °C min^{-1} before use.

6.1.5.2. In-Situ Deposition Method

$Bi(NO_3)_3$ (1.215 g) and EDTA (0.7325 g) were added to HNO_3 (25 mL, 2 M). The solution was sonicated until dissolved and NH_4VO_3 (0.2925 g) was added and dissolved. Samples of FTO were soaked in this solution for 1 min before being dried on a hot plate at 100 °C. The sample was then rinsed with deionised water and dried at 100 °C on a hot plate. This cycle was repeated from 1 to 10 times, to deposit further $BiVO_4$, after which the sample was typically calcined at 450 ˚C for 2 hours, with a ramp rate of 1 ˚C min^{-1}.

6.1.6. Deposition of Cobalt Phosphate Catalyst

The cobalt phosphate (CoPi) catalyst can be deposited in two ways from a solution of $Co(NO_3)_2$ in phosphate buffer. This Co^{2+} solution was used immediately, and could not be kept for future use.

Phosphate Buffer: Na_2HPO_4 (4.62 g) and NaH_2PO_4 (2.40 g) was added to Millipore water (500 mL). The phosphate concentration was 0.1 M and the pH was 7. The buffer was stable for use for several weeks.

Electrodeposition: An applied potential of +1 V vs Ag/AgCl was used for a set amount of time (Table 6-2 gives some examples) to deposit the catalyst. The sample was then rinsed with Millipore water and dried under a gentle flow of N_2.

Table 6-2: Time and current density examples for electrodeposition of CoPi

Time of deposition /s	Photocurrent density at +1 $V_{Ag/AgCl}$ on planar FTO / mA cm^{-2}	Photocurrent density +1 $V_{Ag/AgCl}$ on macFTO / mA cm^{-2}
0	0.0491	0.286
100	0.2020	0.597
200	0.1130	0.537
300	0.1110	0.507
400	0.0812	0.480
600	0.0464	0.515
800	0.0214	0.459
1000	0.0143	0.481
1300	0.0119	0.456

Photoelectrodeposition: An applied potential of +0.3 V vs Ag/AgCl was used in tandem with a 150 W Xe lamp, with a cut on filter at 420 nm, for a set amount of time (Table 6-3 gives some examples) to deposit the catalyst. The sample was then rinsed with Millipore water and dried under a gentle flow of N_2.

Table 6-3: Time and current density examples for photoelectrodeposition of CoPi

Time of deposition /s	Photocurrent density at +1 $V_{Ag/AgCl}$ on planar FTO / mA cm^{-2}	Photocurrent density +1 $V_{Ag/AgCl}$ on macFTO / mA cm^{-2}
0	0.00763	0.286
100	0.0989	0.863
200	0.0586	0.636
300	0.0500	0.656
400	0.0142	0.624
600	0.0177	0.519
800	0.0171	0.339
1000	0.0177	0.349
1300	0.0107	0.284

6.1.7. Immobilisation of Bis(2,2′-bipyridine)-4,4′-dicarboxybipyridine ruthenium(II) dichloride on FTO Surfaces

macFTO (either powdered or film) was taken and submerged in a solution of bis(2,2′-bipyridine)-4,4′-dicarboxybipyridine ruthenium(II) dichloride in ethanol (0.3 mM) for 6 hours. The FTO slide was then removed from the solution and dried (air, room temperature) before being rinsed with pure ethanol and dried once more. This was repeated 3 times to increase the loading of Rudcbpy on macFTO. The loading of Rudcbpy on mac-FTO films could not be confirmed by UV-vis as there was no obvious change to the UV-vis profile of the slide. Evidence for loading comes from the lifetime measurements, as this is a more sensitive technique and the lifetime value changed after loading the dye. For the macFTO-Rudcbpy powder there was far more macFTO than on pFTO slides (0.3 g on macFTO compared to < 1 mg on pFTO) so much more Rudcpby could be adsorbed and therefore UV-vis could be used to monitor the Rudcbpy loading. A maximum of 4 µM could be loaded onto 0.3 g of macFTO, this took 15 soak-dry cycles.

6.1.8. Immobilisation of Coumarin Dye on FTO Surfaces

20 µL of a mixture of coumarin 440 and coumarin 460 (0.20/0.25 g L^{-1} respectively) was deposited, via pipetting, onto the sample surface. The sample was allowed to dry before further depositions to total 100 µL of deposited solution. The sample was then ready for measurement. There was no change in colour of the slide and UV-vis could not confirm the loading on the slide. Evidence for loading comes from the lifetime measurements, as this is a more sensitive technique and the lifetime value changed after loading the dye. The solution had to be pipetted onto the surface in small aliquots as there is no anchoring group on coumarin to bind to the macFTO.

6.2. Characterisation Methods

6.2.1. Optical Properties

The techniques described in this section characterise both the powdered samples and the film samples (made as described above).

6.2.1.1. Diffuse Reflectance

Diffuse reflectance spectroscopy was used to characterise the optical properties of all photonic materials (films and powders). UV-vis spectra were recorded on an Ocean Optics HR2000+ High Resolution Spectrometer with DH-2000-BAL Deuterium/Helium light source (200-1100 nm). A R400-7-UV-Vis reflection probe was used to record diffuse reflectance spectra. Spectra were recorded in Spectra Suite software using, typically, an average of 10 scans with an integration time of 10 seconds and a box car smoothing width of 30.

6.2.1.2. UV-vis Spectroscopy

UV-vis spectroscopy was used to characterise the dyes, UV spectra were recorded on a Shimadzu UV 1800 with a resolution of 5 nm.

6.2.1.3. Fluorescence Spectroscopy

Fluorescence spectroscopy was used to characterise films and powders infiltrated with light absorbing materials. Spectra were recorded on a Hitachi F-4500 Fluorimeter at 60 nm min^{-1} at 25°C. The samples were illuminated at 45°.

The excitation spectrum of Rudcbpy samples were measured using an emission wavelength of 620 nm and the emission spectrum was measured with an excitation wavelength of 450 nm.

The PMT voltage was 700 V, the scan speed was 60 nm/min and the excitation/emission slit widths were 10 nm.

The excitation spectrum of coumarin samples was measured using an emission wavelength of 450 nm and the emission spectra were measured using an excitation wavelength of 415 nm. The PMT voltage was 700 V, the scan speed was 60 nm/min and the excitation/emission slit widths were 2.5 nm.

6.2.1.4. Lifetime Measurements

An Edinburgh Photonics FLS 980 fluorescence lifetime spectrometer was used to acquire data. Three pulsed light sources were used; a 380 nm pulsed LED with a bandwidth of 9.8 nm and a pulse width of 924.9 ps; a 470 nm pulsed diode laser with a pulse width of 71.4 ps and a 560 nm pulsed LED with a bandwidth of 11.2 nm and a pulse width of 1627.7 ps. The detector was a time correlated single photon counting (TCSPC) detector cooled to -23 °C $\pm$ 0.2°C. Spectra were measured at room temperature (21 $\pm$ 2 °C). Data was analysed in the software F980. Samples containing Rudcbpy were analysed using the 470 nm pulsed diode laser and samples containing coumarin were analysed using the 380 nm pulsed LED.

6.2.2. SEM/EDX

Scanning electron microscopy (SEM) was used to characterise the polystyrene spheres (sizing and packing), films and powders (macropore quality etc.). Images were gained using an FEI Sirion scanning electron microscope at a voltage of 5 keV. Energy dispersive x-ray (EDX) was used to determine the composition for the samples using an EDAX Phoenix EDS X-ray spectrometer. A voltage of 15 KeV was used to analyse samples with a 30 second exposure time.

An electrode was typically stuck to an aluminium stub using carbon sticky tape. For powdered samples, a small amount of powder was stuck to the carbon sticky tape. Samples containing polystyrene and $BiVO_4$ were coated with a 10 nm layer of carbon to increase conductivity and therefore resolution.

6.2.3. Structural Analysis

6.2.3.1. XRD

X-ray diffraction (XRD) was also used to indirectly determine the composition of samples using a Bruker-AXS D8 Advance instrument fitted with a Lynx eye detector. The source was Cu Kα

(1.54 Å) with a 1mm slit on the source, and a 2.5 mm slit on the detector. Data was collected from 5 to 90 ° 2θ with a 0.02° step size and a scan speed of 0.1 s per step. Once the data file was acquired it was compared to the ICSD database (JCPDS file numbers are quoted with the relevant data in text).

6.2.3.2. Solid State ^{19}F NMR

For each experiment approximately 100 mg of sample as analysed. Each set of data was then normalised for the quantity of material used.

^{19}F spectra were acquired using a rotor synchronised (ν_{rot} = 10 kHz, one rotor-period) Hahn-echo experiment, using 90- and 180-degree pulse lengths of 2.5 and 5 µs, respectively. PEEK (polyether ether ketone) inserts were utilized to centre the sample within the rotor, ensuring the whole of the sample was within the active region of the detection coil. All ^{19}F chemical shifts are reported relative to $CFCl_3$ and were referenced using solid sodium fluoride (δ_{iso} = -104.2 ppm) as an external secondary reference.

Calcium fluoride dilute with sodium chloride was used as a calibrant (fluorine content 6.9 x 10^{-7} to 3.2 x 10^{-5} moles), and required 16-200 co-added scans, with a 300 s delay between scans to avoid saturation, to generate spectra. FTO samples required 160-320 co-added scans, with a 20 s pulse delay.

Hahn-echo experiments with inter-pulse delays of one to seven rotor periods (total evolution times of 200 to 1400 µs) were acquired to determine the spin-spin relaxation time constant T_2 of calcium fluoride and one sample of FTO in order to correct for signal intensity loss during the Hahn-echo evolution periods. It is assumed that the T_2 is very similar for all FTO samples.

The quality factor (Q) of the impendence-matched probe circuitry was measured using a Wavetek Benchmark 1150 spectrum analyser for all samples as a measure of the intrinsic sensibility of the probe in order to calculate the necessary 90 and 180-degree pulses for each sample and correct measured absolute integrals in analogy to the PULCON method.[276]

6.2.4. (Photo)Electrochemistry

Electrochemical analysis was used to characterise the surface qualities of the films as well as the water splitting capabilities of the electrodes. A BASi Epsilon-EC potentiostat was used to perform all electrochemical experiments. All electrochemical analysis was carried out in a faraday cage, which also served as a black box. Samples were illuminated from the back of the electrode with a 300 W Xe lamp, with a cut-off filter at 420 nm, to ensure only visible light was used. A liquid light guide (40 cm long) was used to centre the light on the electrode, which was positioned as close to the sample as possible, typically at a distance of 1-2 cm. This allowed for the entire sample to be illuminated (1 cm^2), unless otherwise stated.

Electrolyte solutions were prepared using Millipore water (18.2 MΩ cm^{-3}). The electrolyte was degassed with N_2 for 20 minutes prior to use. CdS containing samples were typically measured in aqueous Na_2S/Na_2SO_3 (0.25/0.35 M, 40 mL). All other samples were measured in phosphate buffer (0.1 M, pH7, 40 mL).

6.2.4.1. Standard Cell

In a standard setup, a three electrode system was typically used (Figure 6-1): the reference electrode was Ag/AgCl (3 M NaCl), the counter electrode was a Pt wire (20 mm long by 0.25 mm diameter), and working electrodes were fabricated as described above (section 6.1.). Connection to the working electrode was established using a piece of copper tape, which was wrapped around the bare end of the FTO glass. A crocodile clip was then attached to this.

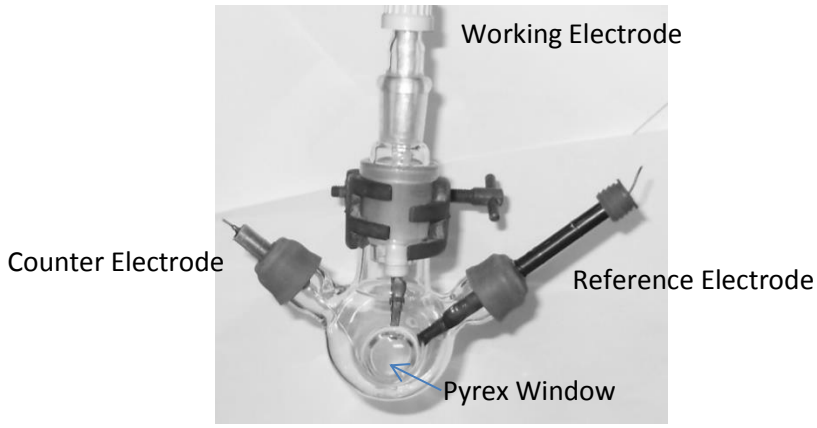

Figure 6-1: Glass cell for electrochemical measurements.

A Pyrex window (diameter 1.5 cm) centred in the middle of the cell (over the working electrode) was used to illuminate the sample with the Xe lamp.

6.2.4.2. Gas Evolution Measurements in a Two Compartment Cell

In a separate 2 compartment cell (Figure 6-2), the gas evolution properties of the electrodes were measured. An Ag/AgCl reference electrode (3 M NaCl) was countered with Pt foil (surface area = 1.4 cm^2). Oxygen evolution occurred in the large compartment (liquid volume = 20 mL, headspace = 20 mL). The two compartments were separated with a Nafion membrane, spun onto a sinter, porosity 4. This side had a liquid volume of 1 mL and a headspace of 10 mL. An inverted burette was used to measure the evolved gas on each half reaction.

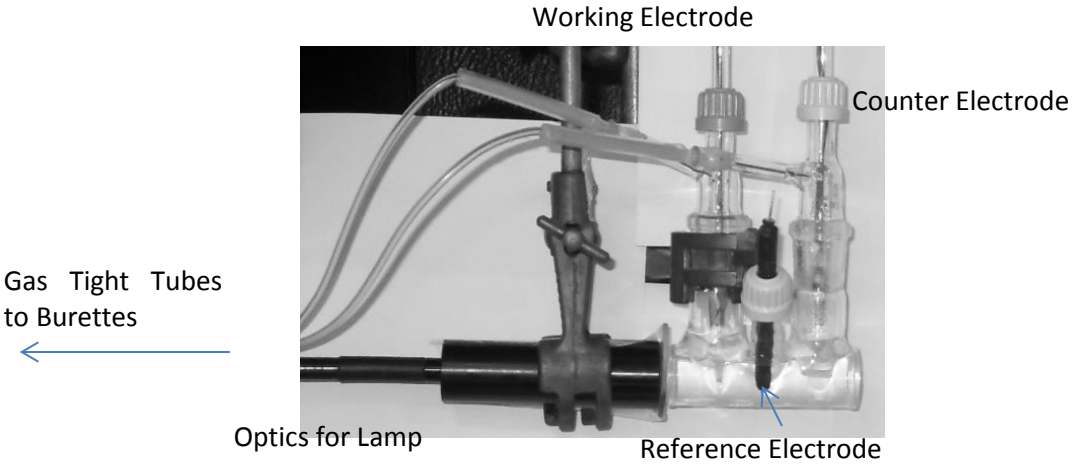

Figure 6-2: Gas evolution cell

6.2.4.3. IPCE Measurements

IPCE measurements were done in a quartz cell (Figure 6-3) with an Ag/AgCl reference electrode (3 M NaCl) and a Pt counter electrode (20 mm long by 0.25 mm diameter). Samples were illuminated with monochromated light with a slit width of 20 nm. The lamp power was measured using an International Light Technologies 1400-A Radiometer Photometer. The cell window was in contact with the filter (Figure 6-2), the electrode was 1 cm from the window to reduce the amount of scattered light.

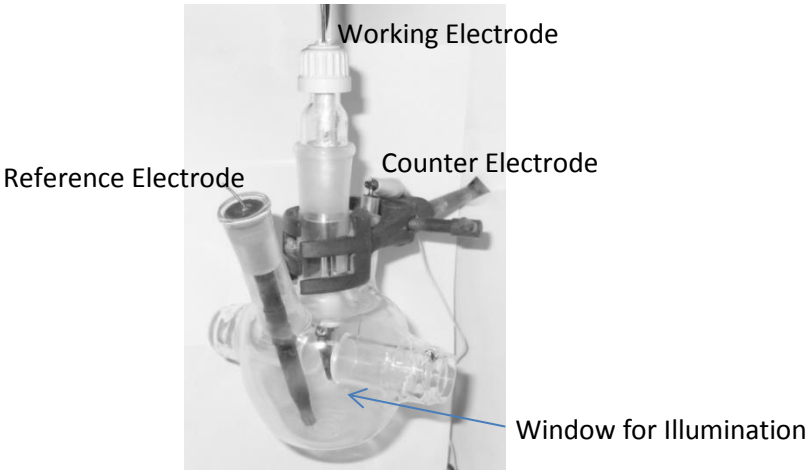

Figure 6-3: Quartz cell for IPCE measurements

Chapter 7
Appendix

Chapter 7. Appendix

This appendix is organised by chapter number. Any relevant data is organised by chapter, and then in order that it appears in the main text.

7.1. Chapter 1: Introduction

No further information.

7.2. Chapter 2: Fabrication and Characterisation of FTO Electrodes

7.2.1. Surface area calculation for macFTO

Table 7-1: Surface area enhancement calculation using the typical dimensions of a macFTO electrode. The electrode height and length were measured using a caliper, the pore diameter and electrode height were measured using the SEM images.

Electrode height (m)	1×10^{-5}
Electrode length (m)	0.01
Electrode width (m)	0.01
Geometric surface area (m^2)	$(0.01 \times 0.01) + (4 \times 0.01 \times 1 \times 10^{-5})$ 1.004×10^{-4}
Pore diameter (m)	4.5×10^{-7}
Surface area of 1 pore (m^2)	$4\pi r^2$ $4 \times \pi \times (2.25 \times 10^{-7})^2$ 6.36×10^{-13}
Number of pores in macFTO	Length x width x height 22 222 x 22 222 x 22 10973936900
Total area of macFTO (m^2)	$10973936900 \times 6.36 \times 10^{-13}$ 0.00698
Surface area enhancement	$0.00524 / 4.5 \times 10^{-7}$ 69.54

7.2.2. Planar samples as a function of fluorine content

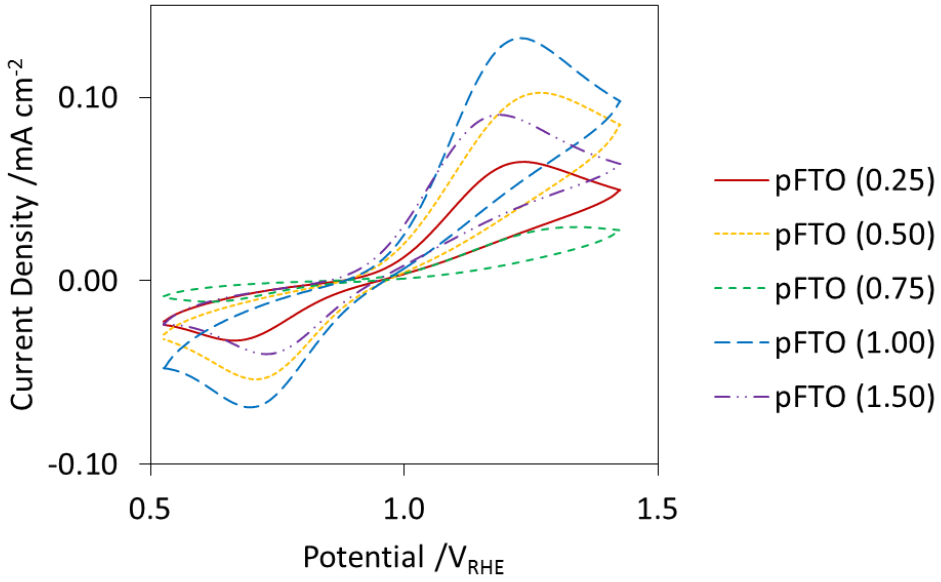

Figure 7-1: CV of pFTO samples with different precursor Sn:F ratio, measured in ferrocene to determine the change in conductivity of the samples.

Table 7-2: Electrochemical parameters for the FTO samples as a function of fluorine content.

Sample	E_a /V_{RHE}	E_c /V_{RHE}	ΔE_p /V	$E_{1/2}$ /V	I_a / mA	I_c / mA
pFTO-comm	1.300	0.873	0.427	1.087	0.113	-0.047
pFTO-0.25	1.214	0.641	0.573	0.928	0.068	-0.033
pFTO-0.5	1.269	0.689	0.580	0.979	0.106	-0.054
pFTO-0.75	1.345	0.600	0.745	0.973	0.030	-0.011
pFTO-1.0	1.203	0.678	0.525	0.941	0.136	-0.069
pFTO-1.5	1.146	0.509	0.637	0.828	0.093	-0.062
Averages	1.235	0.623	0.612	0.929	0.087	-0.046

7.2.3. XRD Spectra

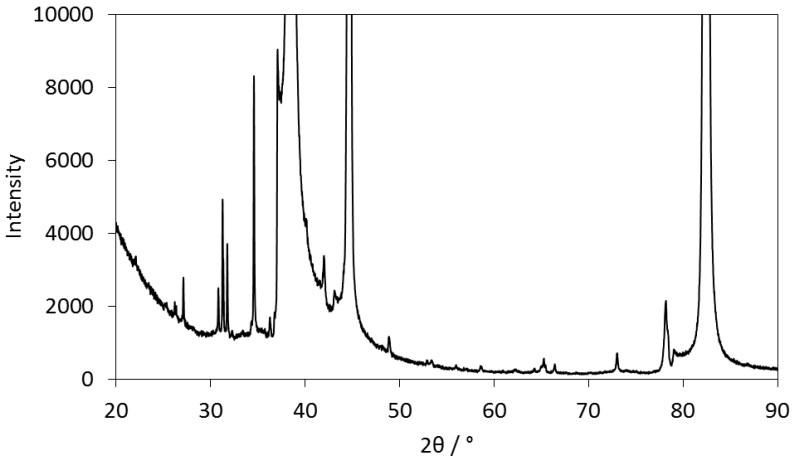

Figure 7-2: XRD of the aluminium holder

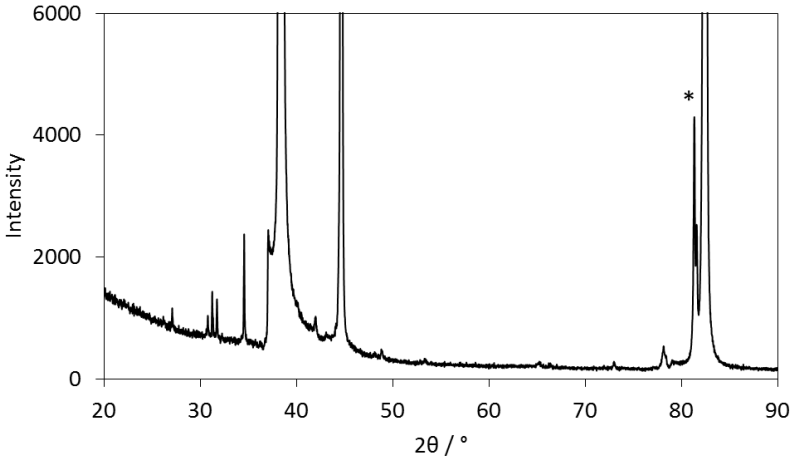

Figure 7-3: XRD of the silica backing glass in the aluminium holder, with peaks due to SiO_2 labelled (*)

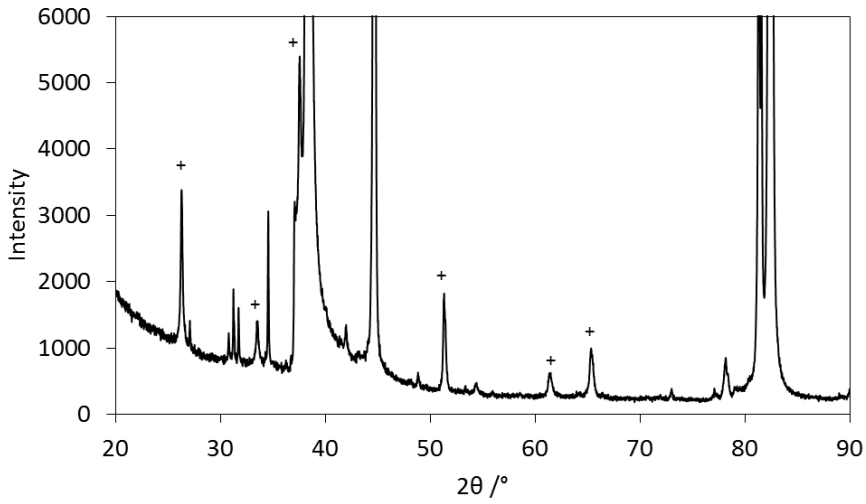

Figure 7-4: XRD of the planar FTO on silica backing glass in the aluminium holder; peaks due to FTO are labelled (+)

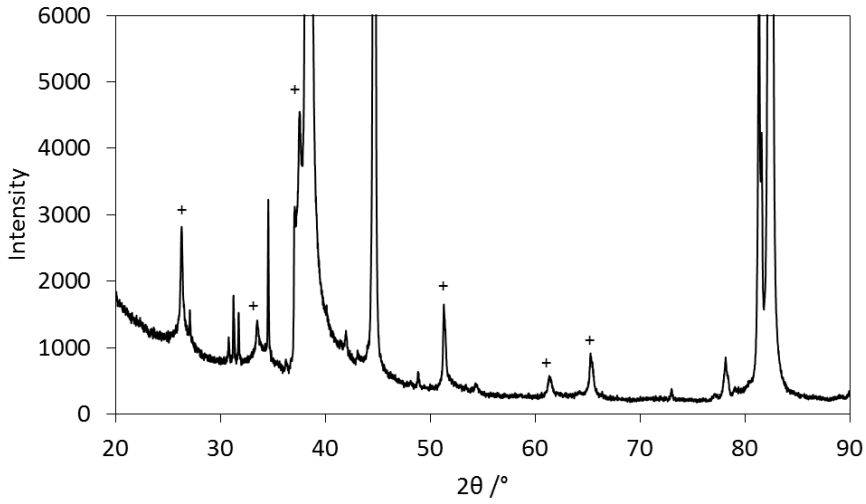

Figure 7-5: XRD of the macFTO on silica backing glass in the aluminium holder; peaks due to FTO are labelled (+)

7.2.4. Method for calculating the capacitance

The capacitance for all samples was determined using an electrochemical technique. A geometric area of 1 cm^{-2} was submerged in a solution of KCl (0.1 M). Each sample was scanned from -0.5 V to +1.0 V and back to -0.5 V (1 scan) at different scan rates (10, 20, 40, 60, 80 and 100 mV s^{-1}), this was repeated 4 times (Figure 7-6, pFTO at 100 mV s^{-1}). For each scan the forwards (anodic) and backwards (cathodic) currents were averaged for each potential (Figure 7-7). This average was then subtracted from both the anodic and cathodic scans (Figure 7-8). This allowed the removal of faradaic current, giving a more accurate measurement of the capacitance.

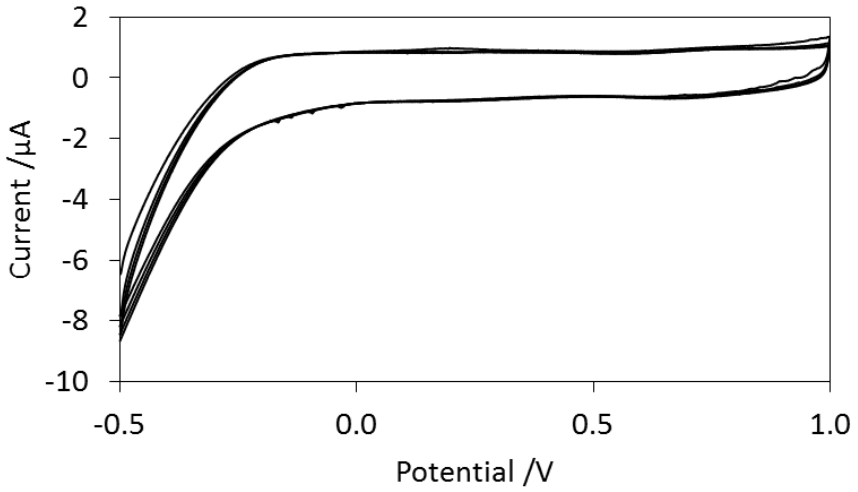

Figure 7-6: First 4 cycles of the CV of pFTO in 0.1 M KCl, which was used to determine the capacitance. Each trace nearly perfectly superimposes over the previous trace, suggesting that the sample is very stable over this measurement range.

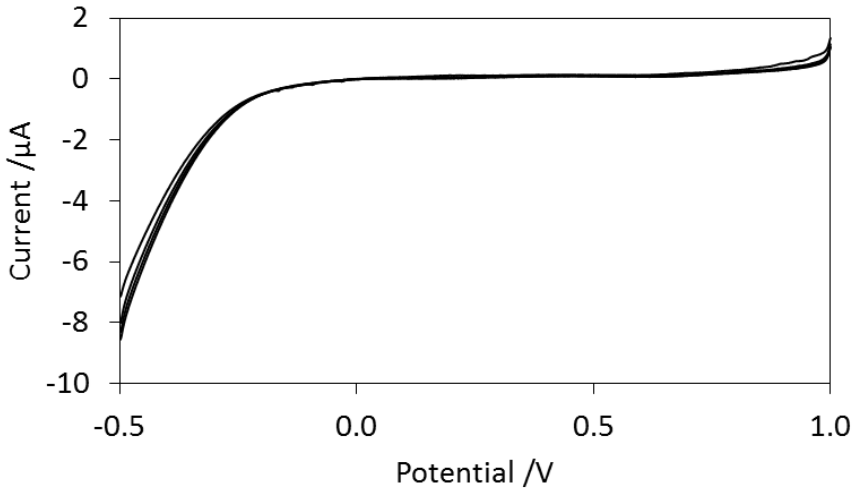

Figure 7-7: Averaged CV trace for pFTO for the first 4 scans.

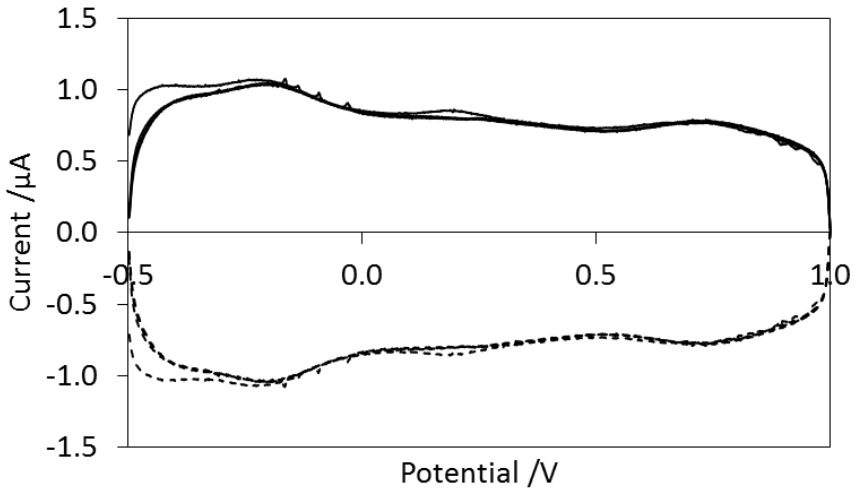

Figure 7-8: Residual current when the averaged scan (Figure 7-7) is subtracted from the raw data (Figure 7-6)

The average current for the anodic and cathodic scans was then taken, and averaged again with the other 3 scans from the same sample. This value was then plotted versus scan speed, with the values from the other scan speeds, producing a linear correlation of current vs. scan speed, the gradient of which is the capacitance (in Coulombs) (Figure 7-9), according to the definition of capacitance:

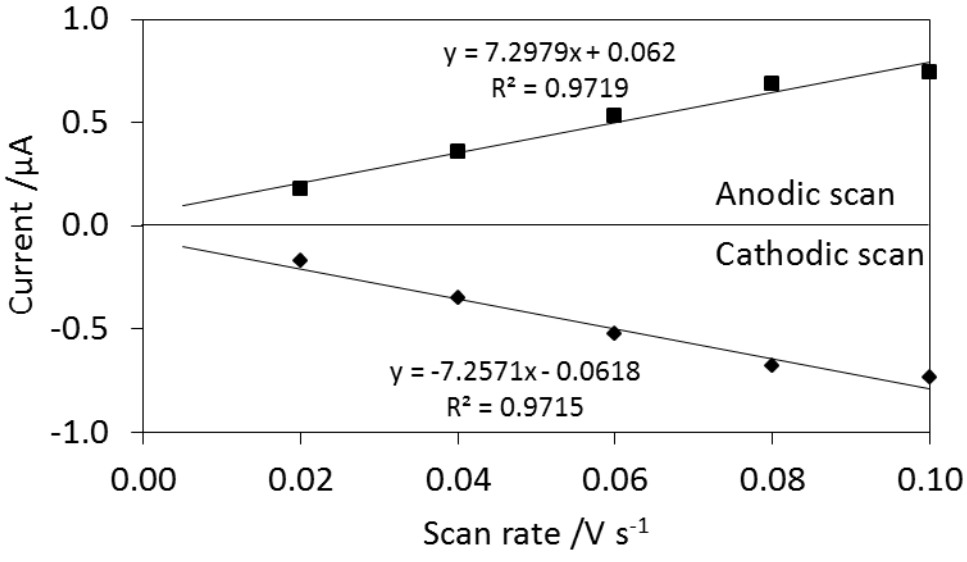

Figure 7-9: Trumpet plot of the average current for pFTO as a function of scan speed. The linearity suggests that the sample is not diffusion controlled.

7.2.5. NMR data – Q values etc

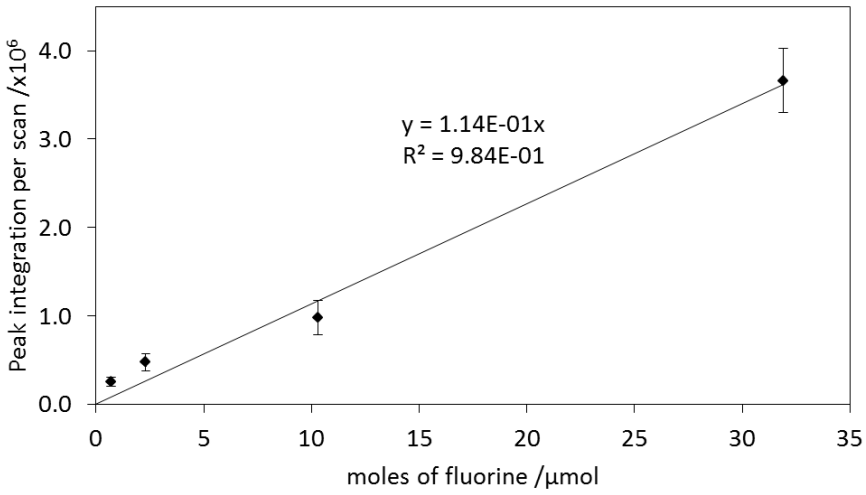

Figure 7-10: Calibration for the fluorine content of FTO samples using CaF_2 in NaCl

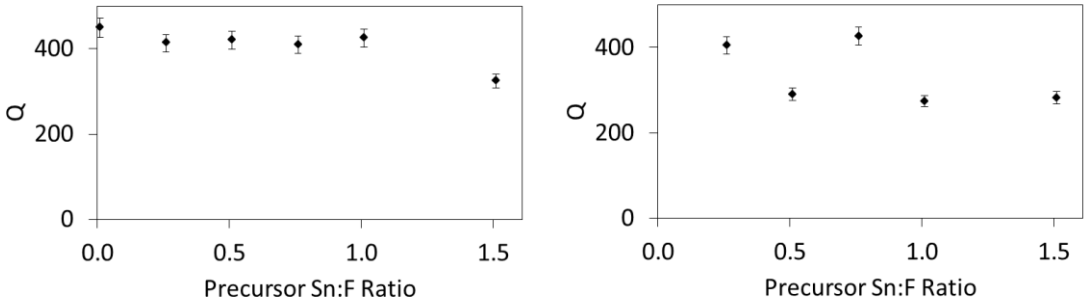

Figure 7-11: Quality factor (Q) for non-templated FTO samples (left) and templated samples (right)

7.2.6. Photoactivity

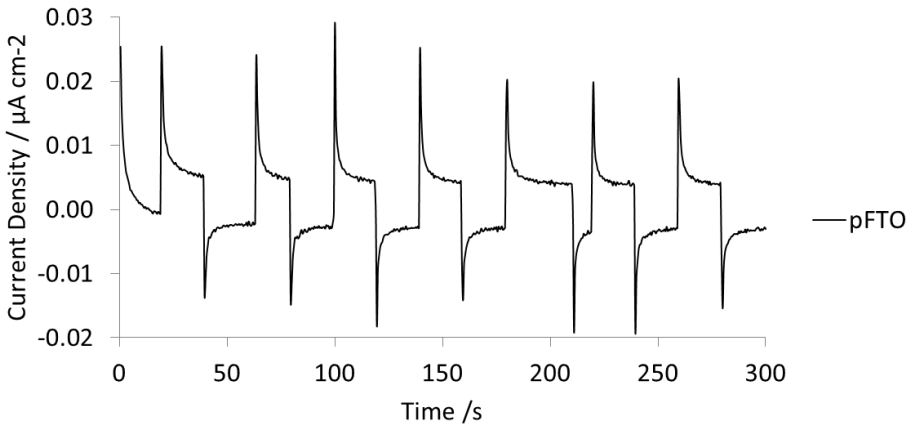

Figure 7-12: Photoactivity of pFTO samples, measured in 0.1 M KCl at 0 $V_{Ag/AgCl}$

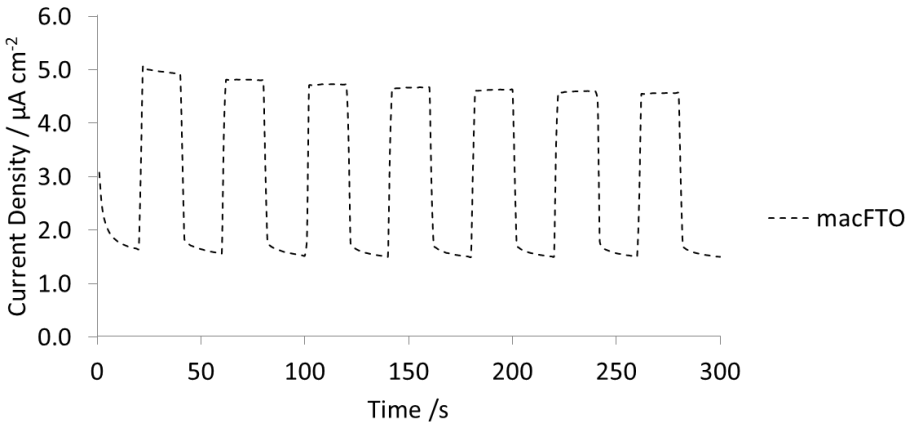

Figure 7-13: Photoactivity of macFTO measured in 0.1 M KCl at 0 $V_{Ag/AgCl}$

7.3. Chapter 3: Angular Dependence of macFTO Photoelectrodes

7.3.1. Diffuse Reflectance Data

$$\lambda = \frac{2d_{hkl}}{m}\sqrt{{n_{av}}^2 - \sin^2\theta}$$

Table 7-3: DR data at different angles of illumination

Angle of Incidence (°)	Position of peak (nm) for each allowed plane			
	111	200	220	311
90	678.7	587.8	415.6	354.4
85	677.2	586.4	414.7	353.6
80	672.6	582.5	411.9	351.3
75	655.1	576.0	407.3	347.3
70	654.7	567.0	400.9	341.9
65	641.8	555.8	393.0	335.1
60	626.4	542.5	383.6	327.1
55	608.9	527.3	372.9	318.0
50	589.8	510.7	361.1	308.0
45	569.3	493.0	348.6	297.3
40	548.1	474.6	335.6	286.2
35	526.7	456.1	322.5	275.1
30	505.8	438.0	309.7	264.1
25	486.1	421.0	297.7	253.9
20	468.1	405.7	286.9	244.7
15	453.7	392.9	277.8	236.9
10	442.5	383.2	271.0	231.1
5	435.5	377.1	266.7	227.4
0	433.1	375.1	265.2	226.2

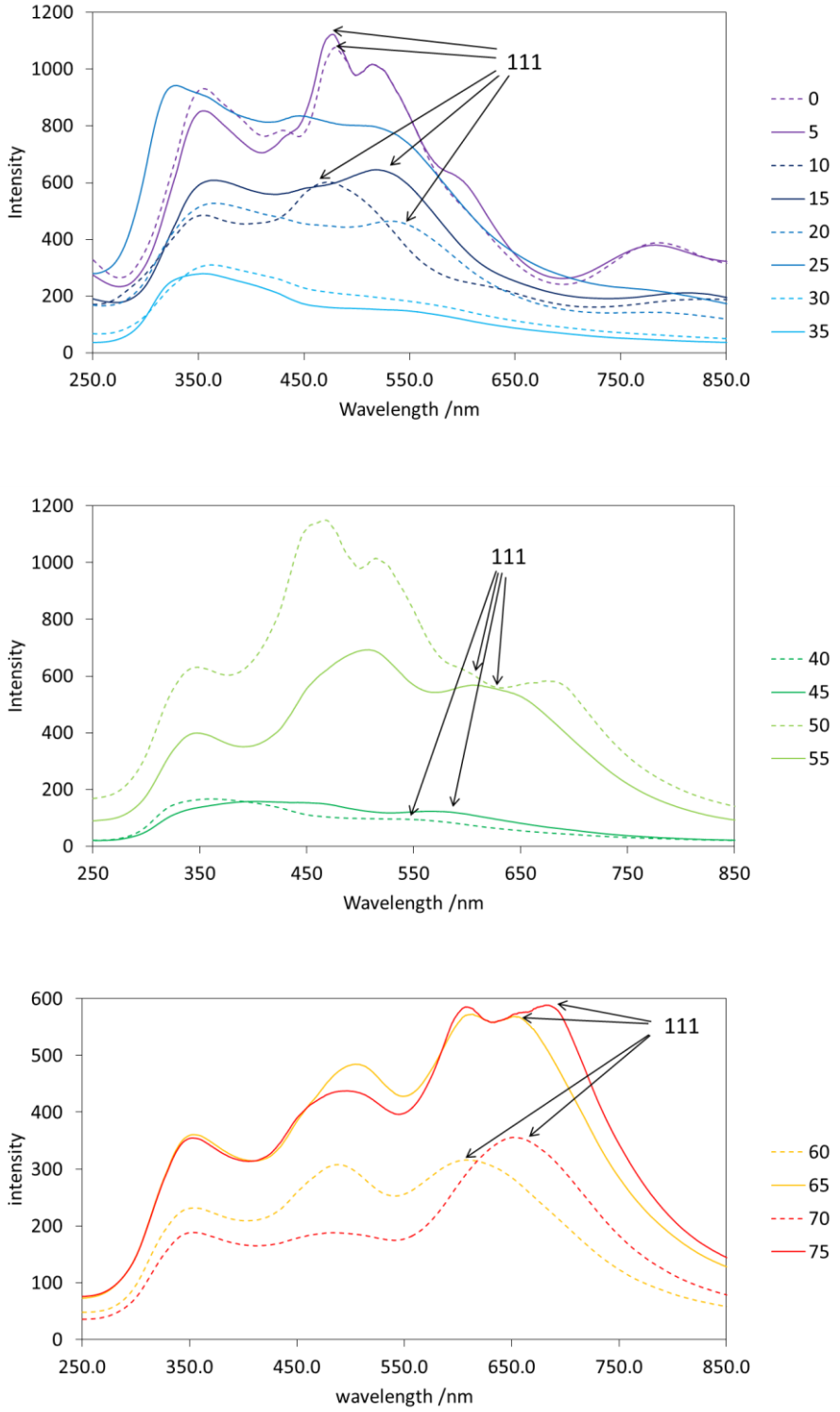

Figure 7-14: All raw data for macFTO as a function of incident angle,

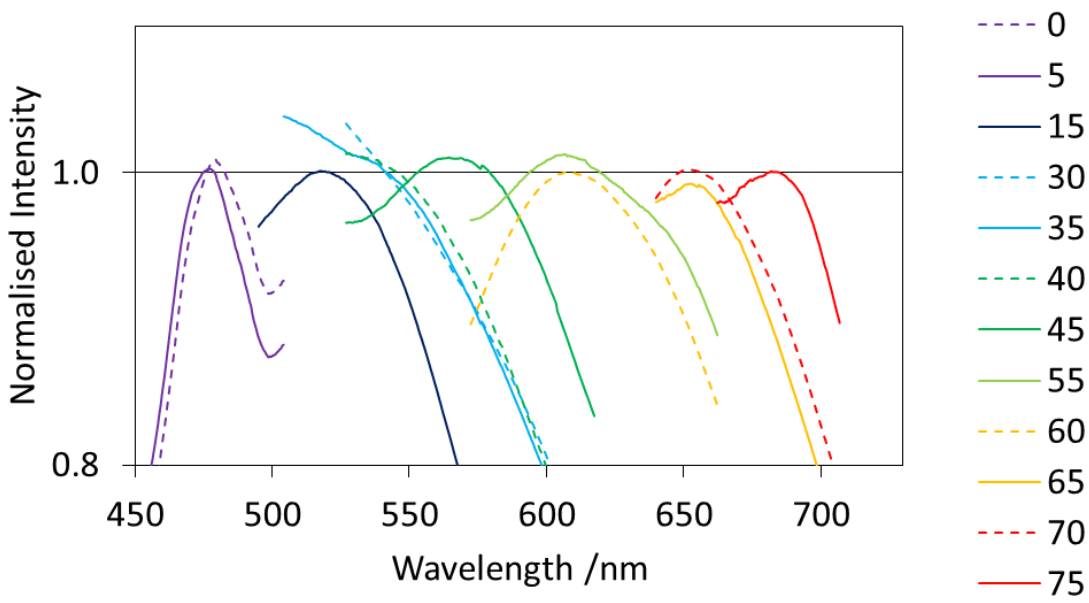

Figure 7-15: Cropped and normalised diffuse reflectance data for macFTO, tracking the [111] plane

7.3.2. Lifetime fits

For solution samples, the instrument response function (IRF) was measured using a solution of Ludox. The data was then fitted using the IRF with a reconvolution fit. The data fitted equally well when using a tail fit method (which excludes the portion of data that overlaps with the IRF).

For solid state samples the IRF was measured using either a blank sample of pFTO or macFTO. The data was the fitted using a tail fit

In each of the following data sets:

A = background noise

Relative % 1/2 = the contribution of the signal to the total decay

Table 7-4: Fitted Parameters Rudcbpy in ethanolic solution

Rudcbpy Solution							
τ_1 /ns	366.54 ± 0.316	B_1	9780 ± 8.486	Relative % 1	100	A	10.0
τ_2 /ns	-	B_2	-	Relative % 2	-	χ^2	1.124

Table 7-5: Fitted parameters for Coumarin 440/460 in ethanolic solution

Coumarin 440/460 Solution – single exponential fit							
τ_1 /ns	3.50 ± 0.002	B_1	6524 ± 43.78	Relative % 1	100	A	29.13
τ_2 /ns	-	B_2	-	Relative % 2	-	χ^2	1.186
Coumarin 440/460 Solution – bi-exponential fit							
τ_1 /ns	3.18 ±	B_1	±	Relative % 1		A	
τ_2 /ns	3.74 ±	B_2	±	Relative % 2		χ^2	1.105

Table 7-6: Lifetime data and fits for pFTO-Rudcbpy

pFTO-Rudcbpy							
5°							
τ_1 /ns	61.80 ± 4.16	B_1	204.00 ± 9.53	Relative % 1	14.94	A	1.37
τ_2 /ns	310.40 ± 12.83	B_2	231.30 ± 10.85	Relative % 2	85.06	χ^2	0.982
10°							
τ_1 /ns	61.21 ± 2.78	B_1	376.90 ± 12.35	Relative % 1	20.28	A	1.05
τ_2 /ns	278.50 ± 9.47	B_2	325.70 ± 14.07	Relative % 2	79.72	χ^2	0.979
15°							
τ_1 /ns	66.51 ± 4.89	B_1	192.80 ± 11.10	Relative % 1	17.49	A	1.05
τ_2 /ns	301.80 ± 15.44	B_2	200.50 ± 12.52	Relative % 2	82.51	χ^2	1.002
20°							
τ_1 /ns	74.84 ± 19.42	B_1	22.48 ± 5.32	Relative % 1	17.58	A	0.51
τ_2 /ns	315.90 ± 59.61	B_2	24.96 ± 588	Relative % 2	82.42	χ^2	1.112
25°							
τ_1 /ns	62.02 ± 10.59	B_1	32.13 ± 3.76	Relative % 1	14.19	A	0.41
τ_2 /ns	321.90 ± 33.67	B_2	37.46 ± 4.28	Relative % 2	85.81	χ^2	1.087
30°							
τ_1 /ns	36.55 ± 8.07	B_1	16.83 ± 1.90	Relative % 1	7.67	A	0.44
τ_2 /ns	230.10 ± 10.79	B_2	32.20 ± 1.80	Relative % 2	92.33	χ^2	1.128
35°							
τ_1 /ns	41.37 ± 7.91	B_1	25.20 ± 2.61	Relative % 1	8.22	A	0.51
τ_2 /ns	230.90 ± 10.00	B_2	50.38 ± 2.74	Relative % 2	91.78	χ^2	1.114
40°							
τ_1 /ns	61.62 ± 11.25	B_1	33.04 ± 3.96	Relative % 1	10.28	A	0.49
τ_2 /ns	350.50 ± 31.38	B_2	50.71 ± 4.51	Relative % 2	89.72	χ^2	1.061

45°							
τ_1 /ns	60.76 ± 8.33	B_1	72.16 ± 8.76	Relative % 1	16.49	A	0.73
τ_2 /ns	219.30 ± 12.92	B_2	101.30 ± 9.76	Relative % 2	83.51	χ^2	0.986
50°							
τ_1 /ns	65.10 ± 16.06	B_1	20.75 ± 3.75	Relative % 1	12.18	A	0.38
τ_2 /ns	324.50 ± 41.36	B_2	30.01 ± 4.25	Relative % 2	87.82	χ^2	1.175
55°							
τ_1 /ns	62.90 ± 8.23	B_1	56.56 ± 5.53	Relative % 1	17.07	A	0.41
τ_2 /ns	286.80 ± 23.89	B_2	60.27 ± 6.27	Relative % 2	92.93	χ^2	0.959
60°							
τ_1 /ns	67.81 ± 7.12	B_1	108.30 ± 8.81	Relative % 1	14.60	A	1.05
τ_2 /ns	324.10 ± 21.26	B_2	132.50 ± 9.93	Relative % 2	85.40	χ^2	1.039
65°							
τ_1 /ns	60.46 ± 11.20	B_1	24.53 ± 3.05	Relative % 1	15.00	A	0.38
τ_2 /ns	317.80 ± 38.09	B_2	26.44 ± 3.46	Relative % 2	85.00	χ^2	1.138
70°							
τ_1 /ns	64.44 ± 6.51	B_1	131.90 ± 10.24	Relative % 1	12.29	A	0.87
τ_2 /ns	296.30 ± 13.70	B_2	204.70 ± 11.54	Relative % 2	87.71	χ^2	1.039
75°							
τ_1 /ns	63.82 ± 4.50	B_1	229.20 ± 13.63	Relative % 1	18.73	A	1.21
τ_2 /ns	250.50 ± 10.35	B_2	253.30 ± 15.27	Relative % 2	81.27	χ^2	1.075
80°							
τ_1 /ns	88.25 ± 13.96	B_1	69.61 ± 11.09	Relative % 1	21.42	A	0.40
τ_2 /ns	389.90 ± 73.61	B_2	57.80 ± 12.05	Relative % 2	78.58	χ^2	0.975
85°							
τ_1 /ns	64.53 ± 1.95	B_1	1405 ± 21.75	Relative % 1	12.23	A	0.80
τ_2 /ns	328.10 ± 13.96	B_2	1984 ± 582.70	Relative % 2	87.77	χ^2	1.247

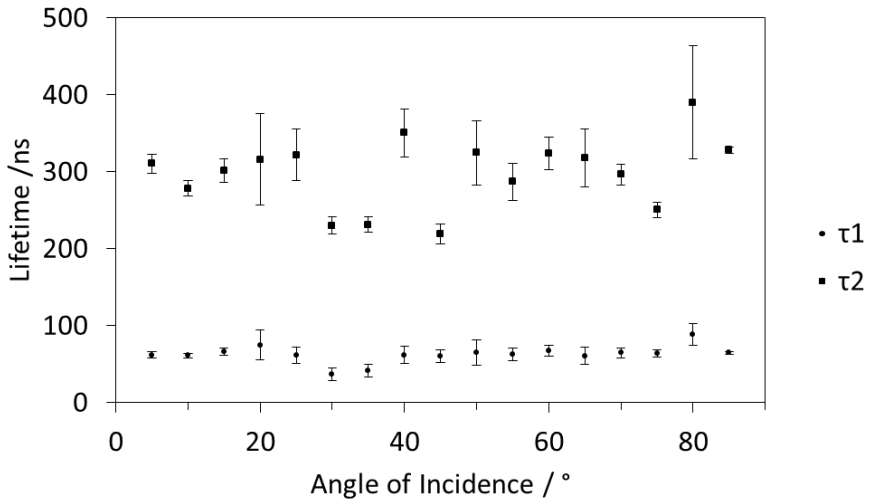

Figure 7-16: Lifetime values for pFTO-Rudcbpy as a function of angle of incidence

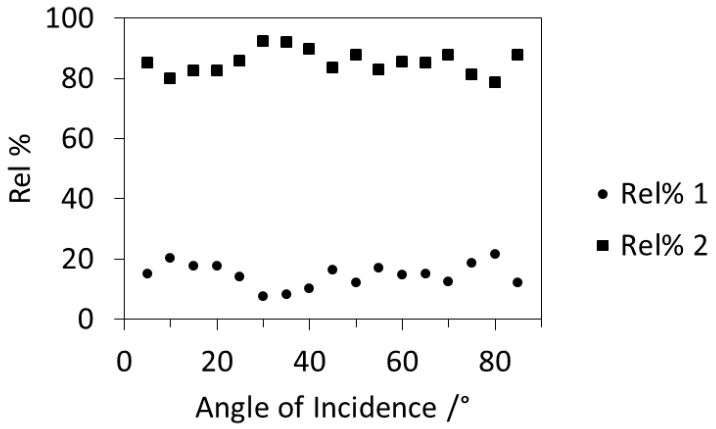

Figure 7-17: Relative percentage contribution of each lifetime of pFTO-Rudcbpy as a function of angle of incidence

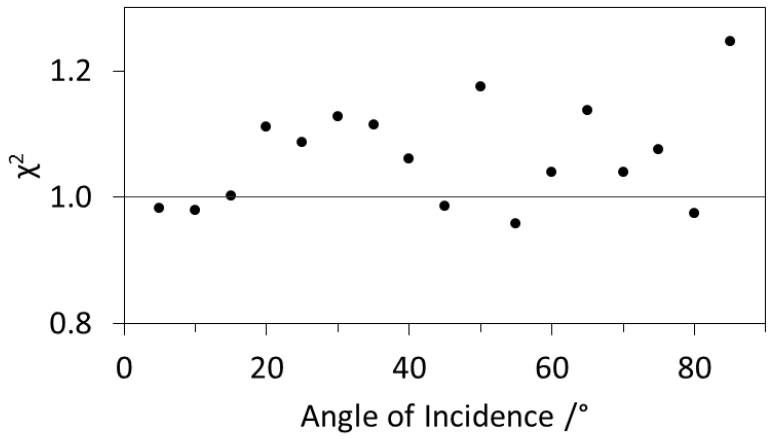

Figure 7-18: Quality of lifetime fit (χ^2) for pFTO-Rudcbpy as a function of angle of incidence

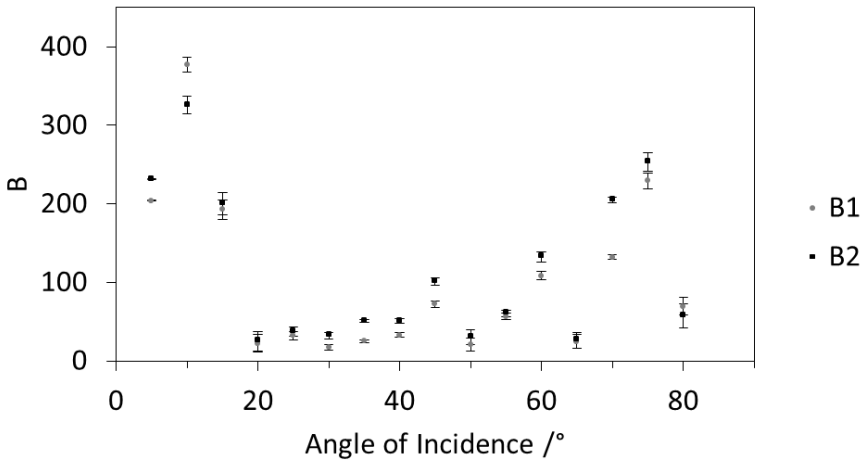

Figure 7-19: Pre-exponential factor (B) for pFTO-Rudcbpy as a function of angle of incidence

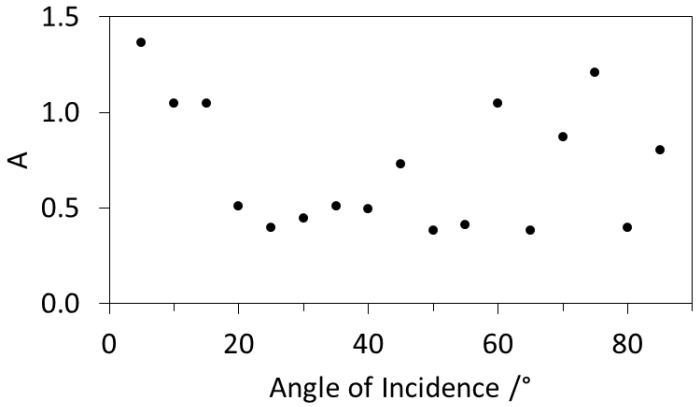

Figure 7-20: Background noise level (A) for pFTO-Rudcbpy as a function of angle of incidence

There are two components to the lifetime of pFTO-Rudcbpy: the first, smaller average lifetime was found to be 62.6 $\pm$ 8.6 ns. The second, longer, average lifetime was found to be 300 $\pm$ 25.4 ns.

Table 7-7: Lifetime data and fits for macFTO-Rudcbpy

macFTO-Rudcbpy							
5°							
τ_1 /ns	412.90 ± 5.13	B_1	433.40 ± 2.42	Relative % 1	100	A	20.42
						χ^2	1.063
10°							
τ_1 /ns	406.10 ± 5.89	B_1	98.17 ± 1.30	Relative % 1	100	A	20.65
						χ^2	1.119
15°							
τ_1 /ns	413.80 ± 7.81	B_1	198.40 ± 1.66	Relative % 1	100	A	12.16
						χ^2	1.1003
20°							
τ_1 /ns	448.30 ± 29.11	B_1	22.25 ± 0.55	Relative % 1	100	A	2.12
						χ^2	1.087
25°							
τ_1 /ns	394.60 ± 9.29	B_1	34.22 ± 0.75	Relative % 1	100	A	5.88
						χ^2	1.209
30°							
τ_1 /ns	465.40 ± 12.77	B_1	32.14 ± 0.75	Relative % 1	100	A	10.16
						χ^2	1.143
35°							
τ_1 /ns	440.70 ± 14.46	B_1	16.38 ± 0.49	Relative % 1	100	A	2.56
						χ^2	1.180
40°							
τ_1 /ns	378.80 ± 7.57	B_1	65.54 ± 1.15	Relative % 1	100	A	20.53
						χ^2	1.240

45°							
τ_1 /ns	451.10 ± 13.33	B_1	25.74 ± 0.66	Relative % 1	100	A	6.94
						χ^2	1.138
50°							
τ_1 /ns	424.80 ± 22.73	B_1	27.26 ± 0.61	Relative % 1	100	A	2.09
						χ^2	1.140
55°							
τ_1 /ns	385.40 ± 19.2	B_1	29.23 ± 0.68	Relative % 1	100	A	3.00
						χ^2	1.157
60°							
τ_1 /ns	388.20 ± 20.67	B_1	28.84 ± 0.69	Relative % 1	100	A	3.92
						χ^2	1.238
65°							
τ_1 /ns	502.50 ± 9.717	B_1	39.71 ± 0.71	Relative % 1	100	A	3.62
						χ^2	1.104
70°							
τ_1 /ns	432.30 ± 6.996	B_1	39.71 ± 0.69	Relative % 1	100	A	0.25
						χ^2	1.204
75°							
τ_1 /ns	360.30 ± 11.37	B_1	24.68 ± 0.70	Relative % 1	100	A	6.54
						χ^2	1.241
80°							
τ_1 /ns	414.70 ± 10.33	B_1	52.37 ± 1.08	Relative % 1	100	A	25.26
						χ^2	1.049
85°							
τ_1 /ns	483.80 ± 29.25	B_1	33.75 ± 0.69	Relative % 1	100	A	4.43
						χ^2	1.178

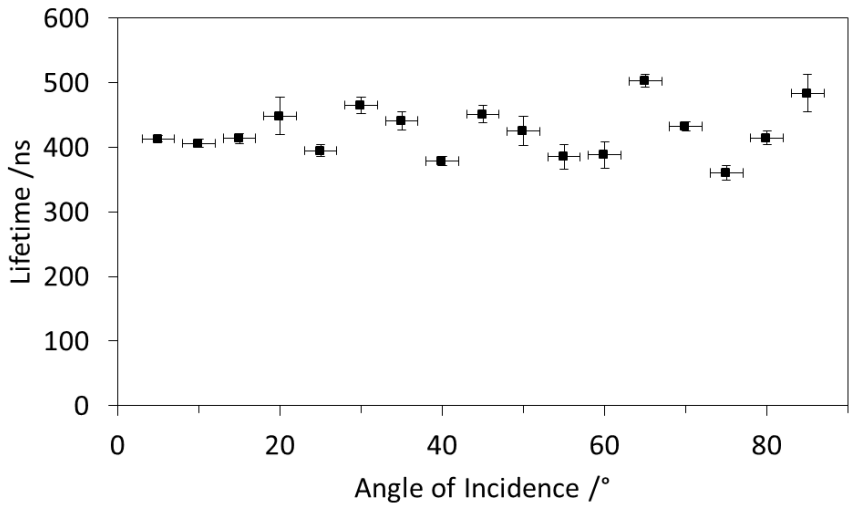

Figure 7-21: Lifetime values for macFTO-Rudcbpy as a function of angle of incidence

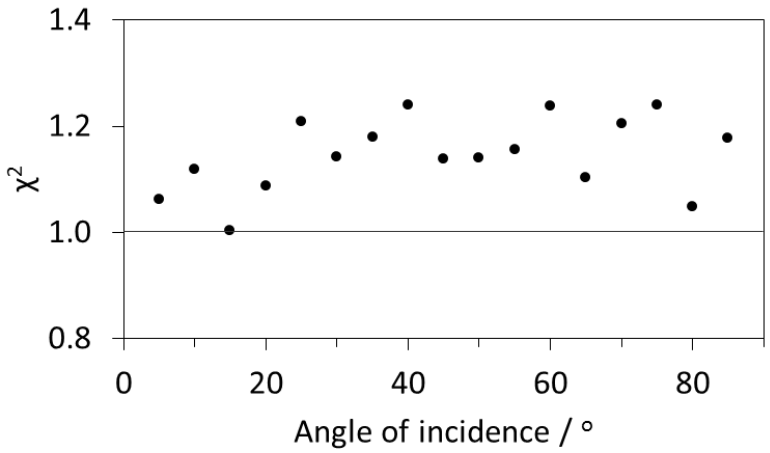

Figure 7-22: Quality of lifetime fit (χ^2) for macFTO-Rudcbpy as a function of angle of incidence

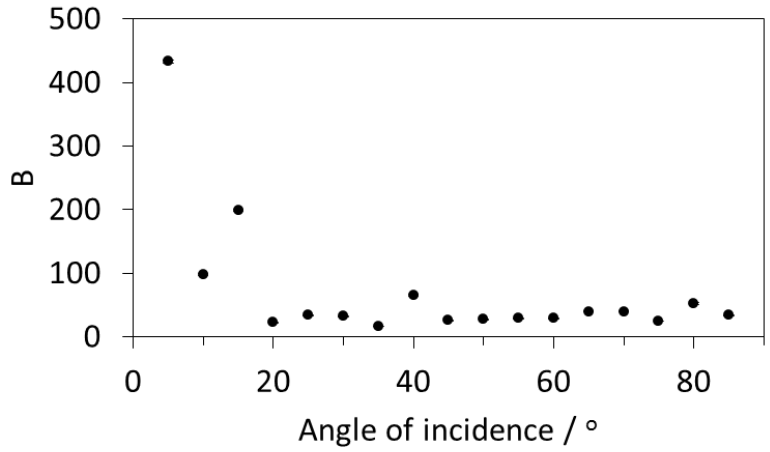

Figure 7-23: Pre-exponential factor (B) for macFTO-Rudcbpy as a function of angle of incidence

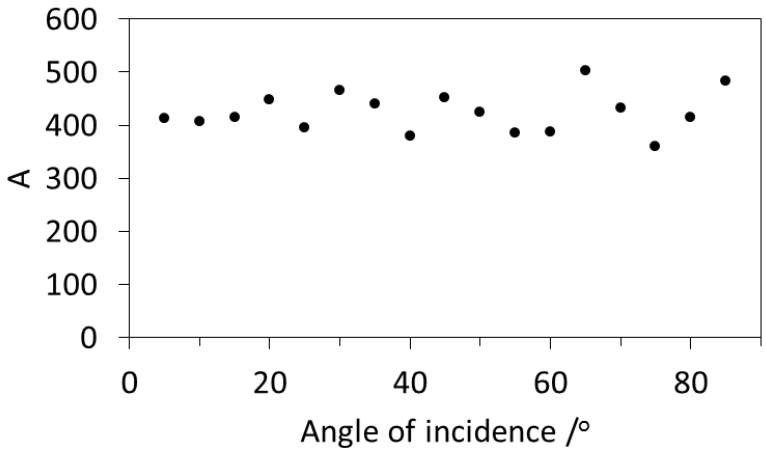

Figure 7-24: Background noise level (A) for macFTO-Rudcbpy as a function of angle of incidence

macFTO-Rudcbpy fit to a single exponential lifetime, which was found to be The average lifetime was calculated to be 420.2 $\pm$ 14 ns on average.

Table 7-8: Lifetime data and fits for pFTO-coumarin

pFTO-coumarin							
5°							
τ_1 /ns	2.92 ± 0.32	B_1	139.50 ± 17.43	Relative % 1	44.9	A	5.69
τ_2 /ns	8.95 ± 1.90	B_2	55.91 ± 18.19	Relative % 2	55.1	χ^2	1.112
10°							
τ_1 /ns	3.06 ± 0.12	B_1	1256.0 ± 59.47	Relative % 1	35.94	A	20.41
τ_2 /ns	9.03 ± 0.45	B_2	759.5 ± 62.07	Relative % 2	64.06	χ^2	0.912
15°							
τ_1 /ns	2.80 ± 0.14	B_1	1094.0 ± 63.09	Relative % 1	27.9	A	26.75
τ_2 /ns	7.88 ± 0.28	B_2	1003.0 ± 66.67	Relative % 2	72.1	χ^2	0.958
20°							
τ_1 /ns	3.05 ± 0.12	B_1	1608.0 ± 81.06	Relative % 1	31.80	A	24.97
τ_2 /ns	8.45 ± 0.32	B_2	1244.0 ± 84.81	Relative % 2	68.20	χ^2	1.020
25°							
τ_1 /ns	3.40 ± 0.14	B_1	1707.0 ± 98.95	Relative % 1	36.29	A	23.75
τ_2 /ns	9.19 ± 0.48	B_2	1110.0 ± 101.8	Relative % 2	63.71	χ^2	1.056
30°							
τ_1 /ns	3.16 ± 0.13	B_1	1604.0 ± 85.27	Relative % 1	31.99	A	26.27
τ_2 /ns	8.78 ± 0.36	B_2	1226.0 ± 88.62	Relative % 2	68.01	χ^2	1.035
35°							
τ_1 /ns	2.97 ± 0.13	B_1	1497.0 ± 80.48	Relative % 1	28.11	A	33.22
τ_2 /ns	8.32 ± 0.28	B_2	1368.0 ± 84.30	Relative % 2	71.89	χ^2	1.095
40°							
τ_1 /ns	2.97 ± 0.14	B_1	1138.0 ± 64.17	Relative % 1	34.78	A	30.88
τ_2 /ns	8.36 ± 0.42	B_2	757.5 ± 67.17	Relative % 2	65.22	χ^2	1.107

45°							
τ_1 /ns	2.80 ± 0.14	B_1	1005.0 ± 60.48	Relative % 1	29.18	A	39.58
τ_2 /ns	8.03 ± 0.34	B_2	850.9 ± 63.67	Relative % 2	70.82	χ^2	1.044
50°							
τ_1 /ns	2.85 ± 0.15	B_1	922.3 ± 57.82	Relative % 1	27.91	A	23.19
τ_2 /ns	8.14 ± 0.33	B_2	834.2 ± 60.89	Relative % 2	72.09	χ^2	0.952
55°							
τ_1 /ns	3.16 ± 0.13	B_1	1204.0 ± 64.79	Relative % 1	39.07	A	21.84
τ_2 /ns	8.91 ± 0.52	B_2	666.0 ± 67.38	Relative % 2	60.93	χ^2	1.117
60°							
τ_1 /ns	2.93 ± 0.13	B_1	1051.0 ± 54.28	Relative % 1	32.24	A	19.24
τ_2 /ns	8.64 ± 0.39	B_2	750.1 ± 57.06	Relative % 2	67.76	χ^2	1.193
65°							
τ_1 /ns	2.87 ± 0.12	B_1	1140.0 ± 55.76	Relative % 1	35.21	A	2.28
τ_2 /ns	8.26 ± 0.38	B_2	727.8 ± 58.86	Relative % 2	64.79	χ^2	1.030
70°							
τ_1 /ns	2.94 ± 0.14	B_1	957.5 ± 55.18	Relative % 1	32.65	A	22.98
τ_2 /ns	8.51 ± 0.42	B_2	682.2 ± 57.88	Relative % 2	67.35	χ^2	1.090
75°							
τ_1 /ns	2.95 ± 0.13	B_1	1016.0 ± 53.93	Relative % 1	34.83	A	20.89
τ_2 /ns	8.58 ± 0.44	B_2	653.2 ± 2.95	Relative % 2	65.17	χ^2	1.028
80°							
τ_1 /ns	2.88 ± 0.14	B_1	987.7 ± 56.876	Relative % 1	31.0	A	21.95
τ_2 /ns	8.26 ± 0.36	B_2	766.90 ± 59.75	Relative % 2	69.0	χ^2	1.052
85°							
τ_1 /ns	2.40 ± 0.44	B_1	76.99 ± 17.39	Relative % 1	32.96	A	2.59
τ_2 /ns	6.20 ± 0.84	B_2	60.62 ± 18.58	Relative % 2	67.04	χ^2	1.254

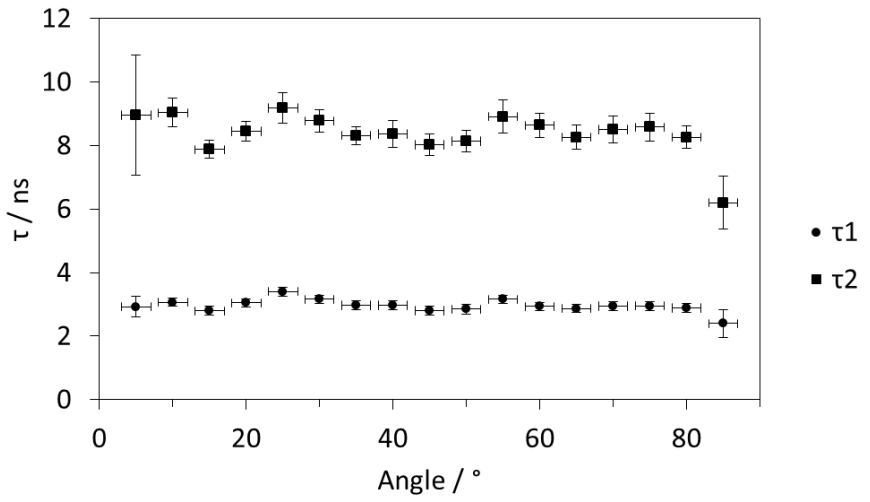

Figure 7-25: Lifetime values for pFTO-Coumarin as a function of angle of incidence

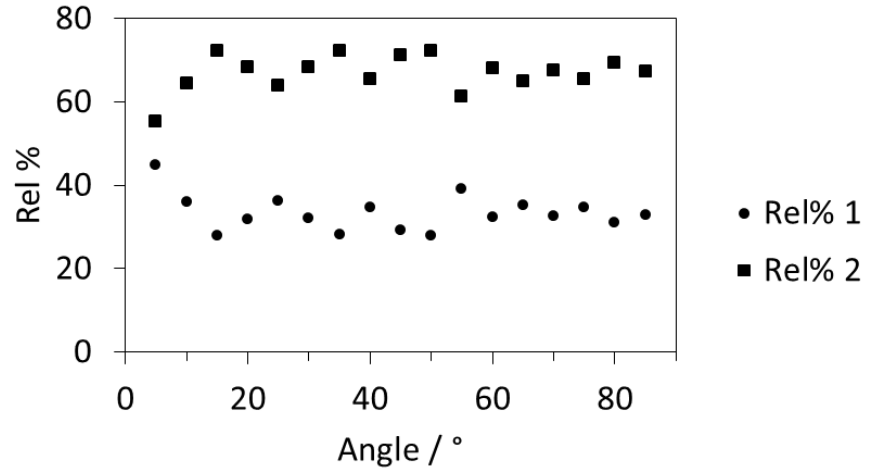

Figure 7-26: Relative percentage contribution of each lifetime of pFTO-Coumarin as a function of angle of incidence

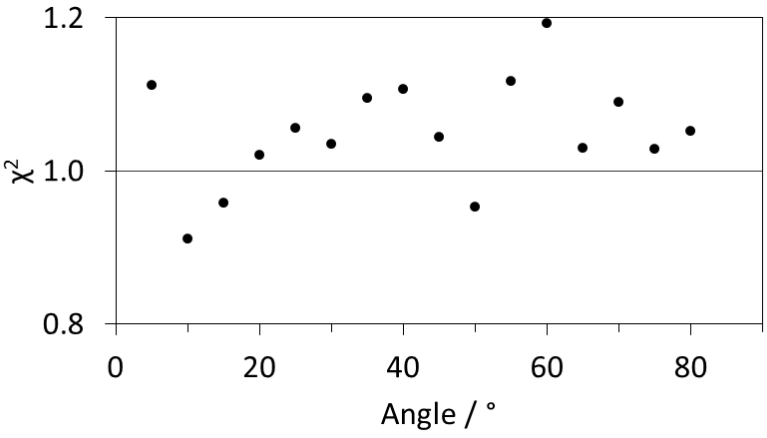

Figure 7-27: Quality of lifetime fit (χ^2) for pFTO-Coumarin as a function of angle of incidence

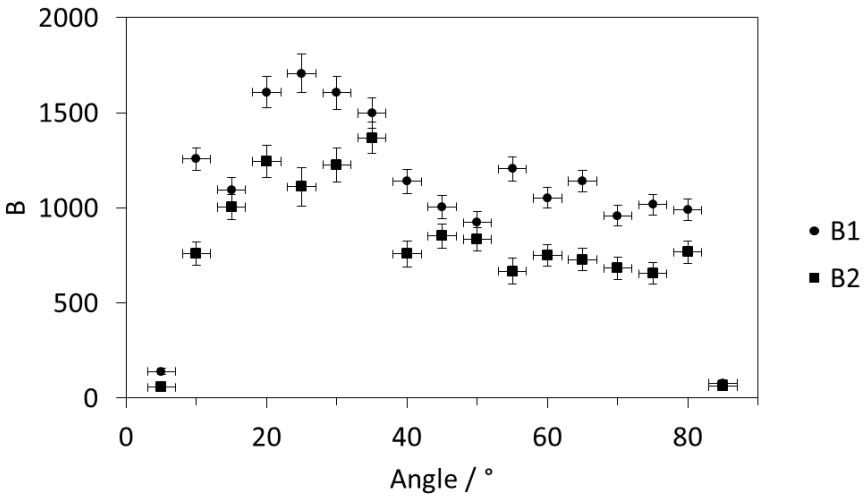

Figure 7-28: Pre-exponential factor (B) for pFTO-Coumarin as a function of angle of incidence

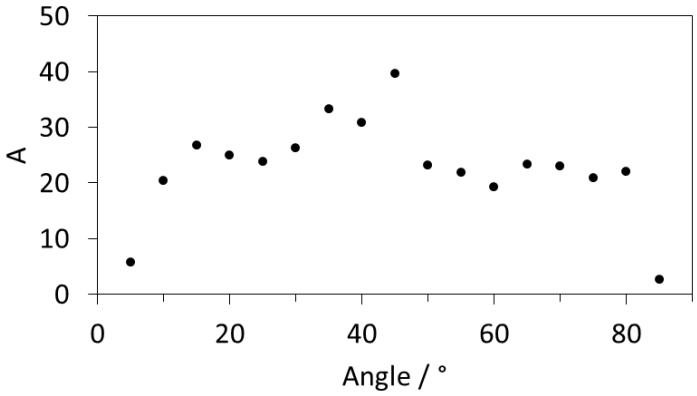

Figure 7-29 Background noise level (A) for pFTO-Coumarin as a function of angle of incidence.

pFTO-coumarin was fitted to a bi-exponential term: the shorter component was found to be 2.95 ±0.16 ns, while the longer term was found to be 8.38 ± 0.05 ns.

Table 7-9: Lifetime data and fits for macFTO-coumarin

macFTO-coumarin							
5°							
τ_1 /ns	3.23 ± 0.05	B_1	2121.0 ± 23.80	Relative % 1	59.71	A	68.86
τ_2 /ns	10.27 ± 0.28	B_2	449.40 ± 26.90	Relative % 2	40.29	χ^2	0.947
10°							
τ_1 /ns	2.86 ± 0.08	B_1	600.3 ± 11.22	Relative % 1	44.34	A	51.49
τ_2 /ns	11.17 ± 0.4	B_2	192.7 ± 12.27	Relative % 2	55.66	χ^2	1.044
15°							
τ_1 /ns	2.99 ± 0.09	B_1	634.8 ± 13.32	Relative % 1	38.36	A	55.69
τ_2 /ns	11.20 ± 0.33	B_2	272.6 ± 14.81	Relative % 2	61.64	χ^2	1.067
20°							
τ_1 /ns	2.95 ± 0.11	B_1	472.1 ± 12.23	Relative % 1	56.07	A	48.55
τ_2 /ns	10.25 ± 0.68	B_2	106.5 ± 13.72	Relative % 2	43.93	χ^2	1.002
25°							
τ_1 /ns	2.94 ± 0.10	B_1	573.8 ± 14.45	Relative % 1	50.69	A	50.54
τ_2 /ns	9.84 ± 0.47	B_2	166.6 ± 16.22	Relative % 2	49.31	χ^2	1.060
30°							
τ_1 /ns	2.89 ± 0.14	B_1	367.3 ± 14.01	Relative % 1	53.5	A	49.42
τ_2 /ns	9.33 ± 0.71	B_2	98.78 ± 15.69	Relative % 2	46.5	χ^2	1.059
35°							
τ_1 /ns	2.53 ± 0.24	B_1	144.5 ± 10.49	Relative % 1	38.44	A	52.02
τ_2 /ns	8.96 ± 0.85	B_2	65.40 ± 11.68	Relative % 2	61.56	χ^2	1.088
40°							
τ_1 /ns	2.75 ± 0.16	B_1	307.3 ± 15.78	Relative % 1	50.1	A	58.33
τ_2 /ns	8.60 ± 0.73	B_2	97.7 ± 17.55	Relative % 2	49.9	χ^2	1.131

45°							
τ_1 /ns	2.43 ± 0.20	B_1	233.7 ± 18.21	Relative % 1	36.6	A	78.12
τ_2 /ns	7.58 ± 0.58	B_2	129.8 ± 20.13	Relative % 2	63.4	χ^2	1.061
50°							
τ_1 /ns	2.43 ± 0.17	B_1	209.8 ± 9.94	Relative % 1	39.63	A	39.94
τ_2 /ns	8.73 ± 0.55	B_2	89.07 ± 11.02	Relative % 2	60.37	χ^2	1.015
55°							
τ_1 /ns	2.96 ± 0.15	B_1	382.70 ± 19.06	Relative % 1	54.61	A	41.69
τ_2 /ns	8.41 ± 0.67	B_2	111.9 ± 21.1	Relative % 2	45.39	χ^2	1.051
60°							
τ_1 /ns	2.93 ± 0.18	B_1	364.1 ± 22.92	Relative % 1	58.25	A	42.72
τ_2 /ns	4.92 ± 0.78	B_2	96.48 ± 25.11	Relative % 2	41.75	χ^2	1.095
65°							
τ_1 /ns	2.99 ± 0.07	B_1	1124.0 ± 24.4	Relative % 1	64.27	A	49.67
τ_2 /ns	8.40 ± 0.42	B_2	222.2 ± 27.34	Relative % 2	35.73	χ^2	1.107
70°							
τ_1 /ns	3.12 ± 0.08	B_1	1004.0 ± 24.46	Relative % 1	67.51	A	48.39
τ_2 /ns	9.62 ± 0.55	B_2	174.80 ± 27.34	Relative % 2	32.49	χ^2	1.069
75°							
τ_1 /ns	2.72 ±0.13	B_1	399.0 ±17.19	Relative % 1	50.75	A	40.41
τ_2 /ns	8.02 ±0.51	B_2	131.40 ± 19.16	Relative % 2	49.25	χ^2	1.085
80°							
τ_1 /ns	2.69 ±0.14	B_1	369.0 ±18.89	Relative % 1	55.88	A	47.51
τ_2 /ns	7.73 ±0.64	B_2	108.70 ±20.96	Relative % 2	44.12	χ^2	1.142
85°							
τ_1 /ns	3.08 ±0.05	B_1	1534.0 ± 22.67	Relative % 1	69.15	A	53.49
τ_2 /ns	9.13 ±0.44	B_2	231.0 ± 25.6	Relative % 2	30.85	χ^2	1.112

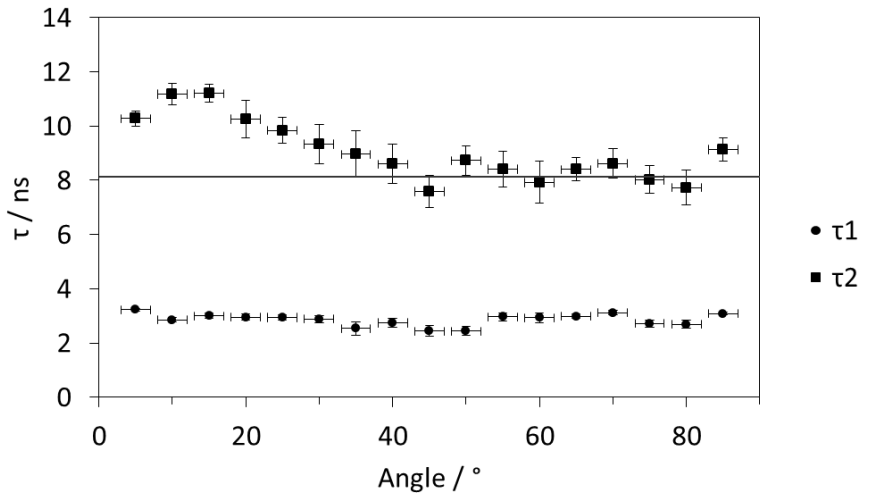

Figure 7-30: Lifetime values for macFTO-Coumarin as a function of angle of incidence

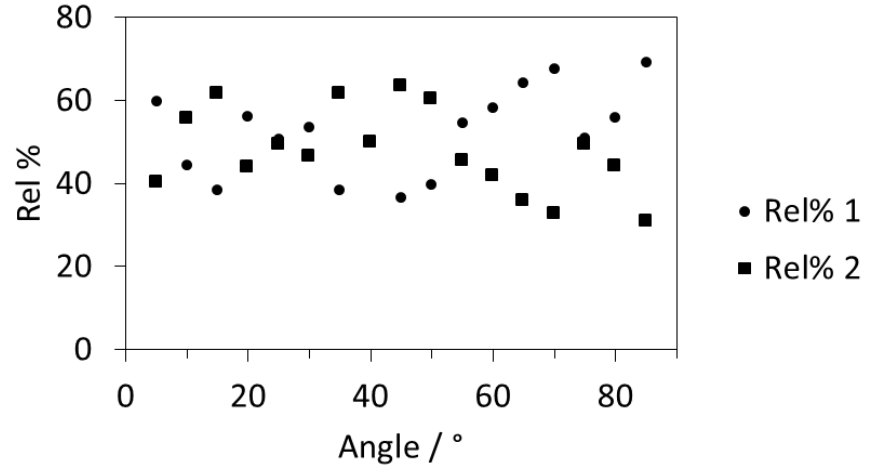

Figure 7-31: Relative percentage contribution of each lifetime of macFTO-Coumarin as a function of angle of incidence

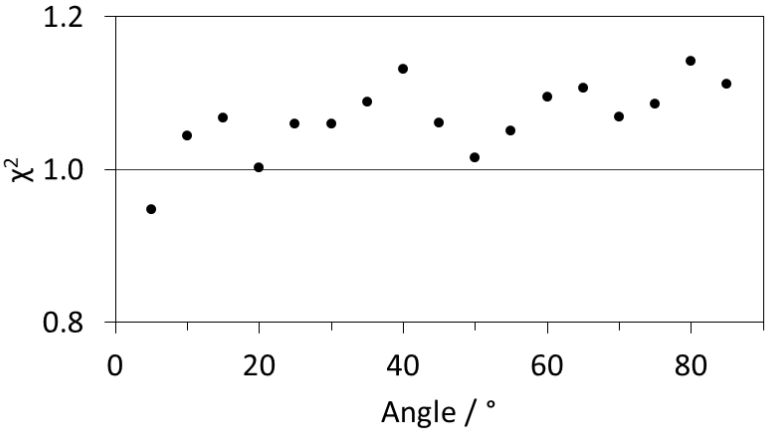

Figure 7-32: Quality of lifetime fit (χ^2) for macFTO-Coumarin as a function of angle of incidence

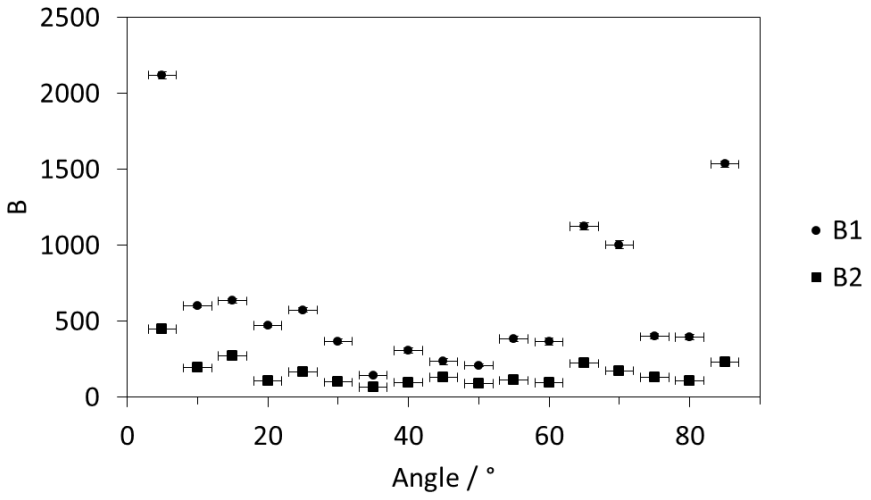

Figure 7-33: Pre-exponential factor (B) for macFTO-Coumarin as a function of angle of incidence

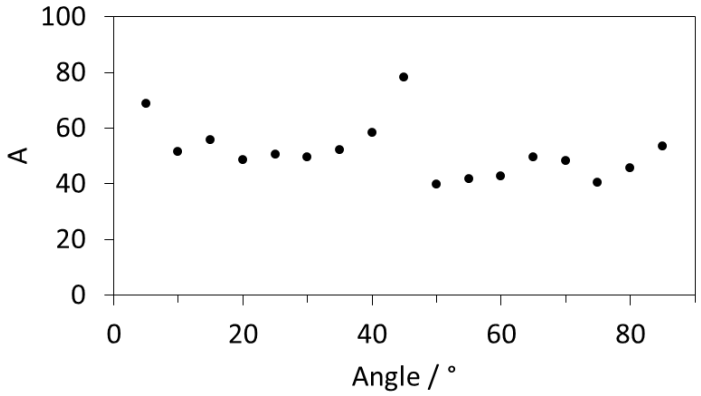

Figure 7-34 Background noise level (A) for macFTO-Coumarin as a function of angle of incidence

macFTO-coumarin was fitted to a bi-exponential fit, the shorter term was found to be 2.85 ± 0.13 ns, while the longer term was found to be 8.37 ± 0.16 ns.

7.4. Chapter 4: Photoelectrodes

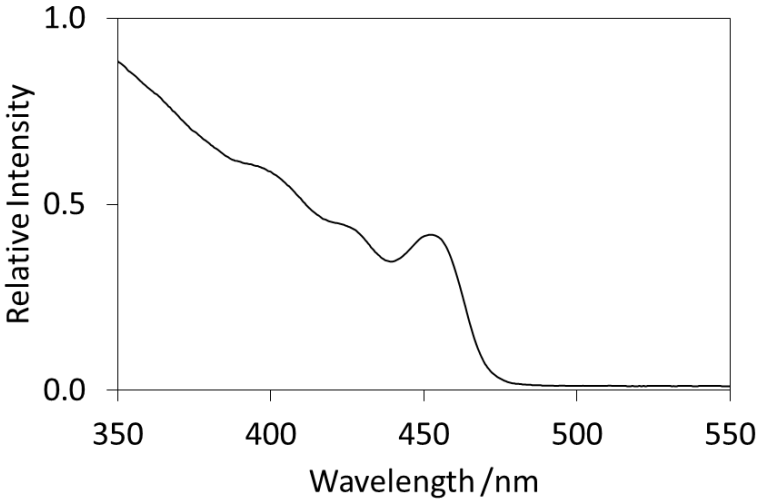

Figure 7-35: UV/vis spectrum of CdS nanoparticles in toluene

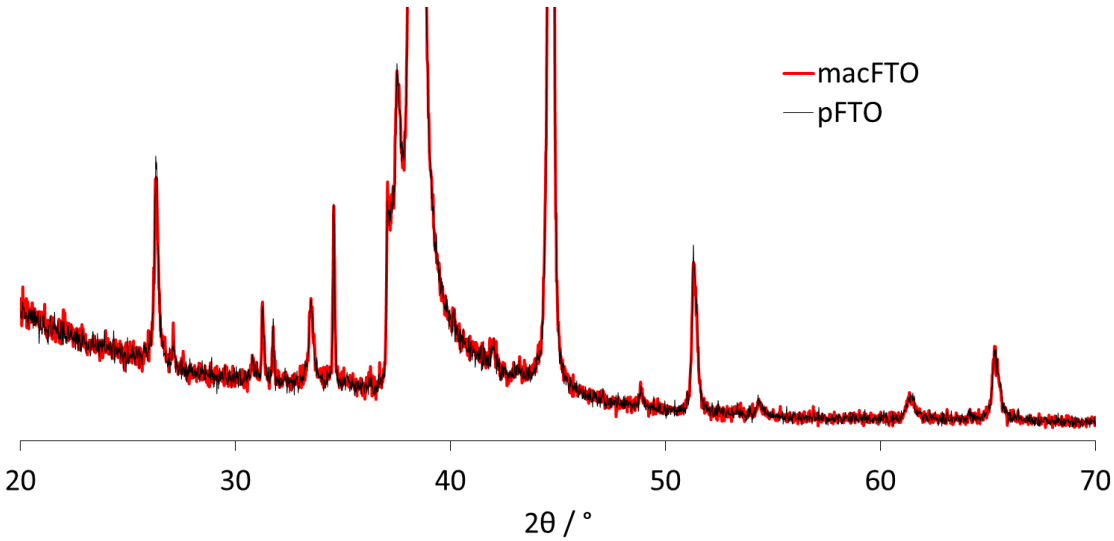

Figure 7-36:XRD of pFTO-$BiVO_4$

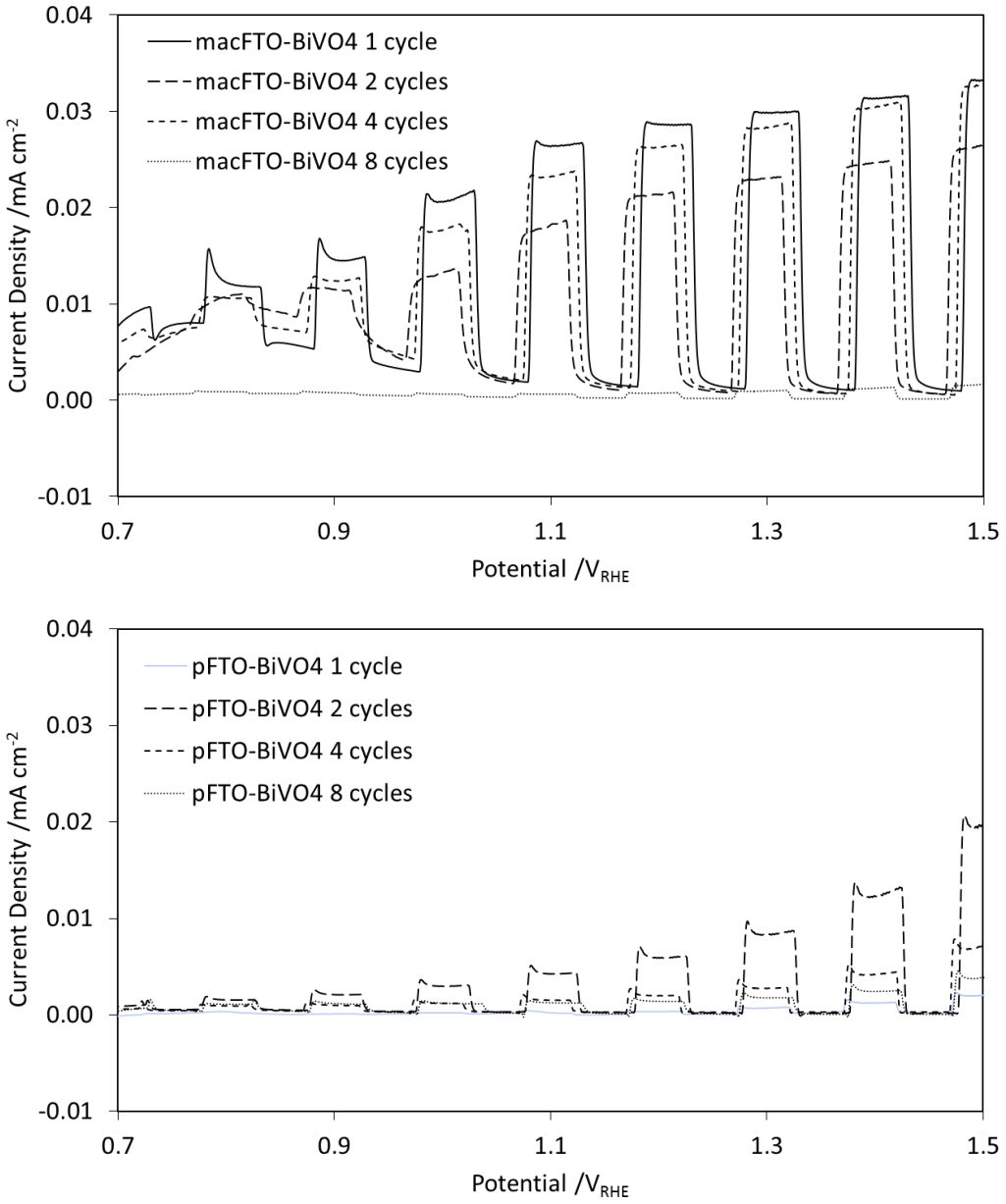

Figure 7-37: LSV chopped traces of macFTO and pFTO BiVO4 as a function of soaks cycles.

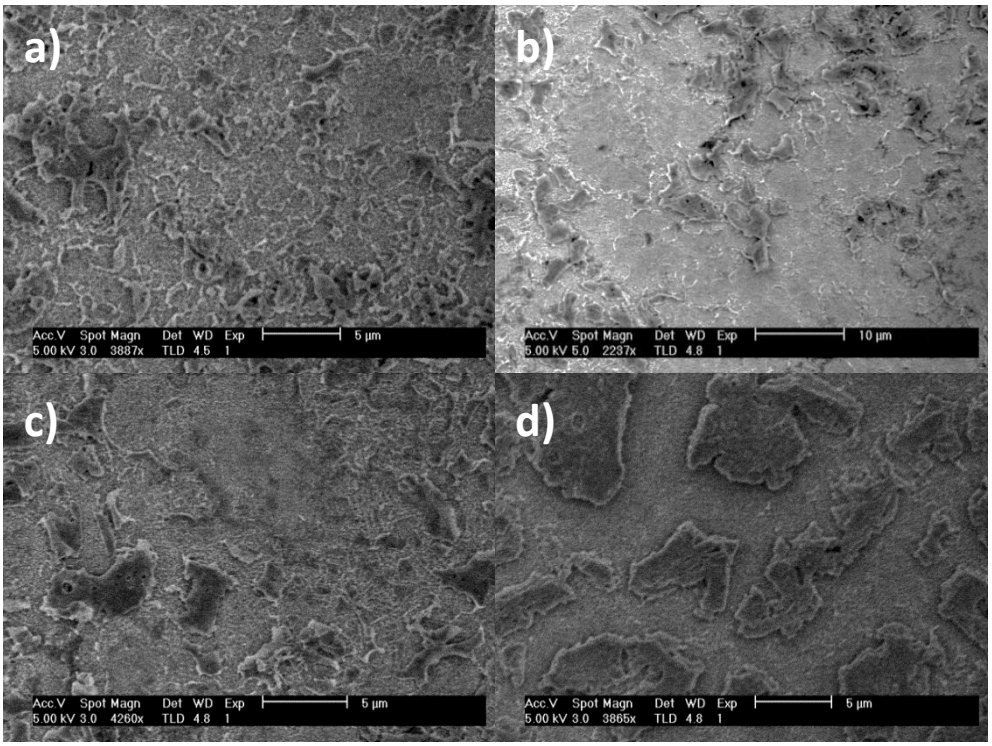

Figure 7-38: SEM of pFTO-BiVO4 soak cycles

7.4.1. Structural Analysis of Gas Evolution Electrodes

A structural analysis of the electrodes before and after electrochemical analysis and before and after CoPi deposition is important because any changes in the structure if the electrodes should be monitored in case structural changes contribute to the increased activity.

SEM images of pFTO-$BiVO_4$ and macFTO-$BiVO_4$ electrodes immediately after deposition and subsequent calcination are shown in Figure 7-39 a) and b) respectively. pFTO-$BiVO_4$ and macFTO-$BiVO_4$ after electrochemical analysis are shown in Figure 7-39 c) and d) respectively. There appears to be no structural change during course of the electrochemical analysis for gas evolution. This shows that the electrodes are quite stable (in conjunction with the stable current density densities). Figure 7-39 e) and f) show the electrodes after CoPi deposition. Despite the fact that the CoPi layer is not visible to the eye, it may still be expected that the CoPi would be visible at high magnification. This is not shown to be the case as the electrodes appear no different compared to images a) and b). This shows that there is very little CoPi on the electrodes, especially because no Co is detected during EDX measurements on these electrodes. It is likely that the amount of CoPi is below the detection limit of the EDX and so cannot be measured. However it is clear from the electrochemical analysis that CoPi is present as the activity of the electrodes towards oxygen evolution increases substantially.

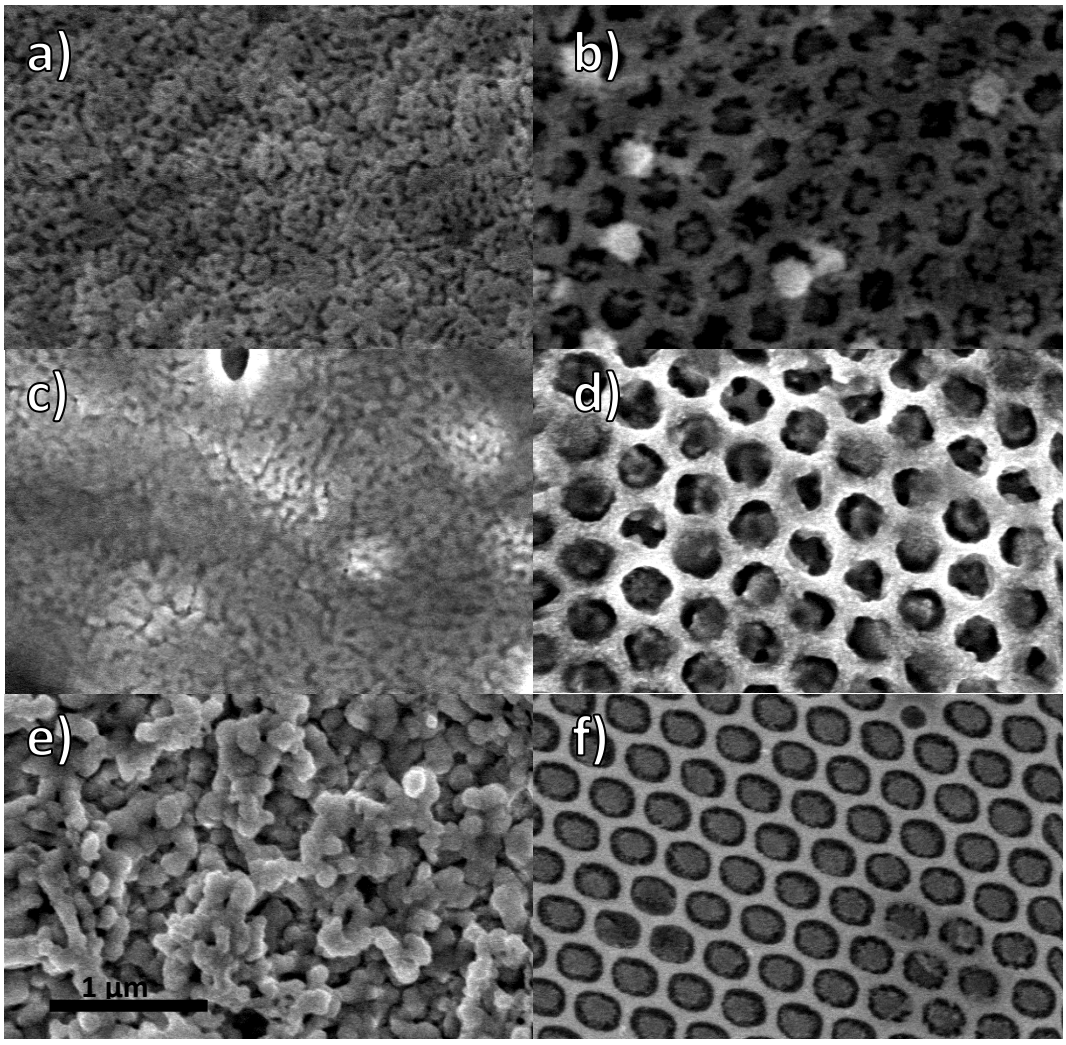

Figure 7-39: SEM images of the CoPi electrode series before and after electrochemical analysis. All images are to the same magnification.

7.5. Chapter 5: Conclusions and Future Work

No further information

7.6. Chapter 6: Experimental

7.6.1. Bis(2,2′-bipyridine)-4,4′-dicarboxybipyridine ruthenium (II) dichloride: NMR

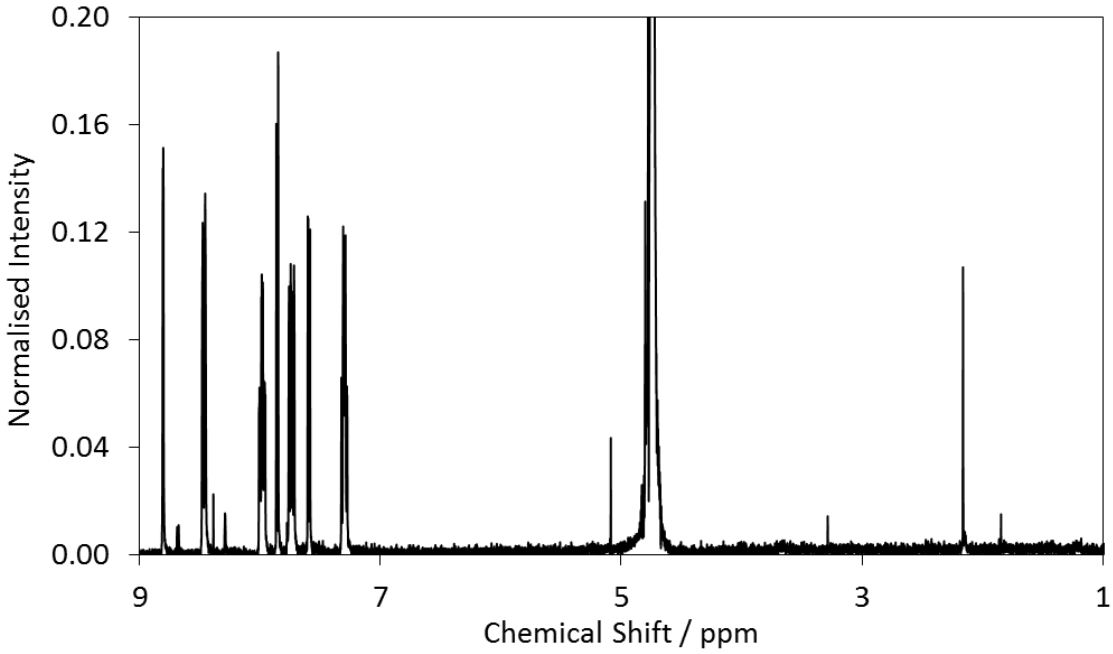

Figure 7-40: NMR spectrum of Rudcbpy

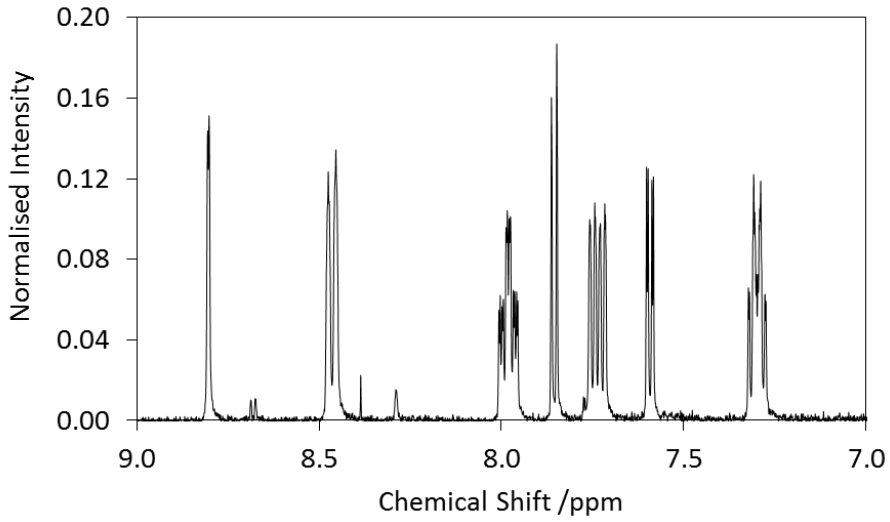

Figure 7-41: NMR spectrum of Rudcbpy, zoomed to the aromatic region

Abbreviations

Ag/AgCl	Silver/Silver chloride electrode
$BiVO_4$	Bismuth vanadate nanoparticles
bpy	Bipyridine
CdS	Cadmium sulfide
CoPi	Cobalt phosphate oxygen evolving co-catalyst
Cou	Coumarin
CPE	Controlled Potential Electrolysis; an electrochemical experiment where the potential is held at the same value for the duration of the experiment.
CV	Cyclic voltammetry: an electrochemical experiment where the potential is scanned at a particular scan rate
dcbpy	4,4'-dicarboxybipyridine
DRUVS	Diffuse reflectance UV-vs Sepctroscopy
DSSC	Dye sensitised solar cell
edep	Electrodeposition/electrodeposited
E_a	Potential of the anodic wave (cyclic voltammetry)
E_c	Position of the cathodic wave (cyclic voltammetry)
E_g	Band gap of a semiconductor
f(θ)	Function of angle of incidence
fcc	face centred cube
FE	Faradaic efficiency, the conversion efficiency of an electrochemical process (from charge to moles, mass or volume of product)
FTO	Fluorine doped tin oxide
GC	Gas chromatography
HER	Hydrogen evolving reaction
io	Inverse opal
IPCE	Incident photon to electron conversion efficiency
IR	Infra-red
LSV	Linear sweep voltammetry: an electrochemical experiment, like a CV, where the potential is swept from one value to another. There is no return scan as with CV.
mac	Macroporous

macFTO	Macroporous fluorine doped tin oxide electrode
NHE	Normal Hydrogen electrode
OER	Oxygen evolving reaction
pedep	Photoelectrodeposition/photoelectrodeposited
pFTO	Planar fluorine doped tin oxide electrode
Pt	Platinum electrode
RHE	Reversible Hydrogen Electrode
Rudcbpy	Bis(2,2'-bipyridine)-4,4'-dicarboxy-2,2'-bipyridine ruthenium (II) dichloride
TCO	Transparent conducing oxide
TW	Tera watt (10^{12})
UV/vis	Ultra violet – visible wavelength range
$V_{Ag/AgCl}$	Volts *vs* the silver/silver chloride reference electrode
V_{RHE}	Volts *vs* the reversible hydrogen electrode
τ	Lifetime
χ^2	Chi squared (goodness of fit parameter for lifetime measurements)

References

1. Menglong Zhang, Unpublished Thesis, University of York, 2015/16.
2. N. P. Group, *Nature*, 1915, **95**, 358-360.
3. A. Rordame, *Popular Astronomy*, 1911, **19**, 153-161.
4. R. Audubert, *C. R. Hebd. Seances Acad. Sci.*, 1929, **189**, 1265-1267.
5. E. S. Rittner, *Phys. Rev.*, 1954, **96**, 1708-1709.
6. D. A. Jenny, J. J. Loferski and P. Rappaport, *Phys. Rev.*, 1956, **101**, 1208-1209.
7. G. R. Timilsina, L. Kurdgelashvili and P. A. Narbel, eds. Environment and D. R. G. Energy Team, The World Bank, edn., 2011, vol. WPS 5845.
8. O. Thulesius, *The Man Who Made the Monitor: A Biography of John Ericsson, Naval Engineer*, McFarland & Co Inc, Jefferson, NC, 2006.
9. N. S. Lewis and D. G. Nocera, *Proc. Natl. Acad. Sci.USA*, 2006, **103**, 15729 - 15735.
10. Kyoto Protocol to the United Nations Framework Convention on Climate Change, United Nations, 1998.
11. L. M. Goncalves, V. d. Z. Bermudez, H. A. Ribeiro and A. M. Mendes, *Energy & Environmental Science*, 2008, **1**, 655-667.
12. K. Tanabe, *Energies*, 2009, **2**, 504-530.
13. W. Y. Wong and C. L. Ho, *Acc. Chem. Res.*, 2010, **43**, 1246-1256.
14. D. Black, *Solar Fuels and Artificial Photosynthesis*, RSC, United Kingdom, 2012.
15. S. Guha and J. Yang, *J. Non-Cryst. Solids*, 2006, **352**, 1917-1921.
16. C. Longo and M. A. De Paoli, *J. Braz. Chem. Soc.*, 2003, **14**, 889-901.
17. M. Armand and J. M. Tarascon, *Nature*, 2008, **451**, 652-657.
18. K. C. Divya and J. Østergaard, *Electric Power Systems Research*, 2009, **79**, 511-520.
19. S. K. Ngoh and D. Njomo, *Renewable and Sustainable Energy Rev.*, 2012, **16**, 6782-6792.
20. U. S. D. o. Energy, *Comparison of specific energy and energy density for several fuels based on lower heating values*, http://energy.gov/eere/fuelcells/hydrogen-storage, Accessed 10th October, 2015.
21. H. B. Gray, *Nat. Chem.*, 2009, **1**, 7.
22. H. R. Pershad, J. L. C. Duff, H. A. Heering, E. C. Duin, S. P. J. Albracht and F. A. Armstrong, *Biochemistry*, 1999, **38**, 8992-8999.
23. K. A. Vincent, A. Parkin and F. A. Armstrong, *Chem. Rev.*, 2007, **107**, 4366-4413.
24. B. Ginovska-Pangovska, A. Dutta, M. L. Reback, J. C. Linehan and W. J. Shaw, *Acc. Chem. Res.*, 2014, **47**, 2621-2630.
25. K. S. Joya, Y. F. Joya, K. Ocakoglu and R. van de Krol, *Angew. Chem. Int. Ed.*, 2013, **52**, 10426-10437.
26. Y. Tachibana, L. Vayssieres and J. R. Durrant, *Nat. Photon.*, 2012, **6**, 511-518.
27. E. S. Andreiadis, M. Chavarot-Kerlidou, M. Fontecave and V. Artero, *Photochem. Photobiol.*, 2011, **87**, 946-964.
28. Y. Gorlin and T. F. Jaramillo, *J. Am. Chem. Soc.*, 2010, **132**, 13612-13614.
29. R. Brimblecombe, A. Koo, G. C. Dismukes, G. F. Swiegers and L. Spiccia, *J. Am. Chem. Soc.*, 2010, **132**, 2892-2894.
30. C. E. Lubner, P. Knörzer, P. J. N. Silva, K. A. Vincent, T. Happe, D. A. Bryant and J. H. Golbeck, *Biochemistry*, 2010, **49**, 10264-10266.
31. H. Krassen, A. Schwarze, B. Friedrich, K. Ataka, O. Lenz and J. Heberle, *ACS Nano*, 2009, **3**, 4055-4061.
32. X. Li, M. Wang, S. Zhang, J. Pan, Y. Na, J. Liu, B. Åkermark and L. Sun, *J. Phys. Chem. B*, 2008, **112**, 8198-8202.
33. C. Baffert, V. Artero and M. Fontecave, *Inorg. Chem.*, 2007, **46**, 1817-1824.

34. X. Hu, B. S. Brunschwig and J. C. Peters, *J. Am. Chem. Soc.*, 2007, **129**, 8988-8998.
35. D. Merki, H. Vrubel, L. Rovelli, S. Fierro and X. Hu, *Chem. Sci.*, 2012, **3**, 2515-2525.
36. O. Khaselev and J. A. Turner, *Science*, 1998, **280**, 425-427.
37. S. Berardi, S. Drouet, L. Francas, C. Gimbert-Surinach, M. Guttentag, C. Richmond, T. Stoll and A. Llobet, *Chem. Soc. Rev.*, 2014, **43**, 7501-7519.
38. S. Y. Reece, J. A. Hamel, K. Sung, T. D. Jarvi, A. J. Esswein, J. J. H. Pijpers and D. G. Nocera, *Science*, 2011, **334**, 645-648.
39. K. Sayama, K. Mukasa, R. Abe, Y. Abe and H. Arakawa, *J. Photochem. Photobiol. A: Chemistry*, 2002, **148**, 71-77.
40. K. Maeda, *ACS Catalysis*, 2013, **3**, 1486-1503.
41. J. Su, L. Guo, N. Bao and C. A. Grimes, *Nano Lett.*, 2011, **11**, 1928-1933.
42. R. E. Rocheleau, E. L. Miller and A. Misra, *Energy Fuels*, 1998, **12**, 3-10.
43. D. G. Nocera, *Acc. Chem. Res.*, 2012, **45**, 767-776.
44. U. I. Gaya and A. H. Abdullah, *Journal of Photochemistry and Photobiology C: Photochemistry Reviews*, 2008, **9**, 1-12.
45. G. Li Puma, A. Bono, D. Krishnaiah and J. G. Collin, *J. Hazard. Mater.*, 2008, **157**, 209-219.
46. S. Gupta and M. Tripathi, *Chin. Sci. Bull.*, 2011, **56**, 1639-1657.
47. A. Fujishima, T. N. Rao and D. A. Tryk, *Journal of Photochemistry and Photobiology C: Photochemistry Reviews*, 2000, **1**, 1-21.
48. A. Fujishima and K. Honda, *Nature*, 1972, **238**, 37-38.
49. J. I. L. Chen, E. Loso, N. Ebrahim and G. A. Ozin, *J. Am. Chem. Soc.*, 2008, **130**, 5420-5421.
50. S. U. M. Khan, M. Al-Shahry and W. B. Ingler, *Science*, 2002, **297**, 2243-2245.
51. S. Kundu, A. Kafizas, G. Hyett, A. Mills, J. A. Darr and I. P. Parkin, *J. Mater. Chem.*, 2011, **21**, 6854-6863.
52. M. K. Nazeeruddin, A. Kay, I. Rodicio, R. Humphrybaker, E. Muller, P. Liska, N. Vlachopoulos and M. Gratzel, *J. Am. Chem. Soc.*, 1993, **115**.
53. M. Li, S. Zhang, Y. Peng, L. Lv and B. Pan, *RSC Advances*, 2015, **5**, 7363-7369.
54. J. W. J. Hamilton, J. A. Byrne, P. S. M. Dunlop, D. D. Dionysiou, M. Pelaez, K. O'Shea, D. Synnott and S. C. Pillai, *J. Phys. Chem. C*, 2014, **118**, 12206-12215.
55. A. Pivrikas, H. Neugebauer and N. S. Sariciftci, *IEEE J. Sel. Top. Quantum Electron.,* 2010., **16**, 1746-1758
56. C.-Y. Kuo and S.-Y. Lu, *Nanotechnology*, 2008, **19**, 1-8.
57. Z. Yang, S. Gao, W. Li, V. Vlasko-Vlasov, U. Welp, W.-K. Kwok and T. Xu, *ACS Applied Materials and Interfaces*, 2011, **3**, 1101-1108.
58. A. Kumar and V. Chaudhary, *Nanotechnology*, 2009, **20**, 10.
59. C. C. Lin, H. C. Chen, Y. L. Tsai, H. V. Han, H. S. Shih, Y. A. Chang, H. C. Kuo and P. C. Yu, *Opt. Express*, 2012, **20**, A319-A326.
60. G. Zhu, L. Pan, T. Xu, Q. Zhao and Z. Sun, *J. Alloy. Compd.*, 2011, **509**, 7814-7818.
61. G. Zhu, F. Su, T. Lv, L. Pan and Z. Sun, *Nanoscale Res. Lett.*, 2010, **5**, 1749-1754.
62. X. Chen and W. Shangguan, *Front. Energy*, 2013, **7**, 111-118.
63. C. Chen, Q. Dai, C. Miao, L. Xu and H. Song, *RSC Advances*, 2015, **5**, 4844-4852.
64. H. Xie, T. Zeng, S. Jin, Y. Li, X. Wang, X. Sui and X. Zhao, *Journal of nanoscience and nanotechnology*, 2013, **13**, 1461-1466.
65. S. V. Gaponenko, V. N. Bogomolov, E. P. Petrov, A. M. Kapitonov, A. A. Eychmueller, A. L. Rogach, Kalosha, II, F. Gindele and U. Woggon, *J. Lumin.*, 2000, **87-9**.
66. P. Lodahl, A. F. van Driel, I. S. Nikolaev, A. Irman, K. Overgaag, D. Vanmaekelbergh and W. L. Vos, *Nature*, 2004, **430**, 7250-7254
67. S. Kelkar, C. Ballal, A. Deshpande, S. Warule and S. Ogale, *Journal of Materials Chemistry A*, 2013, **1**, 12426-12431.
68. B. Iandolo and A. Hellman, *Angew. Chem. Int. Ed.*, 2014, **53**, 13404-13408.
69. D. K. Zhong, J. Sun, H. Inumaru and D. R. Gamelin, *J. Am. Chem. Soc.*, 2009, **131**, 6086-6087.

70. P. Luan, M. Xie, D. Liu, X. Fu and L. Jing, *Scientific Reports*, 2014, **4**, 6180.
71. W.-H. Hung, T.-M. Chien and C.-M. Tseng, *J. Phys. Chem. C*, 2014, **118**, 12676-12681.
72. F. F. Abdi, L. Han, A. H. M. Smets, M. Zeman, B. Dam and R. van de Krol, *Nat Commun*, 2013, **4**.
73. D. Eisenberg, H. S. Ahn and A. J. Bard, *J. Am. Chem. Soc.*, 2014, **136**, 14011-14014.
74. Z.-F. Huang, L. Pan, J.-J. Zou, X. Zhang and L. Wang, *Nanoscale*, 2014, **6**, 14044-14063.
75. Y. Ma, F. Le Formal, A. Kafizas, S. R. Pendlebury and J. R. Durrant, *J. Mat. Chem. A*, 2015, **3**, 20649-20657
76. T. W. Kim and K.-S. Choi, *Science*, 2014, **343**, 990-994.
77. G. P. Nagabhushana, G. Nagaraju and G. T. Chandrappa, *J. Mat. Chem. A.,*2013, **1**, 388-394.
78. Long, Cai and H. Kisch, *J. Phys. Chem. C*, 2008, **112**, 548-554.
79. S. K. Pilli, T. E. Furtak, L. D. Brown, T. G. Deutsch, J. A. Turner and A. M. Herring, *Energy Environ. Sci*, 2011, **4**, 5028-5034.
80. Z. Sun, J. Guo, S. Zhu, J. Ma, Y. Liao and D. Zhang, *RSC Advances*, 2014, **4**, 27963-27970.
81. C.-Y. Lin, Y.-H. Lai, D. Mersch and E. Reisner, *Chem. Sci.*, 2012, **3**, 3482-3487.
82. W. Zhao, W. Fu, H. Yang, C. Tian, M. Li, Y. Li, L. Zhang, Y. Sui, X. Zhou, H. Chen and G. Zou, *Cryst. Eng. Comm.*, 2011, **13**, 2871-2877.
83. S. Berger, H. Tsuchiya, A. Ghicov and P. Schmuki, *Appl. Phys. Lett.*, 2006, **88**.
84. C. Santato, M. Ulmann and J. Augustynski, *Adv. Mater.*, 2001, **13**.
85. J. Luo, J.-H. Im, M. T. Mayer, M. Schreier, M. K. Nazeeruddin, N.-G. Park, S. D. Tilley, H. J. Fan and M. Grätzel, *Science*, 2014, **345**, 1593-1596.
86. S. Shen, J. Zhou, C.-L. Dong, Y. Hu, E. N. Tseng, P. Guo, L. Guo and S. S. Mao, *Scientific Reports*, 2014, **4**, 6627.
87. K. Sivula, F. Le Formal and M. Grätzel, *Chem. Sus. Chem.*, 2011, **4**, 432-449.
88. Y. Park, K. J. McDonald and K.-S. Choi, *Chem. Soc. Rev.*, 2013, **42**, 2321-2337.
89. Q. Jia, K. Iwashina and A. Kudo, *Proc. Natl, Acad. Sci. USA*, 2012, **109**, 11564-11569.
90. P. Wang, X. Wen, R. Amal and Y. H. Ng, *RSC Advances*, 2015, **5**, 5231-5236.
91. C. Santato, M. Odziemkowski, M. Ulmann and J. Augustynski, *J. Am. Chem. Soc.*, 2001, **123**.
92. C. Santato, M. Ulmann and J. Augustynski, *J. Phys. Chem. B*, 2001, **105**.
93. I. Aslam, C. Cao, M. Tanveer, M. H. Farooq, W. S. Khan, M. Tahir, F. Idrees and S. Khalid, *RSC Advances*, 2015, **5**, 6019-6026.
94. J. Xu, G. Liu, J. Li and X. Wang, *Electrochim. Acta*, 2012, **59**, 105-112.
95. J. Xu, D. Aili, Q. Li, E. Christensen, J. O. Jensen, W. Zhang, M. K. Hansen, G. Liu, X. Wang and N. J. Bjerrum, *Energy Environ. Sci*, 2014, **7**, 820-830.
96. H.-G. Jung, Y. S. Jeong, J.-B. Park, Y.-K. Sun, B. Scrosati and Y. J. Lee, *ACS Nano*, 2013, **7**, 3532-3539.
97. P. Du and R. Eisenberg, *Energy Environ. Sci*, 2012, **5**, 6012-6021.
98. A. Singh and L. Spiccia, *Coord. Chem. Rev*, 2013, **257**, 2607-2622.
99. Y. Gu, D. Jia, Y. Peng, S. Song, Y. Zhao, J. Zhang and D. Wang, *RSC Advances*, 2015, **5**, 8882-8886.
100. J. A. Seabold and K.-S. Choi, *J. Am. Chem. Soc.*, 2012, **134**, 2186-2192.
101. B. Klahr, S. Gimenez, F. Fabregat-Santiago, J. Bisquert and T. W. Hamann, *J. Am. Chem. Soc.*, 2012, **134**, 16693-16700.
102. M. Barroso, A. J. Cowan, S. R. Pendlebury, M. Grätzel, D. R. Klug and J. R. Durrant, *J. Am. Chem. Soc.*, 2011, **133**, 14868-14871.
103. L. Han, F. F. Abdi, P. Perez Rodriguez, B. Dam, R. van de Krol, M. Zeman and A. H. M. Smets, *Phys. Chem. Chem. Phys.*, 2014, **16**, 4220-4229.
104. D. K. Zhong, M. Cornuz, K. Sivula, M. Gratzel and D. R. Gamelin, *Energy Environ. Sci*, 2011, **4**, 1759-1764.
105. M. W. Kanan and D. G. Nocera, *Science*, 2008, **321**, 1072-1075.

106. M. W. Kanan, Y. Surendranath and D. G. Nocera, *Chem. Soc. Rev.*, 2009, **38**, 109-114.
107. X. Shi, K. Zhang and J. H. Park, *Int. J. Hydrogen Energy*, 2013, **38**, 12725-12732.
108. J. Brillet, M. Grätzel and K. Sivula, *Nano Lett.*, 2010, **10**, 4155-4160.
109. A. Wolcott, W. A. Smith, T. R. Kuykendall, Y. Zhao and J. Z. Zhang, *Adv. Func. Mater.*, 2009, **19**, 1849-1856.
110. J. H. Park, S. Kim and A. J. Bard, *Nano Lett.*, 2006, **6**, 24-28.
111. H. M. Chen, C. K. Chen, R.-S. Liu, L. Zhang, J. Zhang and D. P. Wilkinson, *Chem. Soc. Rev.*, 2012, **41**, 5654-5671.
112. X. Shi, I. Y. Choi, K. Zhang, J. Kwon, D. Y. Kim, J. K. Lee, S. H. Oh, J. K. Kim and J. H. Park, *Nat. Commun.*, 2014, **5**. 1-8
113. R. A. Pala, A. J. Leenheer, M. Lichterman, H. A. Atwater and N. S. Lewis, *Energy Environ. Sci*, 2014, **7**, 3424-3430.
114. M. F. Lichterman, M. R. Shaner, S. G. Handler, B. S. Brunschwig, H. B. Gray, N. S. Lewis and J. M. Spurgeon, *J. Phys. Chem. Lett.*, 2013, **4**, 4188-4191.
115. A. Blanco, C. Lopez, R. Mayoral, H. Miguez and M. F, *Appl. Phys. Lett.*, 1998, **73**, 1781-1783.
116. L. Berti, M. Cucini, F. Di Stasio and D. Comoretto, *J. Phys. Chem. C*, 2010, **114**, 2403 - 2413.
117. I. S. Nikolaev, P. Lodahl and W. L. Vos, *J. Phys. Chem., C*, 2008, **112**, 7250-7254
118. Z. Cai, J. Teng, Z. Xiong, Y. Li, Q. Li, X. Lu and X. S. Zhao, *Langmuir*, 2011, **27**, 5157-5164
119. M. R. Jorgensen, J. W. Galusha and M. H. Bartl, *Phys. Rev. Lett.*, 2011, **107**, 1-5
120. T. Maka, D. N. Chirgrin, S. G. Romanov and C. M. Sotomayor Torres, *PIER*, 2003, **41**, 307-335.
121. J. M. van den Broek, L. A. Woldering, R. W. Tjerkstra, F. B. Segerink, I. D. Setija and W. L. Vos, *Adv. Func. Mater.*, 2012, **22**, 25-31.
122. M. R. Beaulieu, N. R. Hendricks and J. J. Watkins, *ACS Photonics*, 2014, **1**, 799-805.
123. L. Frezza, M. Patrini, M. Liscidini and D. Comoretto, *J. Phys. Chem. C*, 2011, **115**, 19939-19946.
124. F. Sordello, V. Maurino and C. Minero, *J. Mater. Chem.*, 2011, **21**, 19144-19152.
125. H. Ning, A. Mihi, J. B. Geddes Iii, M. Miyake and P. V. Braun, *Adv. Opt. Mater.*, 2012, **24**, 153-158.
126. J. Huang, X. Wang and Z. L. Wang, *Nano Lett.*, 2006, **6**, 2325-2331
127. R. Mitchell, PhD Thesis, Univerity of York, 2014.
128. R. Schroden, M. Al-Daous, C. Blanford and A. Stein, *Chem. Mater.*, 2002, **14**, 3305 - 3315.
129. X. Chen, J. Ye, S. Ouyang, T. Kako, Z. Li and Z. Zou, *ACS Nano*, 2011, **5**, 4310-4318.
130. X. D. Zhang, Z. Q. Zhang, L. M. Li, C. Jin, D. Zhang, B. Man and B. Cheng, *Phys. Rev. B*, 2000, **61**, 1892-1897
131. J.-C. Hong, J.-H. Park, C. Chun and D.-Y. Kim, *Adv. Func. Mater.*, 2007, **17**, 2462-2469.
132. C. E. Reese, A. V. Mikhonin, M. Kamenjicki, A. Tikhonov and S. A. Asher, *J. Am. Chem. Soc.*, 2004, **126**, 1493-1496
133. F. Fleischhaker, A. C. Arsenault, V. Kitaev, F. C. Peiris, G. von Freymann, I. Manners, R. Zentel and G. A. Ozin, *J. Am. Chem. Soc.*, 2005, **127**, 9318-9319
134. J. P. Ge and Y. D. Yin, *J. Mater. Chem.*, 2008, **18**, 5041-5045.
135. J. Ge, Y. Hu and Y. Yin, *Angew. Chem. Int. Ed.*, 2007, **46**, 5041-5045
136. C. I. Aguirre, E. Reguera and A. Stein, *Adv. Func. Mater.*, 2010, **20**, 2565-2578.
137. C. Becker, S. Linden, G. von Freymann, N. Tetreault, E. Vekris, V. Kitaev, G. A. Ozin and M. Wegener, *Phys. Status Solidi B-Basic Solid State Phys.*, 2006, **243**, 2354-2357.
138. L. D. Tuyen, J. H. Lin, C. Y. Wu, P. T. Tai, J. Tang, L. Q. Minh, H. C. Kan and C. C. Hsu, *Opt. Express*, 2012, **20**, 15418-15426.
139. D.-K. Hwang, H. Noh, H. Cao and R. P. H. Chang, *Appl. Phys. Lett.*, 2009, **95**, 091101 - 091104.
140. S. Kubo, A. Fujishima, O. Sato and H. Segawa, *J. Phys. Chem. C*, 2009, **113**, 11704-11711.

141. J. I. L. Chen, G. v. Freymann, S. Y. Choi, V. Kitaev and G. A. Ozin, *Adv. Mater.*, 2006, **18**, 1915-1919.
142. M. Fujita, S. Takahashi, Y. Tanaka, T. Asano and S. Noda, *Science*, 2005, **308**, 1296-1298
143. M. Barth, A. Gruber and F. Cichos, *Phys. Rev. B*, 2005, **72**, 085129-085133
144. J.-Y. Zhang, X.-Y. Wang, Y.-H. Ye and M. Xiao, *J. Mod. Opt.*, 2004, **51**, 2493-2501.
145. J. Martorell and N. M. Lawandy, *Phys. Rev. Lett.*, 1990, **65**, 1877-1880
146. Z. Y. Li and Z. Q. Zhang, *Phys. Rev. B*, 2001, **63**, 125106-125109
147. M. Megens, J. Wijnhoven, A. Lagendijk and W. L. Vos, *Phys. Rev. A*, 1999, **59**, 4727-4731
148. J. I. L. Chen, G. Von Freymen, V. Kitaev and G. A. Ozin, *J. Am. Chem. Soc.*, 2007, **129**, 1196 - 1202.
149. K. Lee and S. A. Asher, *J. Am. Chem. Soc.*, 2000, **122**, 9534-9537.
150. Y. Z. Zhang, J. X. Wang, Y. Zhao, J. Zhai, L. Jiang, Y. L. Song and D. B. Zhu, *J. Mater. Chem.*, 2008, **18**, 2650-2652.
151. J. Hu, X.-W. Zhao, Y.-J. Zhao, J. Li, W.-Y. Xu, Z.-Y. Wen, M. Xu and Z.-Z. Gu, *J. Mater. Chem.*, 2009, **19**, 5730-5736.
152. Y. Lu, H. Yu, S. Chen, X. Quan and H. Zhao, *Environ. Sci. Techol.*, 2012, **46**, 1724-1730.
153. N. Noor and I. P. Parkin, *J. Mater. Chem. C*, 2013, **1**, 984-996.
154. C. Cheng, S. K. Karuturi, L. Liu, J. Liu, H. Li, L. T. Su, A. I. Y. Tok and H. J. Fan, *Small*, 2012, **8**, 37-42.
155. Y.-Q. Zhang, J.-X. Wang, Z.-Y. Ji, W.-P. Hu, L. Jiang, Y.-L. Song and D.-B. Zhu, *J. Mater. Chem.*, 2007, **17**, 90-94.
156. R. Szamocki, A. Velichko, F. Mücklich, S. Reculusa, S. Ravaine, S. Neugebauer, W. Schuhmann, R. Hempelmann and A. Kuhn, *Electrochem. Commun.*, 2007, **9**, 2121-2127.
157. M. Zhou, J. Bao, Y. Xu, J. Zhang, J. Xie, M. Guan, C. Wang, L. Wen, Y. Lei and Y. Xie, *ACS Nano*, 2014, **8**, 7088-7098.
158. C. Lopez-Lopez, S. Colodrero, M. E. Calvo and H. Miguez, *Energy Environ. Sci*, 2013, **6**, 1260-1266.
159. A. Stadler, *Materials*, 2012, **5**, 661-683.
160. F. Zhu, K. Zhang, E. Guenther and C. S. Jin, *Thin Solid Films*, 2000, **363**, 314-317.
161. D.-J. Kwak, B.-H. Moon, D.-K. Lee, C.-S. Park and Y.-M. Sung, *J. Electr. Eng. Technol.*, 2011, **6**, 684-687.
162. S. K. Park, J. I. Han, W. K. Kim and M. G. Kwak, *Thin Solid Films*, 2001, **397**, 49-55.
163. B. H. Lee, K. Iee Gon, C. Sung Woo and S.-H. Lee, *Thin Solid Films*, 1997, **302**, 25-30.
164. A. L. M. Reddy, B. K. Gupta, T. N. Narayanan, A. A. Marti, P. M. Ajayan and G. C. Walker, *J. Phys. Chem. C*, 2012, **116**, 12803-12809.
165. E. V. A. Premalal, N. Dematage, S. Kaneko and A. Konno, *Electrochem.*, 2012, **80**, 624-628.
166. J. W. Galusha, C.-K. Tsung, G. D. Stucky and M. H. Bartl, *Chem. Mater.*, 2008, **20**, 4925-4930
167. F. E. Akkad and T. A. P. Paulose, *Appl. Surface Sci.*, 2014, **295**, 8-17
168. B. T. Holland, C. F. Blanford, T. Do and A. Stein, *Chem. Mater.*, 1999, **11**, 795-805.
169. A. V. Moholkar, S. M. Pawar, K. Y. Rajpure, C. H. Bhosale and J. H. Kim, *Appl. Surface Sci.*, 2009, **255**, 9358-9364.
170. A. I. Martinez and D. R. Acosta, *Thin Solid Films*, 2005, **483**, 107-113.
171. A. I. Martínez, L. Huerta, J. M. O. R. d. León, D. Acosta, O. Malik and M. Aguilar, *J. Phys. D: Appl. Phys.*, 2006, **39**, 5091.
172. Q. Gao, H. Jiang, C. Li, Y. Ma, X. Li, Z. Ren, Y. Liu, C. Song and G. Han, *J. Alloy. Compd.*, 2013, **574**, 427-431.
173. S. Baco, A. Chik and F. Md Yassin, *J. Sci. Technol.*, 2012, **4**.
174. D. Ali, *J. Opt.*, 2014, **16**, 075001.
175. M. Higashi, K. Domen and R. Abe, *J. Am. Chem. Soc.*, 2013, **135**, 10238-10241.
176. P. P. Edwards, A. Porch, M. O. Jones, D. V. Morgan and R. M. Perks, *J. Chem. Sco., Dalton Trans.*, 2004, 2995-3002.

177. J. Li, Y. Qiu, Z. Wei, Q. Lin, Q. Zhang, K. Yan, H. Chen, S. xiao, Z. Fan and S. Yang, *Energy Environ. Sci*, 2014.
178. F. L. Wang, N. K. Subbaiyan, Q. Wang, C. Rochford, G. W. Xu, R. T. Lu, A. Elliot, F. D'Souza, R. Q. Hui and J. D. Wu, *ACS Appl. Mater. Interfaces*, 2012, **4**, 1565-1572.
179. E. Yablonovitch, *Phys. Rev. Lett.*, 1987, **58**, 2059 - 2062.
180. T. Kaji, T. Yamada, S. Ito, H. Miyasaka, R. Ueda, S.-i. Inoue and A. Otomo, *J. Am. Chem. Soc.*, 2013, **135**, 106-109.
181. V. Jovic, T. Sohnel, J. B. Metson and G. I. N. Waterhouse, Editon edn., 2011, pp. 26-29.
182. Sigma Aldrich, *Product Specification: FTO coated glass*, https://www.sigmaaldrich.com/Graphics/COfAInfo/SigmaSAPQM/SPEC/73/735167/735167-BULK_____ALDRICH__.pdf.
183. R. R. Gagne, C. A. Koval and G. C. Lisensky, *Inorg. Chem.*, 1980, **19**, 2854-2855.
184. D. Pletcher, S. E. Group, R. Greff and R. Peat, *Instrumental Methods in Electrochemistry*, Ellis Horwood, 2001.
185. N. Tsierkezos, *J Solution Chem*, 2007, **36**, 289-302.
186. A. Sanusi, A. U. Moreh, B. Hamza, U. Sadiya, Z. Abdullahi, M. A. Wara, H. Kamaluddeen, M. A. Kebbe and U. F. Monsurat, *Int. J. Innov. Appl. Sci.*, 2014, **9**, 947-955.
187. Y. S. Avadhut, J. Weber, E. Hammarberg, C. Feldmann, I. Schellenberg, R. Pöttgen and J. Schmedt auf der Günne, *Chem. Mater.*, 2011, **23**, 1526-1538.
188. F. E. Akkad and S. Joseph, *J. Appl. Phys.*, 2012, **112**, 023501.
189. A. N. Banerjee, S. Kundoo, P. Saha and K. K. Chattopadhyay, *J. Sol-Gel Sci. Technol.*, 2003, **28**, 105-110.
190. A. Purwanto, H. Widiyandari and A. Jumari, *Thin Solid Films*, 2012, **520**, 2092-2095.
191. J. I. L. Chen and G. A. Ozin, *Adv. Mater.*, 2008, **20**, 4784-4788.
192. E. Yablonovitch and T. J. Gmitter, *Phys. Rev. Lett.*, 1989, **63**, 1950-1953.
193. S. John, *Phys. Rev. Lett.*, 1987, **58**, 2486-2489.
194. S. Colodrero, A. Mihi, L. Häggman, M. Ocaña, G. Boschloo, A. Hagfeldt and H. Míguez, *Adv. Mater.*, 2009, **21**, 764-770.
195. J. N. Winn, Y. Fink, S. Fan and J. D. Joannopoulos, *Opt. Lett.*, 1998, **23**, 1573-1575.
196. T. F. Krauss, R. M. D. L. Rue and S. Brand, *Nature*, 1996, **383**, 699-702.
197. X. a. Zhang, Y. Man, J. Wang, C. Liu and W. Wu, *Sci. China, Ser. E*, 2006, **49**, 537-546.
198. Z. Yang and T. Xu, *Abstr. Pap. Am. Chem. S.*, 2011, **242**, 1-3
199. G. von Freymann, S. John, S. Wong, V. Kitaev and G. A. Ozin, *Appl. Phys. Lett.*, 2005, **86**, 053108.
200. B. Y. Tong, P. K. John, Y. T. Zhu, Y. S. Liu, S. K. Wong and W. R. Ware, *J. Opt. Soc. Am. B: Opt. Phys.*, 1993, **10**, 356-359
201. S. H. A. Lee, N. M. Abrams, P. G. Hoertz, G. D. Barber, L. I. Halaoui and T. E. Mallouk, *J. Phys. Chem. B*, 2008, **112**, 14415-14421.
202. N. Pei-Gen, C. Bing-Ying and Z. Dao-Zhong, *Chinese Physics Letters*, 2002, **19**, 511.
203. Public Domain CC0 1.0, *Refractive Index Database*, http://refractiveindex.info/?shelf=glass&book=soda-lime&page=Rubin-clear, Accessed 17 August, 2015.
204. J. R. Lakowicz, *Principles of Fluorescence Spectroscopy*, 3rd edn., Springer, 2006.
205. F. Ambrosio, N. Martsinovich and A. Troisi, *J. Phys. Chem. Lett.*, 2012, **3**, 1531-1535.
206. F. Schiffmann, J. VandeVondele, J. Hutter, R. Wirz, A. Urakawa and A. Baiker, *J. Phys, Chem. C*, 2010, **114**, 8398-8404
207. P.-H. Xie, Y.-J. Hou, B.-W. Zhang, Y. Cao, F. Wu, W.-J. Tian and J.-C. Shen, *J. Chem. Soc., Dalton Trans.*, 1999, 4217-4221.
208. J. Delgado, Y. Zhang, B. Xu and I. R. Epstein, *J. Phys. Chem. A*, 2011, **115**, 2208-2215
209. D. Wang, R. Mendelsohn, E. Galoppini, P. G. Hoertz, R. A. Carlisle and G. J. Meyer, *J. Phys. Chem. B*, 2004, **108**, 16642-16653.

210. M. J. Lundqvist, E. Galoppini, G. J. Meyer and P. Persson, *J. Phys. Chem. A*, 2007, **111**, 1487-1497.
211. E. Rajkumar and S. Rajagopal, *Photochem. Photobiol. Sci.*, 2008, **7**, 1407-1414.
212. ISS, *Lifetime Data of Selected Fluorophores*, http://www.iss.com/resources/pdf/datatables/LifetimeDataFluorophores.pdf, Accessed 7th September, 2014.
213. D. Magde, G. E. Rojas and P. G. Seybold, *Photochem. Photobiol.*, 1999, **70**, 737-744.
214. G. Veerappan, D.-W. Jung, J. Kwon, J. M. Choi, N. Heo, G.-R. Yi and J. H. Park, *Langmuir*, 2014, **30**, 3010-3018.
215. X. Liu, J. M. Cole, P. G. Waddell, T.-C. Lin, J. Radia and A. Zeidler, *J. Phys. Chem. A*, 2012, **116**, 727-737.
216. Exciton, *Exciton Laser Dye Product List*, http://www.exciton.com/laserdyeslist.html, Accessed 13th August, 2015.
217. G. Jones, W. R. Jackson, C. Y. Choi and W. R. Bergmark, *J. Phys. Chem.*, 1985, **89**, 294-300.
218. X. Dong, X. Wang, L. Wang, H. Song, H. Zhang, W. Huang and P. Chen, *ACS Appl. Mater. Interfaces*, 2012, **4**, 3129-3133.
219. M. J. Price and S. Maldonado, *J. Phys. Chem. C*, 2009, **113**, 11988-11994.
220. L. Zhang, E. Reisner and J. J. Baumberg, *Energy Environ. Sci*, 2014, **7**, 1402-1408.
221. D. Chen, F. Huang, Y.-B. Cheng and R. A. Caruso, *Adv. Mater.*, 2009, **21**, 2206-2210.
222. B. Pejova, T. Kocareva, M. Najdoski and I. Grozdanov, *Appl. Surface Sci.*, 2000, **165**, 271-278.
223. I. Cesar, A. Kay, J. A. Gonzalez Martinez and M. Grätzel, *J. Am. Chem. Soc.*, 2006, **128**, 4582-4583.
224. F. L. Souza, K. P. Lopes, P. A. P. Nascente and E. R. Leite, *Sol. Energy Mater. Sol. Cells*, 2009, **93**, 362-368.
225. K. Balachandra-Kumar and P. Raji, *Recent Research Sci. and Technol.*, 2011, **3**, 48-52.
226. J. M. Ball, M. M. Lee, A. Hey and H. J. Snaith, *Energy Environ. Sci*, 2013, **6**, 1739-1743.
227. G. Li, V. Shrotriya, Y. Yao and Y. Yang, *J. Appl. Phys.*, 2005, **98**, 043704.
228. S. Ito, S. M. Zakeeruddin, R. Humphry-Baker, P. Liska, R. Charvet, P. Comte, M. K. Nazeeruddin, P. Péchy, M. Takata, H. Miura, S. Uchida and M. Grätzel, *Adv. Mater.*, 2006, **18**, 1202-1205.
229. C. Y. Ma, Z. Mu, J. J. Li, Y. G. Jin, J. Cheng, G. Q. Lu, Z. P. Hao and S. Z. Qiao, *J. Am. Chem. Soc.*, 2010, **132**, 2608-2613.
230. X. Dang, X. Zhang, X. Dong, W. Ruan, H. Ma and M. Xue, *RSC Advances*, 2014, **4**, 54655-54661.
231. J. Wang, H.-x. Zhong, Y.-l. Qin and X.-b. Zhang, *Angew. Chem. Int. Ed.*, 2013, **52**, 5248-5253.
232. Z. Lu, W. Zhu, X. Yu, H. Zhang, Y. Li, X. Sun, X. Wang, H. Wang, J. Wang, J. Luo, X. Lei and L. Jiang, *Adv. Mater.*, 2014, **26**, 2683-2687.
233. M. Minakshi, D. Appadoo and D. E. Martin, *Electrochem. Solid-State Lett.*, 2010, **13**, A77-A80.
234. T. Y. Ma, S. Dai, M. Jaroniec and S. Z. Qiao, *J. Am. Chem. Soc.*, 2014, **136**, 13925-13931.
235. S. Min-Jung, Y. Dong-Hwa, J. Joon-Hyung, M. Nam-Ki and H. Suk-In, *Jpn. J. Appl. Phys.*, 2006, **45**, 7197.
236. J. van Brakel and P. M. Heertjes, *Int. J. Heat Mass Transfer*, 1974, **17**, 1093-1103.
237. S. Xin, Y.-G. Guo and L.-J. Wan, *Acc. Chem. Res.*, 2012, **45**, 1759-1769.
238. J. Kibsgaard, Y. Gorlin, Z. Chen and T. F. Jaramillo, *J. Am. Chem. Soc.*, 2012, **134**, 7758-7765.
239. X. Lang, A. Hirata, T. Fujita and M. Chen, *Nat. Nano.*, 2011, **6**, 232-236.
240. M. Florescu, H. Lee, I. Puscasu, M. Pralle, L. Florescu, D. Z. Ting and J. P. Dowling, *Sol. Energy Mater. Sol. Cells*, 2007, **91**, 1599-1610.

241. X. Cui, Y. Wang, G. Jiang, Z. Zhao, C. Xu, Y. Wei, A. Duan, J. Liu and J. Gao, *RSC Advances*, 2014, **4**, 15689-15694.
242. X. Shi, K. Zhang, K. Shin, J. H. Moon, T.-W. Lee and J. H. Park, *Phys. Chem. Chem. Phys.*, 2013, **15**, 11717-11722.
243. L. Zhang, C.-Y. Lin, V. K. Valev, E. Reisner, U. Steiner and J. J. Baumberg, *Small*, 2014, **10**, 3970-3978.
244. Z. F. Liu, T. Ding, G. Zhang, K. Song, K. Clays and C. H. Tung, *Langmuir*, 2008, **24**, 10519-10523.
245. A. F. Koenderink, L. Bechger, H. P. Schriemer, A. Lagendijk and W. L. Vos, *Phys. Rev. Lett.*, 2002, **88**.
246. Y. Ma, J.-F. Chen, Y. Ren and X. Tao, *Colloids Surf., A*, 2010, **370**, 129-125
247. W. W. Yu and X. Peng, *Angew. Chem. Int. Ed.*, 2002, **41**, 2368-2371.
248. W. Sun, M. Xie, L. Jing, Y. Luan and H. Fu, *J. Solid State Chem.*, 2011, **184**, 3050-3054.
249. K. Maeda and K. Domen, *J. Phys. Chem. Lett .,* 2010, **1**, 2655-2661.
250. Q. Liu, Q. Chen, J. Bai, J. Li, J. Li and B. Zhou, *J. Solid State Electrochem.*, 2014, **18**, 157-161.
251. N. Li, X. Zhang, S. Chen, X. Hou, Y. Liu and X. Zhai, *Mater. Sci Eng., B*, 2011, **176**, 688-691.
252. J. Fang, L. Xu, Z. Y. Zhang, Y. P. Yuan, S. W. Cao, Z. Wang, L. S. Yin, Y. S. Liao and C. Xue, *ACS Appl. Mater. Interfaces*, 2013, **5**, 8088-8092.
253. T. Daniels-Race and S. Thiruvengadam, *Microw. Opt. Technol. Lett.*, 2011, **53**, 1018-1021.
254. S. K. Karuturi, J. Luo, C. Cheng, L. Liu, L. T. Su, A. I. Y. Tok and H. J. Fan, *Adv. Mater.*, 2012, **24**, 4157-4162.
255. Y.-L. Lee, C.-F. Chi and S.-Y. Liau, *Chem. Mater.*, 2010, **22**, 922-927.
256. D. Ogermann, T. Wilke and K. Klienermanns, *Open J. Phys. Chem.*, 2012, **2**, 47-57.
257. C. Ching-Fa, L. Shih-Yi and L. Yuh-Lang, *Nanotechnol.*, 2010, **21**, 025202.
258. OPVAP, http://opvap.com/eqe.php.
259. R. Trevisan, P. Rodenas, V. Gonzalez-Pedro, C. Sima, R. S. Sanchez, E. M. Barea, I. Mora-Sero, F. Fabregat-Santiago and S. Gimenez, *J. Phys. Chem. Lett.,* 2013, **4**, 141-146.
260. A. J. E. Rettie, H. C. Lee, L. G. Marshall, J.-F. Lin, C. Capan, J. Lindemuth, J. S. McCloy, J. Zhou, A. J. Bard and C. B. Mullins, *J. Am. Chem. Soc.*, 2013, **135**, 11389-11396.
261. G. Wang, Y. Ling, X. Lu, F. Qian, Y. Tong, J. Z. Zhang, V. Lordi, C. Rocha Leao and Y. Li, *J. Phys. Chem. C*, 2013, **117**, 10957-10964.
262. K. Sayama, A. Nomura, T. Arai, T. Sugita, R. Abe, M. Yanagida, T. Oi, Y. Iwasaki, Y. Abe and H. Sugihara, *J. Phys. Chem. B*, 2006, **110**, 11352-11360.
263. A. Walsh, Y. Yan, M. N. Huda, M. M. Al-Jassim and S.-H. Wei, *Chem. Mater.*, 2009, **21**, 547-551.
264. F. Wang, M. Shao, L. Cheng, J. Hua and X. Wei, *Mater. Res. Bull.*, 2009, **44**, 1687-1691.
265. Y. Ma, S. R. Pendlebury, A. Reynal, F. Le Formal and J. R. Durrant, *Chem. Sci.*, 2014, **5**, 2964-2973.
266. D. Cao, W. Luo, J. Feng, X. Zhao, Z. Li and Z. Zou, *Energy Environ. Sci*, 2014, **7**, 752-759.
267. C. Liu, J. Su, J. Zhou and L. Guo, *ACS Sus. Chem. Eng.*, 2016, **4**, 4492-4497
268. H. R. Kim, G. Kim, S.-I. In and Y. Park, *Electrochim. Acta*, 2016, **189**, 252-258.
269. Y. Surendranath, M. W. Kanan and D. G. Nocera, *J. Am. Chem. Soc.*, 2010, **132**, 16501-16509.
270. S. Zhao, C. Li, H. Huang, Y. Liu and Z. Kang, *J. Materiomics*, 2015, **1**, 236-244.
271. S. K. Pilli, T. G. Deutsch, T. E. Furtak, J. A. Turner, L. D. Brown and A. M. Herring, *Phys. Chem. Chem. Phys.*, 2012, **14**, 7032-7039.
272. S. K. Pilli, R. Janarthanan, T. G. Deutsch, T. E. Furtak, L. D. Brown, J. A. Turner and A. M. Herring, *Phys. Chem. Chem. Phys.*, 2013, **15**, 14723-14728.
273. Y. Zhang, D. Wang, X. Zhang, Y. Chen, L. Kong, P. Chen, Y. Wang, C. Wang, L. Wang and Y. Liu, *Electrochim. Acta*, 2016, **195**, 51-58.
274. H. Liu, R. Nakamura and Y. Nakato, *ChemPhysChem*, 2005, **6**, 2499-2502.
275. T. Shimidzu, T. Iyoda and K. Izaki, *J. Phys. Chem.*, 1985, **89**, 642-645.

276. G. Wider and L. Dreier, *J. Am. Chem. Soc.*, 2006, **128**, 2571-2576.